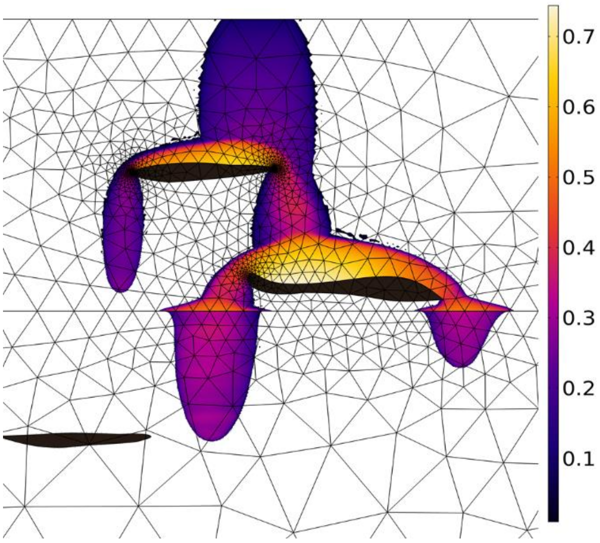

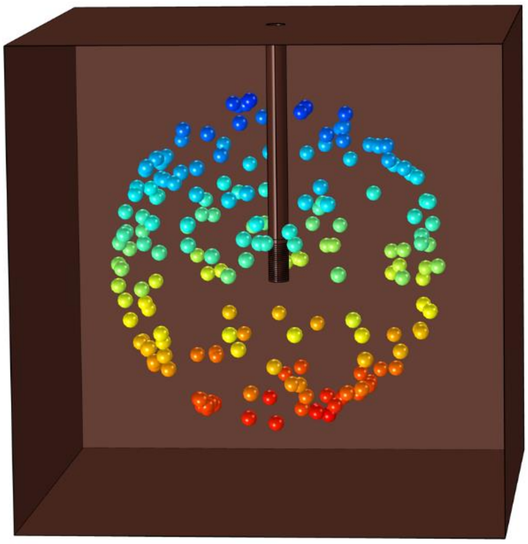

Numerical modelling of the dynamics of chlorinated solvent pollution in aquifers and their remediation with engineered nano-particles: An integrated approach

Shikhar Nilabh

PhD thesis

VNiVERSiDAD
D SALAMANCA
CAMPUS OF INTERNATIONAL EXCELLENCE

AMPHOS 21
SCIENTIFIC AND STRATEGIC ENVIRONMENTAL CONSULTING

VNiVERSiDAD D SALAMANCA
CAMPUS OF INTERNATIONAL EXCELLENCE

AMPHOS 21
SCIENTIFIC AND STRATEGIC ENVIRONMENTAL CONSULTING

Numerical modelling of the dynamics of chlorinated solvent pollution in aquifers and their remediation with engineered nano-particles: An integrated approach

A thesis submitted in fulfilment of the requirements for the degree of Doctor of
Philosophy in the Department of Chemistry under the doctoral program
¨*Geología*¨ at the University of Salamanca

Shikhar Nilabh

Supervisor: Dr. Fidel Grandia
Tutor: Dr. Antonio Martínez Graña

VNiVERSiDAD
Ð SALAMANCA
CAMPUS OF INTERNATIONAL EXCELLENCE

Fidel Grandia, Director de Proyectos en Amphos21 Consulting S.L, Barcelona

Antonio Martínez Graña, Tutor en Departamento de Geología, Universidad de Salamanca

HACEN CONSTAR:

Que el trabajo titulado "*Numerical modelling of the dynamics of chlorinated solvent pollution in aquifers and their remediation with engineered nano-particles: An integrated approach*" ha sido realizado por el Licenciado en geología Shikhar Nilabh para optar al Grado de Doctor en Geología, dentro del Programa de Doctorado "Geología".

Considerando que constituye un trabajo original de investigación, se encuentra concluido, y cumple todos los requisitos exigibles para su defensa pública, autorizan su presentación

En Salamanca, a 11 de Junio de 2021,

Fidel Grandia
Director de Proyectos
Amphos21 Consulting S.L, Barcelona

Antonio Martínez Graña
Departamento de Geología
Universidad de Salamanca

Abstract

The global water shortage is one of the main environmental concerns in the 21st century. The main source of drinking water is the groundwater that flows in the subsurface. The increased agriculture and industrial activities in the last few decades have been proven to be detrimental for groundwater. While these water resources are limited, the scarcity is further triggered by the loss of quality due to anthropogenic activities such as waste deposition and landfill leakage. Contaminants from the anthropogenic waste often migrates through the sub-surface and reach an underlying aquifer. The occurrence of these contaminants threatens the quality of water resources and often requires remediation efforts. Several *in-situ* and *ex-situ* remediation methodologies have been developed and tested in the last decades; recently, the use of Engineered Nano-Particles (ENPs) for *in-situ* contaminant degradation have gained a lot of interest in the field of groundwater remediation. These ENPs have been found to be effective due to their high reactive surface area, minimal disruption of the groundwater system and their aggressive contaminant degradation capabilities. However, the field scale implementation of this remediation technique is often challenging, as each polluted site require a custom design and strategy of remediation.

The field scale remediation of groundwater using ENPs requires a lot of scientific investigation and technical resources, owing to complexity and the limited accessibility of the contamination-groundwater system. Therefore, it is necessary to develop a robust remediation strategy which includes laboratory scale and field scale studies as well as application of a numerical approach. The success in the remediation effort is often limited by lack of detailed understanding of the contaminant and hydrogeological properties of the aquifer. While, the information of contamination-aquifer dynamics can be studied at field, knowledge on the continuous and consistent contamination behavior on both temporal and spatial scale is often missing. The use of an integrated numerical model can be helpful for bridging the gap between the field studies and the relevant insights required for groundwater remediation.

In this PhD thesis, five Research Works (RW) have been developed intended to build an integrated numerical approach for the assessment of the contamination of chlorinated solvents in groundwater and their remediation using ENPs:

- RW1: The development of a multiscale multiphase flow in porous media simulation on the software Comsol Multiphysics and verify the result with reported benchmark study in literature (Chapter 3).
- RW2: The development of a field-scale, DNAPL infiltration model using the available but limited data of aquifer in the Innovation Garage Laboratory in Denmark (Chapter 3).
- RW3: The implementation of a numerical formulation on Comsol Multiphysics for nano-particle injection in a porous media and verify the model result with reported benchmark study in literature (Chapter 4).
- RW4: The implementation of an inverse and forward nano-particle transport simulation in porous m edia at column sand scale and tank sand scale (Chapter 4).
- RW 5: The conceptualization and the development of a numerical simulation for an end-to-end remediation strategy implemented on a hypothetical aquifer (Chapter 5).

In RW1, the objective has been the review of the existing numerical formulations for two-phase flow in a porous media, their implementation into Comsol software, and their validation through benchmark models. First, the infiltration of contaminant (DNAPL) in a 1 -dimension small-scale homogeneous sand has been developed and matched with the benchmark model. In a second stage, a 2-dimensional model has been built with the aquifer domain consisting of several sand layers. The result shows that the numerical formulation is in good agreement with the results from benchmark model. Using this validated numerical formulation, the RW2 has consisted in the development of an upscaled 3D model of a general groundwater system scenario. The objective for this exercise has been the comprehensive study of migration of DNAPL in the real field conditions to demonstrate the potential of numerical modelling in the understanding of the migration pathways of the contaminants. Overall, the results of this RW show that numerical modelling can serve as a very convenient tool in the support of the remediation campaigns.

In RW3, a numerical formulation of the transport of Engineered Nano-particles (ENPs) has been implemented on Comsol software and verified using the benchmark models published in literature. On this verified formulation, the inverse model has been built to determine the parameter values driving the ENPs mobility in sand-filled columns performed in the frame of the Metal-Aid EC-funded project (RW4). The sensitivity analysis has been also performed to demonstrate the extent of the uncertainty associated with each parameter. Finally, the parameters obtained have been used to simulate the ENPs injection in a sand-filled tank. The model uses a simplistic velocity independent parameter for simulation in absence of necessary data, and, thus, the predictive results have been different from the results observed in laboratory. Nevertheless, the modeling exercise in RW4 shows the potential of the numerical approach to simulate nano-particle injection in the aquifer.

Once individual numerical models on contaminant mobility and ENPs transport have been validated, an integrated numerical framework has been built (RW 5). The contaminant infiltration in a 2-dimensional domain has been simulated using the same two-phase formulation as in RW2. The contaminant (TCE) source zone architecture predicted by model has been used for modeling the dissolution and transport of aqueous contaminant. The model predicts that the spatial and temporal distribution of contaminant is very important for the remediation using nano-particles. From these results, the model further predicts the simulation of the injection of ENPs and their transport underground, and the reaction with the contaminant plume.

As a general conclusion, this PhD research demonstrates that the development of a robust numerical approach that can provide an end-to-end modeling solution for a general remediation strategy using ENPs injection in a contaminated aquifer.

Resumen

La escasez mundial de agua es una de las principales preocupaciones ambientales del siglo XXI. La principal fuente de agua potable es el agua subterránea que fluye en el subsuelo. Se ha demostrado que el aumento de las actividades agrícolas e industriales en las últimas décadas es perjudicial para las aguas subterráneas. Si bien estos recursos hídricos son limitados, la escasez se desencadena aún más por la pérdida de calidad debido a actividades antropogénicas como la deposición de desechos y las fugas en vertederos. Los contaminantes de los desechos antropogénicos a menudo migran a través del subsuelo y llegan a un acuífero subyacente. La aparición de estos contaminantes amenaza la calidad de los recursos hídricos y, a menudo, requiere esfuerzos de remediación. En las últimas décadas se han desarrollado y probado varias metodologías de remediación in situ y ex situ; Recientemente, el uso de nanopartículas de ingeniería (ENP) para la degradación de contaminantes in situ ha ganado mucho interés en el campo de la remediación de aguas subterráneas. Se ha descubierto que estos ENP son eficaces debido a su alta superficie reactiva, la mínima interrupción del sistema de aguas subterráneas y sus agresivas capacidades de degradación de contaminantes. Sin embargo, la implementación a escala de campo de esta técnica de remediación a menudo es un desafío, ya que cada sitio contaminado requiere un diseño y una estrategia de remediación personalizados.

La remediación de aguas subterráneas a escala de campo utilizando ENPs requiere mucha investigación científica y recursos técnicos, debido a la complejidad y la accesibilidad limitada del sistema de contaminación-aguas subterráneas. Por lo tanto, es necesario desarrollar una estrategia de remediación sólida que incluya estudios a escala de laboratorio y de campo, así como la aplicación de un enfoque numérico. El éxito en el esfuerzo de remediación a menudo se ve limitado por la falta de un conocimiento detallado de las propiedades hidrogeológicas y de contaminantes del acuífero. Si bien la información sobre la dinámica de la contaminación y el acuífero se puede estudiar en el campo, a menudo se carece de conocimiento sobre el comportamiento continuo y constante de la contaminación, tanto a escala temporal como espacial. El uso de un modelo numérico integrado puede ser útil para cerrar la brecha entre los estudios de campo y los conocimientos relevantes necesarios para la remediación de aguas subterráneas.

En esta tesis doctoral, se han desarrollado cinco Trabajos de Investigación (RW) destinados a construir un enfoque numérico integrado para la evaluación de la contaminación de disolventes clorados en aguas subterráneas y su remediación mediante ENPs:

- RW1: El desarrollo de un flujo multifásico multiescala en la simulación de medios porosos en el software Comsol Multiphysics y verificar el resultado con un estudio de referencia reportado en la literatura (Capítulo 3).

- RW2: El desarrollo de un modelo de infiltración de DNAPL a escala de campo utilizando los datos disponibles pero limitados del acuífero en el Laboratorio de Innovation Garage en Dinamarca (Capítulo 3).

- RW3: La implementación de una formulación numérica en Comsol Multiphysics para la inyección de nanopartículas en un medio poroso y verificar el resultado del modelo con un estudio de referencia reportado en la literatura (Capítulo 4).

- RW4: La implementación de una simulación de transporte de nanopartículas inverso y directo en medios porosos a escala de arena de columna y escala de arena de tanque (Capítulo 4).

- RW 5: La conceptualización y el desarrollo de una simulación numérica para una estrategia de remediación de extremo a extremo implementada en un acuífero hipotético (Capítulo 5).

En RW1, el objetivo ha sido la revisión de las formulaciones numéricas existentes para flujo bifásico en un medio poroso, su implementación en el software Comsol y su validación a través de modelos de referencia. En primer lugar, se desarrolló la infiltración de contaminante (DNAPL) en una arena homogénea de pequeña escala de una dimensión y se comparó con el modelo de referencia. En una segunda etapa, se ha construido un modelo bidimensional con el dominio del acuífero formado por varias capas de arena. El resultado muestra que la formulación numérica está de acuerdo con los resultados del modelo de referencia. Usando esta formulación numérica validada, el RW2 ha consistido en el desarrollo de un modelo 3D mejorado de un escenario general del sistema de agua subterránea. El objetivo de este ejercicio ha sido el estudio integral de la migración de DNAPL en las condiciones reales de campo para demostrar el potencial del modelado numérico en la comprensión de las rutas de migración de los contaminantes. En general, los resultados de este RW muestran que el modelado numérico puede servir como una herramienta muy conveniente en el apoyo de las campañas de remediación.

En RW3, se implementó una formulación numérica del transporte de nanopartículas de ingeniería (ENP) en el software Comsol y se verificó utilizando los modelos de referencia publicados en la literatura. Sobre esta formulación verificada, se ha construido el modelo inverso para determinar los valores de los parámetros que impulsan la movilidad de los ENP en columnas rellenas de arena realizadas en el marco del proyecto financiado por Metal-Aid EC (RW4). El análisis de sensibilidad también se ha realizado para demostrar el alcance de la incertidumbre asociada con cada parámetro. Finalmente, los parámetros obtenidos se han utilizado para simular la inyección de ENPs en un tanque lleno de arena. El modelo utiliza un parámetro simplista independiente de la velocidad para la simulación en ausencia de los datos necesarios y, por lo tanto, los resultados predictivos han sido diferentes de los resultados observados en el laboratorio. Sin embargo, el ejercicio de modelado en RW4 muestra el potencial del enfoque numérico para simular la inyección de nanopartículas en el acuífero.

Una vez que se han validado los modelos numéricos individuales sobre movilidad de contaminantes y transporte de ENP, se ha construido un marco numérico integrado (RW 5). La infiltración de contaminantes en un dominio bidimensional se ha simulado utilizando la misma formulación de dos fases que en RW2. La arquitectura de la zona fuente de contaminantes (TCE) predicha por el modelo se ha utilizado para modelar la disolución y el transporte de contaminantes acuosos. El modelo predice que la distribución espacial y temporal de contaminantes es muy importante para la remediación mediante nanopartículas. A partir de estos resultados, el modelo predice además la simulación de la inyección de ENP y su transporte subterráneo, y la reacción con la pluma contaminante.

Como conclusión general, esta investigación de doctorado demuestra que el desarrollo de un enfoque numérico robusto que puede proporcionar una solución de modelado de extremo a extremo para una estrategia de remediación general utilizando la inyección de ENP en un acuífero contaminado.

Acknowledgements

This doctoral study has been developed as part of the Innovative Training Network (ITN) Metal-Aid project “Metal oxide Aided Subsurface Remediation: From Invention to Injection” funded by the Marie Skłodowska Curie Actions program of the European Commission (contract number 675219).

I would like to express my sincere gratitude to my supervisor Dr. Fidel Grandia for his consistent guidance, motivation and insightful feedback. I am grateful to the collaborators of Metal-Aid project, specially to Flavia Digiacomo and Markus Reischer, for allowing me to use their experimental data required for my research work. I would also like to thank the colleagues at my host institution, Amphos 21 Consulting S.L., for their valuable suggestions and discussion sessions which was helpful in my research work.

I acknowledge with a deep sense of reverence, my gratitude towards my parents for their enormous support and encouragement. Additionally, I am also thankful to my friends back in India, with whom I developed my interest in research during my college days.

Table of Contents

List of Figures

List of Tables

1 Introduction

1.1 The concern about groundwater pollution

Underground aquifer serves as the predominant source for the freshwater for human consumption. However, the availability of this freshwater is limited, with 0.36% of the total water worldwide (Kumar Reddy et al., 2012). Despite water being regarded as the world's most essential natural resource, yet freshwater systems have been adversely affected by human activities (Vörösmarty et al., 2010). The advancement in industrial and agricultural sectors has led to a rapid groundwater exploitation. Figure 1-1 shows the evolution of global water resources used by different sectors. In the recent times, the freshwater resources are majorly consumed by agriculture sector (estimated at 70%), with remaining 30 % used by industries and municipal agencies.

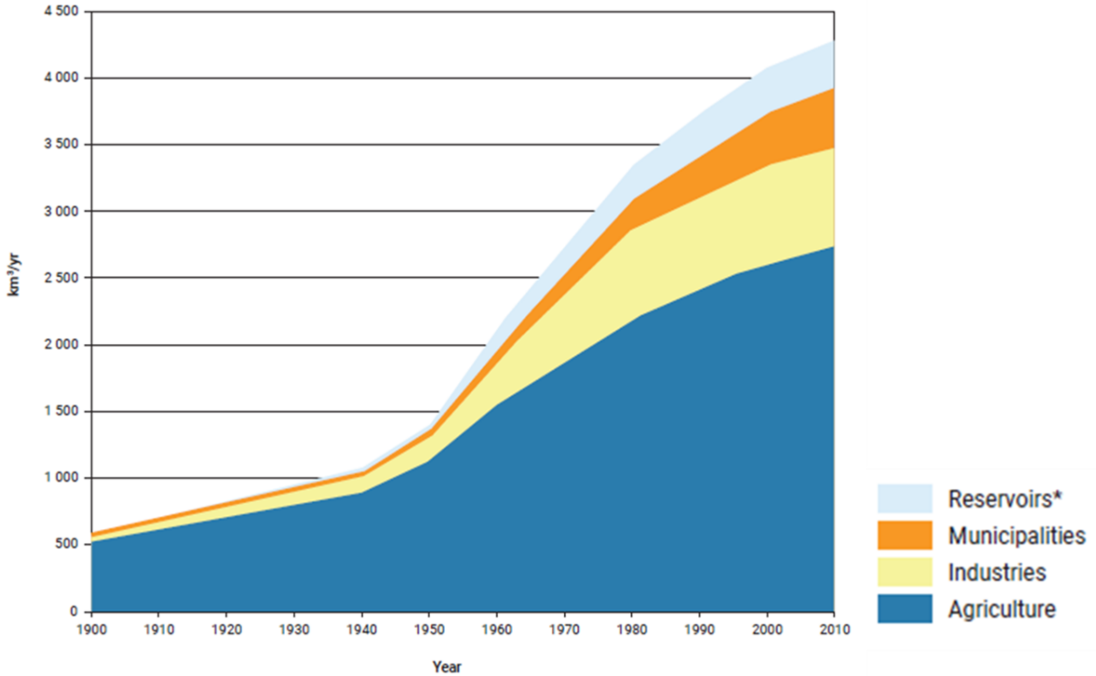

*Evaporation of water from the artificial lakes and reservoir contributes to the consumption of water resources.

***Figure 1-1**: The global evolution of water resources utilization in different sector over a period of 100 years (Source: Aquastat, 2010).*

Presently, 780 million people, or approximately 11% of the world's population, has no access to safe drinking water (UNICEF and World Health Organization, 2012). Many studies indicate that the problem will worsen due to increasing global demands with the increase in population pressure, higher welfare, production of water intensive biofuels, and climatic change (Kummu et al., 2010). With this trend, the global demand for water is expected to nearly double over the next 15 years. The threatening environmental concern endangers the smooth functioning of communities, industries, food production and the environment, eventually leading to the global water crisis.

The water scarcity is triggered by not just the quantity of water resources but also by the quality of water on a global scale. The polluted water endangers the health of 1.2 million people with several water borne diseases (Ganoulis, 2009). Singh and Naidu (2012) estimated more than three million contaminated groundwater sites all over the world. Additionally, a report from the European commission estimates a total of 0.3 million contaminated groundwater sites, out of which 14% requires serious measures for removal of contaminants (Gomes, 2014). While some of the aquifers are polluted by natural processes making the water not potable for drinking, several other aquifers, which are otherwise deemed suitable for drinking, are threatened by anthropogenic waste (Przydatek et al., 2019). The anthropogenic contamination is not a new phenomenon since the advent of mining activities around 1000 years back already impacted groundwaters (Swartjes, 2011). In the past century with the industrial revolution and technological development along with weak environmental protection policies, the soil contamination problem got worse (Vörösmarty et al., 2010).

Currently, the developed countries in North America and Europe have built a legal framework to classify and deal with contaminated soils (Jennings, 2013; Rodrigues et al., 2009). However, the implementation of any legal or remediation measures is undermined due to difficulty in objectively defining the "contaminated land" or "site contamination" (Naidu, 2013).

1.2 The concept of DNAPL

The term Non-Aqueous Phase Liquid (NAPL) was first used for the hazardous waste landfill in Niagara falls during early 1980s (Pankow and Cherry, 1996). Prior to 1980s, such contaminant had been referred to a "fluid immiscible with water" due to their existence in a separate phase in groundwater combined with a hydrophobic nature (Levy, 2003). With time, the sparingly soluble nature of these immiscible fluid was recognized, and NAPL was deemed as a more reasonable term for these fluids (Corey, 1994; Levy, 2003; Morel-Seytoux, 1969). NAPLs occurring in a different phase show a range in the relative density with respect to water. The NAPLs which have higher density that water and, thus, have a tendency to migrate downward in an aquifer system are termed as Dense Non-Aqueous Phase Liquid (Erning, 2013). Because DNAPLs have a density greater than that of water, the gravitational force leads to the major amounts of DNAPL infiltrating through the vadose zone to the capillary fringe all the way down to the aquifer. As DNAPL plume advances in the aquifer, a residual form of DNAPL is left behind due to varying capillary pressure in the small-scale heterogeneities present in the aquifer system (Lerner et al., 2003). These residual DNAPL have a lower saturation ranging from 0.01 to 0.15 (Nambi and Powers, 2003) and are called *DNAPL ganglia*. Additionally, DNAPL plume tends to accumulate at the heterogeneous interface present in the aquifer resulting in a *DNAPL pool* (Heiderscheidt, 2005). Chemically, DNAPL consists of organic or inorganic solvents that are at the liquid form in a natural groundwater setting. A major class of DNAPL comprises chlorinated solvents, frequently encountered in contaminated groundwater site.

1.2.1 Chlorinated solvents

Chlorinated solvents are hydrocarbon compounds where several hydrogen atoms are exchanged with a chlorine atom. The most abundant chlorinated solvents are tetrachloroethylene (PCE), trichloroethylene (TCE), 1,1,1-Trichloroethane, dichloromethane (DCM), trichloromethane (Chloroform), carbon tetrachloride (CT), 1,2-Dichloroethane, 1,2-Dichlorobenzene, 1,3-Dichlorobenzene, 1,1,2-Trichloroethane and 1,1,4-Trichlorobenzene. Chlorinated solvents have been considered among the most serious groundwater contaminants in industrialized countries (Pankow and Cherry, 1996) since nine out of 20 most frequently detected groundwater contaminants are chlorinated solvents (Table 1-1; Levy, 2003).

Table 1-1*: Top 20 contaminants in the subsurface all over the world along with their industrial application (Levy, 2003).*

	Contaminant	**Industrial application**
1	Trichloroethylene (TCE)	Metal cleaning/degreasing
2	Lead gasoline	Mining, construction material (pipes)
3	Tetrachloroethylene (PCE)	Dry cleaning, chemical intermediate
4	Benzene gasoline	Manufacturing
5	Toluene gasoline	Manufacturing
6	Chromium	Metal plating
7	Methylene chloride (DCM)	Aerosol, paint removal, manufacturing
8	Zinc manufacturing	Mining
9	1,1,1-Trichloroethane (TCA)	Metal and plastic cleaning/degreasing
10	Arsenic	Mining, manufacturing
11	Chloroform (TCM)	Solvents, rubber manufacturing
12	1,1-Dichloroethane (1,1-DCA)	Degreasing, solvents, manufacturing
13	Trans-1,2-Dichloroethene (1,2-DCE)	Transformation product of TCA
14	Cadmium	Mining, plating
15	Manganese	Manufacturing, mining
16	Copper	Manufacturing, mining
17	1,1-Dichloroethene (1,1-DCE)	Manufacturing
18	Vinyl chloride	Plastic and record manufacturing
19	Barium	Manufacturing, energy production
20	1,2-Dichloroethane (1,2-DCA)	Solvent, manufacturing

Chlorinated solvents find a lot of utility in industries and the manufacturing sector, such as dry cleaning, metal degreasing, pharmaceutical production, pesticide formulation manufacturing of resin, rubber, fumigant, insecticides, perfume dye and paint (Levy, 2003; Pankow and Cherry, 1996). Chlorinated solvents are characterized by their distinct density, viscosity, interfacial tension with water, component composition, solubility in water, vapor pressure and wettability.

Common physiochemical properties of typical DNAPL are shown in Table 1-2 (Lerner et al., 2003).

Table 1-2: *The general physiochemical properties of common DNAPL at 25ºC (Lerner et al., 2003).*

Chlorinated solvent	Molecular weight	Solubility ($mg \cdot L^{-1}$)	Density ($kg \cdot m^{-3}$)	Vapour pressure (Pa)	Viscosity (cP)	Koc ($l \cdot kg^{-1}$)
Trichloroethylene(TCE)	131.4	1,100	1460	9,000	0.57	126
Tetrachloroethylene(PCE)	165.8	200	1620	2,600	0.9	364
Tetrachloromethane	153.8	790	1590	15,000	0.97	439
Trichloromethane	119.4	8,000	1480	26,000	0.56	44
Chlorobenzene	112.6	500	1110	1,580	0.8	330
1,1,1-trichloroethane	133.4	1,320	1330	16,000	0.84	152

Chlorinated solvents generally have a high volatility (high vapor pressure), and it initially was believed that they would be removed through evaporation before the DNAPL plume encounters water table (Erning, 2013). However, the reality is that chlorinated solvents are a persistent source of dissolved contamination in a temporal scale of decades to centuries in the aquifers (Pankow and Cherry, 1996). Their persistence is attributed to their low solubility in water (from few $mg \cdot L^{-1}$ to $g \cdot L^{-1}$ (Lerner et al., 2003). Despite this low solubility, the concentration of chlorinated solvents dissolved in the aqueous phase exceeds the limit for safe water consumption by several orders of magnitude (Heiderscheidt, 2005). For example, TCE and PCE have solubilities as high as 1.1 $g \cdot L^{-1}$ and 0.2 $g \cdot L^{-1}$ at 20ºC, respectively. The maximum concentration limit (MCL) recommended by the EPA is 5 $\mu g \cdot L^{-1}$ for both compounds (Levy, 2003). Chlorinated solvents exceeding this concentration are also considered a direct health risk to human organs such as respiratory tract, eyes, epidermis, liver, kidney and the central nervous system (Erning, 2013). Also, TCE, chloroform and carbon tetrachloride are suspected to be carcinogens (Pankow and Cherry, 1996).

1.3 Remediation of aquifers polluted by chlorinated solvents: The Zero Valent iron particles

Sites polluted with chlorinated solvent poses a great threat to water resources and a long-term remediation plan becomes important. The remediation of sites polluted with chlorinated solvents has been traditionally dealt with the pump and treat strategy (Powers et al., 1994), which is done by increasing the groundwater flow through pumping which results in enhanced depletion of contaminant source. However, this methodology has a limited success because the dissolution of DNAPL in groundwater is often rate limited and, thus, a persistent contaminant as a free phase continues prevailing in the aquifer (Kaluarachchi, 2000; Keely,1989). The DNAPL source can have much longer persistence than the feasible implementation period of pump and treatment.

On the other hand, chlorinated solvent contamination has long been dealt through their biological degradation (biotic dechlorination) (He et al., 2015; Phenrat et al., 2007). However, bio-remediation has its own disadvantages. For instance, the reaction pathway for biotic degradation results in toxic intermediates such as dichloroethene and vinyl chloride (Han and Yan, 2016; Lojkasek-Lima et al., 2012).

Permeable Reactive Barriers (PRBs) consisting of reactants such as Zero Valent Iron (ZVi) appeared as much efficient *in-situ* method during 1990s (Gillham et al., 1994) This methodology is based on the creation of a reduced zone (low Eh) in the subsurface, where the contaminant undergoes reductive dechlorination. The electron enabling reductive dechlorination is provided by Fe (0) through a surface-mediated reaction. This promotes abiotic degradation of the contaminant. The advantage of this method over the biotic method is that the degradation product of ZVi is much more benign and non-toxic in nature. The disadvantage is that while PRB has been effective in reducing contaminants, its reactivity is limited due to surface passivation. The surface passivation occurs as the oxidized surface iron hinders the electron transfer for contaminant degradation.

In the last two decades, the application of ZVi for groundwater remediation has undergone dramatic changes. In the late 1990s, a high surface area of ZVi sufficient for contaminant degradation was thought to be relevant. Thus, ZVi in the form of nano-particles (nZVi) appeared as a better substitute for granular ZVi. nZVi with its high surface area results in greater reactive sites for contaminant degradation, significantly increasing the degradation capability. Additionally, owing to its small size, nZVi can be injected in the aquifers and soils, and transported where the contaminant removal is more convenient. nZVi has proven to degrade a wide range of products such as chlorinated solvents, heavy metals, pesticides and toxic inorganic ions, and its commercial application has been common in the last two decades (Kocur, 2015; Li, 2006).

The efficiency of chlorinated solvent degradation by reaction with ZVi is often limited by two significant physiochemical phenomena: (1) Particle aggregation of nZVi due to magnetic forces and mobility restriction (Phenrat et al., 2007), and (2) electron capture competition with water molecules.

In the first case, a number of experimental and field studies have found that the mobility of nZVi in the subsurface is in the order of few inches (Li et al., 2006). The combined effect of aggregation and high particle density leads to pore clogging, reducing the flow and the interaction with the contaminant. The electrostatic particle aggregation is overcome by the use of a biopolymer coating of nZVi particles, which reduces the agglomeration of particles by creating steric hindrance (Dalla et al., 2002). While several biopolymers have been tested, the use of carboxymethyl cellulose (CMC), an organic polymer, has gathered the greatest interest in the recent studies (CMC–nZVi, Shi et al., 2015). The surface modification with CMC enhances the mobility of nZVi due to the electrostatic repulsion which counters the effect of magnetic attraction forces (Kocur et al., 2013).

On the other hand, water takes most of the electrons provided by nZVi, leading to little degradation of contaminant and production of H_2 gas. Fan et al. (2017) found in *batch* experiments that 95% of electron was transferred to water and only 5% for contaminant reduction. 60 days after the injection in aquifers, nZVi particles were assumed to get corroded completely by water. Even for the few electrons available for contaminant, the surface reaction is kinetically slow. This is due to the magnetite (Fe_3O_4) and maghemite (Fe_2O_3) formed at the surface that hinders the electron transfer from core to the reactive site (Sarathy et al., 2008). Thus, the reduced effectiveness and persistence of nZVi becomes challenging for an efficient remediation strategy (Kim et al., 2013).

To counter the electron competition problem, a number of studies have focused on the treatment of the surface functionalization for nZVi, which has emerged promising for an efficient remediation strategy (Fan et al., 2017; Li et al., 2017; Rajajayavel et al., 2015; Kim et al., 2011). It has been reported that the incorporation of low valent form of sulfur in the oxide layers results in a selective reduction of organic contaminants with little or negligible hydrogen production (Fan et al., 2017). The higher electron availability for chlorinated solvents results in an aggressive reductive dechlorination. The modification of nZVi surfaces with sulfur (sZVi) has been the focus of the latest geochemical studies, and they have recently reported multiple advantages of the sZVi over untreated nZVi, which are as follows:

(1). Enhanced reactivity as the degradation rate increases due to higher electron available for TCE reduction mediated by sulfur. Before treatment, upto 95% of the electrons would go to reduction of water, but after treatment the water reduction drops drastically (Fan et al., 2017). Research have reported that there is at least one order increase in magnitude of TCE reduction, and in some case up to 60 times (Xu et al., 2019).

(2) H_2 production decreases as reduction equivalent for water decreases when nZVi is substituted with sZVi. This is beneficial because the untreated nZVi leads to formation of H_2 with little reduction of TCE. The H_2 gas promotes bioremediation which causes the reaction pathway to be hydrogenolysis and formation of a toxic daughter product.

(3) The half-life of sZVi increases significantly. For optimal S/Fe ratio, the half-life is around 350 days compared to 60 days for untreated nZVi (Xu et al., 2019).

(4) The sZVi behavior observed in batch reactor remains similar in a field scale. As shown by Kim et al. (2013), sZVi is not sensitive to the dissolved oxygen.

(5) The reactivated sZVi after passivation has higher degradation rate constant than the reactivation by nZVi (Dong et al., 2018).

(6) For sZVi, the degradation rate of PCE increases with pH (for the range 5-8) while the reverse trend is observed for untreated nZVi. Since the natural groundwater condition has normally pH>6, the degradation rate is optimized with sZVi (Dong et al., 2018).

(7) The microecosystem in groundwater is responsible for natural attenuation of contaminant. While both nZVi and sZVi has been found to have a toxic effect on the microorganism such as *e. coli*, sZVi exhibits a weaker toxicity compared to nZVi (Cheng et al., 2019).

(8) sZVi facilitates the particle mobility to an extent by enhancing electrostatic repulsion and lowering the saturation magnetization to a certain degree (Phenrat et al., 2019).

1.4 Assessment of the behaviour of sites polluted by chlorinated solvent and their remediation through numerical modelling

Once infiltrated down into a soil or aquifer, the migration of DNAPL is governed primarily by the heterogeneity and internal structure of the porous media, and it is often very difficult to predict (Illangasekare et al., 1995; Kueper et al., 1991). The understanding of the mobility of the contaminant and its interaction with the porous media is, however, essential to decide which remediation techniques are more convenient from the environmental and cost-efficiency points of view. Aspects like how large the underground volume is impacted by the pollutants, how intense is the pollution, what is the predominant phase (free or dissolved in water), are determined through a field characterization but this is expensive and time consuming. In addition, field characterization only provides a picture of the current state of the site and it does not give clues about the past and future evolution of the contaminant, which is something essential to select the remediation strategy to be applied. In order to fill this gap, numerical modelling comes into play.

The interaction of the contaminant with the rock components and with substances used for remediation (e.g., engineered nano-particles) in the subsurface is driven by a complex interplay of physical, chemical and biological factors. Numerical modelling is able to integrate all these relevant processes and make predictions about the future behavior of the system helping in the optimization of the remediation step. The combination of modelling and field study can illustrate the possible worst-case scenarios of existing contamination, and the possible migration paths and travel times of contaminants. The modelled results can also shed light on the breakthrough curves of contaminant concentration at points relevant for remediation purpose. Additionally, they can help design the monitoring network to assess the real-time performance of the remediation strategy. Figure 1-2 is a flowchart showing the role and the relevance of numerical modelling in the development of remediation strategy.

1.5 Motivation of this PhD. research project

In the recent years, a number of studies exploring both the field and contaminant characterisation on one side, and remediation technologies on the other, have been carried out. The integration of these two aspects is indispensable for the development of a site-specific, optimised remediation strategy. Numerical modelling provides a detailed integration of these two aspects. While there are several remediation treatments being implemented on a contaminated site, the potential of numerical schemes in aiding these remediation processes is still not fully utilized. Such numerical schemes, if implemented, can give relevant predictions for a cost-effective remediation.

This doctoral work has been a part of ´Metal-aid project´, an Innovative Training Network (ITN) funded in the frame of the Marie Sklodovska Curie program of the European Commission. This project is intended to develop engineered nano-particles to be used for groundwater remediation. This PhD work has, as a main objective, the building of a new numerical model scheme for a more comprehensive assessment of chlorinated solvent contamination in sandy aquifers.

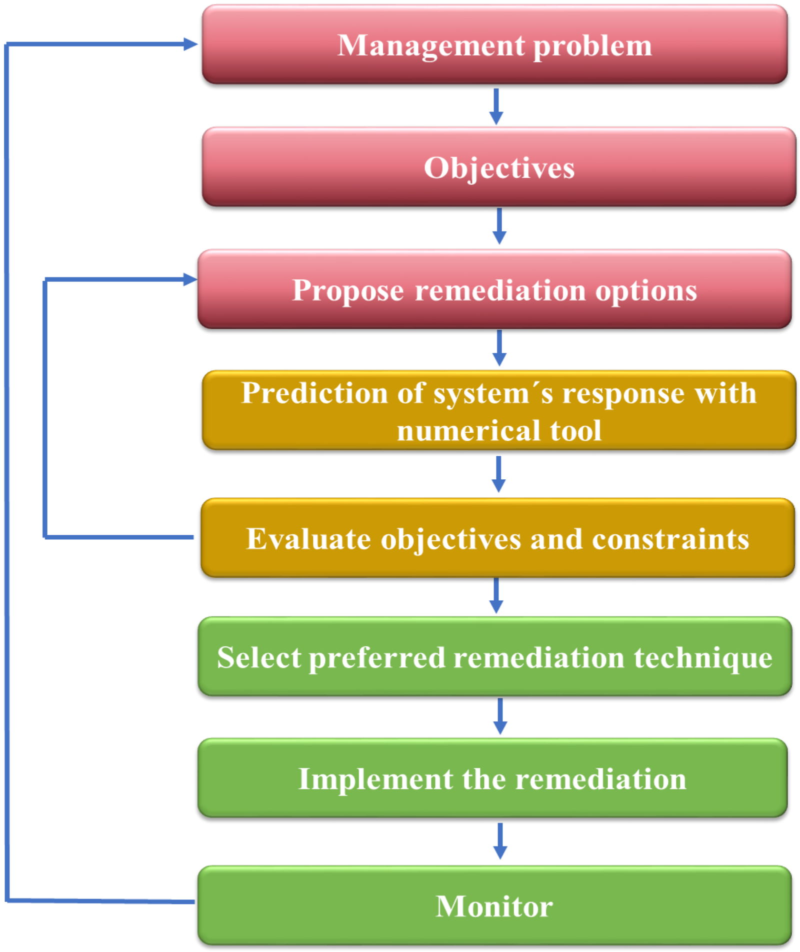

Figure 1-2*: A flowchart for a standard workflow of remediation strategy (from Bear and Cheng, 2010)*

From the scientific point of view, this study has been divided into the following Research Works (RW):

- RW1: The development of a multiscale multiphase flow in porous media simulation on the software Comsol Multiphysics and verify the result with reported benchmark study in literature (Chapter 3).

- RW2: The development of a field-scale, DNAPL infiltration model using the available but limited data of aquifer in the Innovation Garage Laboratory in Denmark (Chapter 3).

- RW3: The implementation of a numerical formulation on Comsol Multiphysics for nano-particle injection in a porous media and verify the model result with reported benchmark study in literature (Chapter 4).

- RW4: The implementation of an inverse and forward nano-particle transport simulation in porous media at column sand scale and tank sand scale (Chapter 4).

- RW 5: The conceptualization and the development of a numerical simulation for an end-to-end remediation strategy implemented on a hypothetical aquifer (Chapter 5).

1.6 References

AQUASTAT. 2010. Global Water Withdrawal. AQUASTAT website. Rome, Food and Agriculture Organization of the United Nations (FAO).

Bear, J., Cheng, A.H.-D., 2010. Modeling groundwater flow and contaminant transport. Springer Science & Business Media.

Cheng, Y., Dong, H., Lu, Y., Hou, K., Wang, Y., Ning, Q., Li, L., Wang, B., Zhang, L., Zeng, G., 2019. Toxicity of sulfide-modified nanoscale zero-valent iron to Escherichia coli in aqueous solutions. Chemosphere 220, 523–530.

Corey, A.T., 1994. Mechanics of immiscible fluids in porous media. Water Resources Publication.

Dalla, E., Hilpert, M., Miller, C.T., 2002. Computation of the interfacial area for two-fluid porous medium systems. J. Contam. Hydrol. 56, 25–48.

Dong, H., Zhang, C., Deng, J., Jiang, Z., Zhang, L., Cheng, Y., Hou, K., Tang, L., Zeng, G., 2018. Factors influencing degradation of trichloroethylene by sulfide-modified nanoscale zero-valent iron in aqueous solution. Water Res. 135, 1–10.

Erning, K., 2013. Multiphase modeling of DNAPL seepage history as possible site investigation tool-Influence of geological material, groundwater flow and subsurface morphology on the pathways of DNAPLs (PhD Thesis). Christian-Albrechts Universität Kiel.

Fan, D., Lan, Y., Tratnyek, P.G., Johnson, R.L., Filip, J., O'Carroll, D.M., Nunez Garcia, A., Agrawal, A., 2017. Sulfidation of iron-based materials: a review of processes and implications for water treatment and remediation. Environ. Sci. Technol. 51, 13070–13085.

Ganoulis, J., 2009. Risk analysis of water pollution. John Wiley & Sons.

Gillham, R.W., O'Hannesin, S.F., 1994. Enhanced degradation of halogenated aliphatics by zero-valent iron. Groundwater 32, 958–967.

Gomes, H.I.C.R., 2014. Coupling electrokinetics and iron nanoparticles for the remediation of contaminated soils.

Han, Y., Yan, W., 2016. Reductive dechlorination of trichloroethene by zero-valent iron nanoparticles: reactivity enhancement through sulfidation treatment. Environ. Sci. Technol. 50, 12992–13001.

He, Y.T., Wilson, J.T., Su, C., Wilkin, R.T., 2015. Review of abiotic degradation of chlorinated solvents by reactive iron minerals in aquifers. Groundw. Monit. Remediat. 35, 57–75.

Heiderscheidt, J.L., 2005. DNAPL source zone depletion during in situ chemical oxidation (ISCO): Experimental and modeling studies. Colorado School of Mines Golden.

Illangasekare, T.H., Ramsey, J.L., Jensen, K.H., Butts, M.B., 1995. Experimental study of movement and distribution of dense organic contaminants in heterogeneous aquifers. J. Contam. Hydrol. 20, 1–25. https://doi.org/10.1016/0169-7722(95)00045-W

Jennings, A.A., 2013. Analysis of worldwide regulatory guidance values for the most commonly regulated elemental surface soil contamination. J. Environ. Manage. 118, 72–95.

Kaluarachchi, J.J., 2000. Groundwater Contamination by Organic Pollutants. American Society of Civil Engineers.

Keely, J.F., 1989. Performance evaluations of pump-and-treat remediations. US Environmental Protection Agency, Center for Environmental Research

Kim, E.-J., Kim, J.-H., Azad, A.-M., Chang, Y.-S., 2011. Facile synthesis and characterization of Fe/FeS nanoparticles for environmental applications. ACS Appl. Mater. Interfaces 3, 1457–1462.

Kim, E.-J., Murugesan, K., Kim, J.-H., Tratnyek, P.G., Chang, Y.-S., 2013. Remediation of trichloroethylene by FeS-coated iron nanoparticles in simulated and real groundwater: effects of water chemistry. Ind. Eng. Chem. Res. 52, 9343–9350.

Kocur, C.M., O'Carroll, D.M., Sleep, B.E., 2013. Impact of nZVI stability on mobility in porous media. J. Contam. Hydrol. 145, 17–25.

Kueper, B.H., Frind, E.O., 1991. Two-phase flow in heterogeneous porous media: 1. Model development. Water Resour. Res. 27, 1049–1057.

Kumar Reddy, D.H., Lee, S.M., 2012. Water pollution and treatment technologies. J Env. Anal Toxicol 2, e103.

Kummu, M., Ward, P.J., de Moel, H., Varis, O., 2010. Is physical water scarcity a new phenomenon? Global assessment of water shortage over the last two millennia. Environ. Res. Lett. 5, 034006.

Lerner, D.N., Kueper, B.H., Wealthall, G.P., Smith, J.W.N., Leharne, S.A., 2003. An illustrated handbook of DNAPL transport and fate in the subsurface.

Levy, L.C., 2003. Experimental and theoretical modeling of DNAPL transport in vertical fractured media (PhD Thesis). Massachusetts Institute of Technology.

Li, B.Q., 2006. Discontinuous finite elements in fluid dynamics and heat transfer. Springer Science & Business Media.

Li, D., Zhu, X., Zhong, Y., Huang, W., Peng, P., 2017. Abiotic transformation of hexabromocyclododecane by sulfidated nanoscale zerovalent iron: Kinetics, mechanism and influencing factors. Water Res. 121, 140–149.

Lojkasek-Lima, P., Aravena, R., Shouakar-Stash, O., Frape, S.K., Marchesi, M., Fiorenza, S., Vogan, J., 2012. Evaluating TCE abiotic and biotic degradation pathways in a permeable reactive barrier using compound specific isotope analysis. Groundwater Monitoring & Remediation 32, 53–62.

Morel-Seytoux, H.J., 1969. Introduction to flow of immiscible liquids in porous media. Flow Porous Media 455–516.

Naidu, R., 2013. Recent advances in contaminated site remediation. Water. Air. Soil Pollut. 224, 1705.

Nambi, I.M., Powers, S.E., 2003. Mass transfer correlations for nonaqueous phase liquid dissolution from regions with high initial saturations. Water Resour. Res. 39.

Pankow, J.F., Cherry, J.A., 1996. Dense chlorinated solvents and other DNAPLs in groundwater: History, behavior, and remediation.

Phenrat, T., Lowry, G.V., 2019. Nanoscale zerovalent iron particles for environmental restoration. Springer.

Phenrat, T., Saleh, N., Sirk, K., Tilton, R.D., Lowry, G.V., 2007. Aggregation and sedimentation of aqueous nanoscale zerovalent iron dispersions. Environ. Sci. Technol. 41, 284–290.

Powers, S.E., Abriola, L.M., Weber Jr, W.J., 1994. An experimental investigation of nonaqueous phase liquid dissolution in saturated subsurface systems: Transient mass transfer rates. Water Resour. Res. 30, 321–332.

Przydatek, G., Kanownik, W., 2019. Impact of small municipal solid waste landfill on groundwater quality. Environ. Monit. Assess. 191, 1–14.

Rajajayavel, S.R.C., Ghoshal, S., 2015. Enhanced reductive dechlorination of trichloroethylene by sulfidated nanoscale zerovalent iron. Water Res. 78, 144–153.

Rodrigues, S.M., Pereira, M.E., da Silva, E.F., Hursthouse, A.S., Duarte, A.C., 2009. A review of regulatory decisions for environmental protection: Part I—Challenges in the implementation of national soil policies. Environ. Int. 35, 202–213.

Sarathy, V., Tratnyek, P.G., Nurmi, J.T., Baer, D.R., Amonette, J.E., Chun, C.L., Penn, R.L., Reardon, E.J., 2008. Aging of iron nanoparticles in aqueous solution: effects on structure and reactivity. J. Phys. Chem. C 112, 2286–2293.

Shi, Z., Fan, D., Johnson, R.L., Tratnyek, P.G., Nurmi, J.T., Wu, Y., Williams, K.H., 2015. Methods for characterizing the fate and effects of nano zerovalent iron during groundwater remediation. J. Contam. Hydrol. 181, 17–35.

Singh, B.K., Naidu, R., 2012. Cleaning contaminated environment: a growing challenge. Springer.

Swartjes, F.A., 2011. Introduction to contaminated site management, in: Dealing with Contaminated Sites. Springer, pp. 3–89.

Vörösmarty, Charles J., McIntyre, P.B., Gessner, M.O., Dudgeon, D., Prusevich, A., Green, P., Glidden, S., Bunn, S.E., Sullivan, C.A., Liermann, C.R., 2010. Global threats to human water security and river biodiversity. nature 467, 555–561.

Vörösmarty, C. J., McIntyre, P.B., Gessner, M.O., Dudgeon, D., Prusevich, A., Green, P., Glidden, S., Bunn, S.E., Sullivan, C.A., Liermann, R.C., 2010. Rivers in crisis: Global water insecurity for humans and biodiversity. Nature 467, 555–561.

Xu, J., Wang, Y., Weng, C., Bai, W., Jiao, Y., Kaegi, R., Lowry, G.V., 2019. Reactivity, Selectivity, and Long-term Performance of Sulfidized Nanoscale Zerovalent Iron with Different Properties. Environ. Sci. Technol.

World Health Organization. (2012). Trend in maternal mortality: 1990 to 2010: WHO, UNICEF, UNFPA and The World Bank estimates.

2 Methodology for the development of the modelling approaches: Governing mechanisms and mathematical equations

2.1 Introduction

This PhD research has been oriented towards the model development and demonstration of the capabilities of a numerical tool to deal with the challenges of the DNAPL infiltration in a groundwater system and the rational approach for its remediation. The thesis consists of 3 main research chapters (Chapter 3, Chapter 4 and Chapter 5) in which the numerical model is developed to understand the behaviour of both contamination flow and remediation processes.

Chapter 3 deals with how the contaminant (perchloroethylene, PCE, a kind of DNAPL) infiltrates down into soils and, further, into the aquifers, with focus on the pathways and the effect of heterogeneities. Since PCE is barely miscible with water, the model developed considers an immiscible two-phase flow in the natural aquifer system. For this, the mass conservation equation for both PCE and water is used. A verified numerical formulation is developed to simulate the PCE infiltration in a 3-dimensional field scale domain.

Subsequently, in Chapter 4, the nano-particle injection is simulated in a one-dimensional sand column a well as a three-dimensional tank scale aquifer. The modelling exercise is intended to help predict the governing processes and parameters driving the mobility of nano-particles inside the rock aquifer.

In Chapter 5, the interaction between contaminant and the aquifer is studied in a two-dimensional domain. This case is simulated using an integrated scheme of contamination and remediation. The simulation exercise includes the infiltration of DNAPL, followed by its dissolution in the aqueous phase, and transport within the aquifer. Also, the remediation process is simulated through nano-particle injection in the same model domain considering all mechanical and physico-chemical mechanisms that controls its mobility in the porous media. Finally, in the last simulation exercise, a reactive transport model is developed to simulate the chemical degradation of contaminant.

An integral part of all these modelling exercises are the governing equations and the processes on which the predictive simulation is developed. Any numerical tool incorporates the mathematical formulation that represents the physical, geological and chemical processes that drive, i.e., the fluid flow, the contaminant transport and reactivity and the nano-particle interaction with the pore space. By solving these mathematical equations, the dependent parameters such as aqueous concentration of contaminant or fluid pressure are predicted. The numerical simulations are based on predicting these dependent variables for all temporal and spatial extension of models with the help of hydrogeological and fluid properties. Once the governing processes are mathematically formulated, a numerical framework such as Finite Element model can be implemented to solve this formulation.

This Chapter 2 is dedicated to reviewing the relevant processes and mathematical equations used in model development along with the discussion of numerical framework and software package.

2.2 Governing processes and equations

All the simulations developed in this thesis are at macroscopic scale, that considers a continuum of fluid and hydraulic properties of an aquifer. At this macroscopic scale, the fluid and host rock are considered as spatially continuous across a macroscopic volume in the aquifer. The continuum value of the relevant parameters governing the fluid dynamics is the spatially averaged estimates of the pore scale fluid properties. As the pore scale fluid properties are spatially discontinuous, the averaged value allows the continuity of these properties in the study area. In a homogeneous system, the minimum volume for which the averaged-out parameters do not vary is the Representative Elementary Volume (REV) (Grant, 2005). For fluid flow simulation, the Darcy law is applicable at REV scale (Bear, 2013).

2.2.1 Formulation for two-phase flow

Dense Non-Aqueous Phase Liquid (DNAPL) are contaminants denser than water that are frequently spilled on the ground in industrial environments and further impacting soil and aquifer quality. The physical processes controlling the movement of DNAPL are the gravitational, capillary and viscous forces (Pankow and Cherry, 1996). Each of these forces originates from the complex interplay of fluid and porous media properties: The gravity force is generated due to the difference in density, capillary force owes to the different pressure at the water-DNAPL interface, and the viscous forces occur due to the fluid pressure gradient. Figure 2-1 shows a typical interplay between infiltrating DNAPL and aquifer components in a field scale scenario.

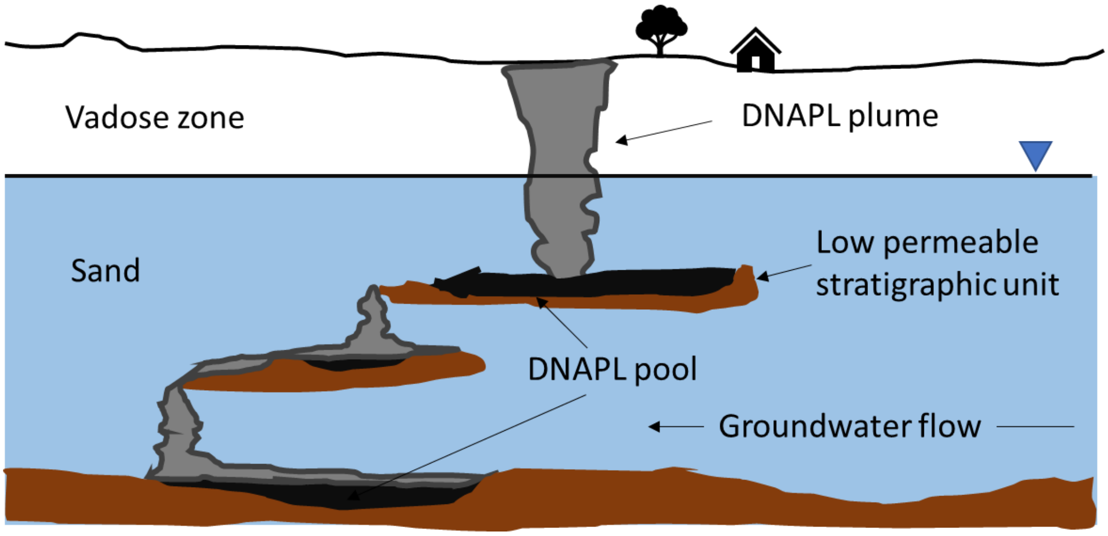

Figure 2-1: *Schematics of DNAPL infiltration in a typical groundwater system.*

The interplay of all three forces (viscous, capillary and gravity) leads to a non-uniform and hard-to-predict migration of DNAPL in both horizontal and lateral directions. The complex nature of DNAPL movement, especially in the lateral direction, is the consequence of heterogeneity in the sand medium (Schwille and Pankow, 1988; Illangasekare *et al.*, 1995). In a natural aquifer system, the DNAPL moves vertically under gravitational forces until it encounters a lower permeability layer (Kueper and Frind, 1991). Such a lower permeability layer holds significance as it can accumulate or divert the natural flow of the DNAPL according to its hydrogeological properties, and clay morphology. The formation of a secondary source of contamination can happen within the aquifer either on top of these low permeability layers or as residual saturation along the migration pathways (Grant, 2005).

The general governing equations for two-phase fluid flow in heterogeneous porous media at field scale were presented by Nelson (1966). The common equation for fluid flow in continuum scale is the Darcy's law, which defines the relationship between the hydraulic gradient and the fluid flow rate (Bear, 1972) and is given by Equation 2.1:

$$Q = -KA(\nabla H) \tag{eq. 2.1}$$

Where Q $[L^{3\cdot}T^{-1}]$ is the volumetric fluid flow rate through a cross section of area A $[L^2]$, K is the hydraulic conductivity $[L\cdot T^{-1}]$ represented by Equation 2.2:

$$K = \frac{k\rho g}{\mu} \tag{eq. 2.2}$$

k $[L^2]$ is the permeability of the porous media. ρ $[M\cdot L^{-3}]$ is the density of the fluid, μ $[M\cdot L^{-1}T^{1}]$ is the viscosity of the same fluid and g $[L\cdot T^{-2}]$ is the gravity constant.

H is the hydraulic head of the fluid represented by Equation 2.3:

$$H = (\frac{\nabla p}{\rho g} + z) \tag{eq. 2.3}$$

Where p $[M\cdot L^{-1}T^{2}]$ is the pressure of the fluid, *z* [L] is the elevation accounting for the potential energy due to gravity in the z direction.

The Darcy velocity is defined as the flow rate of the fluid per unit cross section area and given by Equations 2.4 and 2.5

$$u = \frac{Q}{A} = -K(\nabla H) \tag{eq. 2.4}$$

$$u = -\frac{k}{\mu}(\nabla p - \rho g) \tag{eq. 2.5}$$

Where u is the Darcy velocity of the fluid.

This is a simplified version of the Navier-Stokes equation applicable only for laminar flow of incompressible fluid in a porous media (Grant, 2005). For the multiphase flow in a porous media, the mass conservation equation is given by Equation 2.6:

$$\frac{\partial(\theta\rho_{\propto}S_{\alpha})}{\partial t} = -\nabla.(\rho_{\propto}u_{\propto}) + \rho_{\propto}q_{\propto} \tag{eq. 2.6}$$

Where θ is the porous media, S_{α} is the saturation of fluid phase $\propto$ and $q_{\propto}$ is the volumetric source or sink term for the same fluid $\propto$.

For the multi-phase system, the Equation 2.5 is converted to Equation 2.7

$$u_\propto = -k \frac{k_{r\propto}}{\mu_\alpha}(\nabla p_\alpha - \rho_\alpha g \nabla z) \qquad \text{(eq. 2.7)}$$

Where $k_{r\propto}$ is the relative permeability of the phase $\propto$.

The sum of the saturation of phase equals to unity as given by Equation 2.8

$$\sum_{\propto=1}^{n} S_\propto = 1 \qquad \text{(eq. 2.8)}$$

For the water-DNAPL system, the set of equations becomes (eq. 2.9, 2.10 and 2.11):

$$\frac{\partial(\theta S_w)}{\partial t} = \nabla.\left(k\frac{k_{rw}}{\mu_w}(\nabla p_w - \rho_w g)\right) + q_w \qquad \text{(eq. 2.9)}$$

$$\frac{\partial(\theta S_n)}{\partial t} = \nabla.\left(k\frac{k_{rn}}{\mu_n}(\nabla p_n - \rho_n g)\right) + q_n \qquad \text{(eq. 2.10)}$$

$$S_n + S_w = 1 \qquad \text{(eq. 2.11)}$$

Where the subscript w and n with the variables are water and DNAPL, respectively.

Mathematically, there are four dependent variables: pressure of water, pressure of DNAPL, saturation of water and saturation of DNAPL. Since there are only 3 equations, one more equation is needed to close the system of equations. An empirical relationship between capillary pressure and saturation of water is used for this purpose which empirically relates these two variables (eq. 2.12):

$$p_c(S_w) = p_n - p_w \qquad \text{(eq. 2.12)}$$

A detailed explanation of capillary pressure is included in the next section (Section 2.2.1).

2.2.1.1 Formulation for the capillary pressure

When both DNAPL and water are present in the pore space, the fluid with the strongest molecular attraction coats the pore walls, while the other fluid occupies the central part of the pores. The fluid that coats the surface is called the “wetting fluid” and the other is the “nonwetting fluid”. Generally, among water and DNAPL, water is the “wetting fluid”.

As a single phase, molecules have great attraction to themselves. There is an equilibrium of forces balanced from all directions for the molecules occupying the central space in the pore. However, for the molecule at the interface overlain by air or other immiscible fluid, the molecular force is not balanced. In such a case, both fluids exert self-attraction molecular forces for the corresponding molecules at the interface. As the molecular forces from both sides of the interface are imbalanced, the interface towards the fluid which exerts greater molecular force at the interface as shown in Figure 2-2.

The imbalance of molecular forces at the interface is compensated by the jump of pressure named as capillary pressure (Fitts, 2002). Capillary pressure represents the difference between fluid pressure at the fluid interface and given by Equation 2.13:

$$p_c(S_w) = p_n - p_w \qquad \text{(eq. 2.13)}$$

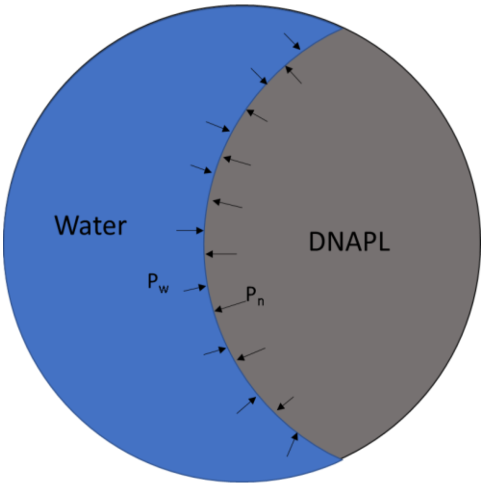

***Figure 2-2**: Scheme for the water and DNAPL interaction at their interface. The difference in pressure from both fluids governs the unique geometry of the interface. Adapted from Fitts (2002).*

Theoretically, the saturation of DNAPL increases with the increase of capillary pressure as high capillary pressure allows the DNAPL front to infiltrate into the water saturated zone (Fitts, 2002). It indicates that there exists a strong correlation between capillary pressure and saturation of the fluid. The most common correlation used for modeling purposes was given by the Brooks and Corey model (Brooks and Corey, 1964) and by Van Genuchten model (Van Genuchten, 1980). This relationship describes the capillary pressure as a non-linear function of effective saturation of the wetting phase. The effective saturation is calculated by considering the residual water saturation and is given by the Equation 2.14:

$$S_e = \frac{S_w - S_{wr}}{1 - S_{wr} - S_{nr}} \qquad \text{(eq. 2.14)}$$

Where S_e is the effective saturation of wetting phase, S_{wr} is the residual saturation of wetting phase, and S_{nr} is the residual saturation of the non-wetting phase.

2.2.1.2 Brooks-Corey and Van Genuchten equations

The capillary pressure given by the Brooks-Corey model is represented by Equation 2.15:

$$p_c(S_w) = p_d S_e^{\frac{-1}{\lambda}} \qquad for\ p_c \geq p_d \qquad \text{(eq. 2.15)}$$

Where P_d is the entry pressure, that is the minimum capillary pressure required for the DNAPL to displace water. If the capillary pressure does not exceed the entry pressure of a porous media, the DNAPL fails to infiltrate into the media. On the other hand, λ is related to the structure of a porous medium, that denotes the size distribution of the sand grains.

The capillary pressure given by Van Genuchten model is expressed as Equation 2.16:

$$p_c(S_w) = \frac{1}{\alpha} \left(S_e^{\frac{-1}{m}} - 1\right)^{\frac{1}{n}} \qquad for\ p_c \geq 0 \qquad \text{(eq. 2.16)}$$

Where α and n are the Van Genuchten model parameters, and $m = 1 - \frac{1}{n}$.

The capillary pressure can be zero in the Van Genuchten model at full water saturation, whereas the Brooks-Corey equation implies that there is a non-zero capillary pressure for a lithological unit fully saturated with saturation. This non-zero capillary pressure is equal to the entry pressure of the porous media and, thus, higher for the low permeable sands. Several studies in the literature have confirmed that one of the governing parameters for DNAPL migration in the subsurface is the entry pressure of different lithological unit (Kueper and Frind, 1991; Niessner, 2006). Figure 2-3 below shows the typical dependence of capillary pressure with saturation for both Van Genuchten and Brooks-Corey equations.

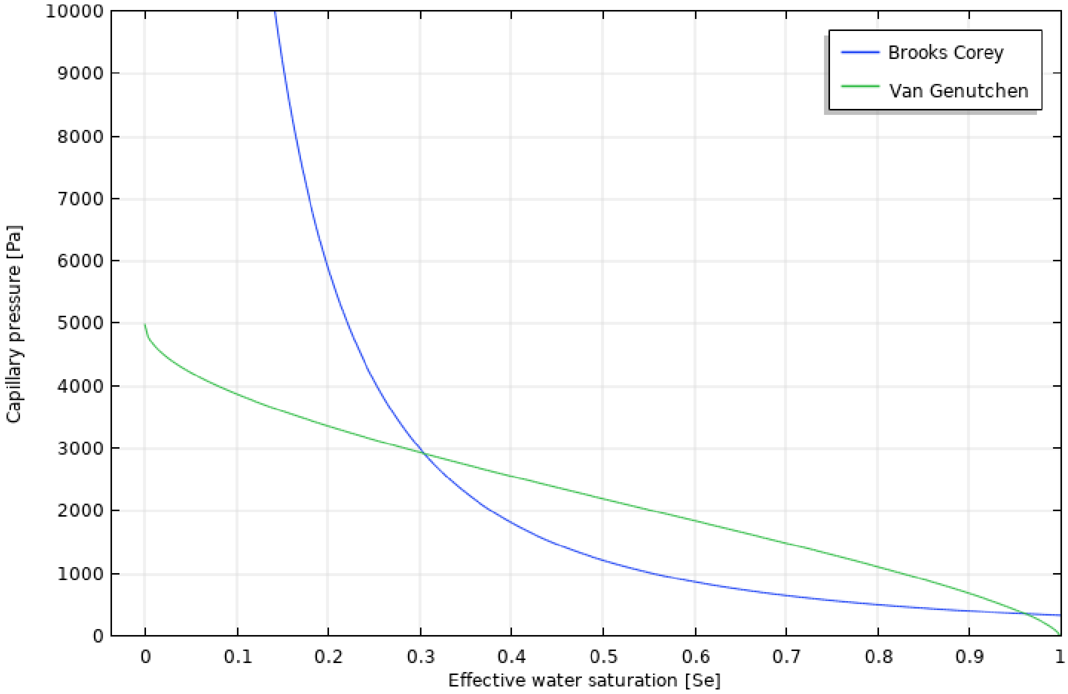

***Figure 2-3**: Plot for a typical capillary pressure-saturation relationship given by Brooks-Corey and Van Genuchten formulations.*

In this thesis, the Brooks-Corey equation has been used to establish the relation between capillary pressure and saturation of two-phase flow.

2.2.1.3 Formulation for the relative permeability

The permeability becomes a relative parameter when more than one fluid flows simultaneously through the porous medium. The relative permeability represents the reduction in the flow rate of a fluid due to the introduction of other fluid. This parameter is dependent on saturation of the fluid and increases with an increase in saturation. Theoretically, it implies that with an increase in saturation of a fluid, the flow becomes higher. Microscopically, as the saturation increases, the fluid occupies more volume resulting in more pore interconnection and leading to a transmissive medium for DNAPL flow.

Several equations have been proposed in the literature to establish the relation between relative permeability and saturation of the fluid. One of the most used relationships for relative permeability and saturation is given by Brooks-Corey relationship (Equations 2.17 and 2.18; Brooks and Corey, 1964; Helmig, 1997):

$$K_{rw}(S_{ew}) = S_{ew}^{3+\frac{2}{\lambda}} \qquad \text{(eq. 2.17)}$$

$$K_{rw}(S_{ew}) = (1-S_{ew})^2\,(1-S_{ew}^{\frac{2+\lambda}{\lambda}}) \qquad \text{(eq. 2.18)}$$

Where λ is pore size distribution coefficient.

In this thesis, Equations 2.17 and 2.18 are used for characterizing the relative permeability as a function of the fluid saturation. The dependence between the relative permeability of the individual fluid and the saturation given by Brooks-Corey equation is illustrated in Figure 2-4. This plot shows that when λ is doubled, the relative permeability significantly changes when both the fluid has a reasonable saturation. At dry or wet conditions, however, there is little change in relative permeability.

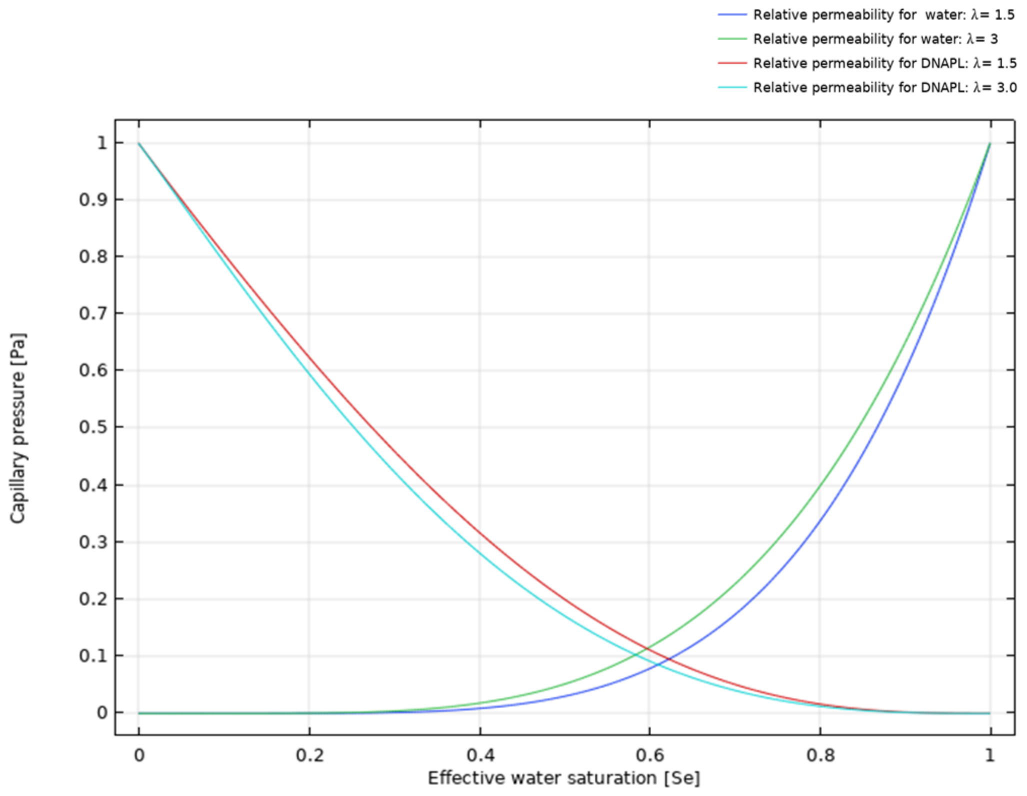

***Figure 2-4**: Plot for a typical relative permeability saturation relationship given by Brooks-Corey model for water (shown by green and blue colored curves) and DNAPL (shown by red and cyan colored curves). The plot shows the sensitivity of relative permeability with different values of pore distribution coefficient ($\lambda = 1.5$ and $\lambda = 3$).*

With the four equations and four independent variables, the set of equation becomes a closed system. Equations 2.19, 2.20, 2.21 and 2.22 show the final set of equations:

$$\theta \frac{\partial (S_w)}{\partial t} = \nabla . \left(k \frac{k_{rw}}{\mu_w} (\nabla p_w - \rho_w g) \right) + q_w \qquad \text{(eq. 2.19)}$$

$$\theta \frac{\partial (S_n)}{\partial t} = \nabla . \left(k \frac{k_{rn}}{\mu_n} (\nabla p_n - \rho_n g) \right) + q_n \qquad \text{(eq. 2.20)}$$

Where S_n and S_w are the saturation of DNAPL and water, respectively, p_n and p_w are the pressure of DNAPL and water, θ is porosity, and k is permeability of the sand. q_w and q_n are the volumetric source term for water and DNAPL, respectively.

$$S_n + S_w = 1 \quad \text{(eq. 2.21)}$$

$$p_c(S_w) = p_d S_e^{\frac{-1}{\lambda}} \quad \text{(eq. 2.22)}$$

Where p_c is the capillary pressure defined as a function of water saturation.

With four variables and four equations, the system of equations can be approximated using the Finite Element Method (Explained in section 2.2.5). However, the four primary variables for solving the set of equations results in higher degrees of freedom (DOFs) for the model. Solving the model with relatively higher DOFs requires big computational resources and time. To reduce the DOFs, several studies have used algebraic modifications to represent the mass conservation equations with reduced degrees of freedom (Wu and Forsyth, 2001; Chenet al., 2006). Using the linear combination of constitutive relationships, the system of equations can be reduced to two equations, with two primary variables. Several studies in literature have used different pairs of primary variables for developing numerical formulation of two-phase flow equations (Helmig, 1997; Wu and Forsyth, 2001; Kolditz et al., 2012). Each of such pairs of primary variables has its own advantages and disadvantages in terms of numerical solution. The formulation could be Coupled Pressure Saturation, Implicit Pressure Explicit Saturation (IMPES), Global Pressure, Capillary pressure and Pressure of the water. A brief review for each relevant pair of dependent variables has been done in the Appendix A.

2.2.1.4 Formulation for the flow behavior at interface of two sand layers: Phase Pressure Saturation with Interface condition

The formulation for two-phase flow in heterogeneous media with Standard Galerkin Finite Element Method can fail to predict the flow behavior at the interface of two different sands layers (Helmig, 1997). The Phase Pressure Saturation with Interface Condition (PPSIC) has been postulated in previous studies to simulate the flow dynamics at the interface of different sand layers (Helmig et al., 2002; Van Duijn et al., 1995). The theory is based on a capillary pressure equilibrium condition at the interface of two different sands encountered by infiltrating DNAPL plume. For an aquifer free of DNAPL, the capillary pressure obtained using the Brooks-Corey relationship is the same as the entry pressure. The different entry pressures for different sands causes discontinuity in the capillary pressure. For the flow of DNAPL from higher permeability to lower permeability sands, the DNAPL encounters a relatively higher entry pressure at the plume front. The movement of DNAPL is restricted until the capillary pressure at the DNAPL front increases up to the entry pressure of low permeable sand. Mathematically, the halting of DNAPL movement can be understood by considering the flow rate of DNAPL given by Equation 2.23:

$$u_n = -k\,\frac{k_{rn}}{\mu_n}(\nabla p_w + \nabla p_c - \rho_n g) \quad \text{(eq. 2.23)}$$

For a finite value of DNAPL flow velocity (u_n), the capillary pressure must be continuous in Equation 2.23. Thus, once the plume touches the interface of the low-permeability sand, the movement of DNAPL is stopped. However, the gravitational forces lead to the accumulation of

DNAPL at the top of interface, while the saturation of DNAPL increases at the upgradient with respect to the sand interface, and the saturation of DNAPL at the downgradient remains zero. The accumulation of DNAPL causes capillary pressure to increase until it is equal to the entry pressure of low-permeability sand. The DNAPL saturation for which the capillary pressure at the upgradient becomes equal to the entry pressure of the downgradient sand is called "threshold saturation". As the threshold saturation is reached, a continuity in the capillary pressure across the interface is established, leading to the achievement of the capillary equilibrium condition. The establishment of capillary equilibrium results in the reactivation of DNAPL flow with non-zero saturation at both sides of the interface. However, the curve for DNAPL saturation remains discontinuous at the interface. Mathematically, this discontinuity can be explained by considering the capillary pressure-saturation relationship at the interface of different sand layers.

The capillary equilibrium at the interface of two sands (Sand A and sand B) with different hydrogeological properties can be expressed as Equations 2.24 and 2.25:

P_c at Sand A = P_c at Sand B (eq. 2.24)

$$p_{d_1} S_{e_1}^{\frac{-1}{\lambda_1}} = p_{d_2} S_{e_2}^{\frac{-1}{\lambda_2}} \quad \text{(eq. 2.25)}$$

Where p_{d_1} and p_{d_2} are the entry pressure of sand A and sand B, respectively. S_{e_1} and S_{e_2} are the effective saturation of wetting phase at the interface for sand A and sand B respectively. λ_1 and λ_2 is the pore distribution coefficient for sand A and sand B, respectively.

As the entry pressure and pore distribution coefficient is inherently different for both the sands, Equation 2.24 yields different values of effective water saturation at the interface. This process is reflected as a discontinuity in the DNAPL saturation curve. Until the capillary pressure equilibrium is not attained, the movement of DNAPL is stopped. As the capillary pressure is attained once the accumulated DNAPL is sufficient to overcome threshold pressure, the movement resumes. Developing two-phase flow formulation without considering PPSIC condition can fail to correctly simulate the flow dynamics in an aquifer with different sand layers. Therefore, for developing the field scale fluid flow simulation, the PPSIC condition is included in the numerical formulation.

2.2.2 Dissolution and transport of contaminants

The contaminant in the groundwater occurs in two different forms: free and dissolved in water (Pankow and Cherry, 1996). As a separate phase from water known as Dense Non-Aqueous Phase Liquid (DNAPL), it migrates downward before it settles at the bedrock or low permeable zones. Additionally, a residual amount of this separate phase is also captured due to the local pore heterogeneity. They are locally immobilized in the pore and are rarely encountered as a free phase in the extracted water from well.

The major form of concern is the dissolved form of contaminant originating from the NAPL phase present in the aquifer. The dissolved form of contaminant has a widespread occurrence in the aquifer, both on spatial and temporal scales (Lerner et al., 2003). To remediate such a contamination, several techniques can be applied to diminish the plume of dissolved contaminant in the water. The contaminant flow is often controlled by a complex interplay of

DNAPL source and aquifer properties (Christ et al., 2010; Falta et al., 2005). Without understanding such properties, the remediation can be ineffective and often leads to reappearance of contaminant plume (Sale and McWhorter, 2001). In such case, an effective remediation strategy would be determining the source of DNAPL and the governing factor that controls the presence of contaminant in the groundwater. The field scale spatial and temporal evolution of the contaminant plume can be estimated by modeling two physicochemical processes: (1) the dissolution process which introduces the contaminant to the water and (2) transport process which leads to formation of contamination plume (Miller et al., 1998; Parker and Park, 2004). The following sections explain both governing processes and their mathematical form.

2.2.2.1 Mechanisms of contaminant dissolution

Dissolution of DNAPL occurs due to the mass transfer of one phase into the other phase at their interface. On the micro scale, the dissolution originates with breaking of weak bonds in the DNAPL phase and formation of cavity in the aqueous phase (Grant, 2005). As the molecules released from DNAPL moves to the cavity in aqueous phase, the weak bonds are formed between the contaminant molecules and adjoining water molecules. As the water passes through the ganglia and DNAPL pool, the dissolved contaminant is transferred to the aqueous phase. Due to the high saturation of the pool, the water flow through the DNAPL is restricted and, thus, the interface for mass transfer is very limited (Parker and Park, 2004). However, for the residual saturation, a large interface area exists between the water and DNAPL. Due to this high interface area for mass transfer combined with low mass of residual DNAPL saturation, the ganglia degrade firstly followed by the DNAPL pool (Carey et al., 2014).

Theoretically, the dissolved contamination is expected to be in thermodynamic equilibrium at the DNAPL water interface. As the mass is transferred from DNAPL to water, the concentration of dissolved contaminant in the water phase increases. Equilibrium is established when the concentration of dissolved contaminant reaches the solubility limit (Sale and McWhorter, 2001). This is considered as Local Equilibrium Assumption (LEA).

Experiments at both the field scale and experiment scale have found that the equilibrium condition is often not achieved in the aqueous phase (Frind et al., 1999; Mercer and Cohen, 1990; Unger et al., 1998). Under realistic conditions, the thermodynamic equilibrium is not generally established, and the dissolution occurs following kinetic rate law of mass transfer.

2.2.2.2 Kinetic mass transfer of contaminants from DNAPL to aqueous phase

The hindrance for the equilibrium-controlled dissolution is imposed by the advective and dispersive transport. The two processes, interphase mass transfer encouraging equilibrium, and the advective flow hindering the equilibrium, compete with each other and the comparatively slower process controls the dissolution (Sale and McWhorter, 2001; Seagren et al., 1994). When interphase mass-transfer rates (i.e., rates of transfer into and out of the NAPL) are much faster than the advective-dispersive, the thermodynamic equilibrium is established (Seagren et al., 1994). Otherwise, the net mass transfer of contaminant from DNAPL to water phase equals the rate of mass transport away from the DNAPL source leading to kinetic mass transfer.

The mechanism for the kinetic mass transfer process is given by the stagnant film theory (Pankow and Cherry, 1996). In this theory, a mass of water at the interface DNAPL mass is considered to be stagnant. The mass transfer of dissolved contaminants from the DNAPL mass to the bulk water mass occurs at two stages. First, there exist an equilibrium condition at the water-DNAPL interface layer, such that the aqueous contaminant at the interface reaches the solubility level. In the second stage, the dissolved mass is transferred to the bulk water mass through diffusion (which is slower process). Thus, the rate of transfer becomes diffusion controlled. A linear formula for DNAPL mass transfer was first established by Sherwood et al. (1975) (Equation 2.26):

$$J = k_l a(C_s - c) \qquad \text{(eq. 2.26)}$$

Where J is the mass flux(M·L^{-2}·T^{-1}), k_l is the average mass transfer coefficient at the DNAPL water interface (m·s^{-1}), a is the specific interfacial area between DNAPL and groundwater (m^{-1}) and C_s is the equilibrium concentration of the contaminant in the water phase (kg·m^{-3}).

The concentration gradient between the interface and the bulk aqueous phase acts as a linear driving force for dissolution. This equation is valid on the REV scale which allows to use the averaged soil and DNAPL properties (Grant et al., 2007).

Numerous laboratory and numerical techniques have been developed to estimate the interfacial area (Dalla et al., 2002; Gvirtzman et al., 1987; Kim et al., 1999; Ronen et al., 1986). All these methods have their own complexity and limitation which undermines the accuracy (Grant, 2005). Owing to difficulty in determining accurate values individual values of k_l and a, Miller et al. (1990) first proposed lumping the mass term together (Equation 2.27):

$$k_l \times a = K_l \qquad \text{(eq. 2.27)}$$

From Equation 2.28 and 2.29, the mass flux of dissolution at water-DNAPL interface can be obtained (Equation 2.28):

$$J = K_l(C_s - c) \qquad \text{(eq. 2.28)}$$

Where J is the mass flux (Kg·m^{-2}·s^{-1}), K_l is the lumped mass transfer coefficient (m·s^{-1}), C_s is the equilibrium concentration of contaminant in water (kg·m^{-3}).

The mass transfer coefficient K_l is generally derived empirically from setting dissolution experiment at laboratory scale. A common mathematical framework for empirically deriving the K_l value is given by modified Sherwood number represented by Equation 2.29.

$$S_h = K_l d_m^2 D_m^{-1} \qquad \text{(eq. 2.29)}$$

Where S_h is the Sherwood number, d_m is the mean particle diameter (m) and D_m is the molecular diffusion coefficient (m^2·s^{-1}).

Many researchers have empirically derived the mass transfer rate coefficient using dissolution experiment at laboratory scale (Table 2-1; Luciano et al., 2018). These transfer rate coefficients are highly dependent on the subsurface condition and geochemical environment. More specifically, the transfer rate has been reported to be dependent on the effective solubilities and diffusivities of the DNAPL components, the DNAPL source zone architecture (Luciano et al., 2018), fluid flow properties (Miller et al., 1990; Nambi and Powers, 2003a; Saba and Illangasekare, 2000), and sand grain properties (Nambi and Powers, 2003a; Powers et al., 1994).

***Table 2-1**: Empirically-derived formulations for the Sherwood number reported in the literature.* eR *is the Reynolds number,* θ_n *is the DNAPL saturation,* S_c *is the Schmidt number,* U_i *is the uniformity index, delta is the* d_{50}/d_m*,* Pe *is Peclet number,* Sh_o *is the modified Sherwood number for local scale-dissolution,* s_{lnk}^2 *and* λ_z *represent the media heterogeneity,* $\frac{M_{II,z}}{M_{II,z}^*}$ *represents source zone architecture.*

Authors	Condition/Dependence	Correlation
Luciano et al. (2018)	Dependence: Dimensionality, velocity, Morphology	$S_h' = \propto Re^{\beta1}S_m^{\beta2}(P/A)^{\beta3}I_y^{\beta4}$
Miller et al. (1990)	Condition: 1D experiment, $0.026 < \theta_n < 0.21$	$S_h' = 12Re^{0.75}\theta_n^{0.60}Sc^{0.5}$
Powers et al. (1992)	Condition: 1D experiment, $0.026 < Re < 0.21$, θ_n is constant	$S_h' = 57.7Re^{0.61}d_{50}^{0.64}U_i^{0.41}$
Powers et al. (1994a)	Condition: 1D experiment, $0.052 < Re < 0.08$	$S_h' = 4.13Re^{0.60}\delta^{0.67}U_i^{0.37}(\frac{\theta_n}{\theta_{ni}})^{\beta}$
Kim and Chrysikopoulos (1999)	Condition: 2D rectangular source zone	$S_h' = 1.58(Pe_x)^{0.34}(Pe_y)^{0.43}$
Saba and Illangasekare (2000)	Condition: 2 D experiment, Dependence: Pool length	$S_h' = 11.34Re^{0.2767}Sc^{0.33}(\frac{d_{50}\theta_n}{\tau L})^{1.037}$
Nambi and Powers (2003)	Condition: $0.0001 < S_n < 0.35$, $0.018 < Re < 0.134$	$S_h' = 37.2Re^{0.61}S_n^{1.24}$
Saenton and Illangasekare (2007)	Dependence: Morphology	$S_h' = sh_o\left(1 + s_{lnk}^2\right)^{1.783}(1 + \frac{\Delta z}{\lambda_z})^{2.35}(\frac{M_{II,z}}{M_{II,z}^*})^{4.157}$
Imhoff et al. (1994)	Condition: $0.0012 < Re < 0.21$ and $0 < Sn < 0.16$	$S_h' = 340Re^{0.75}\theta_n^{0.60}(\frac{x}{d_{50}})^{-0.31}$

For the ganglia dissolution in groundwater, Miller et al. (1990) derived an empirical relationship for the kinetic rate transfer coefficient as a function of fluid properties. Also, Powers et al. (1992) showed that the grain properties can be a relevant proxy for DNAPL dissolution, and Geller and Hunt (1993) explicitly defined the interfacial area by considering the ganglia as spherical droplet. Powers et al. (1994a) derived the transient mass transfer function taking into account the hydrodynamic properties and residual saturation. Imhoff et al. (1994) included in the formulation the effect of preferential pathway formed as the dissolution progresses. Finally, Saba and Illangasekare (2000) included the effect of dimensionality by establishing the empirical relation from 2D experiments.

For the dissolution of DNAPL pool in the groundwater, there have been relatively fewer research done in literature. Kim and Chrysikopoulos (1999) derived an empirical relationship by considering the pool to be rectangular or spherical. Nambi and Powers (2003) developed a transient mass transfer equation by introducing a saturation factor as the factor for interfacial area. Luciano et al. (2018) and Saenton and Illangasekare (2007) incorporated the effect of DNAPL morphology governing the kinetic transfer. This allows to model the dissolution rate due to dynamic change in the interfacial area thus increasing the prediction estimates for the dissolution.

2.2.2.3 Dissolution of contaminants at field scale

The contaminant concentration in groundwater at field scale has been observed to be orders of magnitude lower than the equilibrium concentration of contaminant (Pankow and Cherry, 1996)). Several explanations have been presented in the literature for such field-scale observation. Miller et al. (1998) observed that the kinetic mass transfer gives the near-equilibrium concentration of the dissolved contaminants in the close vicinity of DNAPL mass. Similarly, Frind et al. (1999) conducted a field-scale experiment of DNAPL dissolution at Borden site and concluded that at high DNAPL saturation, the thermodynamic equilibrium is achieved immediately downgradient to the DNAPL mass. But the combined effect of heterogenous aquifer property and disruption in natural groundwater flow-field result in such lowered concentration at the aquifer scale (Parker et al., 2004; Frind et al., 1999).

The formulation developed in the small-scale system does not take into consideration the non-uniform field of groundwater flow caused by the change in relative permeability and the heterogeneous distribution of DNAPL (Nambi and Powers, 2003). Brusseau et al. (2002) stressed on the fact that at the field scale, the heterogeneity in the NAPL distribution and velocity field is the primary driving force for dissolution, and the fluid and subsurface hydrodynamics becomes secondary. Even the pore scale heterogeneities can lead to non-uniform distribution of DNAPL with irregular morphology (Nambi and Powers, 2003). Mayer and Miller (1996) experimentally showed that the predicted dissolution rate for ganglia was much lower for a heterogeneous case compared to homogeneous one. This establishes the fact that a general formulation for DNAPL dissolution is not applicable for all scales. A site-specific mathematical model becomes important to understand the dissolution behavior of DNAPL (Prakash and Nambi, 2012; Vaezihir et al., 2012).

2.2.2.4 Formulation for a multi-conditional dissolution

In this thesis, a combination of formulations is used to simulate the DNAPL dissolution for both pool and ganglia. Since the dissolution mechanism is greatly dependent on initial saturation of DNAPL pool (Nambi and Powers, 2003), a single equation cannot be used to predict the dissolved concentration of contaminant. Therefore, a hybrid approach is adopted which includes application of both Local equilibrium condition and kinetic mass transfer. A kinetic mass transfer rate is implemented for the domain where the saturation of DNAPL was below 0.35. For the contaminant source having saturation greater than 0.35, equilibrium mass transfer is considered. The formulation for the dissolution is given by Equation 2.30 and Equation 2.31:

$c = C_s$ $S_n > 0.35$ (eq. 2.30)

$J = K_l(C_s - c)$ $S_n < 0.35$ (eq. 2.31)

Where J is the mass flux (Kg·m^{-2}·s^{-1}), K_l is the lumped mass transfer coefficient (m·s^{-1}), C_s is the equilibrium concentration of contaminant in water, taken as 1.27 Kg·m^{-3} (Grathwohl, 2012).

From Equation 2.29, the lumped mass transfer coefficient is derived and is represented by Equation 2.32.

$$K_l = S_h d_m^{-2} D_m \quad \text{(eq. 2.32)}$$

Where S_h is the Sherwood number, d_m is the mean particle diameter and (m) and D_m is the molecular diffusion coefficient (m^2·s^{-1}).

The DNAPL ganglia dissolution depends on a different formulation. However, at this stage, when the dissolution data are not available, a simplistic formulation for DNAPL dissolution is used (Miller et al., 1990). Thus, the Sherwood number used in the model is represented by Equation 2.33:

$$S_h^{'} = 12Re^{0.75}\theta_n^{0.60}Sc^{0.5} \quad \text{(eq. 2.33)}$$

R_e is Reynolds number and is represented by Equation 2.34.

$$R_e = \frac{\rho_w v d_m}{\mu_w \theta} \quad \text{(eq. 2.34)}$$

Sc is Schmidt number and is given by Equation 2.35.

$$S_c = \frac{\mu_w}{\rho_w D_m} \quad \text{(eq. 2.35)}$$

Once the kinetic mass transfer flux rate (J) is defined, the transport of dissolved DNAPL is given by mass conservation equation (Equation 2.36):

$$\frac{d(\theta c)}{dt} + \nabla(\mathrm{v}c) - \nabla D(\nabla c) = J \quad \text{(eq. 2.36)}$$

The depletion of DNAPL free phase due to dissolution is given by Equation 2.37.

$$\theta \rho_n \frac{dS_n}{dt} = -J \quad \text{(eq. 2.37)}$$

2.2.2.5 *Transport of contaminant in groundwater*

The dissolved contaminant from the DNAPL source undergoes transport leading to the formation of a contamination plume. Figure 2-5 shows the occurrence of dissolved contaminant originating from an immobilized DNAPL source in the aquifer. As the remediation strategy deals with identifying the contaminant and its distribution, the study of solute transport thus becomes very significant. Such a study enables for locating injecting well and studying the pre- and post-remediation effects. Generally, the transport of dissolved contaminant is a complex combination of hydrological, chemical and biological process (Sethi and Di Molfetta, 2019). A model based on hydrological flow of contaminant can provide us with the insight of spatial distribution of contaminant plume and its temporal evolution. In this thesis, the model is developed based on all the governing physical processes in a natural aquifer. The aqueous contaminant is considered to be chemically stable and conservative in nature. This assumption is supported by the fact that some DNAPL like chlorinated solvents have low retardation coefficient (Lerner et al., 2003).

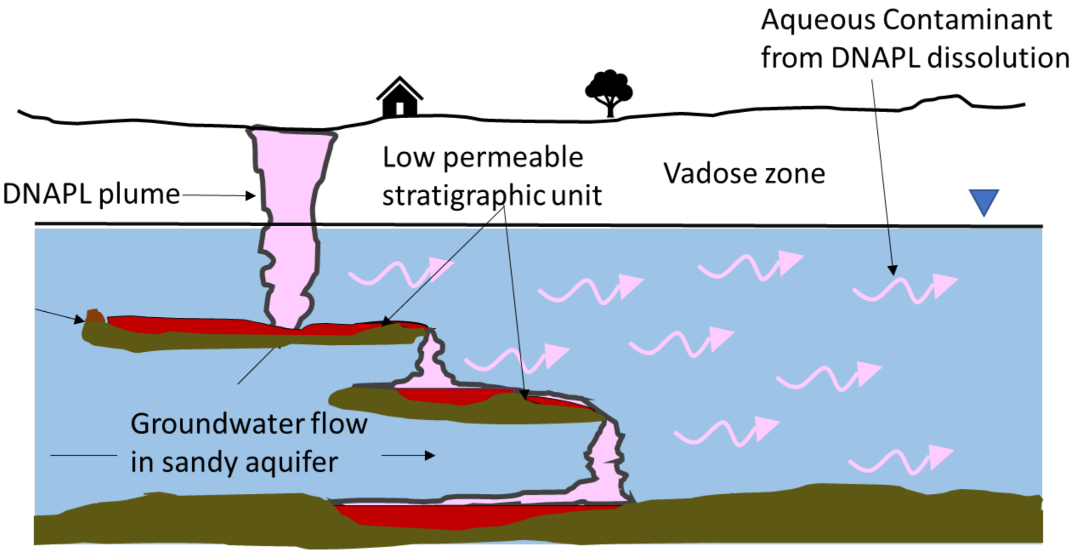

Figure 2-5: Schematics of DNAPL dissolution and its transport in a natural aquifer setting.

Transport of solutes by advection

The advection transport occurs due to the bulk movement of dissolved contaminant in flowing groundwater (Sudicky, 1986). Mathematically, the advection process can be estimated directly by the seepage velocity and the concentration of contaminant. Considering a coordinate system (*x, y, z*) with the groundwater flow direction in the x-axis direction, and the other two being perpendicular to it and to each other (such that $v_x = v; v_y = 0; v_z = 0$), the advective mass flux is given by Equation 2.38:

$$j_a = vc \qquad \text{(eq. 2.38)}$$

Where J_a is the advective flux ($Kg \cdot m^{-2} \cdot s^{-1}$), v is the Darcy velocity ($m \cdot s^{-1}$), and c is the contaminant concentration ($Kg \cdot m^{-3}$).

Notably, the advective flow is different from the actual velocity of fluid in the pore. The actual velocity, also called seepage velocity, is represented by Equation 2.39:

$$v_a = \frac{v}{\theta} \qquad \text{(eq. 2.39)}$$

Where θ is the porosity.

Transport of solutes by molecular diffusion

Molecular diffusion is caused by the random molecular motion of the contaminant due to the thermal kinetic energy (Sethi and Di Molfetta, 2019; Vandenbohede, 2004). The diffusive solute transport occurs along the concentration gradient. The diffusion mass flux is proportional to the concentration gradient and is given by Fick´s second law (Equation 2.40):

$$j_m = -D_d \nabla c \qquad \text{(eq. 2.40)}$$

Where D_d is the molecular diffusion coefficient (m^2·s^{-1}), j_m is the mass flux due to molecular diffusion (Kg·m^2·s^{-1}), *C* is the concentration of the contaminant (Kg·m^{-3}).

Molecular diffusion is isotropic and is independent of flow velocity (Fetter et al., 2017). However, diffusion is very slow and uniform process which reflects a very small and isotropic value of diffusion coefficient. It ranges in the order of 10^{-9} m^2·s^{-1} (Sethi and Di Molfetta, 2019b). The tortuous flow path of fluid in the porous media further decreases the diffusion (Whitaker, 1967). The effective diffusion coefficient is represented by Equation 2.41.

$$D_o = D_d \tau \qquad \text{(eq. 2.41)}$$

Where the unitless quantity τ is called tortuosity. The modified diffusion flux is given by Equation 2.42.

$$j_m = -D_o \nabla c \qquad \text{(eq. 2.42)}$$

Transport of solutes by dispersion

Mass transport due to dispersion is caused by the heterogeneities in the hydrogeological parameters. The non-uniform fluid velocity due to the pore scale heterogeneity leads to a fluid mixing. This forms a mixing zone having different contaminant concentration. The mixing zone also generates a transverse velocity component which accounts for the mass transport in the transverse direction. For the flow in x direction, the mass flux by mechanical dispersion is given by Equations 2.43, 2.44, 2.45 (Delleur, 2006; Domenico and Schwartz, 1998):

$$j_{c,x} = -D_{C,L} \frac{\partial c}{\partial x} \qquad \text{(eq. 2.43)}$$

$$j_{c,y} = -D_{C,T} \frac{\partial c}{\partial y} \qquad \text{(eq. 2.44)}$$

$$j_{c,z} = -D_{C,T} \frac{\partial c}{\partial z} \qquad \text{(eq. 2.45)}$$

Where $D_{C,L}$ and $D_{C,T}$ are the longitudinal and transverse mechanical dispersion coefficient, respectively.

Mechanical dispersion coefficient is proportional to the seepage velocity (Sethi and Di Molfetta, 2019), and is represented by Equation 2.46 and 2.47.

$$D_{C,L} = \propto_L v \qquad \text{(eq. 2.46)}$$

$$D_{C,T} = \propto_T v \qquad \text{(eq. 2.47)}$$

Where $\propto_L$ and $\propto_T$have longitudinal and transverse dispersivity.

Since the mass flux equation for both dispersion and diffusion is proportional to the concentration gradient, the mass transport due to diffusion and mechanical dispersion is often combined under hydrodynamic dispersion (Equation 2.48 and Equation 2.49).

$$D_L = D_o + D_{C,L} = D_o + \propto_L v \qquad \text{(eq. 2.48)}$$

$$D_T = D_o + D_{C,T} = D_o + \propto_T v \qquad \text{(eq. 2.49)}$$

The combined mass flux of mechanical dispersion and molecular diffusion is represented by Equations 2.50, 2.51 and 2.52:

$$j_{d,x} = -D_L \frac{dC}{dx} \quad \text{(eq. 2.50)}$$

$$j_{d,y} = -D_T \frac{dC}{dy} \quad \text{(eq. 2.51)}$$

$$j_{d,z} = -D_T \frac{dC}{dz} \quad \text{(eq. 2.52)}$$

The transverse dispersion leads to a widespread distribution of contaminant in a broad cross-sectional area. This makes the occurrence of contamination at the shallower groundwater level possible irrespective of the contaminant source depth. However, the dispersion in transverse direction is slower compared to longitudinal dispersion (Sethi and Di Molfetta, 2019)

The mass transport equation for contaminant in the aquifer is represented by Equation 2.53:

$$\frac{d(\theta c)}{dt} = -\nabla(j_a + j_d) \quad \text{(eq. 2.53)}$$

Where, j_a and j_d are advective and hydrodynamic dispersion flux.

For the groundwater flow in x direction, the mass transport equation is represented by Equation 2.54:

$$\frac{d(\theta c)}{dt} = -\nabla(vc) + \nabla(D_L \frac{dC}{dx} + D_T \frac{dC}{dy} + D_T \frac{dC}{dz}) \quad \text{(eq. 2.54)}$$

The equation assumes that there is no source or sink term governing the transport of solutes.

2.2.3 Mathematical formulation of the transport and retention of engineered nano-particles (ENPs) in aquifers

The injection and mobility of nano-particles within the porous media is controlled by the transport processes in the groundwater as well as their interaction with the mineral walls. During its interaction with the mineral surfaces, the suspended nano-particles in the groundwater can be retained on the mineral surface. The transport of nano-particles is similar to the contaminants and they are governed by the same processes - advection, diffusion and hydrodynamical dispersion. Therefore, in absence of mineral-particle interaction, the nano-particle mobility can be represented by the Equation 2.54.

Several mechanical and physiochemical processes have been studied to account for the interaction of the suspended particles with mineral surfaces of the host aquifer. The suspended particles in the liquid phase undergoes filtration as it interacts with the rock grains leading to the particle deposition on the pore walls, usually referred in the literature as *attachment* (Yao et al., 1971; Tosco and Sethi, 2010). This retention can be reversible, and the particle can be re-suspended in the water, under a *detachment process* (Raychoudhury, 2011). Mathematically, to account for these processes, the advection and dispersion equation is modified by including attachment and detachment coefficients (Tan et al., 1994; Loveland et al., 2003; Tosco and Sethi, 2009; Equations 2.55 and 2.56):

$$\frac{\partial(\theta C)}{\partial t} + \rho_b \frac{\partial(s)}{\partial t} = -\nabla(vc) + \nabla(D_L \frac{dC}{dx} + D_T \frac{dC}{dy} + D_T \frac{dC}{dz}) \quad \text{(eq. 2.55)}$$

$$\rho_b \frac{\partial(s)}{\partial t} = \theta k_{att} c - \rho k_d s \quad \text{(eq. 2.56)}$$

Where k_{att} and k_d are the first order kinetic attachment and detachment coefficient, respectively, *s* is the deposited particle mass ratio with respect to the rock grains[g/g]. ρ_b is the bulk density of the solid matrix [M·L^{-3}].

The parameter value k_{att} (attachment coefficient) depends on Darcy flow velocity, porosity, affinity of particle to settle down on the mineral surface, and is represented by Equation 2.57 (Krol et al., 2013):

$$k_{att} = \frac{3}{2}\frac{(1-\theta)v\alpha\eta_o}{d_c} \quad \text{(eq. 2.57)}$$

Where d_c is the diameter of a single grain, θ is the effective bed porosity and α *and* η_o are particle-collector attachment efficiency and single-collector contact efficiency.

The porous media bed through which transport occurs is considered to be made up of individual spherical particles and are called *collectors*. The affinity of particles for the collector is defined in two steps: (1) collision of particles with the collector quantified by the single-collector efficiency, and (2) attachment of these particles by the particle-collector attachment efficiency.

The single-collector contact efficiency is a dimensionless parameter and is defined as the ratio of particles colliding onto a collector surface to the total number of particles approaching the collector (Raychoudhury, 2011). Mathematically, it is represented by the Equation 2.58:

$$\eta_o = \eta_I + \eta_D + \eta_G \quad \text{(eq. 2.58)}$$

Where η_I, η_D and η_G represent the contribution of *interception*, *diffusion* and gravitational processes in particle-mineral collision. Calculations of single-collector contact efficiency using the T&E equation (Tufenkji and Elimelech, 2004) indicate the predominance of the diffusion mechanism for a particle with size smaller than a critical value (Raychoudhury, 2011).

On the other hand, the particle-collector attachment efficiency is a dimensionless parameter, and is defined as the ratio of particles that attach onto a collector surface (upon collision) to the total number of particles that collide with that surface. Particle-collector attachment efficiency is a function of solution chemistry and surface properties. The physics of the particle-collector attachment is described briefly in the following section.

2.2.3.1 The theory of the particle-collector interaction

The particle-mineral surface interaction at microscopic level is described by the Derjaguin-Landau-Verwey-Overbeek (DLVO) theory for colloid stability in the water-porous media (Verwey and Overbeek, 1948; Derjaguin and Landau, 1993). This theory describes the total interaction energy experienced by a nano-particle when approaching the collector surface (in the case of deposition). According to the DLVO theory, the deposition of a nano-particle from aqueous phase to mineral phase depends on the net effect of Van der Waals (VDW) and electrical double-layer (EDL) interactions (Petosa et al., 2010). VDW is an attractive force from the electrical and magnetic polarizations, resulting in a non-uniform electromagnetic field at the collector-particle interface. Figure 2-6 shows the typical total interaction energy profile for a particle-collector surface. On the other hand, the Electrical Double Layer (EDL) interaction occurs due to the surface charges of particles and the collector, and such interaction can be attractive or repulsive. When both particle and collector have opposite charges, the electrostatic forces are attractive, and the total energy profile becomes attractive. The energy profile for net attractive force is shown by a dashed blue line in Figure 2-6. The negative DLVO energy denotes net attractive forces, and its magnitude increases with a decrease in the separation distance between the particle and collector. Without repulsive forces acting as energy barrier, the particle is deposited in a close proximity with the collector, at primary minimum and is called *favourable deposition* (Saberinasr et al., 2016).

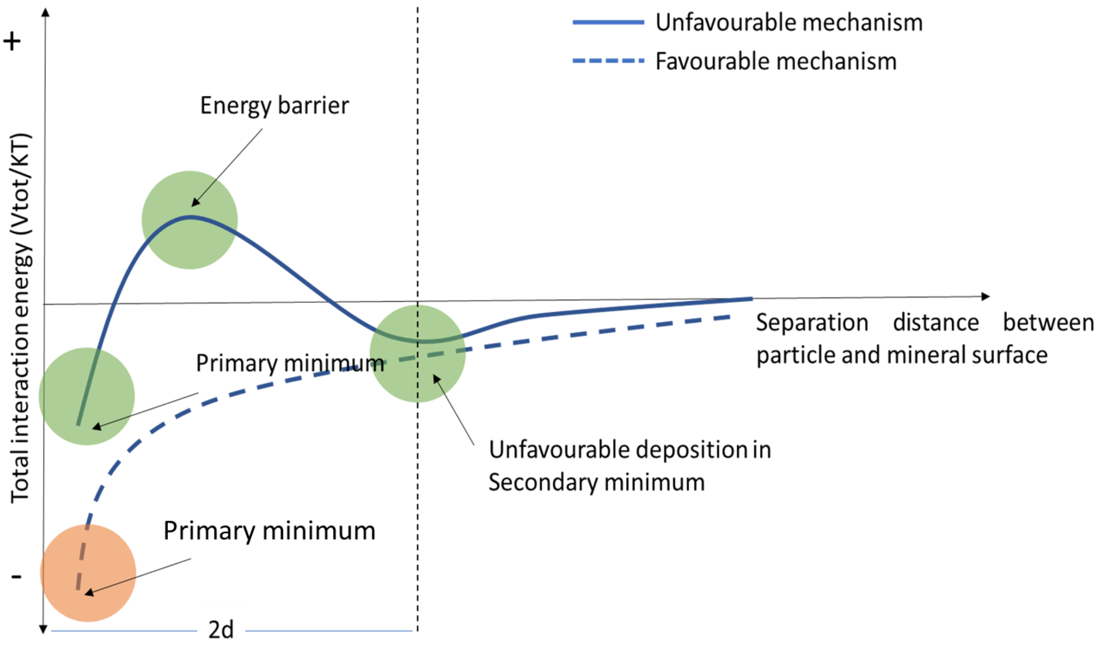

Figure 2-6: *Typical interaction energy profiles showing the particle-collector interaction energy profile. Formation of energy barrier, primary minima and secondary minima on the plot depends on the value of total interaction energy. Adapted from Saberinasr et al. (2016).*

The Colloid Filtration Theory (CFT, Yao et al., 1971) for particle filtration has been traditionally used and is based on the retention of particles at the favorable deposition sites. In this case, the attachment coefficient is considered to be constant with no detachment. Mathematically, CFT can be implemented by simplifying the Equation 2.56 to Equation 2.59.

$$\rho\frac{\partial(s)}{\partial t} = \theta k_{att}c \qquad \text{(eq. 2.59)}$$

When the collector and particle surface charges are the same, a repulsive EDL force governs their interaction (Raychoudhury, 2011). The fate of particle deposition depends on the net effect of repulsive EDL force and attractive Van der Waals force. The total energy profile generated due to this force has a typical trend represented by a solid blue line in Figure 2-6. The EDL force dominates over the Van der Waals force within the region of double-layer formation (given by distance 2d in Figure 2-6). The predominance of EDL force leads to the formation of an energy barrier which hinders the deposition of particles in the primary minimum region. However, due to attractive Van der Waals forces, a secondary minimum of energy is formed, which acts as a conducive site for particle deposition (Petosa et al., 2010). The relatively weak net adhesive force between the particle-collector system leads to a reversible deposition of the particle (Raychoudhury, 2011).

The detachment of the particles deposited under unfavorable conditions can occur when hydrodynamic torque is applied on them (Raychoudhury, 2011). In contrast to colloid filtration theory, the deposition of particles under unfavorable conditions reflects a complex non-linear form of attachment coefficient. Several experiments and model calculations have shown that the mass transfer of CMC-nZVi from mobile to immobile form follows an unfavorable deposition mechanism (Raychoudhury, 2011; Saberinasr et al., 2016). Recent studies have reported that the nano-particle retention is governed by the extended DLVO theory which prescribes the significant role of mechanisms such as steric interactions, magnetic forces (for iron-based nanomaterials), and hydration forces (Yotsumoto and Yoon, 1993; Petosa et al., 2010).

2.2.3.2 Immobilization of engineered nano-particles (ENPs) by physicochemical processes

Mechanical filtration

The process called *mechanical filtration* occurs when a particle encounters a pore channel of smaller size and, thus, its transport gets hindered. *Straining* is one of the mechanical filtration mechanisms, and occurs when colloidal particles are trapped between the space of two or more adjacent grains due to size compatibility (Bradford et al., 2003; Stevik et al., 2004; Raychoudhury, 2011). While some ENPs are clogged in the smaller pores, other ENPs are transported through a connected channel of pores with comparatively larger size.

Figure 2-7 illustrates the deposition of ENPs on the sand surface through straining. A characteristic property of straining is that the attachment coefficient varies with the scale.

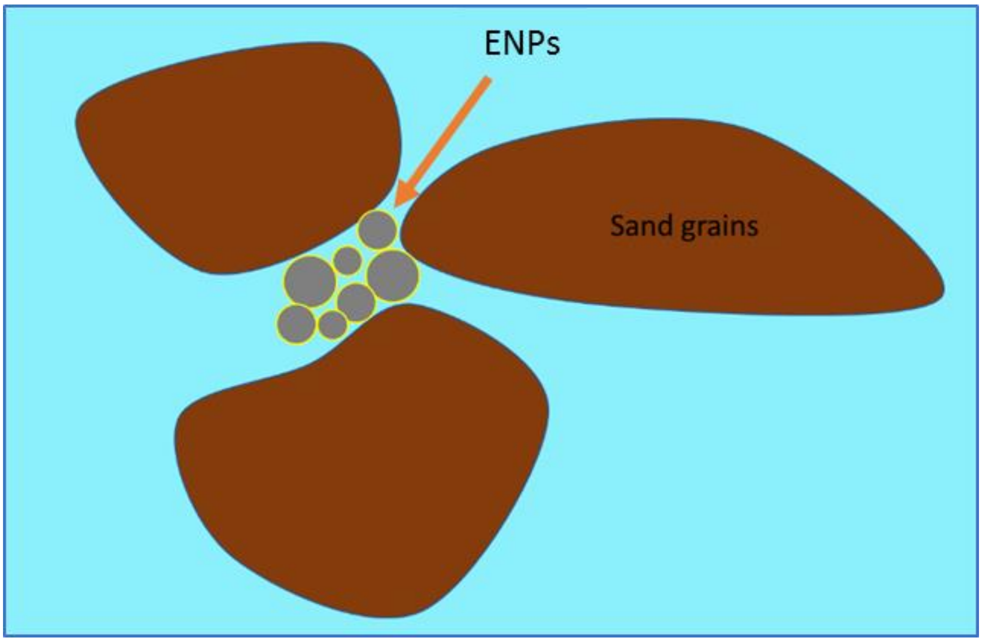

Figure 2-7: *Schematics showing the immobilization mechanisms of ENP by mechanical filtration.*

For a larger distance of transport, the particles with a relatively smaller size remain mobile and, thus, the attachment decreases with length. When the ratio of diameter of particle (d_p) to the diameter of the grain media (d_m) is in the range of 0.002 to 0.06, straining becomes significant (Bradford et al., 2003). The attachment coefficient for straining mechanism as a function of distance from inlet is given by Equation 2.60 (Tosco et al., 2010):

$$k_{att} = k_a \left(1 + \frac{x}{d_{50}}\right)^{\beta} c \qquad \text{(eq. 2.60)}$$

Where k_a is attachment rate, β [-] is the exponent coefficient that defines the interaction dynamics. and d_{50} is the mean diameter of porous media [L].

The straining mechanism governing the mobility of ENPs results in a characteristic pattern of breakthrough curve (BTC) and retention profiles. Considering the injection of ENPs into an experimental column filled with sand, the BTC of particles coming out from the column shows a steady and gradual rise of effluent concentration, after the time period of first arrival (Figure 2-8a). Such an increase in concentration indicates a decline in the number of particles attached to the mineral surface with time. This decrease in the attachment process is related to the formation of channeling where the deposition due to straining is minimal. The *retention profile* is plotted to study the immobilization of nano-particles on the mineral surface. In case of straining, the retention profile shows a hyper-exponential curve (Figure 2-8 b).

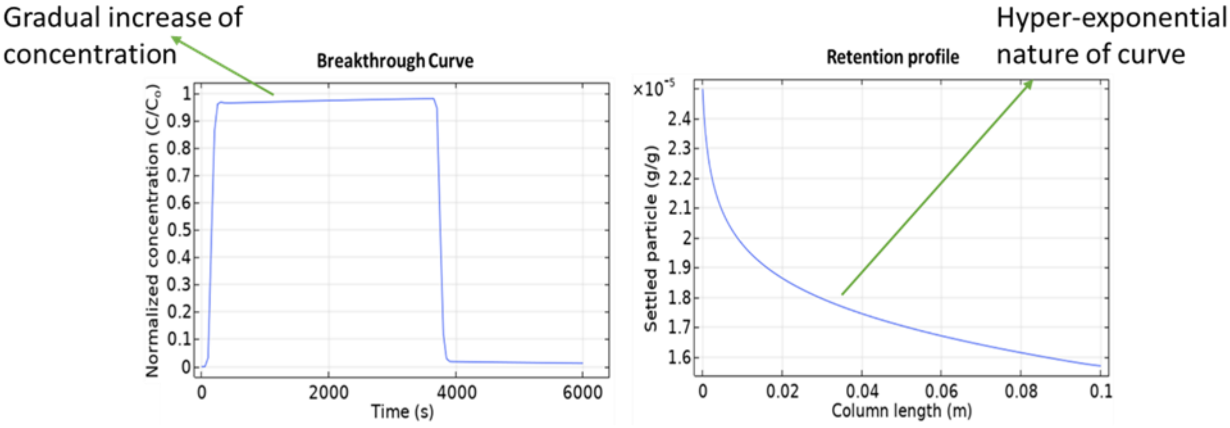

(a) (b)

***Figure 2-8**: A typical breakthrough curve (BTC) obtained for injected ENPs into a sand-filled column undergoing mechanical filtration (a), and the corresponding characteristic retention profile (b).*

Physicochemical linear filtration

Linear filtration of an ENP in the porous media occurs under negligible particle-particle interaction, and its retention is only controlled by particle-mineral surface interaction. According to the net effect of EDL and Van der Waals, nano-particles can get retained in the primary or secondary minima of interaction energy zones depending on the DLVO forces. This process can be mathematically represented by a constant, first order kinetic attachment coefficient. The typical breakthrough curve of ENPs coming out from a sand-filled column shows a steady increasing trend until effluent concentration becomes equal to influent (Figure 2-9). The particle retention profile in the column shows a typical non-linear decrease with the column length. The detachment coefficient can be zero or non-zero depending on the possibility of particle retained in favorable or unfavorable condition.

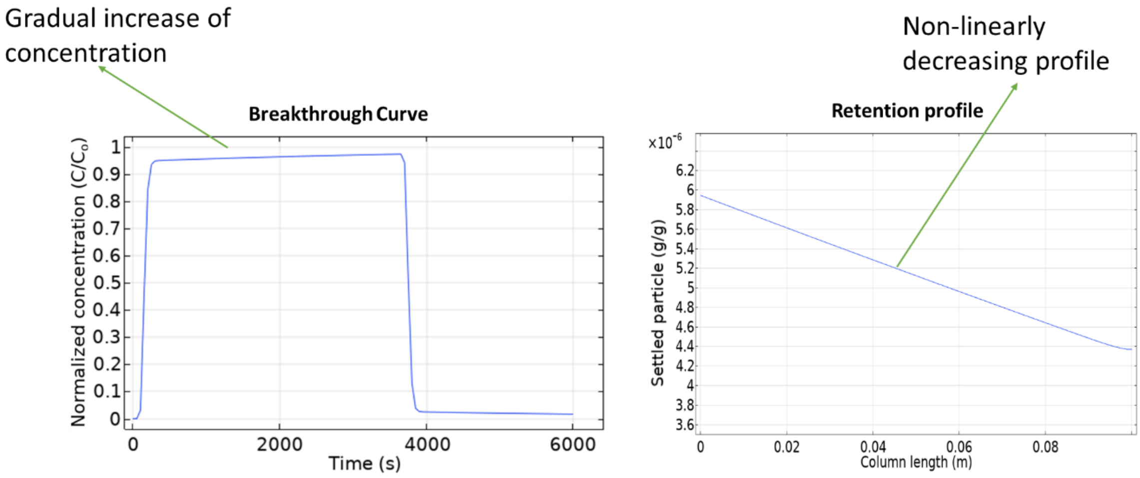

Figure 2-9*: A typical breakthrough curve (BTC) obtained for injected ENPs into a sand-filled column undergoing linear filtration (a), and the corresponding characteristic retention profile (b).*

Physicochemical filtration: Ripening

Ripening is a retention process of ENPs in porous media occurring under a significant particle-particle interaction (Raychoudhury, 2011). The adhesive forces on the settling particle are exerted by both the settled particle and mineral grains. As more particles are deposited, the particle-particle force increases up to the point that it counters particle-mineral surface forces. This leads to the formation of multilayer particle deposition. The retention of particles follows a positive feedback loop leading to a characteristic BTC (Figure 2-10a). This shows a decline in the effluent concentration after attaining a peak value. The corresponding retention curve shows a large amount of particle deposition, predominantly near to the inlet of the column (Figure 2-10b).

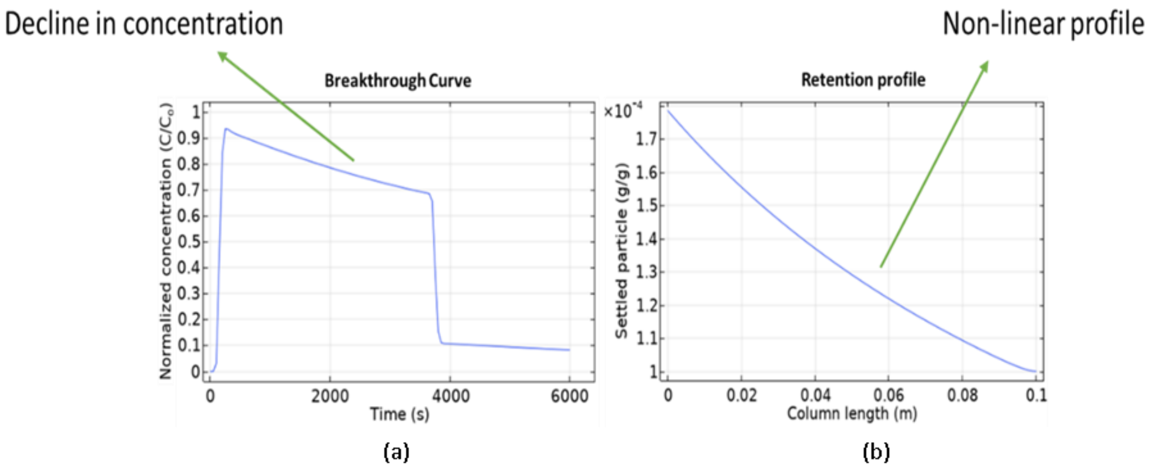

Figure 2-10: *A typical breakthrough curve (BTC) obtained for injected ENPs into a sand-filled column undergoing ripening (a), and the corresponding characteristic retention profile (b).*

Physicochemical filtration: Blocking

The *blocking* mechanism occurs when the particle-particle interaction is repulsive in nature, and, thus, the deposition of particles in close proximity is hindered (Wenjing et al., 2016). The distribution of injected ENPs in the sand-filled column depends on the net effect of particle-mineral grain attractive force and particle-particle repulsion forces. The characteristic distribution pattern leads to a limited availability of the deposition sites and the net deposition rate of particles declines over time. During blocking, the retention of ENPs follows a negative feedback loop with the attachment coefficient decreasing over the time. The characteristic pattern of deposition through the blocking mechanism is illustrated in Figure 2-11. The deposited nano-particles are separated by an optimal distance such that the particle-particle repulsive force is minimized.

The characteristic breakthrough curve in an experiment of ENPs injection into a sand-filled column undergoing blocking mechanism shows that, after a short period of unsteady rise, the effluent concentration becomes equal to influent (Figure 2-12a). The blocking mechanism is typically characterized by a nearly horizontal retention profile (Figure 2-12b).

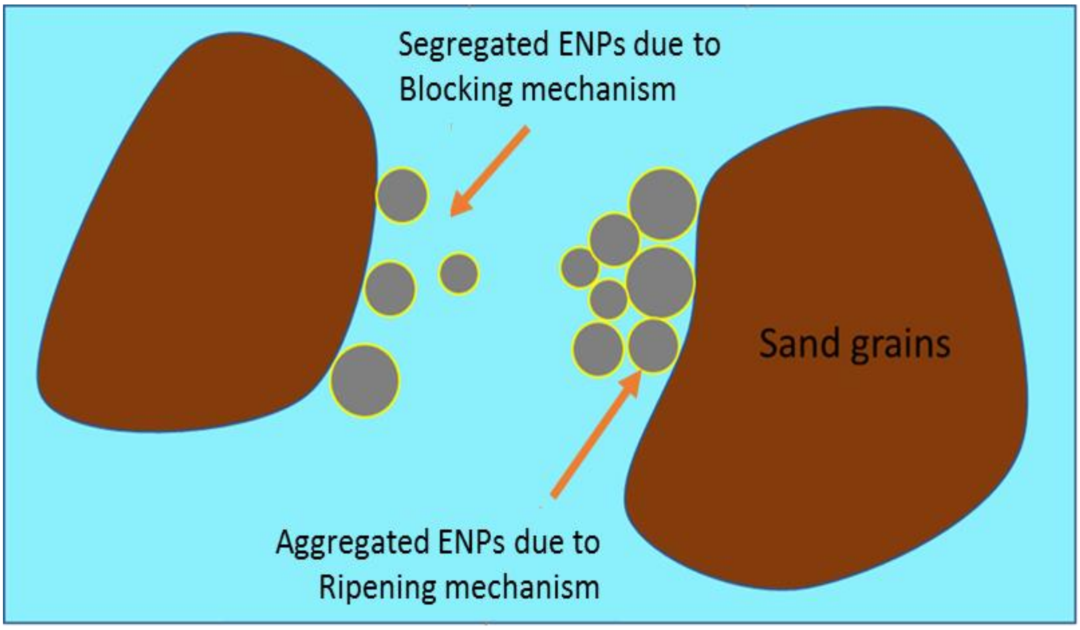

***Figure 2-11**: Schematics for nano-particles transport deposition on sand surface through ripening and blocking mechanism.*

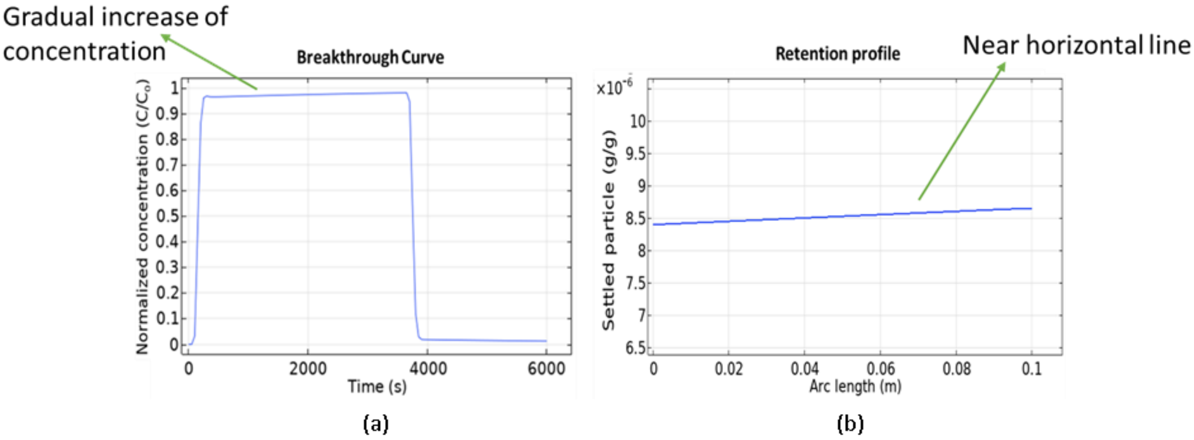

***Figure 2-12**: A typical breakthrough curve (BTC) obtained for injected ENPs into a sand-filled column undergoing blocking (a), and the corresponding characteristic retention profile (b).*

2.2.3.3 Comparison between the impact on ENP retention in porous media caused by the different mechanisms of filtration

Taking as a reference the BTC and retention curves, a comparison between all retention mechanisms can be made and can help identify the main governing mechanisms when investigating the behavior of the particles once injected in column experiments, tank experiments or field scale. The pink curve in Figure 2-13 shows the typical breakthrough curves and retention profiles when two sites of deposition are present. Each mechanism has a characteristic breakthrough curve (BTC) and retention profile. The straining, linear and blocking mechanism have similar breakthrough curves, whereas the ripening shows a characteristically declining trend of effluent particle concentration.

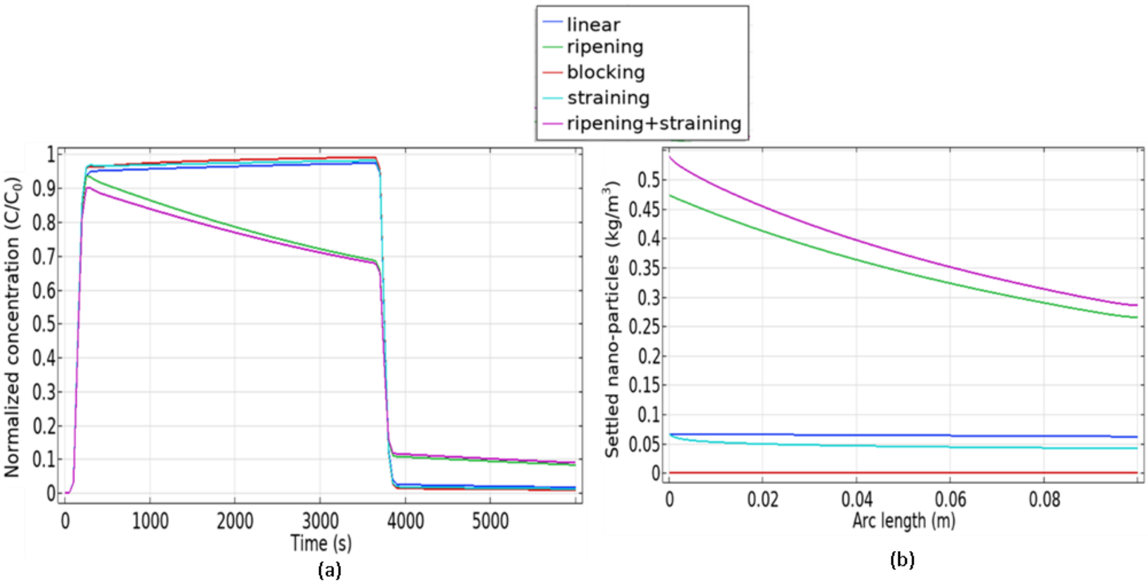

Figure 2-13: Plot for comparison of the effect of the retention mechanisms (ripening, blocking, linear filtration and straining) on ENPs injected in column, tank or field scale experiments (a) Breakthrough curves (b) Characteristic retention profiles.

The curves depicted in Figure 2-13 have been plotted using formulas that express mathematically all these retention mechanisms. A general equation describes the attachment coefficient for ripening and blocking (eq. 2.61; Tosco and Sethi, 2010):

$$k_{att} = \theta k_a (1 + A s^{\beta}) \qquad \text{(eq. 2.61)}$$

Where k_a is attachment rate [T^{-1}], A is multiplier coefficient [-], and B is exponential coefficient [-].

For $A > 0$ and $\beta > 0$, the deposition rate increases with increasing concentration of attached particles, thus, resulting in a ripening. Conversely, for $\beta = 1$, $A = -1/s_{max}$, the blocking occurs, being s_{max} the maximum concentration of particles that can be deposited in the pore space. For A = 0, Equation 2.61 expresses linear filtration conditions.

The plots in Figure 2-13 are calculated considering 0.19 kg·m^{-3} of injected ENPs in a column of 0.1 m long, with a pore velocity of 15mm·min^{-1}. The Table 2-2 shows the values of coefficients were used for comparison of different mechanisms.

Under a general condition, both mechanical as well as physiochemical process of deposition of ENPs in the porous media can be present simultaneously (Bradford et al., 2003; Tosco and Sethi, 2010).

***Table 2-2**: Selected values for the parameters used for building curves in Figure 2-13.*

	Linear	**Straining**	**Ripening**	**Blocking**
K_d *[1/s]*	0.0002	0.0002	0.0002	0.0002
K_a *[1/s]*	0.0004	0.0004	0.0004	0.0004
A	0	–	5000	-100
β	1	0.08	0.7	0.3
d_{50}	–	0.006	–	–

A general two-surface-sites, advection-dispersion-sorption formulation can be written as Equations 2.62, 2.63 and 2.64:

$$\frac{\partial(\theta C)}{\partial t} + \rho_b \frac{\partial(s_1)}{\partial t} + \rho_b \frac{\partial(s_2)}{\partial t} = -\nabla v c + \nabla\left(D_L \frac{dC}{dx} + D_T \frac{dC}{dy} + D_T \frac{dC}{dz}\right) \quad \text{(eq. 2.62)}$$

$$\rho_b \frac{\partial(s_1)}{\partial t} = \theta k_{a,1}\left(1 + A s^{\beta_1}\right) c - \rho k_{d,1} s_2 \quad \text{(eq. 2.63)}$$

$$\rho_b \frac{\partial(s_2)}{\partial t} = \theta k_{a,2}\left(1 + \frac{x}{d_{50}}\right)^{\beta_2} c - \rho k_{d,1} s_2 \quad \text{(eq. 2.64)}$$

Where the variables have suffix as 1 or 2 corresponding to site 1 and site 2, respectively.

2.2.4 Chemical reactions between chlorinated solvents and Zero Valent Iron (ZVi) nano-particles

The Zero Valent Iron (ZVi) consists of unoxidized Fe (0) at the core and iron oxide at the surface. These iron oxides mediate the transfer of electrons from the iron core to the contaminant solutes facilitating their degradation. These reactions are surface mediated, and the chemical interaction of nano ZVi (nZVi) can be categorized in at least three steps in the framework of Langmuir-Hishelwood-Hougen-Watson (LHHW) model (Liu et al., 2005): (1) Adsorption of substrate to reactive sites at the surface, (2) reaction at the surface, and (3) desorption of the reactants. The rate kinetics of the abiotic dechlorination can be controlled by the slowest step among all three.

During the surface reaction, iron oxides act as a barrier for electron transfer, and the direct transfer of electron from Fe (0) to the contaminant is only possible through pit or pinholes. The oxide-mediated transfer of electron happens via the oxide conductive band, impurity band or localized band (Li et al., 2006).

As shown in Figure 2-14, there are three main reaction pathways through which chlorinated solvent undergo abiotic degradation (He et al., 2015):

1. *Reductive dechlorination*: It refers to the reduction of chlorinated solvent by accepting two electron and eliminating two chlorine atoms. This dechlorination process has two

pathways: (1) Alpha elimination is when two chlorides are removed from the same carbon atoms, and (2) Beta elimination is when the two chlorines are removed from two different carbon atoms. These are the most common and predominant reduction pathways in both natural setting and ZVi-injected environments (Fan et al., 2017).

2. *Hydrogenolysis*: In this reaction, hydrogen replaces chlorine from C-Cl bond as the chlorinated solvent accepts two electrons (Tobiszewski and Namieśnik, 2012). This pathway is not favorable from groundwater remediation standpoint, as it results into intermediate products such as DCE and vinyl chloride which are more toxic than TCE or PCE. With nZVi, these reactions are significantly minor.
3. *Dehydrohalogenation*: It refers to the chemical reaction when the C-C bond is formed along the removal of one hydrogen and one chlorine. Since there is no transfer of electron involved as the oxidation state of carbon remains same, it is a non-redox degradation.

The half reactions involved in the reduction of a chlorinated solvent such a TCE are listed below (Liu et al., 2005).

$$Fe^0 \rightarrow Fe^{+2} + 2e^-$$

$$Fe^0 \rightarrow Fe^{+3} + 3e^-$$

$$TCE + ne^- + mH^+ \rightarrow products + 3Cl^-$$

$$2H^+ + 2e^- \ \rightarrow \ H_2$$

Two or three electrons are provided by Fe(0) depending on the transformed oxidation state of the iron.

With sulfidized nZVi (explained in section 1.3), the primary pathway for the chlorine ethenes is the beta elimination leading to the formation of acetylene. However, the end product for TCE degradation is ethane and ethylene due to lesser stability of acetylene (Arnold and Roberts, 2000). Hydrogenolysis is comparatively less frequent, and its byproducts are observed in trace amounts (Arnold and Roberts, 2000). The degradation capacity of nZVi for chlorinated solvents decreases with increase in the degree of chlorination (Arnold and Roberts, 2000; Song and Carraway, 2005)

The reduction potential of Fe (0) is -0.44 V, enabling it to reduce the metal and organic contaminant which would not reduce in the natural condition (Rajajayavel and Ghoshal, 2015). While this is good for remediation, the contaminant also faces competition for acquiring electron from other chemical species including water. Because of hydrophilic nature of iron oxide, the surface remediated reaction reduces water significantly more than chlorinated solvent (Fan et al., 2017).

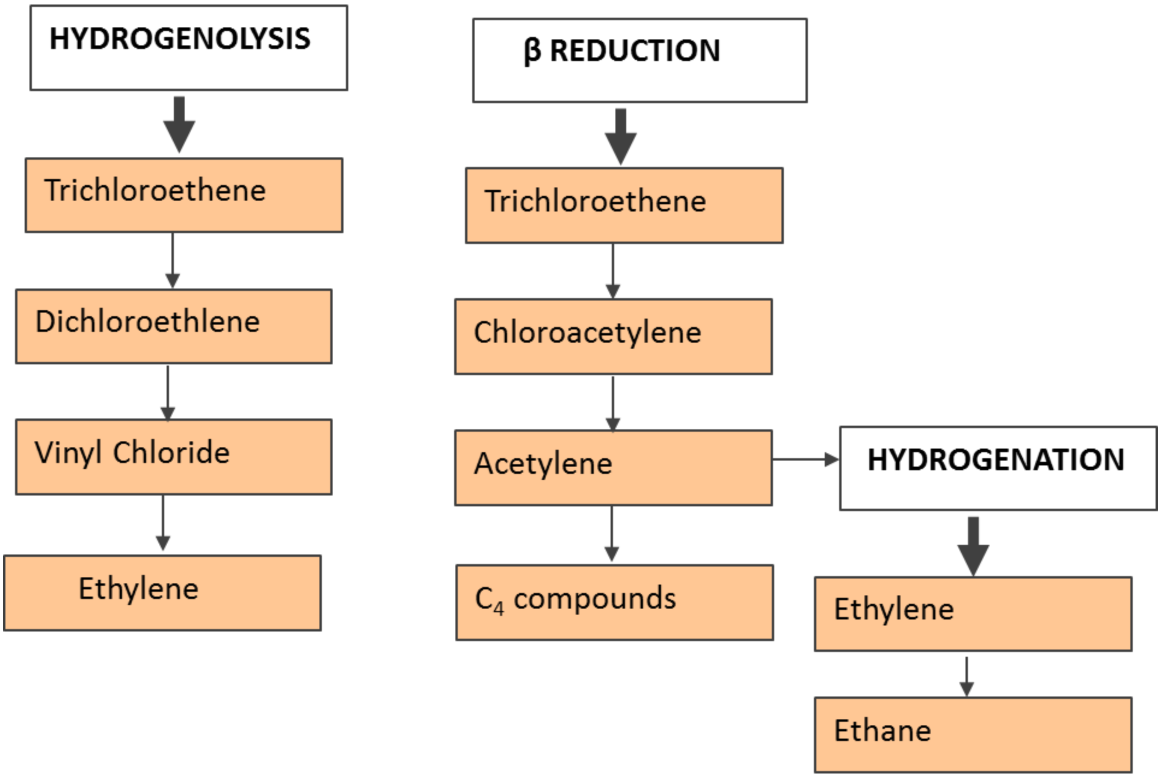

***Figure 2-14**: Three common reaction pathways for reduction of trichloroethene (TCE) each with a unique degradation product.*

2.2.4.1 Degradation rate of chlorinated solvents by nZVi

The degradation rates of chlorinated solvents depend on the mechanism with which the nZVi interacts with them. As the chemical interaction occurs in several electrochemical steps, the rate is given by the slowest step. There are three steps in which the chlorinated solvents interact with untreated nZVi or modified nZVi: (1) adsorption, (2) electron transfer, and (3) desorption. The electron transfer is slowest step and, thus, the degradation rate is dependent on this half reaction (Arnold and Roberts, 2000).

Han and Yan (2016) reported that the nZVi is expected to degrade the 90% of TCE in 21 days but with sulfidized ZVi the time period decreases to 3 days. Several experiments have found a significant increase in the degradation of TCE in the range of up to one order with sZVi. While the TCE degradation increases, the H_2 production decreases. While this looks counterintuitive, Rajajayavel and Ghoshal (2015) attributed this to the property of FeS surface layer on nZVi. The higher binding capacity of FeS than the oxides results in a greater adsorption of TCE and of a conducive transfer of electron which is reflected as higher degradation rates. On the other hand, FeS is less hydrophilic than water.

2.2.4.2 Kinetics of chlorinated solvents degradation by sulfidized nZVi

The degradation of chlorinated solvents under laboratory conditions is decreasingly exponential with time (Arnold and Roberts, 2000; Rajajayavel and Ghoshal, 2015). A pseudo-first-order reaction rate has been widely used in literature which has been found to be directly proportional to the surface area (Han and Yan 2016, Rajajayavel and Ghoshal, 2015). However, other geochemical factors including pH, natural organic matter, coexisting metal ions, and sulfide concentration on ZVi surface can have a role in the degradation rate (He et al., 2015). The equation for kinetic rate is represented by equation 2.65, using TCE as an example:

$$-\frac{dC}{dx} = K_{TCE}c \qquad \text{(eq. 2.65)}$$

Where K_{TCE} is the pseudo first order rate constant (m·s^{-1}), and C is the solute concentration in Kg·m^{-3}.

A surface area normalized rate constant is represented by Equation 2.66:

$$k_{SA} = K_{TCE}/(\propto_s \rho_m) \qquad \text{(eq. 2.66)}$$

Where $\propto_s$ is the surface area m^{2}g^{-1}, and ρ_m is the concentration of the iron distributed in the porous media Kgm^{-3}.

The kinetic equation given by surface area normalized reaction rate is represented by Equation 2.67

$$\frac{dC}{dx} = -k_{SA} \propto_s \rho_m c \qquad \text{(eq. 2.67)}$$

2.2.5 Numerical framework using a software package

The prediction of fluid flow under Eulerian framework requires the conservation of momentum and the total mass in the study domain (Bear, 1972). These equations constitute a set of complex and often non-linear combination of Partial Differential Equations (PDEs) (Bear, 2013; Helmig, 1997). These PDEs are initial boundary value problems where the independent variables are spatial coordinates and time (Huyakorn, 2012). To solve the PDE equations, several analytical methods (Dalla et al., 2002; McWhorter and Sunada, 1990) as well as numerical methods including finite difference analysis (Pruess et al., 1999), finite element analysis (Zyvoloski et al., 2011), and finite volume analysis (Hammond et al., 2012) has been developed. The advantage with using finite element method is its adaptability in the domain discretization, the complex geometry, and the feasibility in dealing with discontinuous gradient of state variables (Dickinson et al., 2014). Therefore, the numerical models in this thesis have been developed using the Finite Element Method.

The software package used for implementation of finite element method in this research work is *Comsol Multiphysics* (Comsol, 2019). Comsol is capable of coupling diverse physical phenomena as well as customizing the mesh and solver for each problem; all these features make it suitable for developing the multiscale multiphysics model in this thesis. Comsol offers a Graphical Interface (GI) to create the geometry of the model domain, to implement the PDE formulation including boundary conditions, and to customize the modelling steps according to the need of the model. Figure 2-15 shows the flowchart for the step followed by Comsol Multiphysics software under Finite Element Analysis framework.

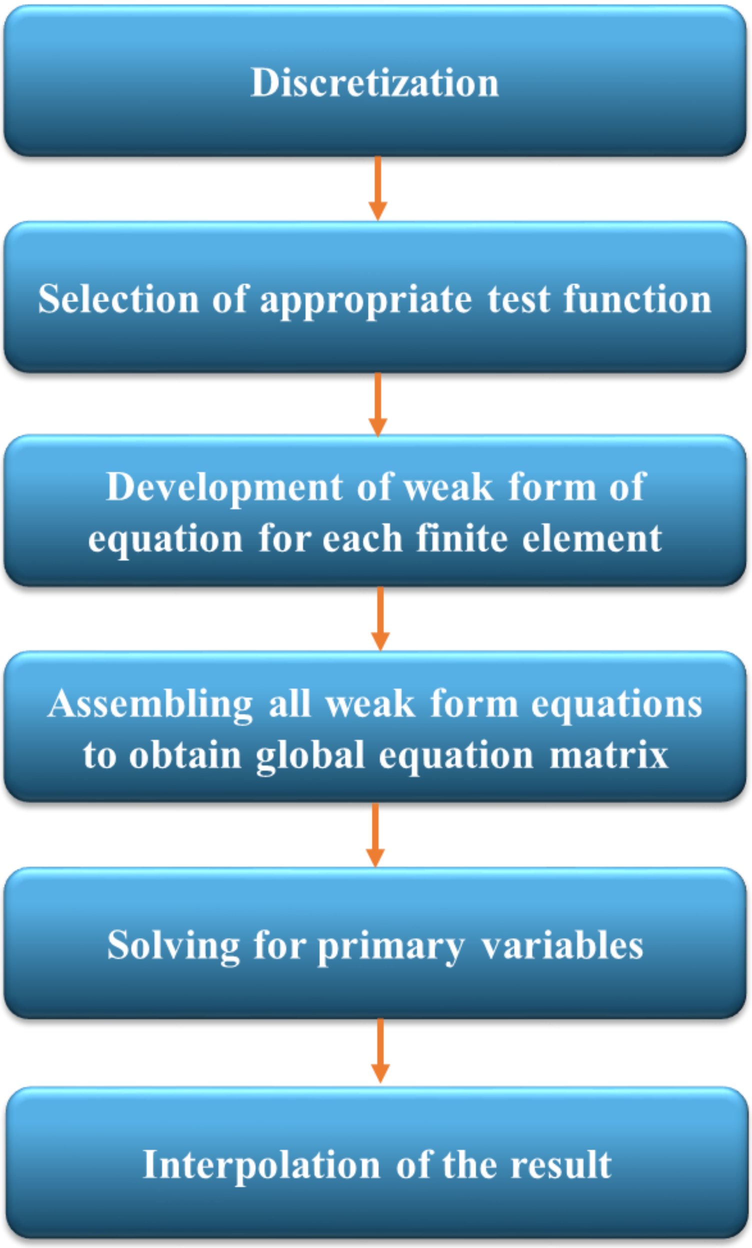

Figure 2-15*: Flowchart for the step-by-step process of numerical operation on Comsol Multiphysics software.*

Firstly, the continuous study domain is discretized into finite elements along which the numerical formulation is applied. These elements can be regular or irregular depending on the complexity of the domain geometry. The element contains the nodes at a specific spatial coordinate where degree of freedom and equations are implemented.

The element size and expansion rate are customized for better approximation of the PDE equation. In the second step, the equation is converted into weak formulation, also called *weighted residual* for which is the weighted integral form of PDE equation using a weight or test function (Reddy, 1993). The weak form relaxes the condition of the PDE equation (also called *strong form*) to be defined at each point. For example, if the derivative of the state variable is discontinuous at a point, leading to degeneration of strong form, the weak form equation is still defined for that point. The weak form of equation is approximated by using a piecewise polynomial function, and are called *basis function*. The implementation of this basis function allows the approximation of local state variables of an element by quantifying the flux variation for the element. This basis function can either be a Lagrange polynomial, which is interpolated evenly over the finite element and bounded by the function values of the local nodes, or it can be a Hermit interpolation polynomial, which incorporates both functional value and its derivative at the element boundary (Hosseini, 2017).

According to the type of basis function used in the weak form equation, there are three main types of finite element method, namely: (1) collocation method where Dirac delta function is used as the test function, and (2) least-squared method, where the integral of the square of residuals is minimized to approximate the unknown (Reddy, 1993), (3) Bubnov-Galerkin (or simply called Galerkin) where shape functions are equal to the weighting functions (Brenner and Scott, 2007; Chao et al., 2002).

The Galerkin method is the most widely used for developing a Finite Element framework. It is based on the establishment of an orthogonal relationship between the residual vectors and basis function (*Galerkin orthogonality*). The advantage of Galerkin method is that it leads to minimum energy norm error and the symmetry of stiffness matrix is preserved (Chao et al., 2002). This method was first popularized by Courant in the early 1940s when it was applied for solving vibration and equilibrium study (Courant, 1943). With its extensive development in the subsequent decades, it finds its application in different field including structural analysis, fluid dynamics, subsurface flow and electromagnetism among others (Bastos and Sadowski, 2003; Reddy, 1993; Zienkiewicz and Taylor, 2005). The wide application of Galerkin method in scientific and technical research owes to its capability for solving any differential problems, ease in modelling complex geometries, and flexible programming format (Donea and Huerta, 2003).

Comsol uses Standard Galerkin, with finite element in Galerkin framework with a standard continuous Lagrange-shape function (Comsol, 2019). However, a set of stabilization method is often necessary as the Galerkin method exhibits a globally propagating oscillation specially in advection-dominated problems (Galeão and Do Carmo, 1988). The model developed in the thesis has used a set of stabilization techniques such as streamline diffusion and crosswind diffusion.

In the last step of model implementation, the individual finite element equation is assembled to form a global equation for the overall domain. The continuity of the primary variable and balance of mass flux is a necessary condition for the assemblage (Reddy and Gartling, 2010). The assembled equation is a linear matrix equation in the form of (Equation 2.68): $k \times u = f$ (eq. 2.68)

Where *K* is stiffness matrix, *f* is force vector, and *u* is the unknown state variables.

Comsol solver is based on Newton-Raphson algorithm, which is used for finding roots of the polynomial equation. The two main solvers in Comsol are direct and iterative solvers; the direct solver solves the system of linear equation based on LU decomposition method. Direct solver requires a relatively higher computational time and resources but is more robust than the iterative method. Direct methods for Finite element Analysis are becoming more efficient with increase in computer power and the use of shared memory and parallel algorithms (Davis, 2006). The direct solvers provided by Comsol are: MUMPS (Fried, 1973), PARDISO (Petra et al., 2014) and SPOOLES (Ashcraft and Grimes, 1999). The results from these solvers are same for all well-conditioned finite element problems and can even solve some quite ill-conditioned problems.

Contrary to direct method, the iterative solver approaches to the solution in a step-by-step fashion. The iterative algorithm used by the solver is mathematically equivalent to Conjugate gradient method (Saad and Schultz, 1986). The iterative solvers available in Comsol are: conjugate gradients (Greenbaum, 1997; Hestenes and Stiefel, 1952; Lanczos, 1952), BiCGStab (van der Vorst, 1992), GMRES (Saad and Schultz, 1986) and FGMRES (Saad, 1993). When the condition number of the matrix system is higher, the solver convergence or computational time can be affected (Fried, 1973), and the iterative solver uses a pre-conditioning procedure that improves the condition number of the matrix.

For a time-dependent problem, Newton iteration can have explicit and implicit states. Comsol mainly uses time implicit solution. Implicit schemes are unconditionally stable and can facilitate higher time steps. However, they can be computationally expensive and can have severe numerical dispersion (Allen, 1984; Settari and Aziz, 1975). Explicit schemes demand less computational resources; however, they are affected by the magnification of round off errors. Therefore, a small-time step is favorable for an explicit scheme, with the length of step limited by a critical Courant number (Plešek et al., 2012). Due to the restriction on time scale, the explicit scheme may require large computational time and thus not suitable to field scale models.

For a non-linearly coupled system represented with two or more state variables, the implicit schemes have two approaches to solve the equations: (1) a fully coupled approach, and (2) a sequential method. In the fully-coupled method, all secondary variables are solved simultaneously at each iteration. This allows a higher accuracy and smaller number of iterations as the propagation of residual error diminishes. However, as the Jacobian matrix can be relatively larger specially for a field scale model, it requires higher computational resources and time.

An alternative for solving coupled equation is the sequential method, where each state variable is solved in a sequential manner, with each step representing a single physics. As the set of equation is subdivided, it requires comparatively less computational resources and time. However, the convergence of solution is likely to be less robust compared to fully implicit.

Comsol Multiphysics offers a flexible software platform, where the user can customize the solutions scheme, tolerance, damping factor, etc, according to the need of the simulation. In this thesis, *backward differential equation* (BDF), a class of implicit scheme, is used with fully coupled or segregated approach according to the degree of freedom of the model. An adaptive time step is used to control the temporal discretization of the PDE equation.

2.3 References

Allen, M.B., 1984. Why upwinding is reasonable, in: Finite Elements in Water Resources. Springer, pp. 13–23.

Arnold, W.A., Roberts, A.L., 2000. Pathways and kinetics of chlorinated ethylene and chlorinated acetylene reaction with Fe (0) particles. Environmental Science & Technology 34, 1794–1805.

Ashcraft, C., Grimes, R.G., 1999. SPOOLES: An Object-Oriented Sparse Matrix Library., in: PPSC.

Bastos, J.P.A., Sadowski, N., 2003. Electromagnetic modeling by finite element methods. CRC press.

Bear, J., 2013. Dynamics of fluids in porous media. Courier Corporation.

Bradford, S.A., Simunek, J., Bettahar, M., van Genuchten, M.T., Yates, S.R., 2003. Modeling colloid attachment, straining, and exclusion in saturated porous media. Environmental science & technology 37, 2242–2250.

Brenner, S., Scott, R., 2007. The mathematical theory of finite element methods. Springer Science & Business Media.

Brooks, R.H., Corey, A.T., 1964. Hydraulic properties of porous media. Hydrology papers (Colorado State University); no. 3.

Brusseau, M.L., Zhang, Z., Nelson, N.T., Cain, R.B., Tick, G.R., Oostrom, M., 2002. Dissolution of nonuniformly distributed immiscible liquid: intermediate-scale experiments and mathematical modeling. Environmental science & technology 36, 1033–1041.

Burdine, N., 1953. Relative permeability calculations from pore size distribution data. Journal of Petroleum Technology 5, 71–78.

Carey, G.R., McBean, E.A., Feenstra, S., 2014. DNAPL Source Depletion: 1. Predicting Rates and Timeframes. Remediation Journal 24, 21–47.

Chao, T.Y., Chow, W.K., Kong, H., 2002. A review on the applications of finite element method to heat transfer and fluid flow. Int J Archit Sci 3, 1–19.

Christ, J.A., Ramsburg, C.A., Pennell, K.D., Abriola, L.M., 2010. Predicting DNAPL mass discharge from pool-dominated source zones. Journal of contaminant hydrology 114, 18–34.

Comsol, A.B., 2019. COMSOL Reference Manual (version 5.5)

Courant, R., 1943. Variational methods for the solution of problems of equilibrium and vibrations. Bull. Amer. Math. Soc. 49, 1–23.

Dalla, E., Hilpert, M., Miller, C.T., 2002. Computation of the interfacial area for two-fluid porous medium systems. Journal of Contaminant Hydrology 56, 25–48.

Davis, T.A., 2006. Direct methods for sparse linear systems. SIAM.

Delleur, J.W., 2006. Elementary groundwater flow and transport processes, in: The Handbook of Groundwater Engineering. CRC Press, pp. 123–168.

Derjaguin, B., Landau, L., 1993. Theory of the stability of strongly charged lyophobic sols and of the adhesion of strongly charged particles in solutions of electrolytes. Progress in Surface Science 43, 30–59.

Dickinson, E.J., Ekström, H., Fontes, E., 2014. COMSOL Multiphysics®: Finite element software for electrochemical analysis. A mini-review. Electrochemistry communications 40, 71–74.

Domenico, P.A., Schwartz, F.W., 1998. Physical and chemical hydrogeology. Wiley New York.

Donea, J., Huerta, A., 2003. Finite element methods for flow problems. John Wiley & Sons.

Falta, R.W., Rao, P.S., Basu, N., 2005. Assessing the impacts of partial mass depletion in DNAPL source zones: I. Analytical modeling of source strength functions and plume response. Journal of Contaminant Hydrology 78, 259–280.

Fan, D., Lan, Y., Tratnyek, P.G., Johnson, R.L., Filip, J., O'Carroll, D.M., Nunez Garcia, A., Agrawal, A., 2017. Sulfidation of iron-based materials: a review of processes and implications for water treatment and remediation. Environmental science & technology 51, 13070–13085.

Fetter, C.W., Boving, T., Kreamer, D., 2017. Contaminant hydrogeology. Waveland Press.

Fitts, C.R., 2002. Groundwater science. Elsevier.

Fried, I., 1973. Bounds on the spectral and maximum norms of the finite element stiffness, flexibility and mass matrices. International Journal of Solids and Structures 9, 1013–1034.

Frind, E.O., Molson, J.W., Schirmer, M., Guiguer, N., 1999. Dissolution and mass transfer of multiple organics under field conditions: The Borden emplaced source. Water Resources Research 35, 683–694.

Galeão, A.C., Do Carmo, E.G.D., 1988. A consistent approximate upwind Petrov-Galerkin method for convection-dominated problems. Computer Methods in Applied Mechanics and Engineering 68, 83–95.

Geller, J.T., Hunt, J.R., 1993. Mass transfer from nonaqueous phase organic liquids in water-saturated porous media. Water resources research 29, 833–845.

Grant, G.P., 2005. The evolution of complex DNAPL releases: Rates of migration and dissolution.

Grathwohl, P., 2012. Diffusion in natural porous media: contaminant transport, sorption/desorption and dissolution kinetics. Springer Science & Business Media.

Greenbaum, A., 1997. Iterative methods for solving linear systems. SIAM.

Gvirtzman, H., Magaritz, M., Klein, E., Nadler, A., 1987. A scanning electron microscopy study of water in soil. Transport in Porous Media 2, 83–93.

Hammond, G.E., Lichtner, P.C., Lu, C., Mills, R.T., 2012. PFLOTRAN: Reactive flow & transport code for use on laptops to leadership-class supercomputers. Groundwater reactive transport models 141–159.

Han, Y., Yan, W., 2016. Reductive dechlorination of trichloroethene by zero-valent iron nanoparticles: reactivity enhancement through sulfidation treatment. Environmental science & technology 50, 12992–13001.

He, Y.T., Wilson, J.T., Su, C., Wilkin, R.T., 2015. Review of abiotic degradation of chlorinated solvents by reactive iron minerals in aquifers. Groundwater Monitoring & Remediation 35, 57–75.

Helmig, R., 1997. Multiphase flow and transport processes in the subsurface: a contribution to the modeling of hydrosystems. Springer-Verlag.

Helmig, R., Jakobs, H., Class, H., 2002. Multiphase flow and transport modeling in heterogeneous porous media, in: Developments in Water Science. Elsevier, pp. 233–240.

Hestenes, M.R., Stiefel, E., 1952. Methods of conjugate gradients for solving linear systems. Journal of research of the National Bureau of Standards 49, 409–436.

Hosseini, S.A., 2017. Sensitivity analysis of the Galerkin finite element method neutron diffusion solver to the shape of the elements. Nuclear Engineering and Technology 49, 29–42.

Huyakorn, P.S., 2012. Computational methods in subsurface flow. academic press.

Illangasekare, T.H., Ramsey, J.L., Jensen, K.H., Butts, M.B., 1995. Experimental study of movement and distribution of dense organic contaminants in heterogeneous aquifers. Journal of Contaminant Hydrology 20, 1–25. https://doi.org/10.1016/0169-7722(95)00045-W

Kim, H., Rao, P.S.C., Annable, M.D., 1999. Gaseous tracer technique for estimating air–water interfacial areas and interface mobility. Soil Science Society of America Journal 63, 1554–1560.

Kim, T.-J., Chrysikopoulos, C.V., 1999. Mass transfer correlations for nonaqueous phase liquid pool dissolution in saturated porous media. Water Resources Research 35, 449–459.

Kokkinaki, A., 2013. Modelling of dissolution and bioremediation of chlorinated ethene DNAPL source zones (PhD Thesis).

Kolditz, O., Bauer, S., Bilke, L., Böttcher, N., Delfs, J.-O., Fischer, T., Görke, U.J., Kalbacher, T., Kosakowski, G., McDermott, C.I., 2012. OpenGeoSys: an open-source initiative for numerical simulation of thermo-hydro-mechanical/chemical (THM/C) processes in porous media. Environmental Earth Sciences 67, 589–599.

Kueper, B.H., Frind, E.O., 1991. Two-phase flow in heterogeneous porous media: 1. Model development. Water Resources Research 27, 1049–1057.

Lerner, D.N., Kueper, B.H., Wealthall, G.P., Smith, J.W.N., Leharne, S.A., 2003. An illustrated handbook of DNAPL transport and fate in the subsurface.

Li, X., Zhang, W., 2006. Iron nanoparticles: The core- shell structure and unique properties for Ni (II) sequestration. Langmuir 22, 4638–4642.

Liu, Y., Majetich, S.A., Tilton, R.D., Sholl, D.S., Lowry, G.V., 2005. TCE dechlorination rates, pathways, and efficiency of nanoscale iron particles with different properties. Environmental science & technology 39, 1338–1345.

Loveland, J.P., Bhattacharjee, S., Ryan, J.N., Elimelech, M., 2003. Colloid transport in a geochemically heterogeneous porous medium: aquifer tank experiment and modeling. Journal of contaminant hydrology 65, 161–182.

Luciano, A., Mancini, G., Torretta, V., Viotti, P., 2018. An empirical model for the evaluation of the dissolution rate from a DNAPL-contaminated area. Environmental Science and Pollution Research 25, 33992–34004.

Mayer, A.S., Miller, C.T., 1996. The influence of mass transfer characteristics and porous media heterogeneity on nonaqueous phase dissolution. Water Resources Research 32, 1551–1567.

Mercer, J.W., Cohen, R.M., 1990. A review of immiscible fluids in the subsurface: properties, models, characterization and remediation. Journal of contaminant hydrology 6, 107–163.

Miller, C.T., Christakos, G., Imhoff, P.T., McBride, J.F., Pedit, J.A., Trangenstein, J.A., 1998. Multiphase flow and transport modeling in heterogeneous porous media: challenges and approaches. Advances in Water Resources 21, 77–120.

Miller, C.T., Poirier-McNeil, M.M., Mayer, A.S., 1990. Dissolution of trapped nonaqueous phase liquids: Mass transfer characteristics. Water Resources Research 26, 2783–2796.

Molnar, I.L., Johnson, W.P., Gerhard, J.I., Willson, C.S., O’Carroll, D.M., 2015. Predicting colloid transport through saturated porous media: A critical review. Water Resources Research 51, 6804–6845.

Nambi, I.M., Powers, S.E., 2003. Mass transfer correlations for nonaqueous phase liquid dissolution from regions with high initial saturations. Water Resources Research 39.

Nelson, R.W., 1966. Flow in heterogeneous porous mediums: 1. Darcian-type description of two-phase systems. Water Resources Research 2, 487–495.

Niessner, J., 2006. Multi-scale modeling of multi-phase-multi-component processes in heterogeneous porous media.

Pankow, J.F., Cherry, J.A., 1996. Dense chlorinated solvents and other DNAPLs in groundwater: History, behavior, and remediation.

Parker, J.C., Park, E., 2004. Modeling field-scale dense nonaqueous phase liquid dissolution kinetics in heterogeneous aquifers. Water Resources Research 40.

Petosa, A.R., Jaisi, D.P., Quevedo, I.R., Elimelech, M., Tufenkji, N., 2010. Aggregation and deposition of engineered nanomaterials in aquatic environments: role of physicochemical interactions. Environmental science & technology 44, 6532–6549.

Petra, C.G., Schenk, O., Anitescu, M., 2014. Real-time stochastic optimization of complex energy systems on high-performance computers. Computing in Science & Engineering 16, 32–42.

Plešek, J., Kolman, R., Gabriel, D., 2012. Estimation of the critical time step for explicit integration. Engineering mechanics 292.

Powers, S.E., Abriola, L.M., Weber Jr, W.J., 1994. An experimental investigation of nonaqueous phase liquid dissolution in saturated subsurface systems: Transient mass transfer rates. Water Resources Research 30, 321–332.

Powers, S.E., Abriola, L.M., Weber Jr, W.J., 1992. An experimental investigation of nonaqueous phase liquid dissolution in saturated subsurface systems: Steady state mass transfer rates. Water Resources Research 28, 2691–2705.

Prakash, P., Nambi, I.M., 2012. Dissolution and contaminant transport in aquifers with spatially and temporally variable hydraulic properties. Special Topics & Reviews in Porous Media: An International Journal 3.

Pruess, K., Oldenburg, C.M., Moridis, G.J., 1999. TOUGH2 user's guide version 2. Lawrence Berkeley National Lab.(LBNL), Berkeley, CA (United States).

Rajajayavel, S.R.C., Ghoshal, S., 2015. Enhanced reductive dechlorination of trichloroethylene by sulfidated nanoscale zerovalent iron. Water research 78, 144–153

Raychoudhury, T., 2011. Transport of surface-modified iron nanoparticles through model subsurface porous media. McGill University (Canada).

Reddy, J.N., 1993. An introduction to the finite element method. New York 27.

Reddy, J.N., Gartling, D.K., 2010. The finite element method in heat transfer and fluid dynamics. CRC press.

Ronen, D., Magaritz, M., Paldor, N., Bachmat, Y., 1986. The behavior of groundwater in the vicinity of the water table evidenced by specific discharge profiles. Water Resources Research 22, 1217–1224.

Saad, Y., 1993. A flexible inner-outer preconditioned GMRES algorithm. SIAM Journal on Scientific Computing 14, 461–469.

Saad, Y., Schultz, M.H., 1986. GMRES: A generalized minimal residual algorithm for solving nonsymmetric linear systems. SIAM Journal on scientific and statistical computing 7, 856–869.

Saba, T., Illangasekare, T.H., 2000. Effect of groundwater flow dimensionality on mass transfer from entrapped nonaqueous phase liquid contaminants. Water Resources Research 36, 971–979.

Saberinasr, A., Rezaei, M., Nakhaei, M., Hosseini, S.M., 2016. Transport of CMC-stabilized nZVI in saturated sand column: The effect of particle concentration and soil grain size. Water, Air, & Soil Pollution 227, 394.

Saenton, S., Illangasekare, T.H., 2007. Upscaling of mass transfer rate coefficient for the numerical simulation of dense nonaqueous phase liquid dissolution in heterogeneous aquifers. Water Resources Research 43.

Sale, T.C., McWhorter, D.B., 2001. Steady state mass transfer from single-component dense nonaqueous phase liquids in uniform flow fields. Water Resources Research 37, 393–404.

Schwille, F., Pankow, J.F., 1988. Dense chlorinated solvents in porous and fractured media-model experiments.

Seagren, E.A., Rittmann, B.E., Valocchi, A.J., 1999. A critical evaluation of the local-equilibrium assumption in modeling NAPL-pool dissolution. Journal of contaminant hydrology 39, 109–135.

Sethi, R., Di Molfetta, A., 2019. Groundwater Contaminants, in: Sethi, R., Di Molfetta, A. (Eds.), Groundwater Engineering : A Technical Approach to Hydrogeology, Contaminant Transport and Groundwater Remediation, Springer Tracts in Civil Engineering. Springer International Publishing, Cham, pp. 169–192. https://doi.org/10.1007/978-3-030-20516-4_9

Settari, A., Aziz, K., 1975. Treatment of nonlinear terms in the numerical solution of partial differential equations for multiphase flow in porous media. International Journal of Multiphase Flow 1, 817–844.

Sherwood, T. K., Pigford, R. L., Wilke, C. R.: Mass transfer. New York: McGraw-Hill 1975

Song, H., Carraway, E.R., 2005. Reduction of chlorinated ethanes by nanosized zero-valent iron: kinetics, pathways, and effects of reaction conditions. Environmental science & technology 39, 6237–6245.

Stevik, T.K., Aa, K., Ausland, G., Hanssen, J.F., 2004. Retention and removal of pathogenic bacteria in wastewater percolating through porous media: a review. Water research 38, 1355–1367.

Sudicky, E.A., 1986. A natural gradient experiment on solute transport in a sand aquifer: Spatial variability of hydraulic conductivity and its role in the dispersion process. Water Resources Research 22, 2069–2082. https://doi.org/10.1029/WR022i013p02069

Tan, Y., Gannon, J.T., Baveye, P., Alexander, M., 1994. Transport of bacteria in an aquifer sand: Experiments and model simulations. Water resources research 30, 3243–3252.

Tosco, T., Bosch, J., Meckenstock, R.U., Sethi, R., 2012. Transport of ferrihydrite nanoparticles in saturated porous media: role of ionic strength and flow rate. Environmental science & technology 46, 4008–4015.

Tosco, T., Sethi, R., 2010. Transport of non-Newtonian suspensions of highly concentrated micro-and nanoscale iron particles in porous media: a modeling approach. Environmental science & technology 44, 9062–9068.

Tosco, T., Sethi, R., 2009. MNM1D: a numerical code for colloid transport in porous media: implementation and validation. American journal of environmental sciences 5, 517.

Tufenkji, N., Elimelech, M., 2004. Correlation equation for predicting single-collector efficiency in physicochemical filtration in saturated porous media. Environmental science & technology 38, 529–536.

Unger, A.J.A., Forsyth, P.A., Sudicky, E.A., 1998. Influence of alternative dissolution models and subsurface heterogeneity on DNAPL disappearance times. Journal of contaminant hydrology 30, 217–242.

Vaezihir, A., Zare, M., Raeisi, E., Molson, J., Barker, J., 2012. Field-scale modeling of benzene, toluene, ethylbenzene, and xylenes (BTEX) released from multiple source zones. Bioremediation Journal 16, 156–176.

Van der Vorst, H.A., 1992. Bi-CGSTAB: A fast and smoothly converging variant of Bi-CG for the solution of nonsymmetric linear systems. SIAM Journal on scientific and Statistical Computing 13, 631–644.

Van Duijn, C.J., Molenaar, J., De Neef, M.J., 1995. The effect of capillary forces on immiscible two-phase flow in heterogeneous porous media. Transport in porous media 21, 71–93.

Vandenbohede, A., 2004. Solute transport in heterogeneous aquifers: Parameter identification and its use in groundwater pollution and salt water intrusion problems.

Verwey, E.J.W., Overbeek, J.T.G., 1948. Theory of the stability of lyophobic colloids. Elsevier, Amsterdam. Theory of the stability of lyophobic colloids. Elsevier, Amsterdam.

Wenjing, Z., Jingjing, Z., Dan, L.I.U., Haoyang, L.I., Xipeng, Y.U., Ying, H., 2016. A review: research methods that describe the environmental behavior of colloids in groundwater. 水科学进展 27, 629–638.

Whitaker, S., 1967. Diffusion and dispersion in porous media. AIChE Journal 13, 420–427.

Wu, Y.-S., Forsyth, P.A., 2001. On the selection of primary variables in numerical formulation for modeling multiphase flow in porous media. Journal of contaminant hydrology 48, 277–304.

Xu, J., Wang, Y., Weng, C., Bai, W., Jiao, Y., Kaegi, R., Lowry, G.V., 2019. Reactivity, Selectivity, and Long-term Performance of Sulfidized Nanoscale Zerovalent Iron with Different Properties. Environmental science & technology.

Yao, K.-M., Habibian, M.T., O’Melia, C.R., 1971. Water and waste water filtration. Concepts and applications. Environmental science & technology 5, 1105–1112.

Yotsumoto, H., Yoon, R.-H., 1993. Application of extended DLVO theory: I. Stability of rutile suspensions. Journal of colloid and interface science 157, 426–433.

Zienkiewicz, O.C., Taylor, R.L., 2005. The finite element method for solid and structural mechanics. Elsevier.

Zyvoloski, G.A., Robinson, B.A., Dash, Z.V., Kelkar, S., Viswanathan, H.S., Pawar, R.J., Stauffer, P.H., Miller, T.A., Chu, S., 2011. Software users manual (UM) for the FEHM application version 3.1-3X. Los Alamos National Laboratory, Los Alamos.

3 Multi-scale modeling of DNAPL infiltration in a porous media: insights for groundwater remediation*

3.1 Introduction

Dense Non-Aqueous Phase Liquid (DNAPL) are contaminants denser than water often encountered in an anthropogenically-polluted aquifer. They are an environmental concern because they act as a long-term source for contamination in the groundwater. The infiltration, migration and immobilization of the DNAPL plume in an aquifer depends on the gravitational, capillary and viscous forces (Pankow and Cherry, 1996). These forces combined with heterogeneities in the aquifer often leads to a complex migration pathway of the DNAPL plume (Schwille and Pankow, 1988; Illangasekare et al., 1995).

Before the implementation of measures for the aquifer remediation, the characterization of the impacted area, including the extent and intensity of the contamination along with its past and future physico-chemical evolution, is required. This extensive field characterization can be expensive and time consuming (Mohan et al., 2005), and a predictive insight from numerical modelling can help understand the contamination characteristics complementing the information provided by the field survey. Also, the decision for the selection of a remediation strategy may involve reconstructing the DNAPL infiltration event in a laboratory to examine the governing factors for contamination. Numerical modelling can be helpful for an efficient design and set-up of such experiments (Pankow and Cherry, 1996). Lastly, by reproducing the experimental results (model calibration), the unknown governing parameters can be evaluated and the sensitivity of two-phase flow on these parameters can be predicted (Finsterle, 2004).

The general governing equations for two-phase fluid flow in heterogeneous porous media at field scale were presented by Nelson (1966) and has been reviewed in Chapter 2. Because of complex and non-linear character of the DNAPL infiltration in aquifer, the existing analytical solutions are limited, and several studies have attempted to provide numerical solutions for these equations (Bredehoeft and Pinder, 1973; Bresler, 1973; Essaid, Bekins and Cozzarelli, 2015). Among them, the common numerical tools that have been used are STOMP (Nichols et al., 1997), Tough2 (Pruess et al., 2011), UTCHEM (CPGE, 2000), VENT2D (Benson, 1994). Although there is a large number of models based on finite difference or finite volume methods for multi-phase flow, the flexible geometry and intrinsic boundary adaptation of those models are limited. A model based on Finite Element Method (FEM) offers more flexibility with the numerical environment and thus can be more robust and upscalable (Yu and Li, 2019). Despite these advantages, a FEM-based numerical model for simulating DNAPL infiltration in a field scale scenario is still uncommon in published literature (Yu and Li, 2019).

---

*This chapter is based on the research article “Role of the clay lenses within sandy aquifers in the migration pathway of infiltrating DNAPL plume” submitted to *Journal of Contaminant Hydrology*” by Nilabh S., Grandia F. (2021).

In this Chapter 3, the numerical formulation for two-phase flow in porous media reported in previous studies is reviewed for its implementation in a multi-scale model. The overall objective of this chapter is to develop a multi-scale model with the capacity to predict the migration of DNAPL infiltration in a real field scale scenario. The work has been divided into several relevant steps. In the initial step, the background for numerical formulation is described. Subsequently, a numerical formulation for DNAPL infiltration in a porous medium in one and two dimensions is implemented. To verify the accuracy of the numerical formulation, the model results are compared with several benchmark models. In the last step, the formulation is used in developing as a numerical tool for predicting DNAPL migration in three-dimension field case. The numerical results show the efficiency of the simulation tool for predicting the fluid flow behavior in a general aquifer. Additionally, predictions from a general field case scenario are derived for developing an efficient remediation strategy at any typical contaminated site.

3.2 Model implementation

The simulation of DNAPL in an aquifer is implemented in three stages. In the first stage, the objective is to develop a simple 1D formulation for two-phase flow (DNAPL and water) in the porous media. The model is intended to simulate the complex interplay of capillary and viscous forces governing the fluid flow. In the second stage, the previous formulation is extended to a two-dimensional aquifer with different sand layers. The effect of gravity is included in the model, thus replicating the DNAPL infiltration in a small-scale aquifer. In the third stage, the formulation is upscaled to model a field scale scenario of DNAPL infiltration.

3.2.1 Benchmark exercise 1: Simulation of DNAPL flow in one-dimension, homogeneous aquifer

A set of numerical formulations is implemented in the Comsol Multiphysics software with the aim of modeling 1D, two-phase flow in a porous media. A fundamental step before modelling a case study is the verification of the implemented formulation. This step is done in this study by comparing the results yielded by the computer model with the analytical solution developed in previous studies reported in the scientific literature. In this work, the comparison has been made with the McWhorter and Sunada (1990) analytical solution. In their work, these authors developed a quasi-analytical solution for the calculation of the displacement process of oil by water where both viscous forces and capillary forces are present; the gravity force was not considered in their study. The quasi-analytical solution estimates the saturation profile of the water phase as a complex non-linear function of hydrogeological and the fluid properties. Considering the model domain properties used in their study, a number of simulations have been developed each with different pairs of primary variables as described in Appendix A.

The McWhorter and Sunada case study is based on a 1D sand column with a length of 2.6-meters (Figure 3-1). Initially (t=0), the porous medium is considered to be completely saturated with the non-wetting phase (DNAPL). From the left end (x= 0), the wetting phase (water) enters the sand column with a pressure of 0.2 MPa and saturation of one. The right side of the wall is closed and thus the movement of fluid through this part is stopped.

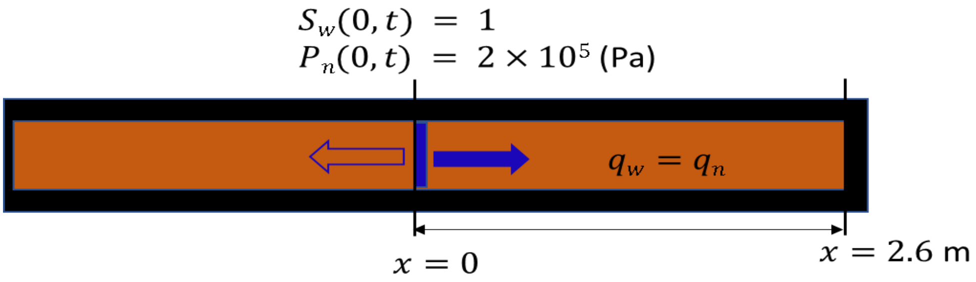

***Figure 3-1**: Porous medium domain for McWhorter and Sunada case study. The wetting phase infiltrates at x =0. The porous medium is initially filled with a non-wetting phase. Adapted from (McWhorter and Sunada, 1990).*

Table 3-1 shows the hydrogeological and fluid properties used in the model implemented in Comsol Multiphysics to simulate two-phase flow. The Brooks-Corey equation has been used to determine the capillary pressure and the relative permeability. The model result from each numerical formulation described in Appendix A is compared with the result derived from the analytical solution.

***Table 3-1:** Fluid properties used for the development of the two-phase flow simulation in 1D sand column. The data are taken from McWhorter and Sunada (1990).*

Property	**Symbol**	**Value**
Column length	L	2.6 m
Wetting dynamic viscosity	μ_w	0.001 Pa·s
Non-wetting dynamic viscosity	μ_{nw}	0.001 Pa·s
Wetting phase density	ρ_w	1000 kg·m^{-3}
Non-wetting phase density	ρ_{nw}	1000 kg·m^{-3}
Permeability	K	1×10^{-10} m^2
Porosity	θ	0.3
Residual saturation of water	S_{rw}	0
Residual saturation of oil	S_n	0
Entry pressure	*p_t*	5000 Pa
Soil distribution index	λ	2

Six models, each with a different set of primary variables, have been developed with the aim of comparing the results with the analytical results developed by McWhorter and Sunada (1990). For a sand-filled column with a constant porosity and permeability, the profile for the wetting phase saturation after 140 seconds of flow has been calculated for each model as well as the analytical results (Figure 3-2). The analytical solution, represented by a dashed line, estimates a non-linear curve with the wetting phase front located at 1.6 meter from the point of infiltration. Each model result shows a reasonable match with the curve derived from the analytical solution given by McWhorter and Sunada (1990). They have a minor but different numerical dispersion. For example, compared to the analytical result, the modelled result predicts a gentler spatial gradient of wetting phase saturation at the point of infiltration. Additionally, the two formulations (global pressure formulation and coupled water pressure (P_w), and DNAPL saturation (S_n) formulation) slightly overestimate the wetting phase front extent. On the other hand, the model formulation with decoupled water pressure (P_w) and DNAPL saturation (S_n) formulation shows a minor undershooting in the prediction. The formulation with capillary pressure (P_c) and DNAPL saturation (P_n) as primary variables shows a better match with the analytical solution. Overall, each model results reasonably reproduce the analytical solution, confirming the successful implementation of the formulation into Comsol Multiphysics.

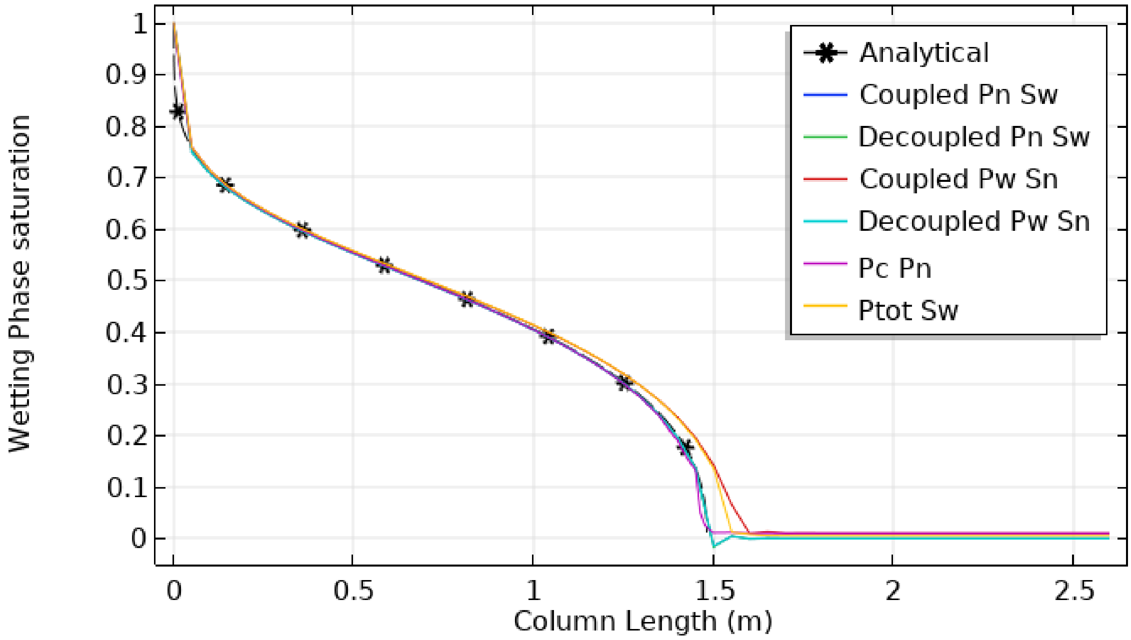

Figure 3-2: *Comparison between formulations implemented into numerical models and the analytical solution of McWhorter and Sunada (1990). Results from six formulations with different pair of primary variables: Coupled DNAPL pressure (Pn) — water saturation (Sw), decoupled DNAPL pressure — water saturation (Sw), coupled water pressure(Pw) — DNAPL saturation (Sn), decoupled water pressure(Pw) — DNAPL saturation (Sn), Capillary pressure — DNAPL pressure (Pn), global pressure (Ptot) — water saturation (Sw).*

3.2.2 Benchmark exercise 2: Upscaling of multiphase flow to a 2-D small-scale aquifer with several sand layers

For the validation of the correct implementation of the formulation in Comsol in 2D, an experiment of two-phase flow in a 2D heterogeneous porous media (Kueper and Frind, 1991) is modelled. It is worth mentioning that this benchmarking exercise has been frequently done in literature to check numerical implementation of two-phase flow models (Helmig, 1997; Ataie-Ashtiani et al., 2000; Kolditz et al., 2012).

In the benchmarking exercise, the model domain consists of a tank with dimensions of 60 cm-high, 80-cm wide with heterogeneities in the form of sand layers having different hydrogeological properties (Figure 3-3 and Table 3-2).

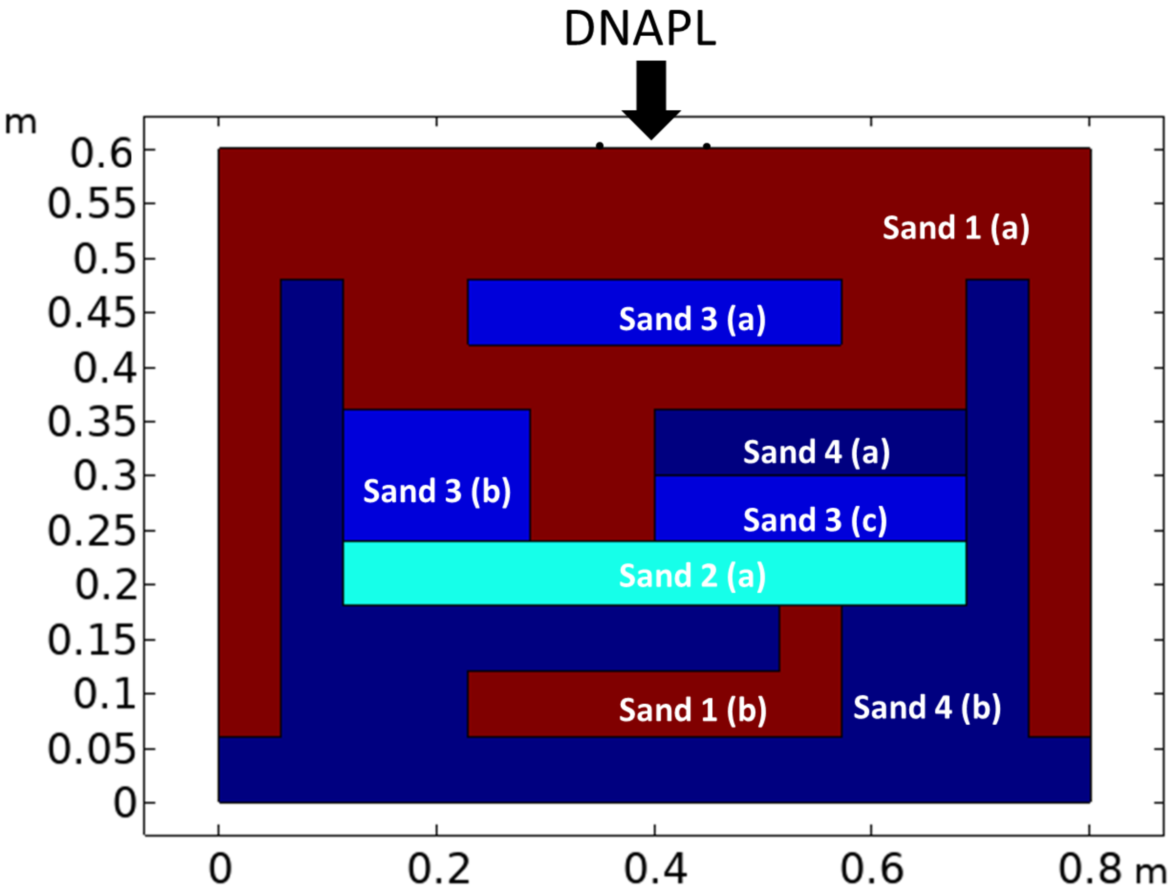

***Figure 3-3**: Domain of the 2D benchmark exercise based on Kueper and Frind (1991). Four different layers of sands are considered, each with different hydrogeological properties.*

Four types of well-sorted silica sands have been used in the model set-up, forming discrete layers. The model domain initially contains water at hydrostatic condition and does not consider initial DNAPL saturation within the entire domain. The boundary condition includes an inlet at the top of the domain (Figure 3-3). At this inlet, a Dirichlet condition of DNAPL saturation of 0.38 and a water pressure of 203 Pa is implemented. Left and right boundaries of the domain are assigned as a Dirichlet boundary condition with water pressure and DNAPL saturation to be the same as the initial condition. These boundary conditions ensure a correct representation of water leaving in the experimental setting. The other external boundaries are assigned with no flow conditions.

Table **3-2** shows the fluid properties used for the simulation of the simultaneous flow of water and DNAPL. Table 3-3 shows the hydrogeological properties of each sand implemented in the model.

The capillary pressure and the relative permeability are estimated by using the Brooks-Corey model. Figure 3-4 shows the capillary pressure saturation relationship for each of the four kinds of sands implemented in the model. The sand no. 4, with the smallest permeability, exhibits higher capillary pressure for the same saturation compared to other sand layers. The Phase Pressure Saturation with Interface Condition is implemented at each sand interface to study the role of capillary pressure equilibrium condition.

The model for simulating two-phase flow in a small-scale aquifer is built with the implemented formulation on Comsol Multiphysics. For this, the decoupled water pressure (P_w) and DNAPL saturation S_n formulation, also known as IMPES formulation, is used owing to its flexibility in defining the initial and boundary condition. The time length of the simulation is 500 seconds. Figure 3-5 (right) shows the model prediction for DNAPL infiltration of 0.08 m depth with a saturation of 0.38 after 34 seconds.

Table 3-2: *Fluid properties used for simulating the simultaneous flow of a DNAPL (tetrachloroethylene) and water in the model domain. The fluid properties for both water and tetrachloroethylene are taken from literature (Lerner et al., 2003).*

Property	Symbol	Value
Wetting dynamic viscosity	μ_w	0.001 Pa·s
Non-wetting dynamic viscosity	μ_{nw}	0.0009 Pa·s
Wetting phase density	ρ_w	1000 kg·m^{-3}
Non-wetting phase density	ρ_{nw}	1630 kg·m^{-3}

Table 3-3: *Porous media properties for the four different sand layers used for simulating the heterogeneous material in the benchmarking exercise. The data are taken from the experimental study reported in the literature by Kueper and Frind (1991).*

Property	Sand 1	Sand 2	Sand 3	Sand 4
Permeability	5.04×10^{-10} m^2	2.05×10^{-10} m^2	5.26×10^{-11} m^2	8.19×10^{-12} m^2
Porosity	0.4	0.39	0.39	0.41
Water residual saturation	0.078	0.069	0.098	0.189
Oil residual saturation	0	0	0	0
Entry pressure	369 Pa	434.5 Pa	1323.95 Pa	3246.15 Pa
Soil distribution index	3.86	3.51	2.49	3.3

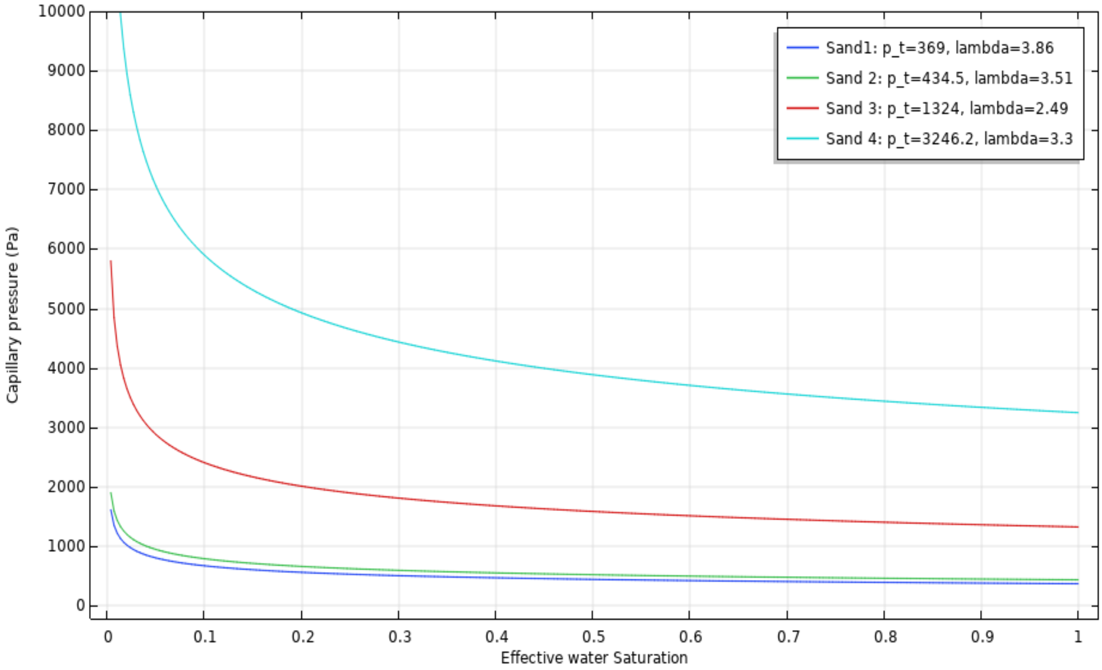

***Figure 3-4**: Plot showing the dependence of capillary pressure on effective water saturation for each of the sand media used in the benchmarking exercise of the two-phase flow in porous media.*

The results are in good agreement with the results from the benchmark model result (Figure 3-5). The model result illustrates the complexity of the DNAPL flow behavior at the interfaces of different sand layers. The model predicts accumulation of DNAPL on the top of *sand 1a* - *sand 3a* interface as the simulated plume fails to enter the *sand 3a*. This implies that the capillary pressure at the simulated DNAPL front is lower than the entry pressure of *sand 2*. The model calculation shows that a threshold DNAPL saturation of 0.99 is required to overcome the entry pressure. The accumulation of simulated DNAPL leads to increase in DNAPL saturation from 0.3 to 0.85, beyond which the accumulation stops as the branches of DNAPL are formed along the lateral edge of *sand 3a*.

After 184 seconds, the DNAPL plume is predicted to have two branches, each reaching up to the *sand 3b* and *sand 4a*. The capillary pressure of the simulated DNAPL branches increases from 484 to 501 Pa, which, however, is still lower than the corresponding underlying sands. Therefore, the model predicts the onset of DNAPL accumulation at *sand 1a-sand 3b* and *sand 1-sand 4a* interfaces after 184 seconds (Figure 3-5). The model result is again in agreement with the estimation by benchmark model for DNAPL flow after 184 seconds. The model prediction shows that the accumulation on the top of *sand 3b* and *sand 4a* continues for the extended time. The Figure 3-5 further shows the model prediction after 245 seconds of infiltration. The result estimates a DNAPL pool of 0.035 and 0.05 m height is formed on the top of *sand 3b* and *sand 4a* respectively, with saturation increased up to 0.88. However, the threshold saturation required for the DNAPL to infiltrate the underlying sands is greater than 0.99; therefore, the model predicts no infiltration of DNAPL plume in the underlying sands. The lateral migration of simulated DNAPL plume on top of *sand 3b*, leads to its arrival at the edge of *sand 3b*, beyond which the onset of vertical DNAPL infiltration is predicted by the model.

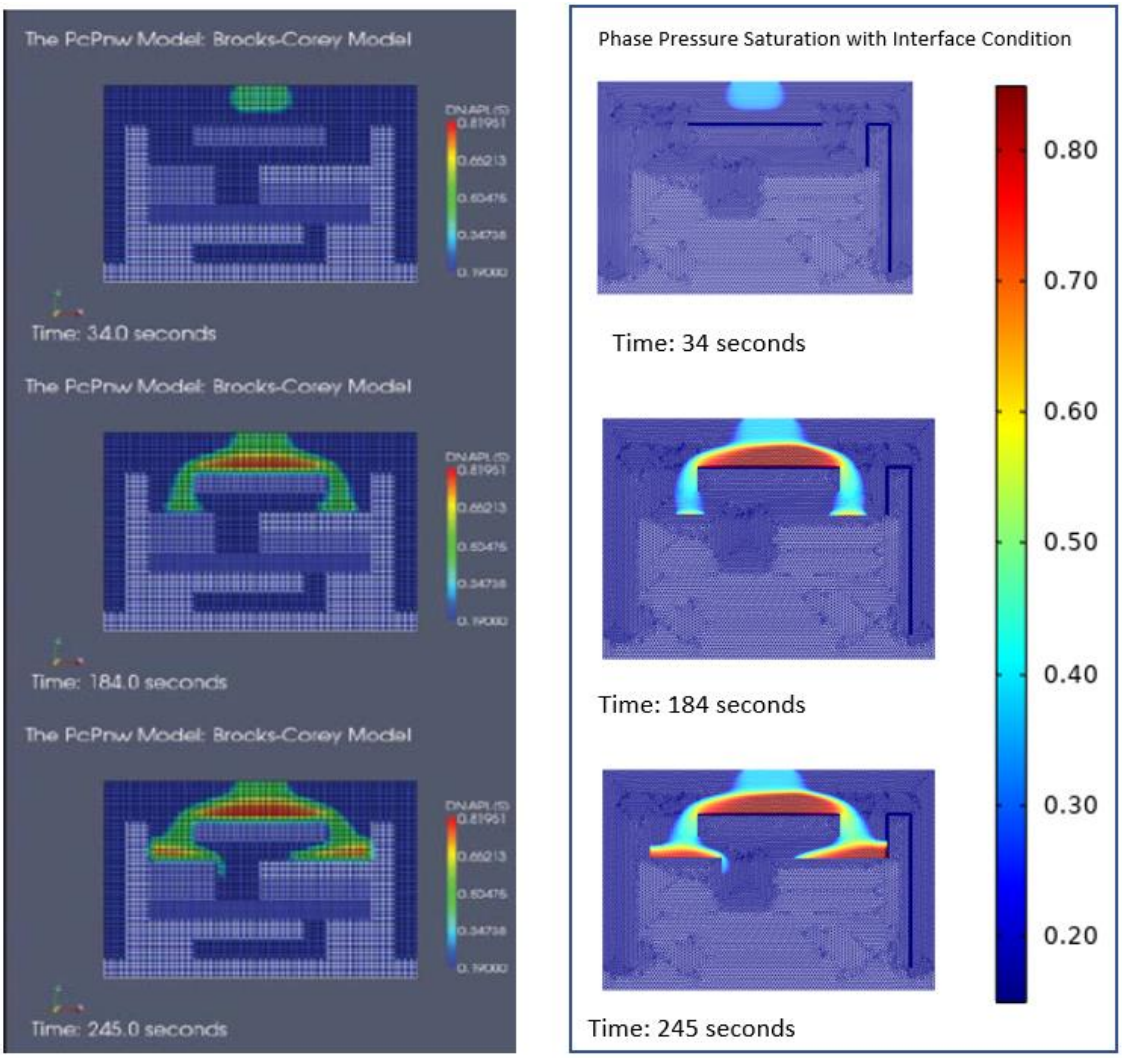

***Figure 3-5**: (right) The model prediction for two phase flow in the Kueper experimental set up (Kueper and Frind, 1991) for t =34 seconds, t = 184 seconds and t=245 seconds. The model precisely matches with the benchmark model result (left) reported in the literature (Kolditz, 2012).*

Comparing the results with the benchmark result shown in Figure 3-5, the establishment of a reasonable match indicates that the model successfully replicates the result. Therefore, the model result confirms the validity of two-phase flow formulation implemented in Comsol Multiphysics highlighting its ability to successfully simulate the DNAPL infiltration in a heterogeneous aquifer. Thus, in the next stage, the same numerical formulation is used to develop the 3D field scale model.

3.2.2.1 Role of Phase Pressure Saturation with Interface Condition (PPSIC)

A complex plume geometry during DNAPL infiltration is predicted by the model, with branching as well as accumulation of DNAPL. The model predicts that the DNAPL fails to infiltrate the *sand 3a*, *sand 3b* and *sand 4a*, whereas the simulated DNAPL plume successfully infiltrated the *sand*

2a layer. However, the movement of DNAPL in the sand *4b* layer ceases as it fails to infiltrate the *sand 4b* layer. A significant height of DNAPL pool formation is predicted on the top of each sand interface where DNAPL fails to infiltrate. The failure and success of DNAPL plume to infiltrate the underlying sand layer can be explained by the PPSIC condition implemented in the model. Figure 3-6b shows the capillary pressure in the study domain predicted by the model after 500 seconds. The predicted capillary pressure is the same as the entry pressure of the respective sand, where the DNAPL saturation is zero in the domain. As the DNAPL plume infiltrates in the model domain, the capillary pressure rises in accordance with the Brooks-Corey relationship (Equation 2.22). Figure 3-6b shows that the capillary pressure is relatively higher on the top of different sand interfaces. This increase in capillary pressure can be explained by the Brooks-Corey formulation implemented in the model, which leads to increase in capillary pressure with increase in DNAPL saturation. Therefore, the higher capillary pressure at the sand interfaces is a consequence of accumulation of DNAPL on top of the aquifer. However, this increase in capillary pressure fails to overcome the capillary pressure in the underlying sand layer at all the sand interfaces except *sand 2a* layer.

A detailed study of DNAPL movement near to the sand interfaces requires the consideration of the flow behavior in a linear profile. A cross section from top to bottom (called AF) is taken as the reference line for study as shown in Figure 3-6c. The Line AF passes midway through the simulated aquifer and, thus, the flow behavior along this line can give insightful results. The line is further divided into different line segments, AB; BC CD and DE and EF to represent the different simulated sand layers encountered by the line AF.

Figure 3-6e shows the capillary pressure predicted by model along the line AF at time t = 0 and t = 500 seconds. The dashed line shows the capillary pressure at t = 0, i.e., when the infiltration started. The capillary pressure represented by the dashed line is the same as the entry pressure of the different sand layers, which results in the discontinuity at each sand interface. For t = 500 seconds, the solid line represents the capillary pressure increases due to increase in DNAPL saturation. At the aquifer height of 0.4 marked by point B, the capillary pressure is 691 Pa at the top whereas the capillary pressure just below point B is 1323 Pa. Since the capillary pressure equilibrium is essential for infiltration of DNAPL in the underlying sand layer, the simulated DNAPL plume fails to infiltrate sand layer 2. This flow behavior is illustrated in Figure 3-6d, which represents the predicted DNAPL saturation with aquifer height after 500 seconds.

The graph shows the DNAPL saturation increasing from 0.3 to 0.5 on the top 0.2 m of the aquifer. However, as the threshold DNAPL saturation required for the infiltration of the underlying *sand 3a* is 0.99, the saturation curve remains discontinuous at an aquifer height of 0.3 to 0.35, and the saturation curve shows the accumulation of DNAPL plume, resulting in a saturation of 0.76. As the threshold DNAPL saturation for *sand 2a* infiltration is only 0.46, the infiltration successfully occurs. This is reflected in the continuity of the capillary pressure curve at *sand 1a-sand 4a* interface, marked by point D. With the infiltration, the saturation at *sand 2a* is predicted to become non-zero; however, the discontinuity in the saturation curve still exists at the interface of *sand 1a-sand 2a*. This is in accordance with the PPSIC theory and, thus, the model shows its successful implementation. The simulated plume meets the *sand 4a* at a height of 0.18 marked by point D, which has the highest entry pressure of 3200 Pa. Figure 3-6d shows the model predicting the increase in saturation at the *sand 2a- sand 4a* interface. The model also estimates the increase in capillary pressure at the point E, though this increase is not high enough to overcome the entry pressure of the underlying sand layer. As the capillary equilibrium condition fails to meet at point E, the capillary pressure and saturation remains discontinuous at the point E (Figure 3-6d and Figure 3-6e).

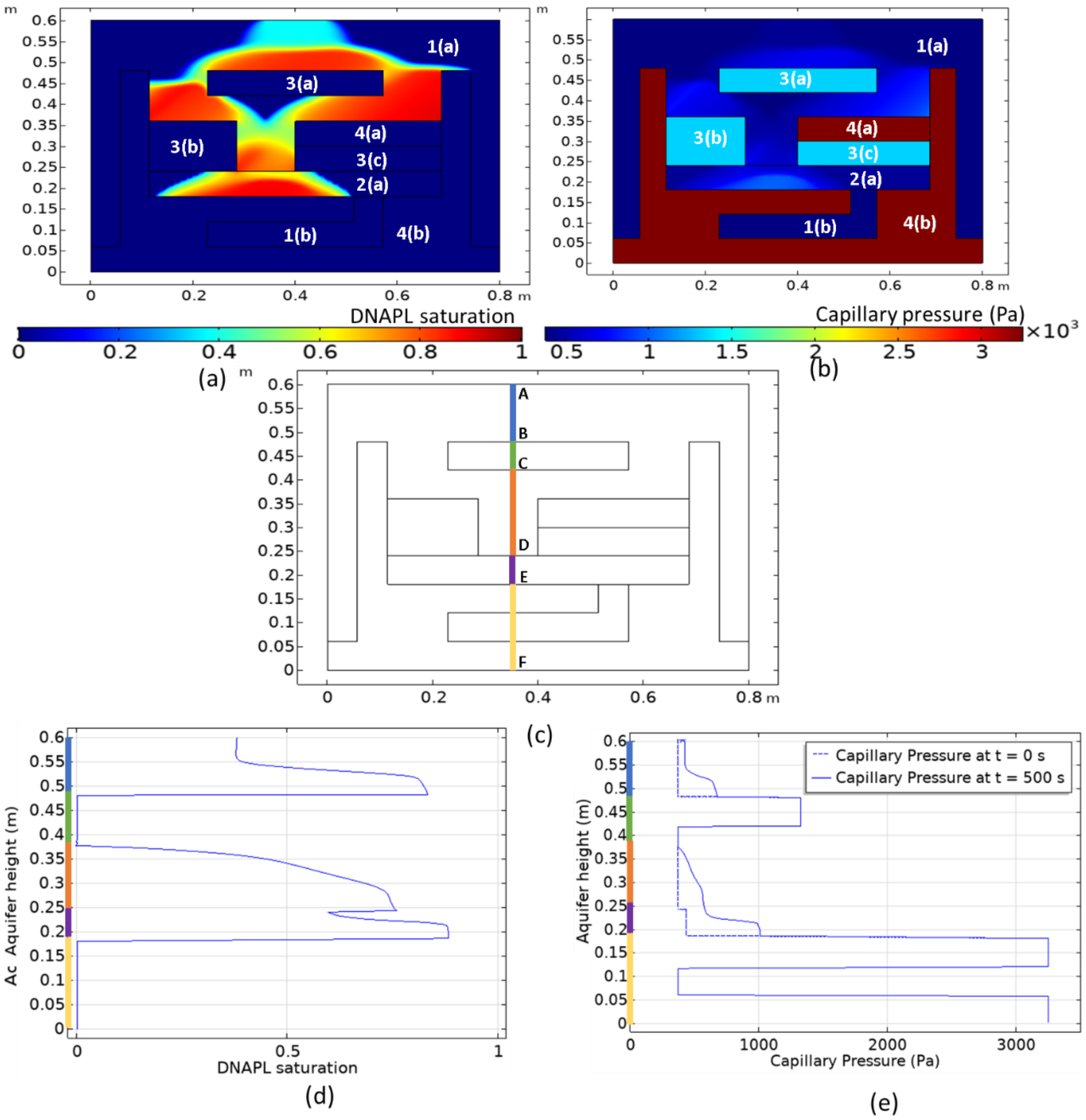

***Figure 3-6**: a) Model prediction of the influence of heterogeneity on DNAPL infiltration after 500 seconds. (b) Capillary pressure estimated by model after 500 seconds. (c) Line AF is considered along which the profile for DNAPL saturation and capillary pressure is studies (d) Model prediction for DNAPL saturation with the height of the simulated aquifer with discontinuity arising due to the capillary equilibrium condition (e) Model estimation for capillary pressure at t =0 given by dashed line and at t=500 given by solid lines.*

3.2.3 Field scale model of two-phase flow in porous media

Once the model implementation of two-phase flow formulation in Comsol has been verified, the next step is two-fold: (1) to demonstrate the model capability to simulate the infiltration of a DNAPL at field scale, and (2) to study the migration pathways and time evolution of DNAPL flow in a real groundwater system.

Real aquifers in nature show a relatively large range of hydraulic and geological properties, and then, the prediction of the behavior of DNAPL will be a function of this range. To narrow this variability, this model exercise has selected a real polluted site by DNAPL (PCE), called The Innovation Garage, located at Skovlunde Byvej 96 in the Copenhagen region (Denmark; Figure 3-7). This site was a former industrial area, and the underlying soils and aquifers were impacted by chlorinated solvent spilling. Now, this site is being used by technicians and researchers from The Capital Region of Denmark as a reference site for a better understanding of the evolution of this kind of pollution and for testing new remediation methodologies (The Capital Region of Denmark, 2017). This site has been used also as a reference in some Early-Stage Researcher projects in the ITN-Metal-Aid project, which the present thesis is part of.

The objective of this modeling exercise is then to determine 1) the migration pathway for DNAPL phase, 2) The time period of infiltration, 3) the DNAPL accumulation and branch formation, 4) effect of clay lenses on the migration pathway, 5) the DNAPL source zone architecture, 6) the amount of DNAPL pool and ganglia formed, 7) the implementation of PPSIC boundary condition and capillary forces, 8) mass conservation of the DNAPL in the model domain, and 9) the insights for real case of chlorinated solvent pollution.

(a)

(b)

__Figure 3-7__: (a) Location of The Innovation Garage, Eastern Denmark. (b) Photo of the innovation garage ground facilities (Source: danishsoil.org).

3.2.3.1 Geology and hydrogeology of the Innovation Garage

The geology of the Innovation Garage consists of sedimentary rocks of Miocene-Quaternary age. From bottom to top (Frederiksen et al., 2003; Houmark-Nielsen, 2004): (1) an Early Paleocene basement consisting of limestone and chalk, (2) an alluvial, fine-grained sands with silt and clay layers of Quaternary deposit (20 m thick), and (3) a fractured glacial clay till (6 to 8 m thick) formed due to the multiple episodes of glacial sedimentation during the Quaternary. The water table usually reaches up to 5 meters below the sand-till contact, so part of the sandy aquifer is not fully water-saturated. The average hydraulic gradient in the aquifer is 0.001 resulting in a slow groundwater flow in the range of $4 cm \cdot day^{-1}$ (The Capital Region of Denmark, 2017).

Currently, the impact of DNAPL in the site has been reported to be significant as free phase or dissolved DNAPL in the clay till and a dissolved DNAPL in water in the sandy aquifer. DNAPL was released from a dry-cleaning industry operating between 1960 and 1987. The amount of DNAPL that infiltrated underground is estimated to be 2 tons of tetrachloride (PCE) (Anders, 2017). Most of it is thought to be in the vadose zone in the fractured clay till, although there is evidence of DNAPL reaching the sandy aquifer. Possibly, the DNAPL has been accumulated as a free-phase in low-permeability layers or fracture dead ends in the till, acting as a secondary contaminant source of DNAPL. This is apparently why we have still releases of PCE into the underlying aquifer today.

3.2.3.2 Brief description of perchloroethylene (PCE) as a pollutant in the environment

As already mentioned in Chapter 1, NAPLs can be lighter and denser relative to water and called DNAPL and LNAPL, respectively. Among typical DNAPLs, we have chlorinated solvents, polychlorinated biphenyls, coal tar, creosote and crude oil. Chlorinated solvents are a group of DNAPL compounds that includes tetrachloroethene (PCE), trichloroethene (TCE), dichloroethane (DCE) and tetrachloromethane (carbon tetrachloride, CT). PCE is sparingly soluble in water (200 mg_{PCE}/L_{water} at 25ºC) but even such a dissolved amount is very toxic to humans (detailed explanation in section 1.2.1). Due to its higher density coupled with a low viscosity, it takes merely months to years for the PCE to reach to the bottom of the aquifer and gets immobile. On the other hand, the dissolution from the free phase to the aqueous phase can proceed for several decades or even centuries (Pankow and Cherry, 1996). Because of the partitioning coefficient (K_{oc}) value (Lerner *et al.*, 2003), the mass transfer of DNAPL in the porous media is significantly low. Therefore, in the model simulation, an immiscible nature of DNAPL during its interaction with groundwater is assumed,

3.2.3.3 Model implementation

The field scale model of two-phase flow in porous media has been implemented in a cuboid of dimension 50 m×15m×15m (Figure 3-8). This model represents a sandy aquifer of homogenous hydraulic properties (porosity, permeability), although heterogeneity has been reported at centimeter scale in the real sandy aquifer. The bottom boundary of the model is a relatively impervious limestone rock underlying the sandy aquifer. This rock is assumed to be impenetrable for the DNAPL.

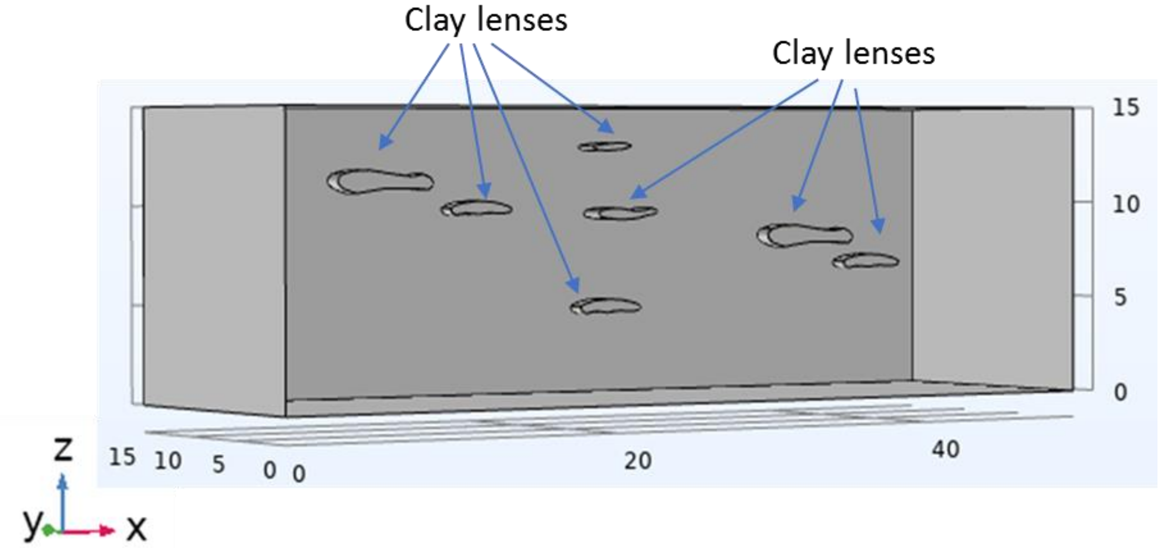

Figure 3-8*: The model domain used for simulation of two-phase flow. The domain simulates homogeneous sand with randomly placed clay lenses.*

One of the key questions concerning the migration of DNAPL in sandy aquifers is the impact of clay-bearing lenses or clay plugs, which are frequent in many examples of sandy layers in literature, and possibly, also in the underground of the Innovation Garage. To see such an impact, seven clay lenses have been also included in the model (Figure 3-8). These clay lenses have random spatial location, geometry, with lengths varying from 1 to 2 m. These clay lenses are hydraulically of much lower permeability compared to the surrounding sand (1.5×10^{-10} m^2 vs. 5×10^{-14} m^2), and, thus, the DNAPL flow is expected to be hindered at the sand-clay interface. The properties used in the model are taken from the Innovation Garage reports. The missing parameters have been taken from literature of similar sites (Table 3-4). Considering the impervious nature of the clay lenses, the model results are not expected to be sensitive to the hydrogeological properties other than clay permeability in those cases where the model predicts failure of DNAPL infiltration. Finally, the model assumes that the water table, recharge rate and all the intrinsic properties does not change through the simulation period.

Table 3-4*: Hydraulic properties used in the 3D, two-phase model of DNAPL infiltration in the Innovation Garage site case. The permeability and porosity of the sand layers are taken from the reported data (The Capital Region of Denmark, 2017). The remaining data are taken from the literature (Kueper and Frind, 1991).*

Property	**Sand**	**Clay**
Permeability	1.5×10^{-10} m^2	5×10^{-14} m^2
Porosity	0.3	0.2
Water residual saturation	0.098	0.19
Oil residual saturation	0.01	0.008

Property	Sand	Clay
Entry pressure	1323 Pa	4500 Pa
Soil distribution index	3.86	3.51

3.2.3.4 Initial and boundary conditions

The decoupled water pressure (P_w) and DNAPL Saturation (S_n) formulation, also known as Implicit Pressure, Explicit Saturation (IMPES) formulation has been selected as a numerical scheme. The primary variable is the pressure of water and the saturation of the DNAPL, and the numerical framework requires initial and boundary conditions for these primary variables. The water in the aquifer is considered to be hydrostatic and free of DNAPL at t=0. In the real aquifer system, the pressure would not be hydrostatic due to the groundwater flow; however, the groundwater flow in the Innovation Garage area has been reported to be slow (in the range of 4 $\text{cm}\cdot\text{day}^{-1}$) and its influence is considered to be negligible. This is in accordance with the previous studies, which reported negligible influence of groundwater flow on DNAPL migration, given the natural flow velocity is less than 10 $\text{cm}\cdot\text{day}^{-1}$ (Zheng et al., 2015).

As the aquifer is considered to be free of DNAPL at the onset of simulation, the initial DNAPL saturation should be zero. However, a minimal DNAPL saturation of 0.001 has been considered in the initial state of aquifer to make the achievement of the numerical convergence criteria.

The available information from the Innovation Garage suggests that most of the DNAPL is currently stuck in the vadose zone (i.e., the clay till), and there no clue about where the original infiltration point at ground level was. In the model, the DNAPL has been considered to infiltrate down from a rectangular shaped inlet with dimensions of 0.5 m × 0.5 m at the top of the domain.

A similar uncertainty exists for the rate of DNAPL infiltration from ground to glacial clay till. In this mesh size and geometry have been adjusted such that the spatial gradient of the state variables can be reasonably captured in the discretization (Figure 3-9). Here, the mesh size of a finite element signifies the length of the longest edge of that element. As the infiltration of DNAPL is implemented from the central top, a relatively smaller mesh size is used throughout the central vertical section of the model. For the region away from the central part of the domain, a relatively coarser element size has been used. The maximum element size used is 10.2 meters in length, while minimum size used is 1.7 centimeters. After several iterations, an optimized mesh configuration has been used at the expected DNAPL flow path. Figure 3-9b shows the mesh elements used along the expected flow path of the DNAPL plume for the upper half of model domain. Finer elements in the range of 2 centimeters to 15 centimeters are used at the periphery of the clay lens to capture the flow behavior of DNAPL at the lithological interfaces. For the lower half of the model domain, a hexahedral system of mesh elements has been used along the expected flow path of the DNAPL (Figure 3-9c). The finer mesh is generated at the base of the bedrock to capture the accumulation of DNAPL plume.

For the time discretization, an adaptive time discretization method is used. The initial time step has been considered to be 1×10^{-7} seconds, but according to the convergence criteria, the time discretization becomes coarser for an efficient computational time. The simulation of the DNAPL infiltration in a field scale domain has been run for 1500 hours.

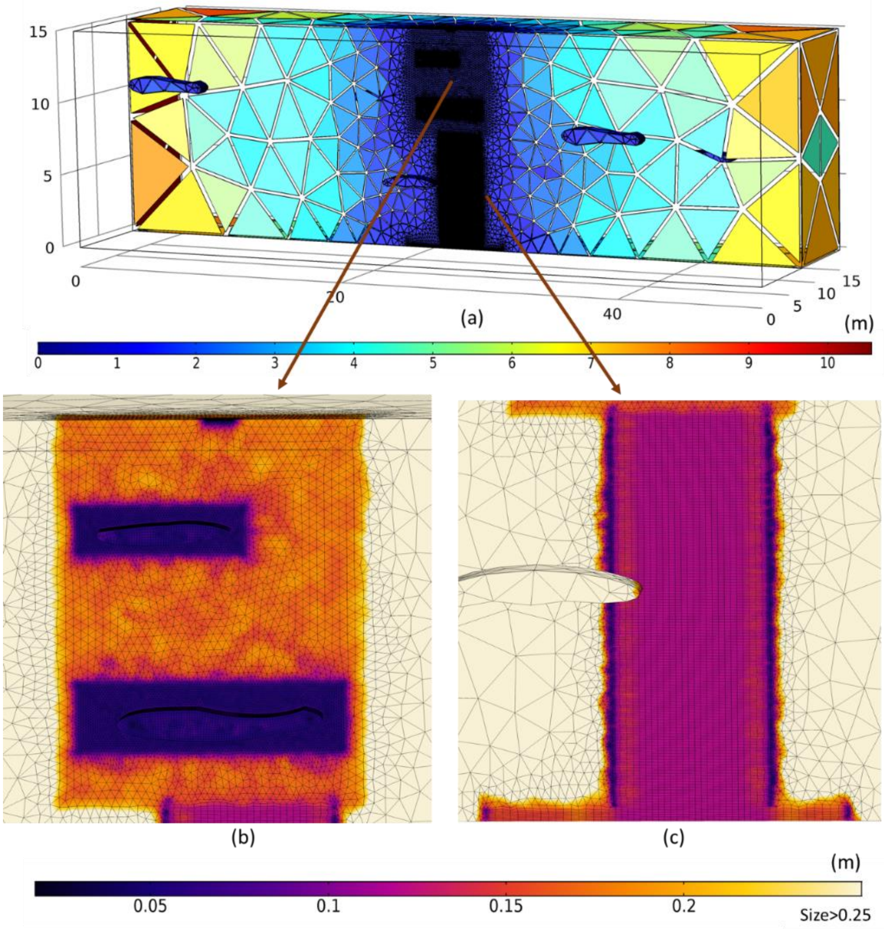

Figure 3-9: (a) Spatial discretization of the study domain for finite element approximation with tetrahedral and hexahedral elements of size ranging from 0.017 to 10.2 m. (b,c) Enlarged image of mesh elements used along the expected DNAPL flow path.

3.3 Model results for the field scale case

For understanding the results from the model, the DNAPL infiltration has been studied along two cross section planes XY and YZ, as shown in Figure 3-10. These planes crosscut the aquifer symmetrically into two halves to capture the DNAPL movement dynamics.

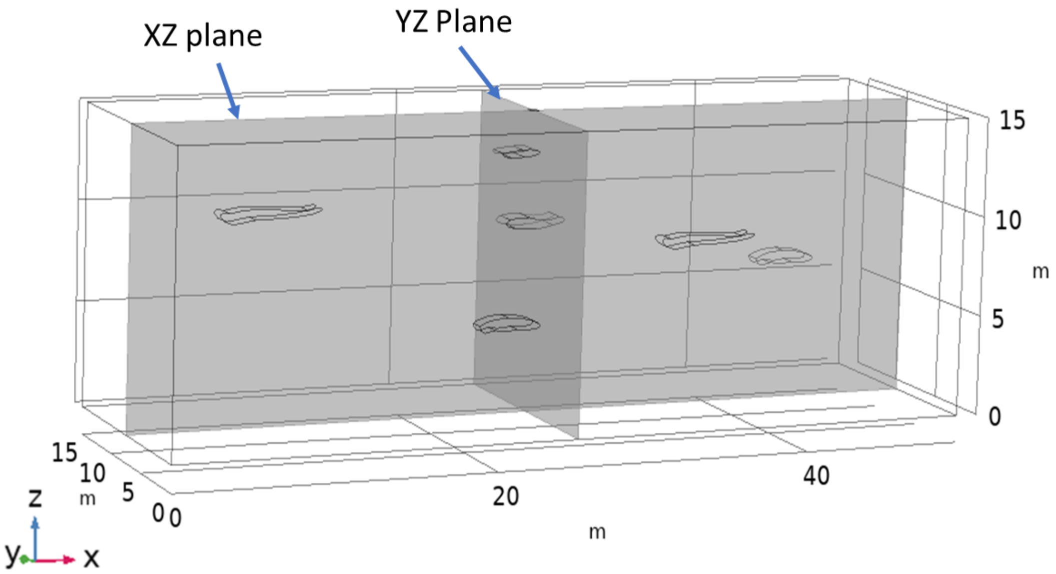

__Figure 3-10__: Two reference cross section planes aligned in XZ and YZ directions and dividing the simulated aquifer into symmetrical halves. These planes are used for result visualization.

The model predicts that DNAPL infiltration takes 42 days to reach the bottom of the aquifer. The migration path is quite unique and dependent on both aquifer characteristics as well as DNAPL properties. The model also predicts that DNAPL enters the aquifer system with a saturation of 0.15 with a vertical infiltration of 1.5 meter after the end of the first day (Figure 3-11). The horizontal extent of DNAPL predicted by model is 0.5 m which is nearly the same as the dimension of inlet. Therefore, the predominant migration pathway aligns with the vertical direction. This result implies that the gravitational forces are the dominant for the DNAPL migration compared to viscous and capillary forces. This illustrates that, for the field with homogeneous sand, the DNAPL source architecture is likely to have a simple vertical geometry with minimal lateral migration of the plume.

The predicted DNAPL plume infiltrates with steady state saturation for 34 hours until it meets the clay lens occurring at a depth of 1.9 meters. At the clay lens, the model predicts accumulation of DNAPL (Figure 3-11c-d), leading to the increase of DNAPL saturation from 0.15 to 0.41 in the following 18 hours. This accumulation causes lateral migration of DNAPL both along the width and the length of the clay lens. The model predicts that the DNAPL lateral movement along the width is much slower compared to that along the length of the clay lens. This highlights the formation of preferred channels along which most of the DNAPL moves along the length of the clay. Such preferred channels forms because the lateral DNAPL plume movement is estimated to reach the end of the clay lens comparatively faster than the plume along the width. This leads to re-occurrence of vertical movement of simulated DNAPL plume in the sandy aquifer, while its movement is still lateral along the width. The formation of preferred channels of DNAPL plume leads to the formation of unique DNAPL plume geometry. After 3 days, the model predicts the DNAPL plume infiltration up to 3.5 meters deep.

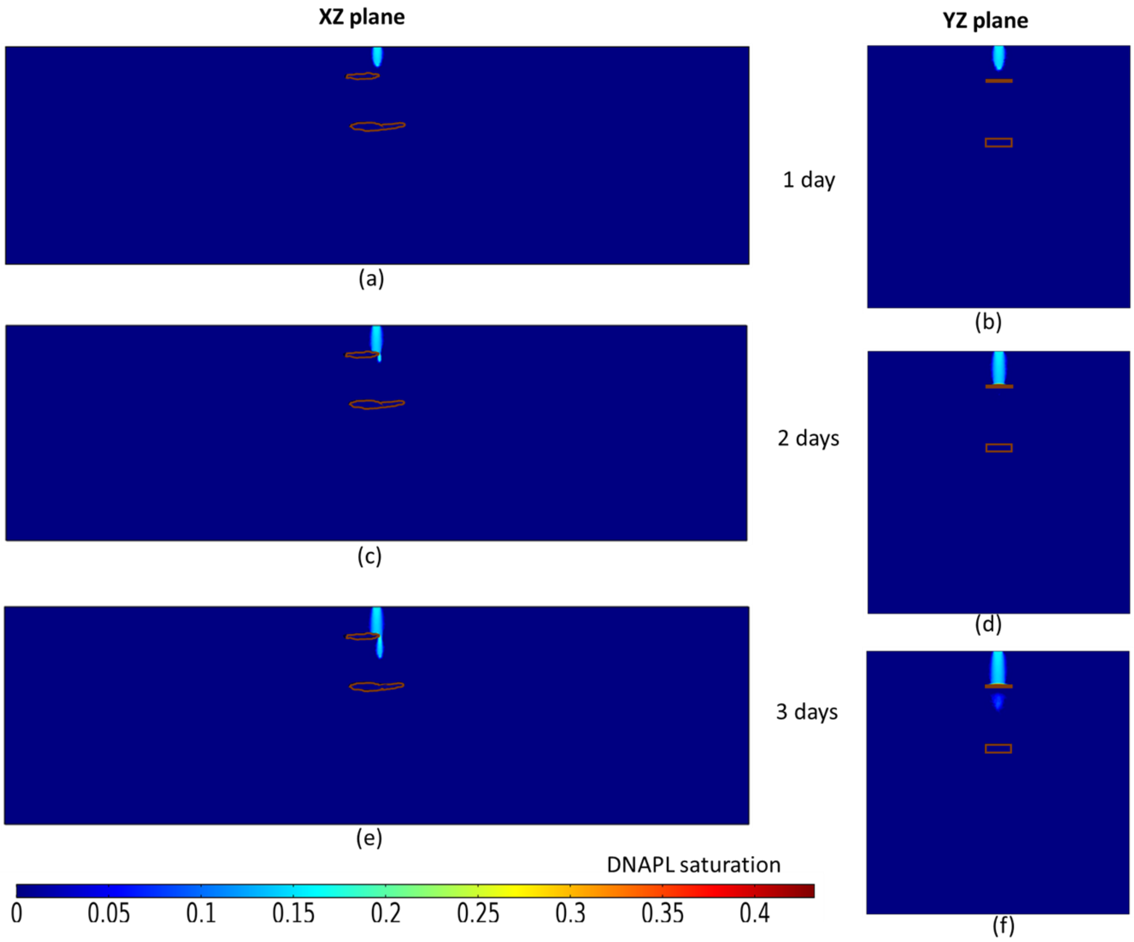

***Figure 3-11**: Model prediction for DNAPL saturation in the study domain along the XZ plane (a) and YZ plane (b). After 2 days the model predicts infiltration along the XZ plane (c) and YZ plane (d). After 3 days, when the source condition is removed, the model estimation shows the DNAPL profile along the XZ plane (e) and YZ plane (f). The clay lenses are outlined with brown color outline for a better visualization.*

The model also predicts that the multiple branches of DNAPL would form around the clay in the aquifer. After 5.5 days of infiltration, the DNAPL plume is predicted to reach the lower clay lens occurring at 9.5 meters deep. Figure 3-12 shows the model prediction for DNAPL migration for 6 days, 10 days and 15 days, respectively. The accumulation of DNAPL over the clay lens is predicted to result at DNAPL saturation of 0.45, until the plume forms the branch. The model also predicts DNAPL plume branching along the width of the lower clay, after 7 days. The branches of DNAPL infiltrate further down the aquifer domain. After 15 days, the DNAPL plume reaches up to 9 meter in depth with 2 main branches in the YZ plane. The simulated DNAPL movement along the length of the clay is limited as shown in the XZ section (Figure 3-12e).

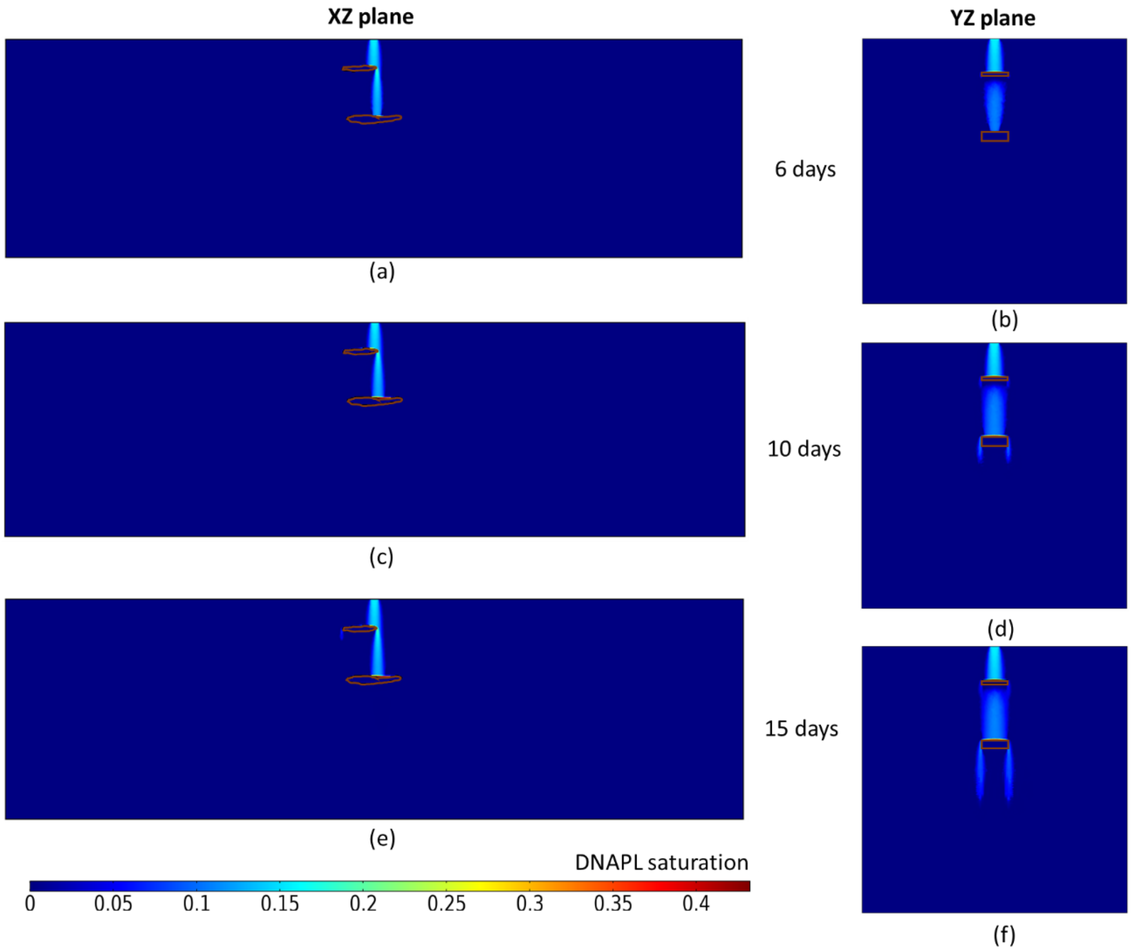

***Figure 3-12**: Model prediction for DNAPL saturation in the study domain along the XZ plane (a) and YZ plane (b). After 6 days and after 10 days, the model predicts infiltration along the XZ plane (c) and YZ plane (d). After 15 days, when the source condition is removed, the model estimation shows the DNAPL profile along the XZ plane (e) and YZ plane (f).*

For a better visualization of DNAPL flow in the aquifer, the iso-surface of DNAPL has been studied. Figure 3-13 shows the isosurface with 0.1 DNAPL saturation after 15 days of infiltration in the aquifer. The iso-surface geometry highlights the role of clay in the interruption of vertical movement of DNAPL. The model predicts lateral movement of DNAPL plume on the top of upper clay while the major mass of DNAPL plume follows the original vertical path (Figure 3-13b). Interestingly, the influence of the lower clay lens on the DNAPL flow path is different from the upper clay lens (Figure 3-13c). The model predicts a complete halting of the vertical migration of the main DNAPL plume at the top of the lower clay lens. Consequently, two new branches of DNAPL plume are predicted to form along the periphery of the lower clay lens in the model domain. The different flow behavior for the upper and lower clay lenses can be attributed to the different morphology, dimension and position of the clay lenses.

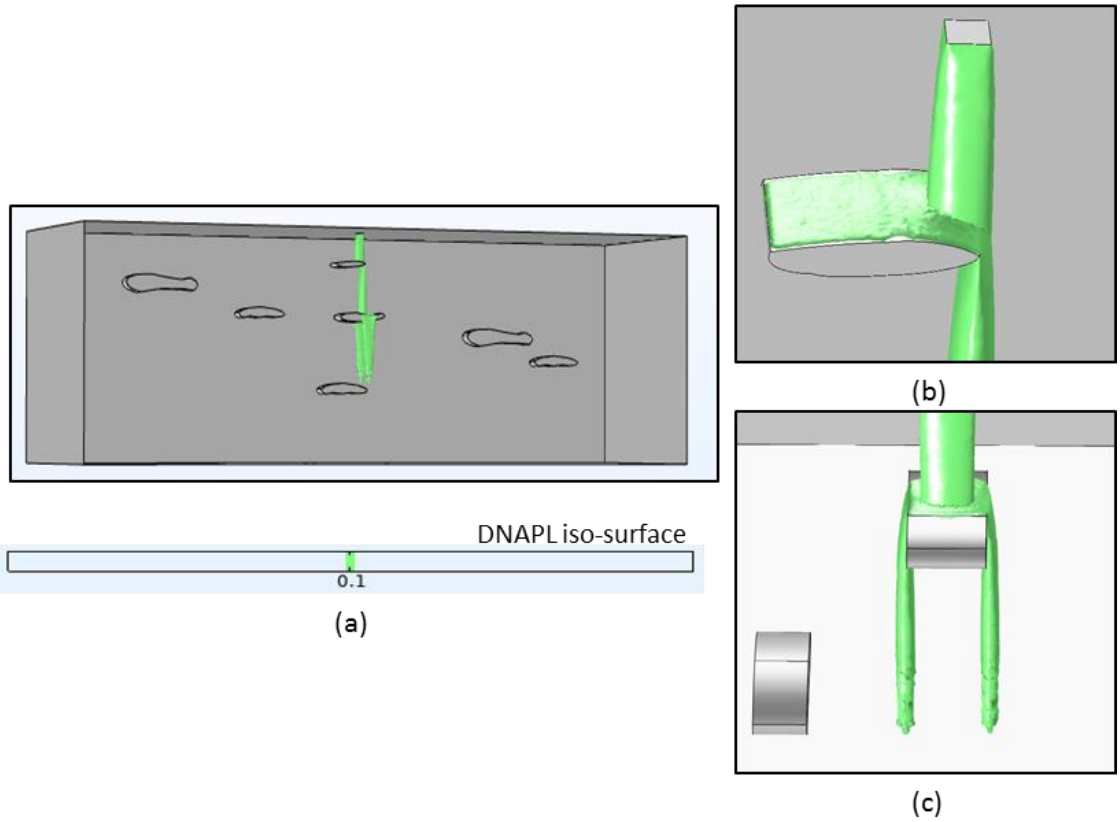

__Figure 3-13__: Green colored iso-surface of 0.1 DNAPL saturation predicted by model after 15 days of infiltration(a). A closer view for influence of clay lens on the DNAPL movement is shown as an enlarged image along the XZ plane (b) and YZ plane (c).

3.3.1 DNAPL flow dynamics at clay-sand interfaces

The model predicts that DNAPL plume is unable to infiltrate in the clay lenses. This behavior can be explained by studying the capillary pressure and DNAPL saturation at the sand-clay interface after 15 days (Figure 3-14). These parameters are plotted along the red line as shows in the Figure 3-14a. The red line passes through the center of inlet down to the two-clay lenses along the path of DNAPL migration. Figure 3-14b and Figure 3-14c show the occurrence of two discontinuous peaks for both saturation and the capillary pressure at the sand-clay interface. The DNAPL saturation just above the interface reaches the peak of 0.41 and 0.45 for shallower and deeper clay, respectively. These peaks represent the accumulation of DNAPL over the clay lens. Beyond the interface, however, the DNAPL inability to infiltrate the clay lens is reflected as the sharp decrease of saturation to zero in the plot. This inability to infiltrate can be explained by the capillary pressure plot (Figure 3-14), that ranges from 1323 to 1395 Pa when the medium is sand. The variation of capillary pressure is a function of DNAPL saturation as given by Brooks-Corey formulation. At the sand-clay interface, a stark discontinuity of DNAPL saturation exists due to high entry pressure of 1400 Pa for the clay lens. Figure 3-14c shows that the capillary pressure increases with increasing DNAPL saturation; however, the increase is not sufficiently to overcome the entry pressure. The model estimation shows that a threshold saturation of 0.96 is required to obtain the capillary pressure equilibrium. Since the maximum saturation of simulated DNAPL on top of the clay is 0.45, therefore the simulated DNAPL plume fails to infiltrate the clay lens.

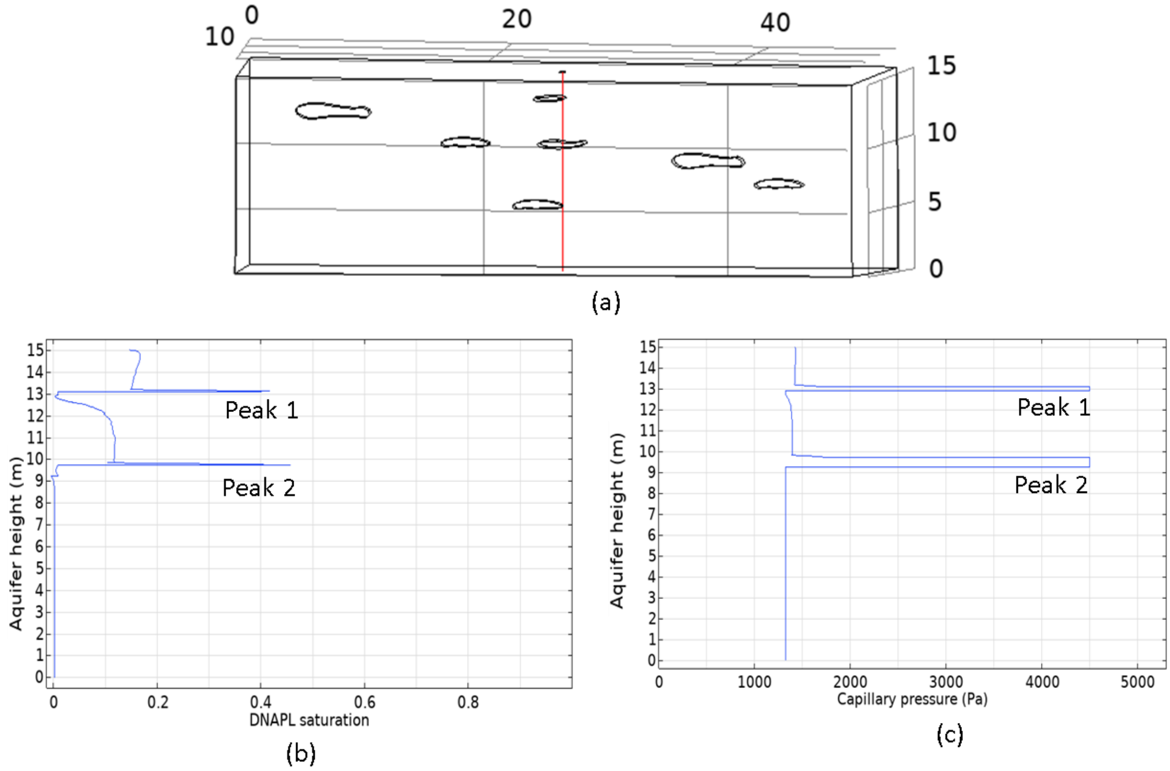

***Figure 3-14**: Profile for DNAPL saturation (b) and capillary pressure (c) plotted along the central line in the simulated domain shown by the red color (a). The formation of two peaks in both DNAPL saturation profile and capillary pressure profile indicates the DNAPL accumulation at the top of clay lenses.*

3.3.2 Prediction of DNAPL migration after source removal

Once the infiltration of the DNAPL from the source has stopped, the model predicts that the DNAPL plume flows down, although with a slower velocity. After 60 days, the flow of DNAPL becomes negligible leading to the formation of stable DNAPL distribution. Figure 3-15a and 3-15 c show the iso-surface of DNAPL with saturation equal to 0.02 after 1500 hours from different angles of view. The iso-surface represents the model prediction of the formation of a continuous DNAPL ganglia (the interconnected network of residual DNAPL saturation) down to the depth of 5.2 meters below which two vertical branches of DNAPL ganglia occur from the lower clay. The DNAPL saturation profile along the central XZ plane and YZ plane at the end of the model run is shown in Figure 3-15b and 3-15d, respectively. The model calculates that the plume front touches the bedrock after 45 days of infiltration leading to the gradual formation of a DNAPL pool on the bedrock. The gradual formation is caused by the slower flow of DNAPL. The DNAPL plume travels 6 meters in 30 days after the source is stopped, making the average velocity 7.5 times slower than the velocity with active infiltration. The decrease of the flow speed can be explained by the drop in the relative permeability due to the decrease of DNAPL saturation. Additionally, as the saturation decreases from the top, the capillary forces start acting upwards due to change in direction of DNAPLs saturation gradient. This leads to the capillary force and gravity force acting in opposite direction. The overall force dynamics results in the formation of a stable DNAPL source zone after 1500 hours. The force dynamics also explains why ganglia have saturation slightly higher than the residual saturation of DNAPL. The final DNAPL source zone has ganglia extending continuously throughout the vertical dimension of the simulated aquifer.

In the lateral direction, the model predicts the ganglia extending up to 2.5 meters. The negligible movement of DNAPL predicted by model leads to the formation of unique plume geometry with ganglia having a DNAPL saturation in the range of 0.02 to 0.05. This agrees with the previous studies (Nambi and Powers, 2003), which reported that the DNAPL ganglia can be in the range of 0.01 to 0.15. This heterogenous distribution of ganglia is such that a low saturation of ganglia is predicted near the water table, while a comparatively higher saturation is predicted with depth. This can be explained by the gravity fed motion of finite DNAPL at the source, leading to diminishing saturation starting from the top. The simulated pool formed on the top of clay has decreased from 0.45 to 0.16 after removal of the source. The decrease in DNAPL pool saturation can be attributed to the DNAPL fraction contribution in the vertical motion of the plume. The DNAPL pool formed at the bedrock has the highest saturation of 0.34.

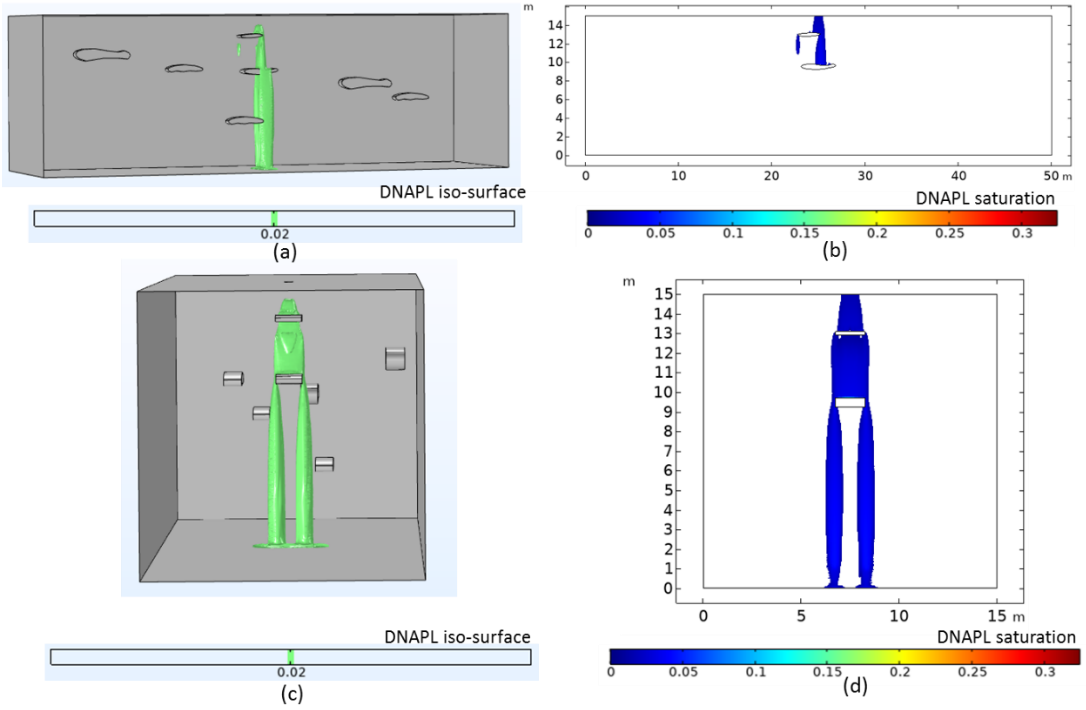

Figure 3-15*: Model prediction for iso-surface of 0.02 DNAPL saturation in the study domain after 1500 hours viewed along the XZ plane (a) and YZ Plane (c). The range of DNAPL saturation after 1500 hours predicted by model along the reference plane XZ (b) and YZ(d).*

3.4 Discussion

The evolution of contaminant plume in the simulated aquifer can be studied by plotting the temporal evolution of total mass of DNAPL, ganglia and DNAPL pool (Figure 3-16). The constant rate of DNAPL infiltration in the simulated domain is reflected as the straight curve shown by orange line for time shorter than 15 days. A total of 500 kg of DNAPL infiltration has been simulated by the model in the first fifteen days, and, as the source is removed after 15 days, the total mass of DNAPL remain conserved as represented by flat portion of the orange curve. For the first fifteen days, the simulated DNAPL plume saturation remains higher than 0.16 thus forming a pool of DNAPL along the migration pathway. The DNAPL mass represented by green curve shows the predominant fraction of DNAPL mass as DNAPL pool.

After 15 days, as the source is removed, the gravity leads to reduction of saturation along the migration pathway resulting in formation of ganglia. Then, a rise in the amount of ganglia with a diminishing amount of DNAPL pool is predicted. Finally, as the DNAPL plume reaches the bedrock, a new pool is predicted to form slightly increasing its mass proportions. The model estimates a total of 465 kg of ganglia and 32 kg of DNAPL pool at the end of the simulation.

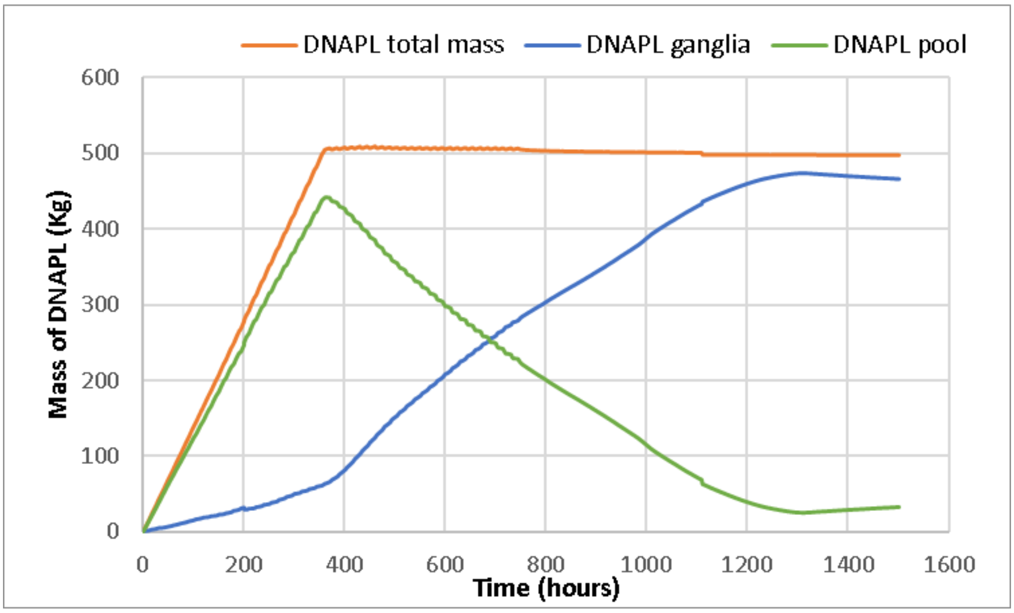

Figure 3-16: *Relative masses of DNAPL states predicted by model after 1500 days. The green curve represents the amount of DNAPL pool, blue curve the amount of ganglia, and the orange curve the total amount of DNAPL entered in the simulated domain.*

The numerical model presented in this study is aimed to predict the flow behavior of DNAPL in a case study. However, its results can be further applied to understand the migration of DNAPL in many other similar aquifers worldwide. Importantly, this kind of predictions are very convenient for the assessment, selection and optimization of application of remediation technologies.

A first implication from the modelling results is that if the morphology of clay lenses is known, the DNAPL plume geometry can be predicted. This is because the model results indicate that the vertical branching depends on both DNAPL plume and the clay size and shape. The preferred pathway for vertical motion of DNAPL below the clay is oriented along the direction with minimum lateral migration of DNAPL over the clay. The lateral migration over the clay becomes negligible as the preferred pathway for vertical migration is developed, resulting in the failure of DNAPL branch formation in other directions. A consequence of this is that the field characterization can be misleading if not done carefully. During the field study, if a vertically limited DNAPL infiltration in the field is observed, still a large infiltration of DNAPL is possible along the other side of the clay lens. To illustrate this, Figure 3-17 shows the DNAPL saturation, with a non-uniform formation of branches in the aquifer. The black circle shows a small ganglia formation predicted by model. These ganglia could be the model representation of a small pocket of DNAPL, extending up to 4.2 meter in depth. Therefore, this indicates that tracing the interconnected residual plume requires careful study as the predictive insights from model indicates the possibility of an isolated contamination source in the aquifer.

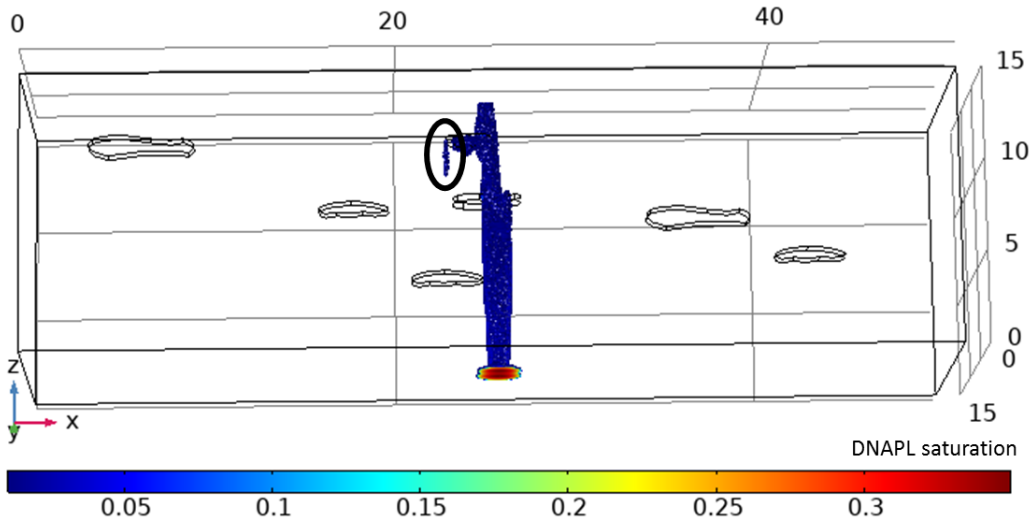

Figure 3-17: DNAPL saturation predicted by the model after 1500 hours of DNAPL infiltration in the study domain. The black circle shows the prediction of isolated DNAPL ganglia separated from the main DNAPL plume structure.

Another interesting output from the numerical model is that the DNAPL accumulated over the clay lens has reduced from 0.45 on day 5 to 0.16 after removal of the source. The highest saturation (0.35) of DNAPL occurs at the bedrock. This means that the natural DNAPL attenuation occurs at the shallower level of the aquifer, due to its downward motion leading to accumulation of DNAPL at the bottom. Then, DNAPL is more likely to be present at the bottom part of the aquifer including the top of bedrock in mature fields with a moderate heterogeneity, and having history of DNAPL infiltration extended in time. With the maturity of the field, the ganglia dissolve leading to its exhaustion (Carey et al., 2014) with only DNAPL pool remaining in the aquifer system. The fate of the DNAPL pool depends on the morphology of each impervious clay lens that the DNAPL plume encounters. For a more flat- or concave-shaped lens surface, the DNAPL pool saturation decreases over time as predicted by the model.

Model results also predicts that the branching of DNAPL plume may or may not re-join. According to the model, DNAPL plume at the shallower clay is infiltrates as a continuous vertical mass. In contrast, the plume branching at the second clay lens in depth is already discontinuous, and depending on the clay lens geometry, the branches can later re-join. Therefore, at a field scale observation, the DNAPL plume below a clay lens should not be expected to occur only as a discrete form.

The spread of the DNAPL plume in the model at The Innovation Garage is up to 3.7 meter laterally indicating the role of the non-permeable layers in the DNAPL migration. While the initial DNAPL source inlet has a dimension of 0.5m × 0.5 m width, the lateral movement of DNAPL has led to its widespread distribution. The lateral extension depends on the number of impermeable layers it encounters. The extent of vertical migration of DNAPL, however, depends on the heterogeneity of the aquifer as well as on the mass of infiltrated DNAPL. For a small mass infiltrating down into the aquifer with higher heterogeneity, the DNAPL plume may not reach the bedrock of the aquifer. Such high heterogeneity of the aquifer can lead to accumulation of DNAPL on the less permeable layer, thus leading to the limited vertical movement of DNAPL. Additionally, the higher heterogeneity in an aquifer can lead to higher lateral migration of DNAPL in the aquifer system.

Ganglia to pool ratio can become an important variable when assessing the remediation strategy. Knowledge of this ratio can help not only in the selection of the remediation method but also for its optimization. While it is almost impossible to tell the ganglia to pool ratio from the field study, the model result can give the reasonable insight for estimating this ratio through time (Figure 3-18).

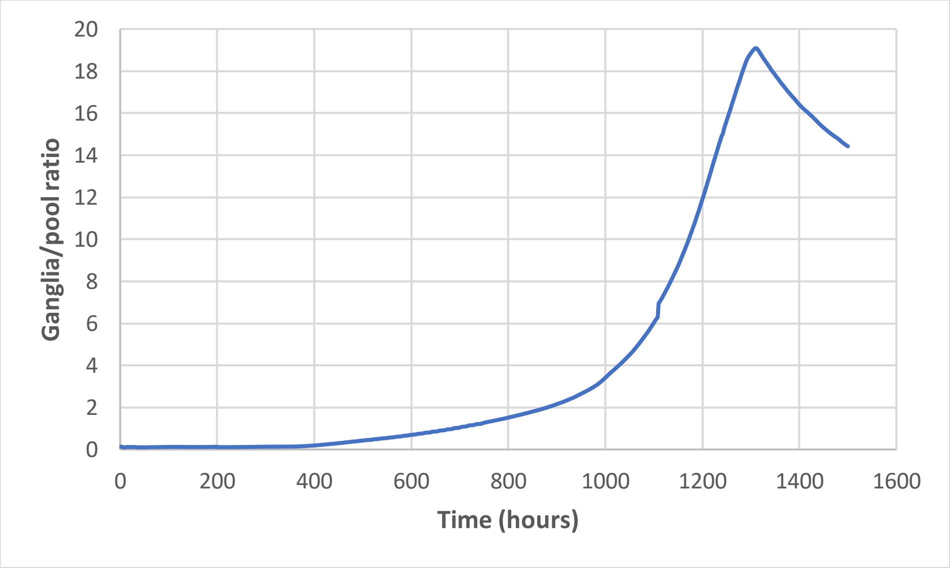

***Figure 3-18**: Plot showing the dependence of ganglia-to-pool ratio on the timeframe of simulated DNAPL infiltration.*

The model result predicts a natural attenuation of DNAPL pool as the pool acts as a source of underlying ganglia formation. This phenomenon is reflected by the continuous increase of ganglia-to-pool ratio for the first 1250 hours of DNAPL infiltration (Figure 3-18). A tiny but sharp upsurge in the plot at 1150 hours is an artifact occurring due to the change in mesh configuration for improvement of the simulation results. Subsequently, the formation of DNAPL pool on the bedrock leads to a decline in ganglia-to-pool ratio as reflected in the curve between 1250 and 1500 hours. In an aquifer with the ganglia mass higher than the pool, passive remediation strategy such as pump and treatment could be viable. Due to lower saturation of ganglia compared to DNAPL, the pump and treatment could lead to the DNAPL source depletion within a reasonable time period. However, for a field containing higher DNAPL pool mass than ganglia, a more active remediation strategy such as ENP injection may be required.

The remediation strategy includes attacking the high-saturation DNAPL pool in the aquifer. While DNAPL ganglia is easy to encounter, such pool is usually elusive and difficult to encounter in a field setting. The model result can help pinpoint not only the location of DNAPL, but also the amount of DNAPL pool present in the aquifer.

3.5 Conclusions

The field scale remediation strategy requires a lot of effort and resources, owing to complexity and inaccessibility of the contaminant aquifer system. Therefore, it is indispensable to develop a robust remediation strategy. Without it, several attempts of remediation have failed or has been inefficient as reported in literature. The success is often limited by lack of detailed understanding of the contaminant and hydrogeological properties of the aquifer. This lack of understanding owes to limited of data obtained during the site characterization stage. While, the information of contamination-aquifer dynamics can be studied at the well location, a continuous and consistent contamination behavior on both temporal and spatial scale is often missing. This is where the modeling can bridge the gap in information obtained by field study.

Here, the two-phase flow model has been developed in three stages. For the first stage, the objective was to verify the Comsol implementation of different formulations for a homogenous 1D porous domain. The reasonable match of the model result with analytical solution confirms the successful implementation. In the second stage, the model has been upscaled to simulate DNAPL flow in 2D heterogeneous porous media. The objective also included simulating the DNAPL flow behavior in the presence of impermeable sand layers. The model results successfully predict the DNAPL flow in the 2D aquifer and the result is in good agreement with the previously reported study. Thus, the second stage exhibits the model capability to simulate the two-phase flow in a complex domain. In the final stage, the upscaled 3D model has been developed with a general groundwater system scenario. The objective for this exercise included a comprehensive study of fate of DNAPL in a real field scenario. As only with the field data the DNAPL flow behavior remains incomplete, such a model shows its potential in understanding the migration pathways and timeline. Additionally, the model developed in final stage, gives a preliminary insight for designing field characterization as well as remediation strategy. Overall, the results show the model potential for developing and facilitating the remediation of groundwater contaminants.

3.6 References:

Ataie-Ashtiani, B., Raeesi-Ardekani, D., 2010. Comparison of numerical formulations for two-phase flow in porous media. Geotechnical and Geological Engineering 28, 373–389.

Anders Jurin, H., n.d. Investigation of Aquifer Geochemistry and Modelling of Effects of In-situ Remediation. Master´s thesis.

Benson, D.A., 1994. User’s manual to VENT2D: A multicompound vapor transport and phase distribution model. Claremont St, Reno, Nevada.

Bredehoeft, J.D., Pinder, G.F., 1973. Mass transport in flowing groundwater. Water Resources Research 9, 194–210.

Bresler, E., 1973. Simultaneous transport of solutes and water under transient unsaturated flow conditions. Water Resources Research 9, 975–986.

Carey, G.R., McBean, E.A., Feenstra, S., 2014. DNAPL Source Depletion: 1. Predicting Rates and Timeframes. Remediation Journal 24, 21–47.

The Capital Region of Denmark., 2017. Data Compilation Report Skovlunde Byvej 96A, Ballerup, Denmark. Internal report.

Delshad, M., Pope, G.A., Sepehrnoori, K., 2000. Utchem version 9.0 technical documentation. Center for Petroleum and Geosystems Engineering, The University of Texas at Austin, Austin, Texas 78751.

Essaid, H. I., Bekins, B. A., & Cozzarelli, I. M., 2015. Organic contaminant transport and fate in the subsurface: Evolution of knowledge and understanding. Water Resources Research, 51(7), 4861-4902.

Finsterle, S., 2004. Multiphase inverse modeling: Review and iTOUGH2 applications. Vadose Zone Journal 3, 747–762.

Helmig, R., 1997. Multiphase flow and transport processes in the subsurface: a contribution to the modeling of hydrosystems. Springer-Verlag.

Illangasekare, T.H., Ramsey, J.L., Jensen, K.H., Butts, M.B., 1995. Experimental study of movement and distribution of dense organic contaminants in heterogeneous aquifers. Journal of Contaminant Hydrology 20, 1–25.

Kolditz, O., Bauer, S., Bilke, L., Böttcher, N., Delfs, J.-O., Fischer, T., Görke, U.J., Kalbacher, T., Kosakowski, G., McDermott, C.I., 2012. OpenGeoSys: an open-source initiative for numerical simulation of thermo-hydro-mechanical/chemical (THM/C) processes in porous media. Environmental Earth Sciences 67, 589–599.

Kueper, B.H., Frind, E.O., 1991. Two-phase flow in heterogeneous porous media: 1. Model development. Water Resources Research 27, 1049–1057.

Lerner, D.N., Kueper, B.H., Wealthall, G.P., Smith, J.W.N., Leharne, S.A., 2003. An illustrated handbook of DNAPL transport and fate in the subsurface.

McWhorter, D.B., Sunada, D.K., 1990. Exact integral solutions for two-phase flow. Water Resources Research 26, 399–413.

Mohan Kumar, M.S., Mathew, M., 2005. Modeling of DNAPL Migration in Saturated Porous Media. Water Encyclopedia 5, 668–672.

Nelson, R.W., 1966. Flow in heterogeneous porous mediums: 1. Darcian-type description of two-phase systems. Water Resources Research 2, 487–495.

Nichols, W.E., Aimo, N.J., Oostrom, M., White, M.D., 1997. STOMP subsurface transport over multiple phases: Application guide. Pacific Northwest Lab.

Pankow, J.F., Cherry, J.A., 1996. Dense chlorinated solvents and other DNAPLs in groundwater: History, behavior, and remediation.

Pruess, K., Oldenburg, C.M., Moridis, G.J., 1999. TOUGH2 user's guide version 2. Lawrence Berkeley National Lab. (LBNL), Berkeley, CA (United States).

Schwille, F., Pankow, J.F., 1988. Dense chlorinated solvents in porous and fractured media-model experiments.

Yu, W., Li, H., 2019. Development of 3D Finite Element Method for Non-Aqueous Phase Liquid Transport in Groundwater as Well as Verification. Processes 7, 116.

Zheng, F., Gao, Y., Sun, Y., Shi, X., Xu, H., Wu, J., 2015. Influence of flow velocity and spatial heterogeneity on DNAPL migration in porous media: Insights from laboratory experiments and numerical modelling. Hydrogeology Journal 23, 1703–1718.

4 Numerical modelling of injection and transport of engineered nano-particles into polluted aquifers

4.1 Introduction

Engineered nano-particles (ENPs) are man-made colloids that have recently triggered a significant interest among the environmental scientific community owing to its potential capability for remediating sites contaminated with industrial contaminants (Shaikh et al., 2020; Tosco et al., 2018; Danish et al., 2016). Normally, these ENPs are injected into aquifers creating a sort of an *in-situ* reactive barrier, which is, in many cases, a more efficient and cost-effective solution than *ex-situ* treatments. Once injected, the interaction between the ENP and the underground pore space is hard to predict since each particle type and aquifer have particular geological (rock type, layering), geochemical (mineralogy, water chemistry) and hydrogeological (porosity, pore shapes) properties. Understanding the mobility of these ENPs in the subsurface becomes, then, crucial to achieve an optimal remediation. The use of numerical models to help in the prediction of such interaction have started to be common in the last decade (Molnar et al., 2015; Taghavy et al., 2013; Cullen et al., 2010) and has been studied at both pore-scale (May et al., 2013, Guzman et al., 2006) and column scale (Torkzaban et al., 2010; Tosco and Sethi, 2010; Uyusur et al., 2010; Lecoanet et al., 2004).

The use of ENPs is quite novel and not many particles have been designed, tested and commercialized yet. The well-known and used ENP is nano Zero-Valent iron (nZVi), which has been widely used as a solution for groundwater contamination owing to its capacity of degrading chlorinated solvents as well as other organic contaminants (Tosco et al., 2014; Johnson et al., 2013; O'Carroll et al., 2013). The efficiency and applicability to real remediation cases of nZVi has been evaluated at both the laboratory (O'Carroll and Sleep, 2013; Berge and Ramsburg, 2009; Phenrat et al., 2009) and pilot and field scales (Johnson et al., 2013; Kocur et al., 2013). The nZVi acts as a reducing agent with the availability of free electron, resulting in the in-situ degradation of contaminant.

The application of nZVi at field scale has been found to be limited due to the aggregation of particles because of electrostatic forces, making its transport through the pore space difficult (Tratnyek et al., 2006). To avoid such aggregation, some substances have been tested as nZVi-surface modifiers. One of them is a polymer called carbomethyl cellulose (CMC). Its application enhances the transport by reducing aggregation and deposition of nZVi through steric hindrance, making the particles remain dispersed in water for a prolonged time (Kocur et al., 2013; O'Carroll et al., 2013). This increased transport of the ENPs is on the range of a few centimeters to several meters.

The surface-modified nZVi is necessary for groundwater remediation because the bare nano-particle has a very limited mobility and degradation capability (Kim et al., 2013). Recently, several studies have reported promising results of CMC-coated sulfidized nZVi (CMC-sZVi), which shows an enhanced transport and reactivity (He et al., 2020; Xu et al., 2020; Garcia et al., 2019). The sulfidized surface of nZVi helps the reactivity by making it relatively less hydrophilic while the CMC coating enhances the transport by reducing the particle-particle aggregation through steric hindrance. A detailed review of transport and reactivity characteristic of CMC-sZVi is given in Chapter 2.

The mobility of ENPs once injected in an aquifer depends on its advective flow with water and on the particle-grain and inter-particle interactions (Tosco and Sethi, 2010). During the ENP transport, the interaction with the aquifer rocks leads to complex and dynamic changes in the mobility of the ENPs, which can result in their permanent or temporary settlement.

The prediction of such complex transport and deposition of ENPs often requires the use of numerical simulations, which cannot only help quantitatively estimate the ENPs mobility but also design and optimize the injection campaigns. A number of numerical tools are available in the literature for ENPs transport and retention (Tosco and Sethi, 2010; Becker et al., 2015; Johnson et al., 2013; Katzourakis and Chrysikopoulos, 2014). In this Chapter 4, the formulation for the prediction of ENPs transport and deposition has been developed for the characterization of the CMC-sZVi injection, transport and immobilization in water-saturated sand.

Chapter 4 in this thesis has aimed at:

1) The development of a nano-particle injection model in saturated sand implemented on the Comsol Multiphysics software and verify it using existing models in the literature.

2) The use of inverse modelling to obtain parameters controlling the mobility of ENPs by calibration of experiments of injection in columns in the laboratory.

3) The performance of sensitivity analysis for all the relevant parameters in the ENPs-porous media interaction.

4) The development of a 3D model for ENP injection in a pilot plant (tank experiment).

The first 3 objectives are the preliminary exercises to build the 3D model of an outstanding experiment developed in a sand-filled tank conducted by the Metal-aid project partnership (Reischer, 2020). The ENP-sand interaction parameters in the 3D model have been derived from column experiments developed in the frame of the same project; this is an initial approach since the attachment rate and detachment coefficient for ENPs transport at tank scale will not be constant due to the non-uniform flow field, which is just true for 1D columns. Therefore, the results yielded by the 3D model are not expected to perfectly match with the data collected by the experiment. However, this approach is reasonable since the aim of this exercise is to demonstrate the validity of the model implementation at scales close to real aquifers.

4.2 Methodology

4.2.1 Implementation and validation of ENP transport in Comsol Multiphysics platform

The governing mechanisms and mathematical equations of ENP transport and interaction with the porous media have already been discussed in Chapter 2. In this Chapter 4, equations from 2.62 to 2.64 in Chapter 2 have been implemented in Comsol Multiphysics.

$$\frac{\partial(\theta C)}{\partial t} + \rho_b \frac{\partial(s_1)}{\partial t} + \rho_b \frac{\partial(s_2)}{\partial t} = -\nabla(vc) + \nabla(D_L \frac{dC}{dx} + D_T \frac{dC}{dy} + D_T \frac{dC}{dz}) \qquad \text{(eq. 2.62)}$$

$$\rho_b \frac{\partial(s_1)}{\partial t} = \theta k_{a,1}\left(1 + As^{\beta_1}\right)c - \rho k_{d,1} s_2 \qquad \text{(eq. 2.63)}$$

$$\rho_b \frac{\partial(s_2)}{\partial t} = \theta k_{a,2} \left(1 + \frac{x}{d_{50}}\right)^{\beta_2} c - \rho k_{d,1} s_2 \quad \text{(eq. 2.64)}$$

Where ka is attachment rate [T^{-1}], kd is detachment rate [T^{-1}], θ is the porosity of sand matrix, c is the aqueous concentration of ENP ($M \cdot L^{-3}$), s is the amount of particle deposited relative to the sand mass [-], A is multiplier coefficient [-], β is exponential coefficient [-]. The suffix 1 and 2 are the deposition site of ENP on the sand grains.

For a further use of the implemented formulation, a mandatory exercise of benchmarking needs to be performed by comparison with cases from the literature. So, two different models of injection of ENPs have developed on Comsol Multiphysics and compared with the model results from the code called MNMs (Tosco and Sethi, 2009).

The benchmark exercise consists of the transport of ENPs in a sand column with a linear mechanism of deposition, and the parameters used have been taken from literature (Tosco and Sethi, 2009). The model reproduces a generic experiment consisting of a water-saturated, sand-filled column. The experimental set-up has a sand of porosity 0.4, and it is filled in a column of length 10 cm. The ENPs are injected from one end of this sand column with a Darcy velocity of 0.08 $mm \cdot s^{-1}$. The effluent concentration from the other end of the column is used to generate the breakthrough curve while the spatial distribution of the retained particle at the end of the experiment is used to plot the retention profile. Two different ENPs are injected at east step (Model I and Model II). In the Model I scenario, the attachment coefficient (K_a) and detachment coefficient (K_d) are considered to be 0.004 s^{-1} and 0.008 s^{-1}, respectively. Conversely, for the model II, the attachment coefficient (K_a) and detachment coefficient (K_d) are considered to be 0.008 s^{-1} and 0.004 s^{-1}, respectively.

***Table 4-1**: Parameters used in the benchmark exercise of ENP injection into a sand-filled column using Comsol Multiphysics and MNMs.*

	Model I	**Model II**
Column length	10 cm	10 cm
Darcy velocity	0.08 $mm \cdot s^{-1}$	0.08 $mm \cdot s^{-1}$
Porosity	0.4	0.4
Dispersion coefficient	1×10^{-7} $m^2 \cdot s^{-1}$	1×10^{-7} $m^2 \cdot s^{-1}$
Attachment Coefficient (K_a)	0.004 s^{-1}	0.008 s^{-1}
Detachment Coefficient (K_d)	0.008 s^{-1}	0.004 s^{-1}

Figure 4-1 show two plots with the results from the calculations using Comsol and MNMs. A perfect match is observed. For Model I, the results show a relatively slow attainment of peak in the breakthrough curve compared to Model II. Thus, Model I predicts a higher deposition of ENPs compared to Model II (Figure 4-1a). The Comsol model is successfully able to match the rise and fall of the peak in the breakthrough curve (Figure 4-1b). The breakthrough curve predicted by model II is also well in agreement with the result from MNMs model. The tailing effect in the breakthrough curve can be attributed to the detachment coefficient implemented in the equation (Figure 4-1c). Finally, Figure 4-1d shows that Comsol model closely replicates the tailing effect in breakthrough curve as that of MNMs model. The result indicates that the ENPs injection model developed on Comsol Multiphysics is able to correctly model the transport of ENPs and their deposition in the sand pore space.

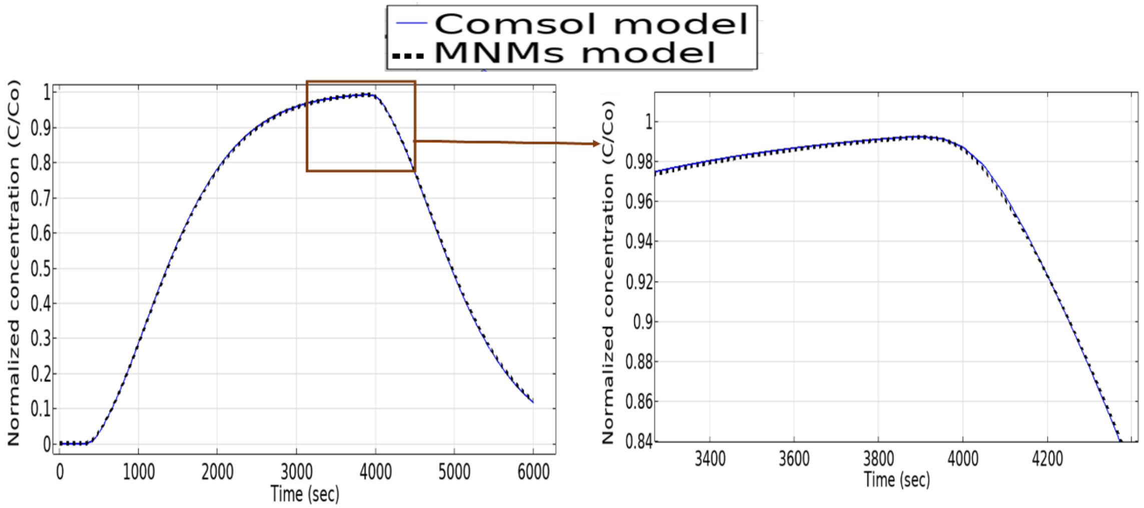

(a) Model I

(b) Model I

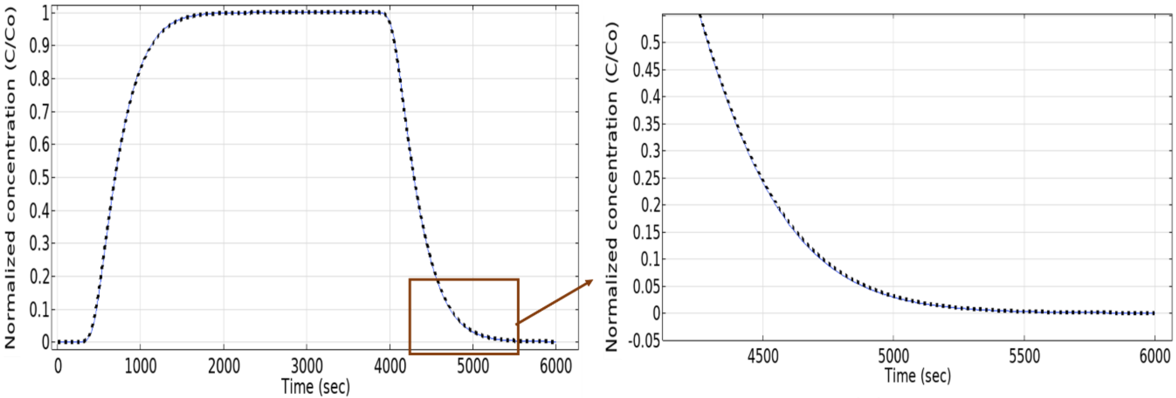

(c) Model II

(d) Model II

***Figure 4-1**: Prediction for breakthrough curves calculated with Comsol (represented by blue curve) and MNMs (represented by black dots) for injection of ENPs in column experiments (model I, a-c; model II, c-d).*

4.2.2 Modelling of the injection of CMC-coated, sulfidized nZVi (CMC-sZVi) in sand-filled columns in laboratory

Two different general approaches exist when modelling the evolution of a natural or laboratory-based system: *forward* and *inverse*. In a forward modeling study, the relevant parameters are known and what is predicted is the evolution in past, current of future scenarios. On the other hand, in the inverse modelling, such evolution is already known but there is missing information on the relevant parameters driving it, and the model is intended to estimate these parameters.

The inverse modeling involves assumptions, and several iterations are usually required to estimate the parameter that leads to best fitting model result.

Inverse modeling can be used to be predict the parameters governing the attachment and detachment of ENPs to/from the mineral surfaces. In this work, this exercise has been done using the data from column sand experiment performed by Digiacomo et al. (2019) in the frame of the Metal-Aid. In the first step, porosity and dispersity of the filling material in the columns (a well-sorted sand) have been estimated using the tracer Breakthrough Curves (BTC). In the second step, the attachment and detachment coefficients have been estimated by the best fitting curve for the BTC and retention profile of ENPs in the sand-filled column.

A different experimental setting has been used to derive the hydraulic property of column sand and the governing parameters for nano-particle mobility. These experiments are performed by one of the collaborators from Karlsruhe Institute of Technology, Germany, under the framework of the Metal-Aid project. A column of length 16.2 cm and diameter of 1 cm has been filled with a homogeneous sand of size 200 to 400 µm. The sand has been flushed with water from one end leading to the full saturation of sand-filled column. The flow rate of injected water has been maintained at 1 ml·min^{-1}. $NaNO_3$ has been used as the tracer and injected with a concentration of 70 mM. The tracer injection lasted for 1 hour leading to the total injection of 45 mL tracer solution. The effluent concentration emitting from the other end of the sand column has been measured with the help of a spectrometer.

The same experimental condition has been reproduced in the model with the help of a 1D domain representing the sand-filled column. A total of 100 mesh elements have been used for the discretization of this domain. The modeling exercise involve a best fitting curve to match the experimental result for tracer test. Figure 4-2 shows the best fitting curve estimated by model in comparison with the experimental result. From this model, a porosity of 0.34 and dispersivity is 0.027 m for the column sand has been calculated.

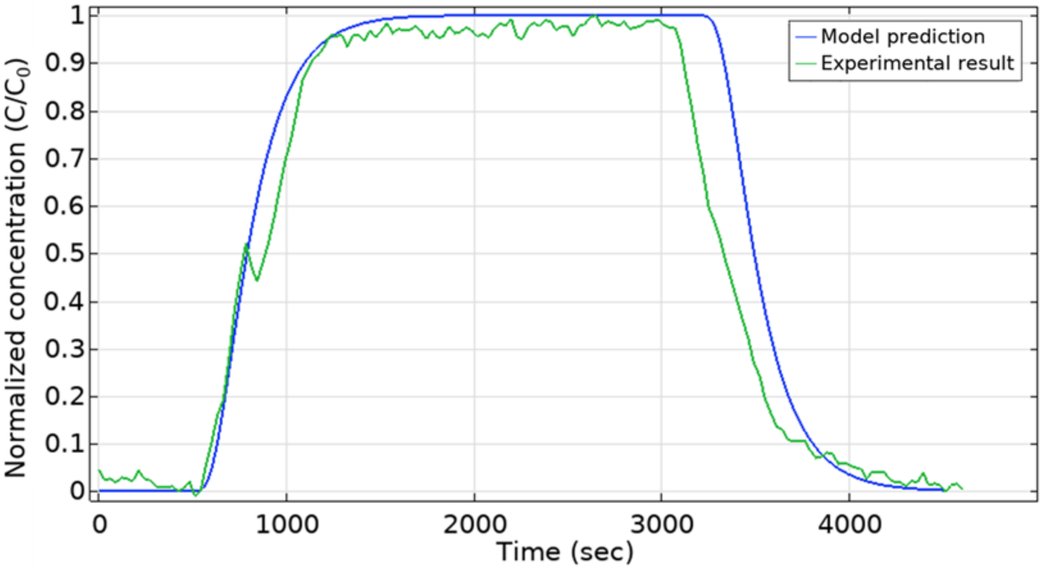

Figure 4-2: *Model prediction for best fitting curve of the injected tracer (represented by blue curve) reproducing the experimental data (represented by green curve) from Digiacomo et al. (2019). The model estimates a porosity of 0.34 and dispersivity of 0.027 m.*

In the second stage, Digiacomo et al. (2019) injected CMC-coated sZVi particles in the sand-filled column. The experimental setup consisted of a sand-filled column of 12.5 cm in length and 1.4 cm in diameters. Two set-up of ENPs injection in column experiments have been tested: (1) 0.5 $g_{particle} \cdot L^{-1}{}_{water}$ of sZVi injected with Darcy velocity of 0.108 $mm \cdot s^{-1}$ for the injection period of 8350 seconds, and (2) 0.25 $g_{particle} \cdot L^{-1}{}_{water}$ of sZVi injected with a Darcy velocity of 0.216 $mm \cdot s^{-1}$ for the duration period of 4000 seconds (Table 4-2). For both cases, a constant CMC concentration of 5 $g_{cmc} \cdot L^{-1}{}_{water}$ has been used in the injection fluid. The CMC used in the experimental scenario has a molecular weight of 250,000 $g \cdot mol^{-1}$ (CMC 250K).

***Table 4-2**: Time periods for the simulation of CMC pre-flushing, nano-particle injection and CMC post-flushing in the sand-filled column in the inverse model exercise simulating the Digiacomo et al. (2019) column experiments.*

	CMC pre-flushing	Nano-particle injection	CMC post-flushing
Setup 1 (flow rate = 0.108 mm/s)	2960 sec	2760 sec	2630 sec
Setup 2 (flow rate = 0.216 mm/s)	1040 sec	1219 sec	1741 sec

A modeling exercise has been done to estimate the parameters governing the mobility of these ENPs in the sand-filled columns. Two different retention mechanisms have been considered: (1) a non-linear ripening, and (2) a mechanical filtration (straining) (Tosco and Sethi, 2010). The model has been based on the verified numerical formulation for the transport and retention of ENPs in a porous media developed (section 4.2.1).

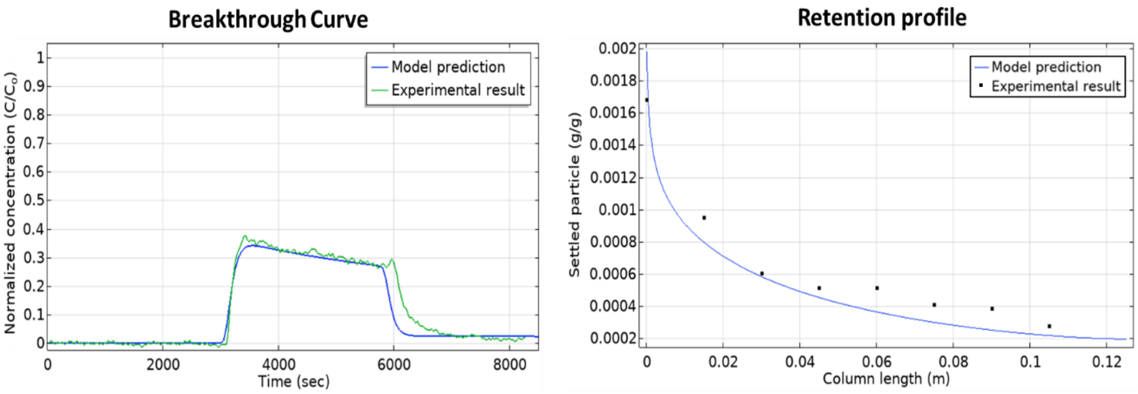

***Figure 4-3:** Best fitting model for the breakthrough (left plot) and retention curves (right plot) for the injected sZVi ENPs from Di Giacomo et al. (2019) experiments (case with Darcy velocity of 0.108 $mm \cdot s^{-1}$).*

Using the porosity and dispersivity values from the fitting of tracer test, the 1D model predicts the arrival of ENPs, 90 seconds after injection of sZVi for the case of smaller Darcy velocity (Figure 4-3). The peak normalized concentration of ENPs estimated by model is 0.34. The arrival of the

ENPs is best explained if ripening is the relevant retention mechanism, which implies an increased particle-particle interaction with time. After 8350 seconds, the plot shows a reasonably close match between the model prediction and the experimental result (Figure 4-3).

Concerning the model with an increased flow rate of 0.216 mm·s^{-1} and initial sZVi concentration of 0.25 g·L^{-1}, the breakthrough curve predicted by model has an arrival time is 60 seconds while the maximum normalized concentration reached is 0.68 (Figure 4-4). The model predicts that out of 11.3 grams of EPNs injected in the column, 7.6 grams of ENPs comes out suspended in the aqueous phase while 3.7 grams gets deposited in the sand. This denotes that 67% of the particle is coming out of the system suggesting a comparatively lower retention of sZVi.

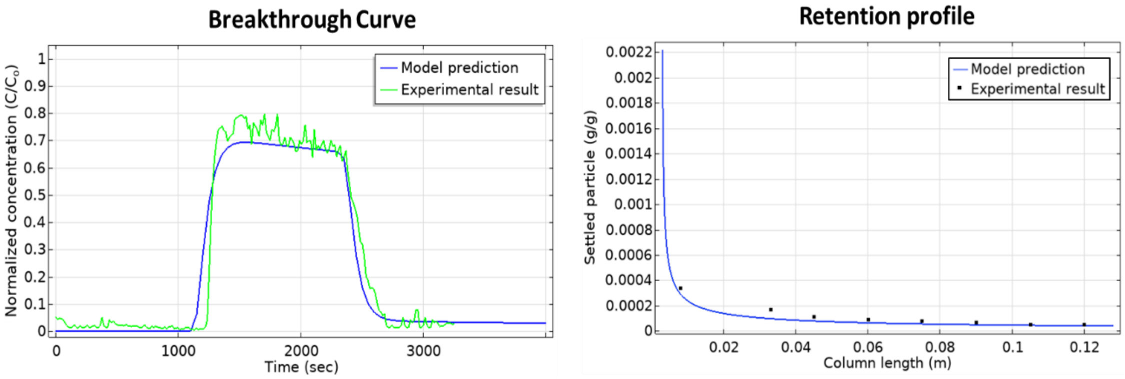

Figure 4-4: *Best fitting model for the breakthrough (left plot) and retention curves (right plot) for the injected sZVi ENPs from Di Giacomo et al., (2019) experiments (case with Darcy velocity of 0.216 mm·s^{-1}).*

The governing parameters characterizing the sZVi transport and retention in the sand-filled column have been obtained from the curve fitting exercise (Table 4-3). The model predicts a lower degree of straining and ripening mechanism for flow rate of 0.216 mm·s^{-1} in the column compared to the case with smaller Darcy velocity. The relatively lower deposition of ENPs in the column sand can be attributed to higher flow rate used for injection. The result indicates the dependence of attachment rate and detachment coefficient on the flow rate and sZVi concentration. The uncertainty attached with each derived parameter is further tested with sensitivity analysis (Appendix B).

Table 4-3: *Estimation of the parameters for particle retention mechanisms for the experiments by Digiacomo et al. (2019).*

Parameters	**Set-up 1**	**Set-up 2**
Ripening		
Attachment rate (k_a)	0.00918 s^{-1}	0.0003 s^{-1}
Detachment coefficient (k_{dt})	0.00068 s^{-1}	0.00034 s^{-1}

Parameters	Set-up 1	Set-up 2
β	0.702	0.7
A	1050	6750
Straining		
Attachment rate (k_a)	0.001	0.06435 s^{-1}
Detachment coefficient (k_{dt})	0.000107	0.000053 s^{-1}
β	0.23	0.6

4.3 Modelling of the mobility of ENPs injected in a sand-filled tank experiment

4.3.1 Introduction

After the validation of the implementation of the formulation for the injection and mobility of ENPs in porous media, in this section all this information is exported to model an experiment at pilot plant scale, much closer to the real injection in the field. Although the conditions from columns to tank scales are not exactly the same, they can be used as a starting point to numerically assess the injection at a scale closer to the real remediation cases.

The objective of this chapter is to develop a field scale numerical formulation to predict the behavior of ENPs in a small-scale aquifer. The model has been developed on the verified numerical formulation (section 4.2.1) and the performance of the model is compared with a real case scenario. For this, the experimental result of nano-particle injection in a tank scale has been used. The experiment has been conducted by colleagues of the Metal-Aid project at University of Copenhagen (KU). The experiment has been led by Markus Reischer from KU over the period of Autumn 2019-20, as part of his PhD project. The result from his work has been used as a starting point for the numerical assessment. The model features have been set up such that a close resemblance of the experimental processes reported by Reischer (2020) is established.

4.3.2 Description of the tank experiment

A tank filled with sand has been used to reproduce the fluid and ENPs dynamics in a general sandy aquifer on a laboratory scale (Figure 4-5). The tank has a dimension of 1.2 m of length, 1 m of width and 1.1 m of height. The tank has been filled up with fine grained homogeneous sand (d_{50} = 0.179 mm, uniformity 1.66) with a permeability of 6.5 × 10^{-12} m^2. The injection well is located at the center and has a cylindrical shape of 25 mm in radius and 60 cm in height. A well screen with total of 60 slots each with a size of 35 mm length, 0.3 mm width, have been placed at the center of the tank. A total of 20 grams of CMC coated sZVi ENPs has been injected for 70 minutes from the well screen. The total injection period has been 160 minutes, including 45 minutes of pre-flushing and 45 minutes post-flushing of tank with CMC-water solution. Sampling points have been installed at different depths in the tank to study the transport of CMC-sZVi through the sand. The retention of sZVi has also been determined and further studied by analyzing sand samples after injection. Figure 4-5b shows the visual appearance of sZVi settled in the sand-filled tank. Most of the ENPs are retained within the radius of 10 cm from the well screen.

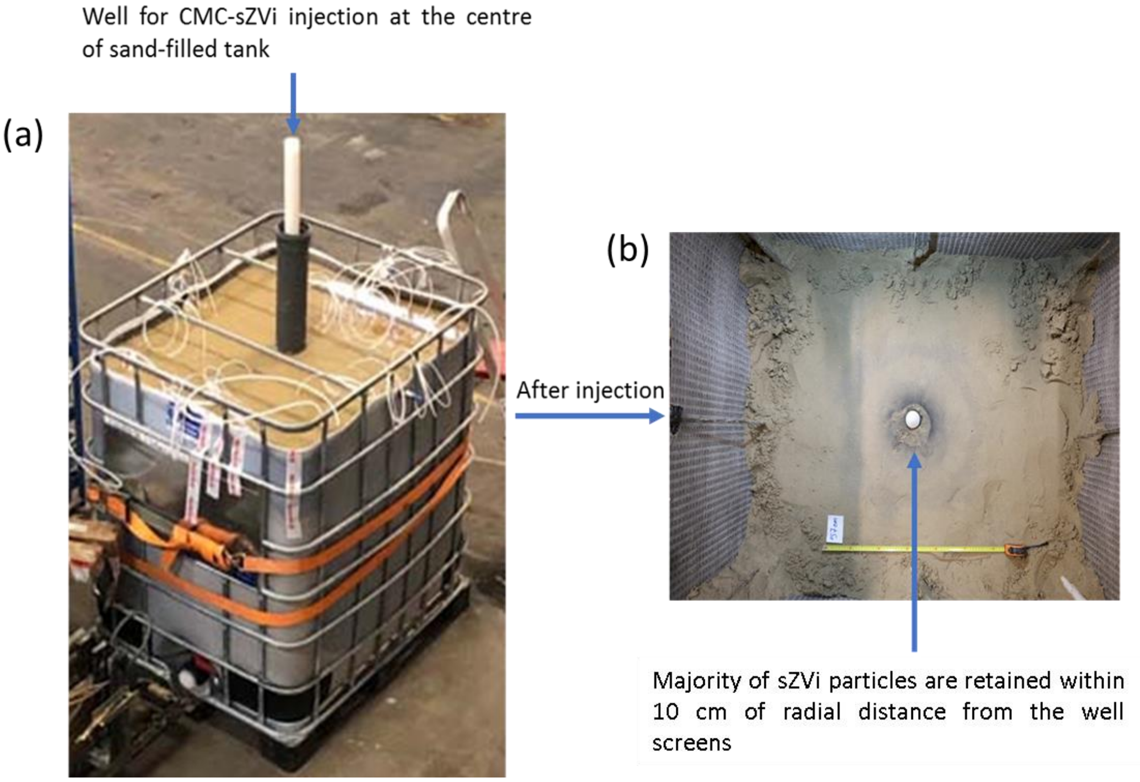

***Figure 4-5**: (a) Sand-filled tank used for CMC-sZVi injection through the well deployed at its center. (b) Zenithal view of ENPs retained in the sand appearing as black rings around the well. The tank experiment has been set up and performed by the collaborators under the framework of Metal-Aid project (Reischer, 2020).*

The transport and retention of ENPs depends on the sand properties, the fluid medium and the nano-particle itself. Therefore, prior to the ENPs injection, two preliminary experiments have been performed to study the sand and fluid characteristics.

In the first step, a tracer injection experiment has been conducted in the sand-filled tank to determine the hydraulic properties of the system. For this, the sand has been made to be fully-saturated with water. KCl has been used as a tracer and it has been injected through the well screen for 4 minutes. The viscosity of the fluid (consisting of tracer solution in water) is considered to be 0.001 Pa·s and remained unaffected by the presence of the tracer. The arrival of these tracer has been studied through the sampling points placed at different depth of the tank. Figure 4-6 shows the result of breakthrough curve obtained from a sampling point located at a distance of 20 cm radially from the well and at a height of 0.55 m from the bottom of the tank. The analysis for tracer concentration at 7 different time steps have been measured as represented by the black dots. The green curve connects all these dots to see the general pattern of the breakthrough curve for the tracer. The experimental results indicate the first arrival of the tracer after 2.3 minutes, and the maximum recovery observed at this sampling point is 57%. The modeling exercise done in this Chapter 4 estimates the best-fitting curve to estimate the relevant hydraulic parameters.

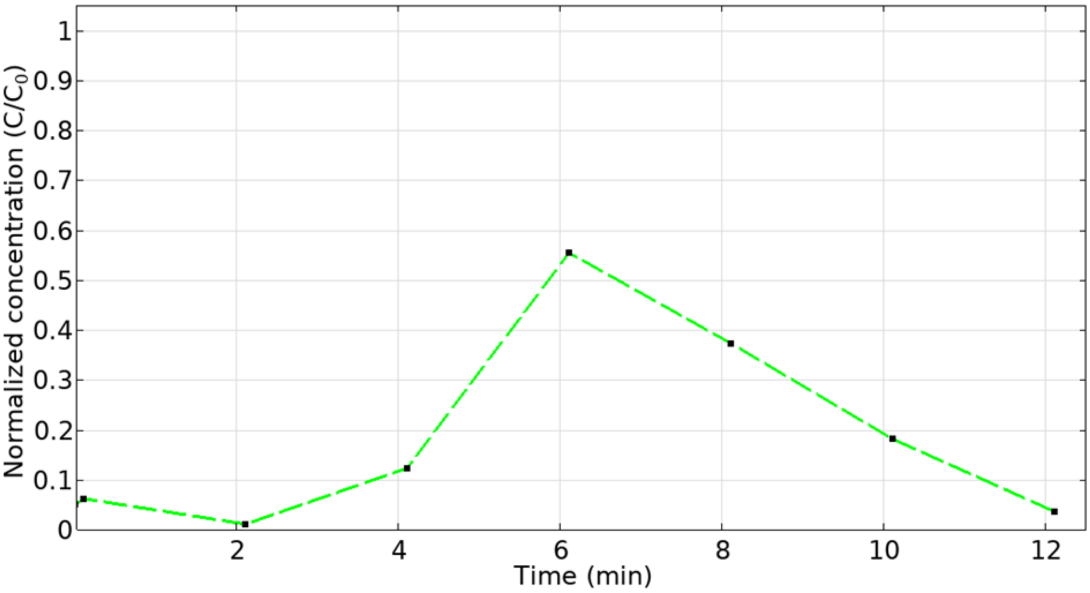

***Figure 4-6**: Breakthrough curve of injected tracer in the sand-filled column and observed at a radial distance of 20 cm from the central well screen (Reischer, 2020).*

The tracer test in the first step has a constant viscosity. But during the injection of CMC-sZVi nano-particles, the viscosity is expected to change in the presence of CMC (Li et al., 2015). The viscosity of the fluid varies as a function of CMC concentration in the injected fluid. Thus, to study the viscosity variance during injection, a separated experiment has been performed in the second step which consisted of injecting a CMC-water solution in the sand-filled tank. Contrary to the tracer experiment, the experiment design has been changed for CMC-water injection: Instead of putting the water table at 1.1 m, the water table has been put at a height of 0.65 meters measured from the base of the tank. A wet sand with capillary water has been put on the top overlying the saturated sand. While the water table changes during the injection near the well, a constant water table of 0.45 m in height has been maintained at the boundary wall. This change in experimental set-up has been done to resemble the design of sZVi injection experiment carried in the following step. The solution has been injected at a different flow rates (544 ml·min^{-1}, 609 ml·min^{-1}, 683 ml·min^{-1}, 760 ml·min^{-1}) in a stepwise manner. The pressure build-up at the well screen has been studied and plotted along with the flow rate variation (Figure 4-7). The plot shows the increase of the fluid pressure in a step wise manner with increase in the flow rate.

In this thesis, the numerical model has been developed to generate the best fitting curve for the plot in Figure 4-7. With this best fitting curve, viscosity for the water with 5 $Kg_{cmc}\cdot m^{-3}{}_{water}$ of CMC dissolved has been predicted. Once the viscosity is predicted for 5 $Kg_{cmc}\cdot m^{-3}{}_{water}$ of CMC, the viscosity variation as a function of CMC concentration has been determined by using the Grunberg and Nissan equation (Krol et al., 2013) (equation 4.1):

$$ln\ (\mu_{wc})\ =\ \frac{C_c}{C_{c_0}}(ln\ (\mu_{wc_o} - ln\ \mu_w\ )\ +\ ln\ \mu_w \qquad \text{(eq. 4.1)}$$

Where C_c is the variable CMC concentration, μ_{wc} is the viscosity of aqueous phase as a function of CMC concentration C_c, C_{c_0} is the reference CMC concentration taken as 5 $Kg_{cmc}\cdot m^{-3}{}_{water}$, μ_{wc_o} is the viscosity of aqueous phase for the reference CMC concentration, and μ_w is the viscosity of pure water (0.001 Pa·s). This equation assumes that due to the low CMC concentration, the mole fraction of water in the water CMC solution is 1.

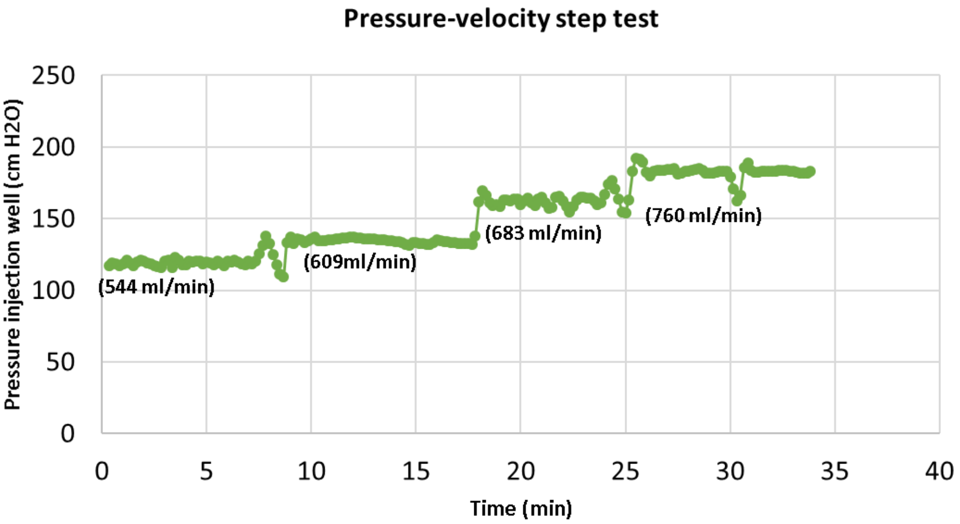

Figure 4-7: Change in pressure at the well screen due to the increase of flow rate from 544 ml·min^{-1} to 760 ml·min^{-1} in 4 steps, in the ENP injection in a sand-filled experiment (Reischer, 2020).

In the third and final step, a total of 20 g of CMC-sZVi particles has been injected in the duration of 70 minutes of fluid injection. Similarly as in the previous step, an initial water table of 65 cm measured from the tank bottom has been set-up and maintained all throughout the experiment. The 70-minute long injection of CMC-sZVi has been preceded by 45 minutes of pre-flushing with CMC, and followed by 45 minutes of post-flushing with CMC with no sZVi. Therefore, the total injection period including pre-flushing, CMC-sZVi injection and post-flushing has lasted for 160 minutes. Figure 4-8 shows the experimental observation of pressure at one of the slots in the well screen through which injection done in the sand-filled tank. The time period includes the 70 minutes of CMC-sZVi injection (represented by orange dotted line) followed by the 45 minutes of CMC post-flushing (represented by blue dotted line). This pressure is mentioned as equivalent water pressure head in centimeters and measured over the whole injection period of 115 minutes (CMC-sZVi injection and post-flushing with CMC solution). The pressure shows gradual increase from 1020 cm at the onset of CMC-sZVi injection to 1146 cm at the end of the injection (time =70 minutes). The formation of a fracture in the tank sand has been observed after 3 minutes resulting in the drop in the pressure represented by the equivalent water pressure head from 1177 cm to 1033 cm. The pressure drop can be attributed to the preferential flow of injected fluid along the formed fracture in the sand. Therefore, the experiment has been stopped and started again after sealing the sand in the fracture by pouring additional sand. The fluid pressure has recovered to the normal trend after the re-injection of sZVi with 1120 cm equivalent water pressure head. The fluid pressure at the well screen at the end of CMC-sZVi injection and onset of post-flushing is 1146 cm equivalent of water pressure head. During the 45 minutes of post -flushing with CMC solution the fluid pressure slightly has increased from 1146 cm to 1175 cm equivalent water pressure head.

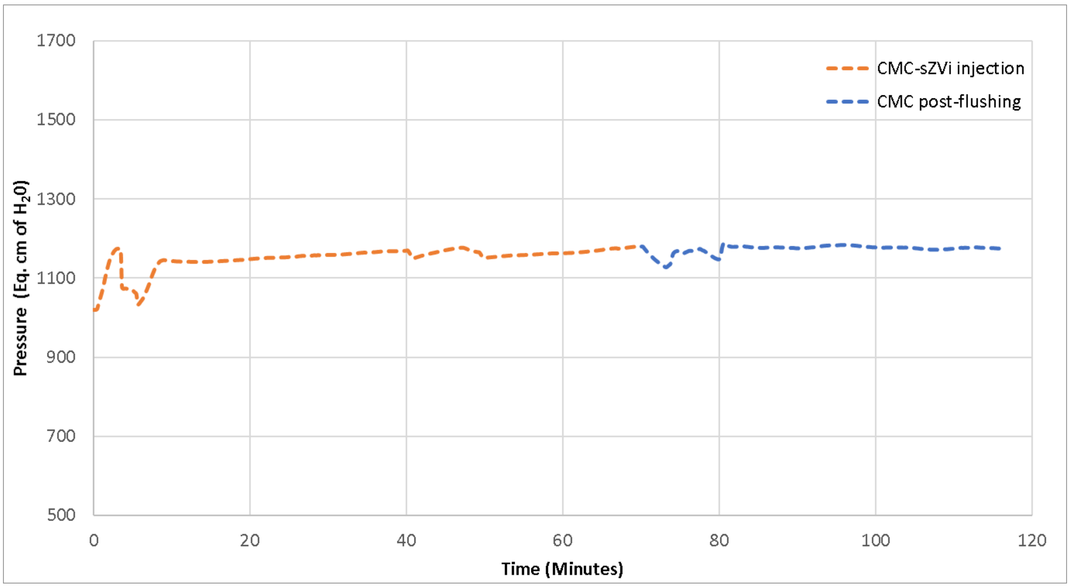

Figure 4-8: Fluid pressure at the well screen measured during the injection of CMC and sZVi in the sand-filled tank (Reischer, 2020). The dotted orange curve represents the fluid pressure during the CMC-sZVi injection while the dotted blue line represents the fluid pressure during the post-flushing with CMC solution after sZVi injection.

The concentration of sZVi has been maintained at 0.5 $Kg_{particle}\cdot m^{-3}_{water}$ whereas the CMC concentration has been 5 $Kg_{cmc}\cdot m^{-3}_{water}$ during the 70 minutes of CMC-sZVi injection. Similar to the tracer experiment, several sampling points have been put at different locations within the sand-filed tank. These sampling points have been used to collect and analyze the CMC-sZVi water solution that flowed through the sand grains. The concentration of sZVi from these points has been studied to calculate the breakthrough curve at different radial distances. Figure 4-9a shows the breakthrough curve at a distance of 10 cm from the tank, whereas Figure 4-9b shows the breakthrough curve at 20 cm from the well screen. Both sampling points have been placed at the height of 55cm measured from the bottom of the tank.

After the end of the injection experiment, a geochemical analysis of the sand has been done to study the retained sZVi. Figure 4-10a shows the sand at a depth of 0.55 m from the top with the retained sZVi forming a black-stained halo around the well. Samples of this halo have been analysed with Optical Emission spectrometer (ICP-OES) to determine their iron content (Reischer, 2020). Figure 4-10b shows the concentration of retained ENPs at 55 cm deep, observed along the red line. The plot shows that just next to the well screen, the concentration of retained sZVi is 300 $\mu g_{ENP}\cdot g_{sand}^{-1}$. The concentration of retained sZVi increases initially with the radial distance from the well screen. The concentration peaks at a radial distance of 3 cm after which it decreases rapidly. This increasing and decreasing pattern of the concentration can be the consequence of presence of a variable granulometry of the sand around the well. The variable granulometry in the tank originates due to the presence of gravel apart from the sand in the tank domain. With a radial thickness of 6 cm, this gravel encompasses the well screen through which sZVi is injected. Due to relatively higher porosity of the gravel, the retention of particles is comparatively smaller, and as the sZVi encounters the finer sand, the straining mechanism becomes significant and thus high retention occurs at the gravel-sand interface. Along with the further radial distance, the retained sZVi concentration decreases and becomes negligible after 10 cm from the well screen.

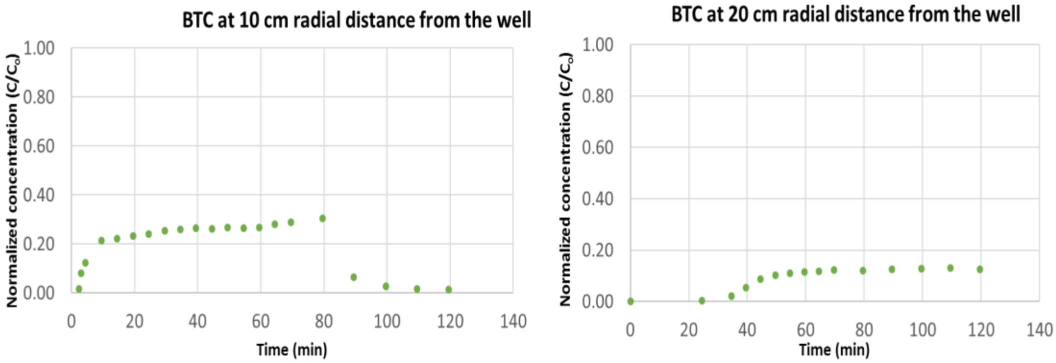

(a) (b)

Figure 4-9*: Breakthrough curve of injected sZVi in the sand-filled tank, observed at a distance of 10 cm (a) and 20 cm (b) from the central well screen (Reischer, 2020).*

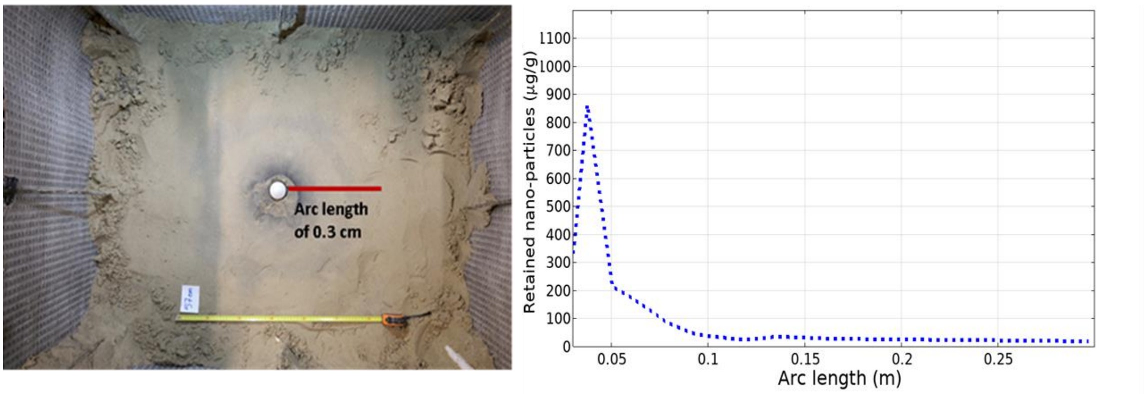

(a) (b)

Figure 4-10*: (a) Visual evidence of nano-particle retention in the sand during the tank experiment, shown as a black-stained halo (Reischer, 2020). (b) Radial retention profile of sZVi obtained along the red line shown in the sand-filled tank in (a).*

In a tank scale injection experiment, the behavior of sZVi is thought to be governed by the dynamically varying interaction coefficients defined in Equations 2.63 and 2.64. These interaction coefficients vary spatially and temporally in the sand-filled tank due to the varying Darcy velocity of the injected fluid. These coefficients can be estimated by performing several column experiments and deriving the governing parameters from best fitting curve (Tosco and Sethi, 2010). However, under the framework of Metal-Aid project, only data from sZVi injection experiments in two columns have been available. Among these two, only one of them uses a sZVi concentration of $0.5\ \text{Kg}_{particle}\cdot\text{m}^{-3}_{water}$ which is the same as for the injection in sand-filled tank. Therefore, the dynamically varying governing coefficients characterizing the nano-particle retention and transport behavior in the sand-filled tank remain unknown. Due to this limitation, a constant value for the interaction coefficients has been used for developing the sZVi injection model in sand-filled tank. The parameters obtained from the inverse model of column experiment (for the setting with Darcy velocity of $0.108\ \text{mm}\cdot\text{s}^{-1}$ of Darcy velocity and $0.5\ \text{g}_{cmc}\cdot\text{L}^{-1}_{water}$ of influent sZVi concentration) have been used. Although the model prediction obtained with the constant governing parameters cannot be fully used to match the experimental values, it is useful for showing the capability of the numerical model implementation to simulate the sZVi injection in an aquifer which is the objective of this research work.

4.3.3 Model set-up of the ENPs injection in the tank experiment

For modeling the particle transport and retention in the tank, a model geometry consisting of a cuboid with dimensions of 1.2 m × 1 m × 1.1 m has been considered (Figure 4-11). The length of tank (1.2 m) aligns with X axis, width of tank (1 m) aligns with Y axis, and height of tank (1.1 m) aligns with Z axis. The vertical distance between two adjacent slots of the well screen is 4.7 mm while the horizontal distance for the same is 26.9 mm. A small cube-shaped region with dimension of 11 cm ×11 cm ×11 cm represents the homogeneous gravel sand surrounding the well screen. The model domain has been simulated with different initial hydraulic heads to reproduce the experimental tests. A fixed datum altitude of z =0 is assigned for calculating hydraulic heads at each step of the modeling exercises.

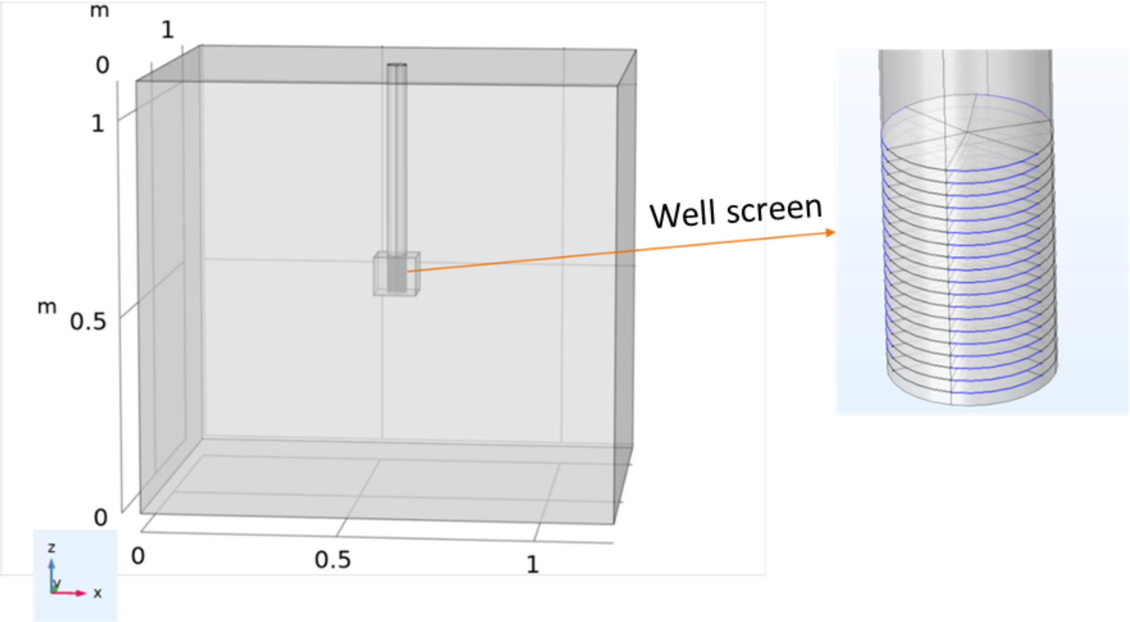

__Figure 4-11__: Geometry of the model domain representing the tank experiment developed in the frame of the Metal-Aid project (Reischer, 2020). Central to the tank, a well is placed through which the injection of ENPs is simulated. The enlarged image of the well screen shows the tiny slots acting as an inlet for ENPs.

4.3.4 Initial and boundary conditions

The numerical simulation of the tracer experiment has been performed considering that the sand and gravel are fully water-saturated. A hydrostatic initial condition with a hydraulic head as the height of the tank (1.1 m) has been prescribed. An injection flow of 2.5 $L\cdot m^{-3}$ with a tracer concentration of 1 $Kg_{tracer}\cdot m^{-3}{}_{water}$ has been implemented to come out from all of the simulated slots of the well during 4 minutes. For the tracer transport, a Robin-type boundary condition (equation 4.2; Corey and Auvermann, 2003) has been applied to each well slot:

$$(qC - (D\nabla c)) = q_o C_0 \qquad \text{eq. (4.2)}$$

Where, qC is the advective flux $[M\cdot L^{-3}\cdot T^{--1}]$, $(D\nabla c)$ is the hydrodynamic dispersive flux $[M\cdot L^{-3}\cdot T^{--1}]$, q_o is the Darcy velocity for injection $[L\cdot T^{-1}]$, and C_0 is the inlet concentration of tracer $[M\cdot L^{-3}]$.

The remaining part of the well has been prescribed with no flux boundary for both water flow and solute transport. The background concentration of tracer in the model domain has been considered to be zero. The lateral boundary of the model domain has been implemented with a Dirichlet boundary of 1.1-meters hydraulic head. For the tracer transport, an open boundary has been prescribed at the lateral wall of the model domain. For the top and bottom wall of the model domain, a no flow boundary has been implemented for both tracer transport and Darcy flow.

For the ENP transport, a different set of initial and boundary conditions has been used according to the changes in the experimental set-up (see above). The model domain has been implemented with a hydraulic head of 0.65 measured from the ground. The sand layer above the water table has been considered to be saturated with capillary water. An inlet flow rate of 565 $ml\cdot min^{-1}$ has been implemented at the well slots. The ENP injection has been considered to enter from all of 60 well slots with a concentration of 0.5 $Kg_{particle}\cdot m^{-3}{}_{water}$.

For the CMC injection, a Robin-type boundary condition (equation 4.2) has been implemented. In the case of CMC, the inlet concentration taken has been 5 $Kg_{cmc}\cdot m^{-3}{}_{water}$. The CMC injection has been simulated for 160 minutes while the nano-particle injection has been simulated to start from the 45th minute up to 115th minute of fluid injection. The water pressure at the four lateral walls has been set at hydrostatic pressure with a hydraulic head of 0.65. The top and bottom walls act as no flow boundary.

4.3.5 Meshing

The domain has been spatially discretized with finite elements (see Chapter 2 in this manuscript for details on discretization). The size of mesh elements has been varied to optimally discretize the gradient of the dependent variable (Figure 4-12). Since the pressure and ENP concentration is expected to have a lower value of spatial gradient away from the well, a coarser mesh of size range between 0.1 and 0.25 m has been used. A section of model domain is presented in Figure 4-12b to show the mesh geometry inside the model domain. This figure shows a relatively finer mesh near the well. A finer mesh with elements of size of the order of few centimeters has been used for discretizing the small cube representing the layer of gravel near the well. A very fine mesh elements of size 0.005 m has been used for discretizing the well slots. As the well slots act as an inlet for fluid injection, their millimeter-sized geometry requires an extremely fine mesh. A mesh size of 0.001 m has been implemented for each of the well slots.

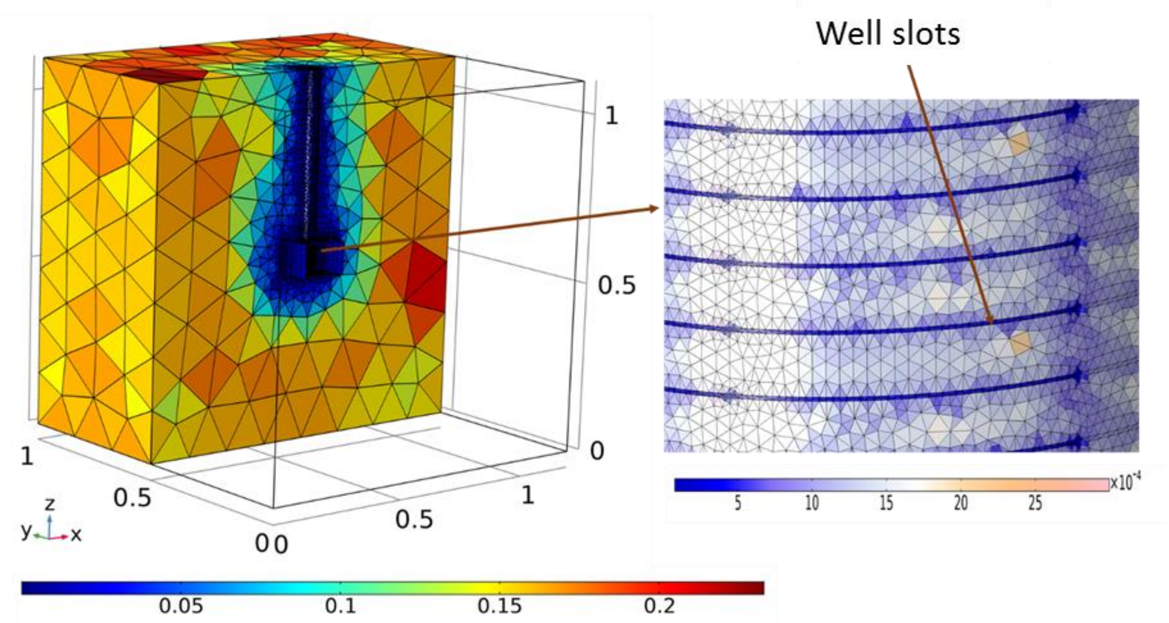

Figure 4-12*: Mesh used in the modelling of the ENP injection in a tank experiment (just a half of the model domain is shown). A tetrahedral-element mesh has been used to spatially discretize most of the model domain. Additionally, a very fine mesh has been used to discretize the well slots (enlarged figure on the right-hand side). The scale colors indicate the mesh size in meters.*

4.3.6 Numerical formulation of ENPs mobility implement in the model

The Comsol Multiphysics software has been used for simulating the transport of tracer and ENPs in the tank injection experiment. The Darcy formulation has been included in the Comsol module for solving physics, and it calculates the Darcy velocity, the pressure of the fluid and the concentration of solutes at each spatially discretized element node.

Porosity and permeability of the sand and gravel are the main unknown parameters in the tank experiment. Additionally, the viscosity of water as a function of aqueous CMC concentration is also required. All these parameters have been estimated in the tracer test and CMC-pressure step test with curve-fitting technique. These parameters have been then used to develop the nano-particle transport and retention in the sand-filled tank. In the same way as the simulation of column experiment, Equations 2.62, 2.63 and 2.64 have been used for the numerical formulation.

4.3.7 Results

4.3.7.1 Case 1: Parameter estimation from tracer test in sand-filled tank

ENP transport in the tank is mainly governed by parameters like permeability porosity and viscosity. Permeability of the sand layers has been already known from experimental data (Reischer, 2020) but porosity was not known. It is important to mention that the whole permeability and porosity of the tank system is a combination of these properties in the sand and in the gravel.

After several trial-and-error testing, two best fitting curves each for: (1) the pressure velocity step test, and (2) the breakthrough curve of the tracer have been generated. The estimated values from the best fitting curve are shown in Table 4-4.

The model results also provide the pathways (*streamlines*) predicted to be followed by the tracer during the injection (Figure 4-13). The symmetric distribution of these streamlines coming out from the well slots indicates a steady state flow of fluid in all directions. The model predicts that the flow of water has not only been limited to the longitudinal direction of the injected fluid velocity. The vertically upward and downward motion of the water leads to advection of tracer in transverse direction. The model estimates a tracer profile after 6 minutes as illustrated by the color gradient in the streamlines. The result predicts a tracer transport of 27 centimeters from the well after 6 minutes of fluid injection. The maximum recovery of tracer after 6 minutes is 55% at 20 cm from the well center. The tracer concentration in the model domain remains zero in the radius of 5 cm from the tank center beyond which the concentration increases. Due to post-flushing with pure water, the model predicts no tracer in the vicinity of the well screen. The rise of predicted tracer after 6 minutes is maintained for a radial distance of 5 cm to 27 cm (Figure 4-13).

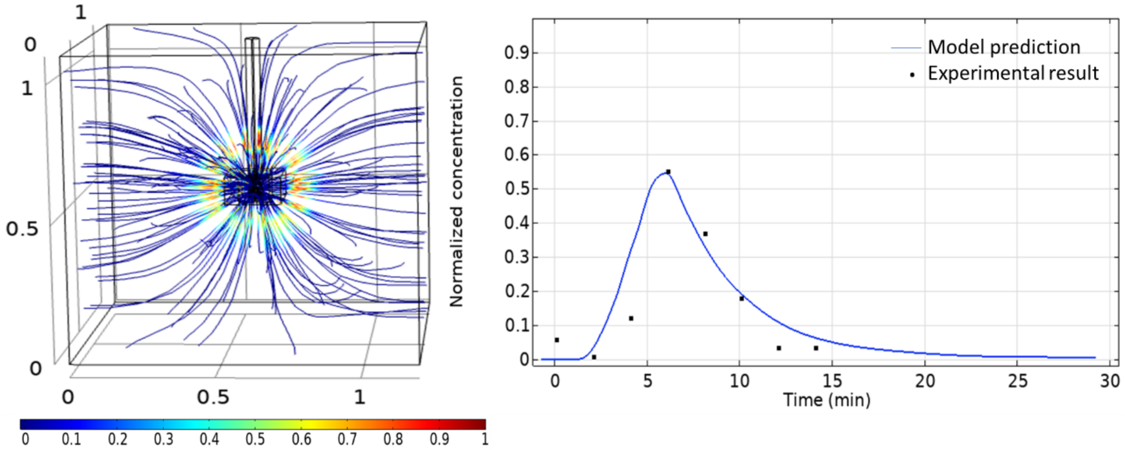

***Figure 4-13**: Streamlines of fluid flow predicted during the tracer injection in the tank experiment (left). Best-fitting predicted curve matching with the experimental data for tracer breakthrough curve at 20 cm from the well (right). Experimental data are provided by collaborators under the framework of Metal-Aid project (Reischer, 2020).*

The predicted curve shows a reasonably good match with the experimental result. The parameter estimation from the best-fitting curve determines a porosity of 0.33 for the tank material. Additionally, the model predicts a porosity of 0.44 and permeability of 6.5×10^{-9} m^2 for the gravel in the vicinity of the well screen. The comparatively sharp rise and fall of tracer breakthrough curve means a lower dispersivity compared to the particle transport in column scale. A longitudinal dispersivity of 0.005 m leads to best fitting curve for trace injection. This is 5.4 times lower than the dispersivity determined in column scale injection. The difference in the dispersivity can be attributed to the slightly finer sand used in the tank set-up compared to that of the column set-up. For the dispersion in the transverse direction, the model estimates a transverse dispersivity of 0.001 m.

Table 4-4*: Estimation of the hydraulic parameters in the tank experiment from best-fitting of pressure and breakthrough curves.*

Parameters	Estimated Value
Porosity of sand in the tank	0.33
Porosity of gravel in vicinity of the well	0.44
Longitudinal dispersivity of the sand	0.005 m
Transversal dispersivity of the sand	0.001 m

4.3.7.2 Case 2: Estimation of viscosity of CMC-bearing fluid from CMC injection experiments

Once the hydraulic parameter for the sand-filled tank have been estimated, a steady-state fluid flow field can be drawn using these parameters (Figure 4-14a). These flow field has been generated considered an inlet velocity of 0.0158 m·s^{-1} at each of the 60 well slots. In Figure 4-14, the variation in the velocity is indicated by red arrows coming out from the well slots. The length of the arrows is proportional to the velocity magnitude, whereas the direction of the arrows indicates the flow direction. In Figure 4-14b, an enlarged view of these arrows is provided; the decrease in the size of the arrows away from the well screen indicates a decrease in the flow speed. A quantitative analysis of velocity has been done in section 4.3.7.3.

A best-fitting curve of the pressure variation at the middle of well screen has been also calculated by the model. The blue point in Figure 4-14b shows the middle part of the well screen at which the pressure variation has been studied. The model predicts that, with the flow rate increase, the pressure increases in a non-linear order. The model estimates an equivalent water pressure head of 125 cm for flow rate of 544 ml·min^{-1}, 140.5 cm for flow rate of 609.8 ml·min^{-1}, 156 cm for flow rate of 683 ml·min^{-1}, and lastly, 172 cm for flow rate of 760 ml·min-1. These estimates are in close agreement with the step variance of pressure from the experimental data as shown in Figure 4-14c.

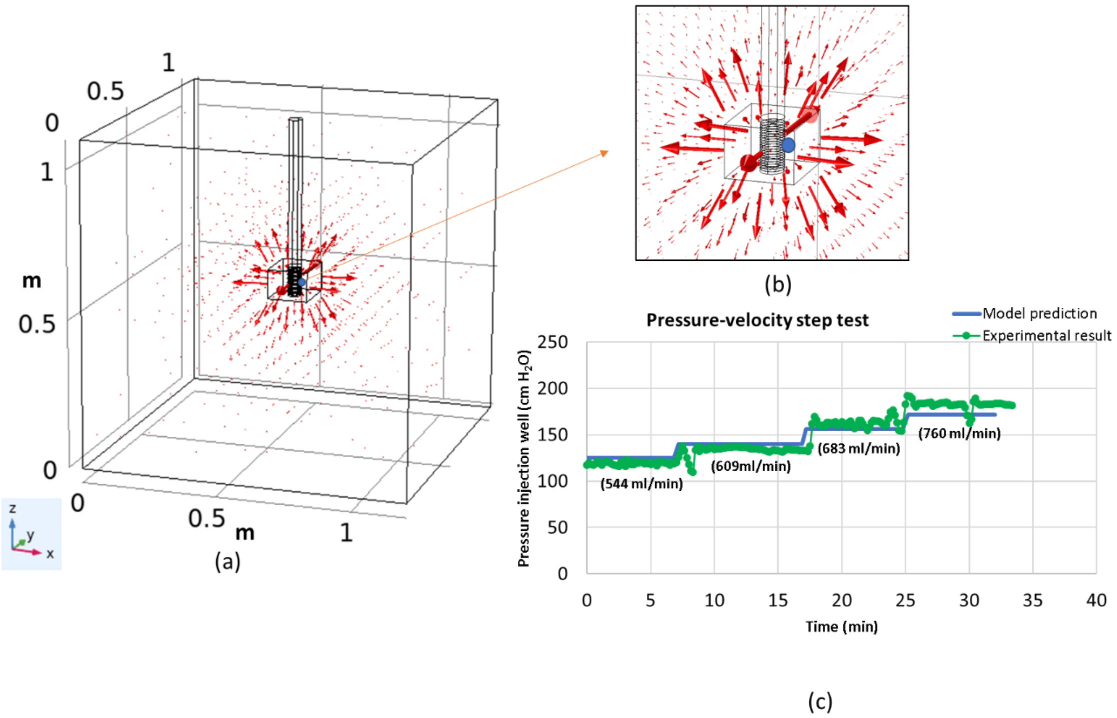
(a)
(b)
(c)

__Figure 4-14__: (a) Model prediction for the velocity field in the model domain for CMC injection. The red arrows represent the fluid flow direction and its size is proportional to the Darcy velocity. (b) Enlarged image of the velocity field at the center of the well. The blue dot shows the point for which model estimates the pressure generated due to tank injection. (c) The best-fitting curve of pressure predicted by model matching with the experimental data (Reischer 2020).

Pressure data has been estimated after a steady state flow. With the best-fitting curve (represented by blue curve in Figure 4-14c), the model estimates a viscosity of 0.0082 Pa·s for 5 $Kg_{cmc}{\cdot}m^{-3}{}_{water}$ of CMC. The result implies 8.2 times higher viscosity compared to the pure water. The estimated velocity falls in the range of viscosity for CMC 250K found in previous research work from literature (Li et al., 2015). As the viscosity for a particular CMC concentration is known, Equation 4.1 has been applied to estimate the varying viscosity as a function of CMC concentration. Figure 4-15 shows the viscosity of the fluid with CMC concentration having an exponentially increasing trend.

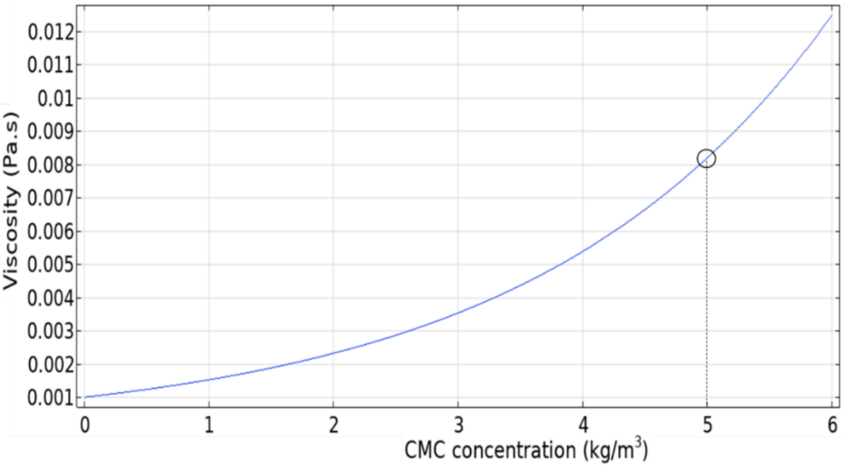

__Figure 4-15__: Plot for viscosity of the CMC-water fluid as a function of CMC concentration obtained using Equation 4.1.

4.3.7.3 Case 3: Modelling of ENP injection in the tank experiment

The injection of fluid with CMC-sZVi in the sand-filled tank experiment is numerically simulated in three stages following an integrated approach. To simulate the event of CMC injection prior to CMC-sZVi injection, a pre-flushing model has been developed (Stage I) from time (t) = 0 minute to time (t) = 45 minutes. In the second stage (Stage II), the injection of CMC-sZVi fluid has been studied with the help of the numerical formulation described in Section 4.2.1 for nanoparticle injection in a sand-filled tank. The model output for the end of Stage I has been used as the initial condition for Stage II. The time duration for Stage II is from time (t) =45 minutes to time (t) = 115 minutes. Finally, the simulation for post-flushing with CMC solution in the tank experiment has been simulated in the Stage III. The model output at the end of the Stage II has been used as the initial condition for the Stage III. The time from (t) = 115 minutes to time (t) = 160 minutes has been considered for the post-flushing event. The continuous dynamics of CMC transport and hydraulic dynamics has been studied combining all the stages.

Transport and hydraulic dynamics of CMC solution in the model domain

The CMC injection in the experiment has been used for pre-flushing with no sZVi (Stage I), sZVi injection along with CMC for optimized transport (Stage II) and post-flushing with only CMC (Stage III). CMC has been, therefore, injected in all three stages in the sand-filled tank. Figure 4-16 shows the model prediction of the streamlines for the CMC flow the time at 45 minutes (end of stage I) and 115 minutes after injection (end of stage II). The predicted flow behavior demonstrated by streamlines is similar to the tracer transport, when predicted fluid flow in both transverse and longitudinal directions with respect to well screen. The color legend in Figure 4-16a shows the model prediction for CMC transport after 45 minutes of fluid injection. The model estimates CMC transport of 35 cm in longitudinal direction and 36 centimeter in vertically up direction. The predicted CMC transport in all direction gives rise to an ellipsoidal plume geometry of CMC. The CMC transport behavior is reflected in increase of calculated viscosity shown by different colors in Figure 4-16c. The model predicts a maximum viscosity of 0.0082 Pa·s in a radius of 14 centimeters after 45 minutes of fluid injection. For radial distances between 14 cm to 35 cm, the model predicts a CMC concentration lower than that of inlet CMC, and, thus, the estimated viscosity ranges from 0.001 Pa·s to 0.0082 Pa·s. Beyond 35 centimeters from the tank center, the model predicts water free of CMC and the viscosity is maintained at 0.001 Pa·s. The same nature of trend is observed after 115 minutes of fluid injection, as shown in Figure 4-16b. An estimated transport of 50 cm of CMC in radial distance gives rise to the viscosity profile shown in Figure 4-16d. The viscosity is estimated to be 0.0082 Pa·s for the radial distance of 21 cm, after which a transition of viscosity occurs for the radial distance of 50 centimeters.

The streamlines in Figure 4-16 shows the water flowing out from the inlet and spreading in all directions. The streamlines in the Figure 4-16 shows a constant flow direction over the time irrespective of the viscosity increase in the model domain. The model predicts a steady-state velocity direction; Darcy velocity has been estimated along the red line shown in Figure 4-17a (Figure 4-17b). This plot shows that the maximum Darcy velocity is 0.0135 m·s^{-1} with a hyper-exponential decline in velocity with radial distance. The enlarged image of the velocity profile shows the model prediction for the velocity variation in the gravel sand. The velocity magnitude is reduced by 100 times in the first 5 cm of the radial distance. However, there is negligible difference in the estimated velocity magnitude for the time t =0 min (onset of pre-flushing stage), t = 45 min (end of CMC pre-flushing; onset of CMC-sZVi injection), t =115 min (end of CMC-sZVi injection; onset of CMC post-flushing), and t = 160 min (end of CMC post-flushing). Therefore, the result indicates that although spatial velocity change is significant, temporal change in velocity predicted by the model is negligible, i.e., a steady state flow is expected for the whole duration of fluid injection.

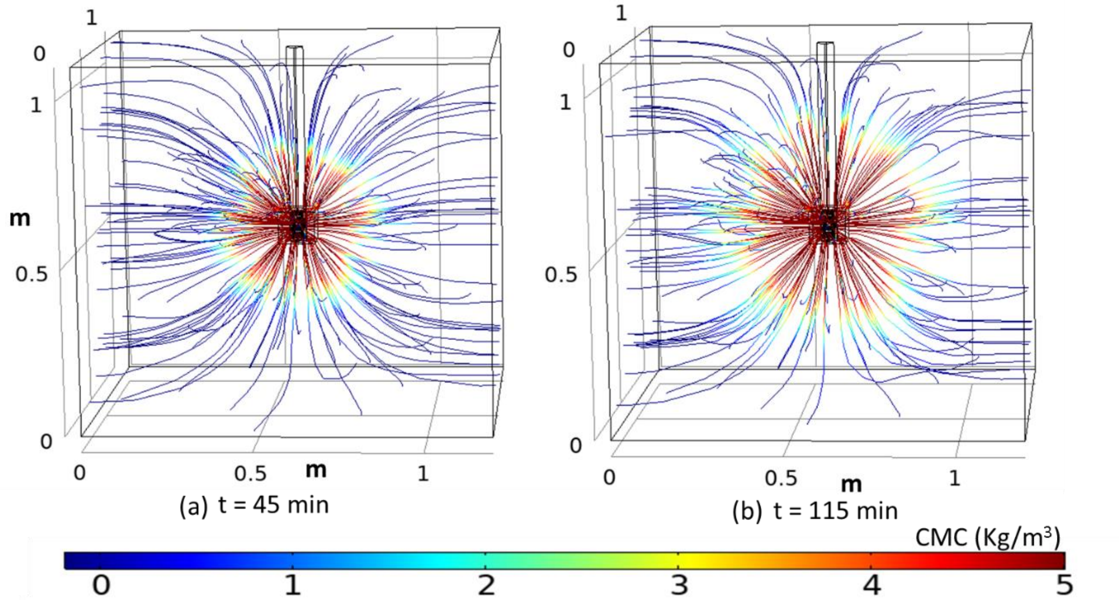

(a) t = 45 min

(b) t = 115 min

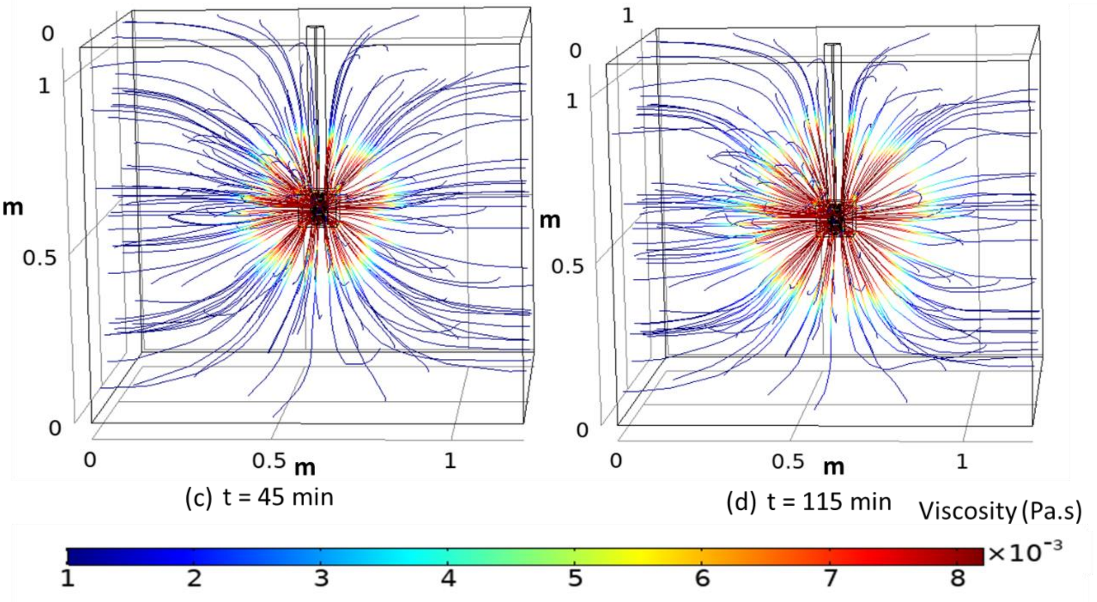

(c) t = 45 min

(d) t = 115 min

Figure 4-16*: Plots show a steady state streamline of simulated fluid for nano-particle injection in the tank. Model prediction for CMC concentration after (a) 45 minutes (i.e., the beginning of nano-particle injection in the model domain) and (b) 115 minutes (i.e., termination of nano-particle injection). Model estimation for CMC concentration dependent viscosity after (c) 45 minutes and (d) 115 minutes.*

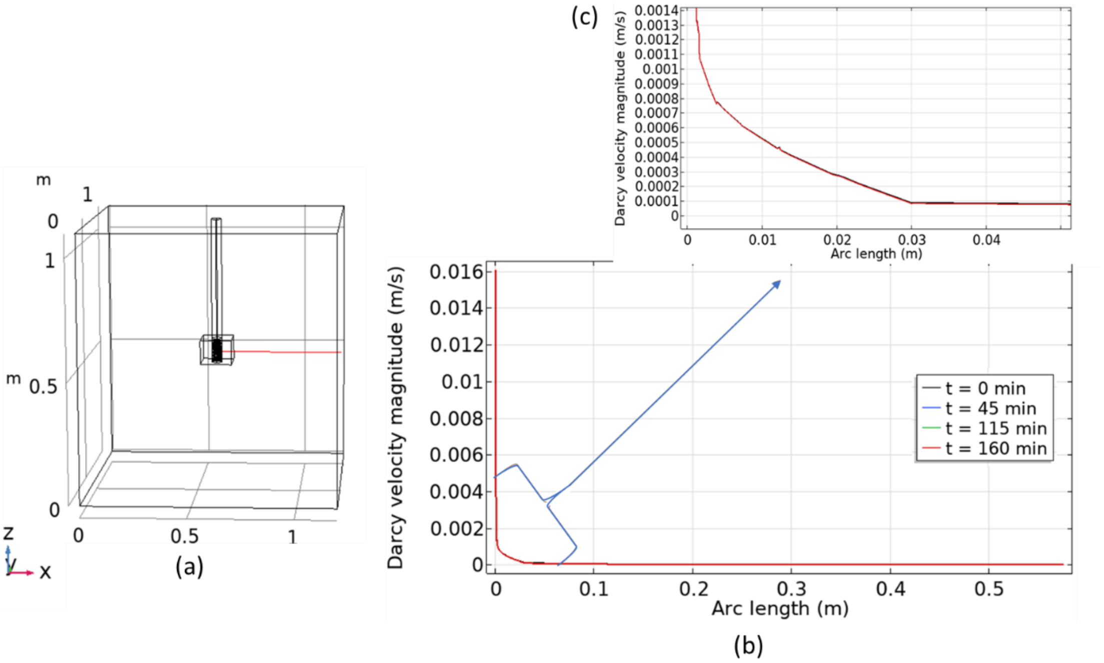

__Figure 4-17__: (a) Darcy velocity estimated along the red line in the model domain, (b) model prediction for Darcy velocity magnitude along the red line for times (t) = 0, 45, 115 and 160 minutes. (c) Enlarged plot focusing on the estimated Darcy velocity magnitude for the first 5 cm from the well.

While maintaining a steady state of flow rate for injection of fluid in the sand-filled tank, the fluid pressure in the tank is expected to vary with time. Figure 4-18 shows the calculated pressure profile taken along the XZ plane for the saturated water at three times: (t) = 0 minutes, t = 45 minutes and t =115 minutes, respectively. At the onset of CMC solution injection (Stage I) marked by t =0 minutes, the model shows that water in the pores of the sand is at hydrostatic condition with the hydraulic head of 65 cm measured from the bottom (Figure 4-18b). This is same as the initial condition set for simulating the injection of fluids in the tank. At t = 45 min (Stage II; Onset of CMC-sZVi injection), the model estimates an increase in pressure at the vicinity of the well screen (Figure 4-18c). This increase in pressure reflects an increase in the hydraulic head of 74 cm, at the well center. Finally, at the end of nano-particle injection simulation at t =115 min (stage III), the model predicts the pressure increase reflected in the hydraulic head rise of 0.77 m at the well center (Figure 4-18d).

The injected fluid pressure calculated at one of the well slots for CMC-sZVi injection during Stage II (represented by solid orange line) and in the CMC post-flushing period during Stage III (represented by solid blue lines) are shown in Figure 4-19. The model prediction has been compared with the experimental result (represented by orange and blue dotted lines). The comparison yields a good match between the model prediction and experimental result. The model predicts 1053 cm of equivalent water pressure head due to injected fluid pressure at the onset of injection exercise, which is 23 cm higher than the experimental result. The model prediction has a more gradual increase in pressure compared to the experimental result. At the end of post-flushing event, the model prediction for fluid pressure becomes equal to the experimental result with and estimation of 1174 cm of equivalent water pressure head. This reasonable agreement strongly suggests that the model is successfully able to numerically reproduce the hydraulic dynamics of the injection experiment.

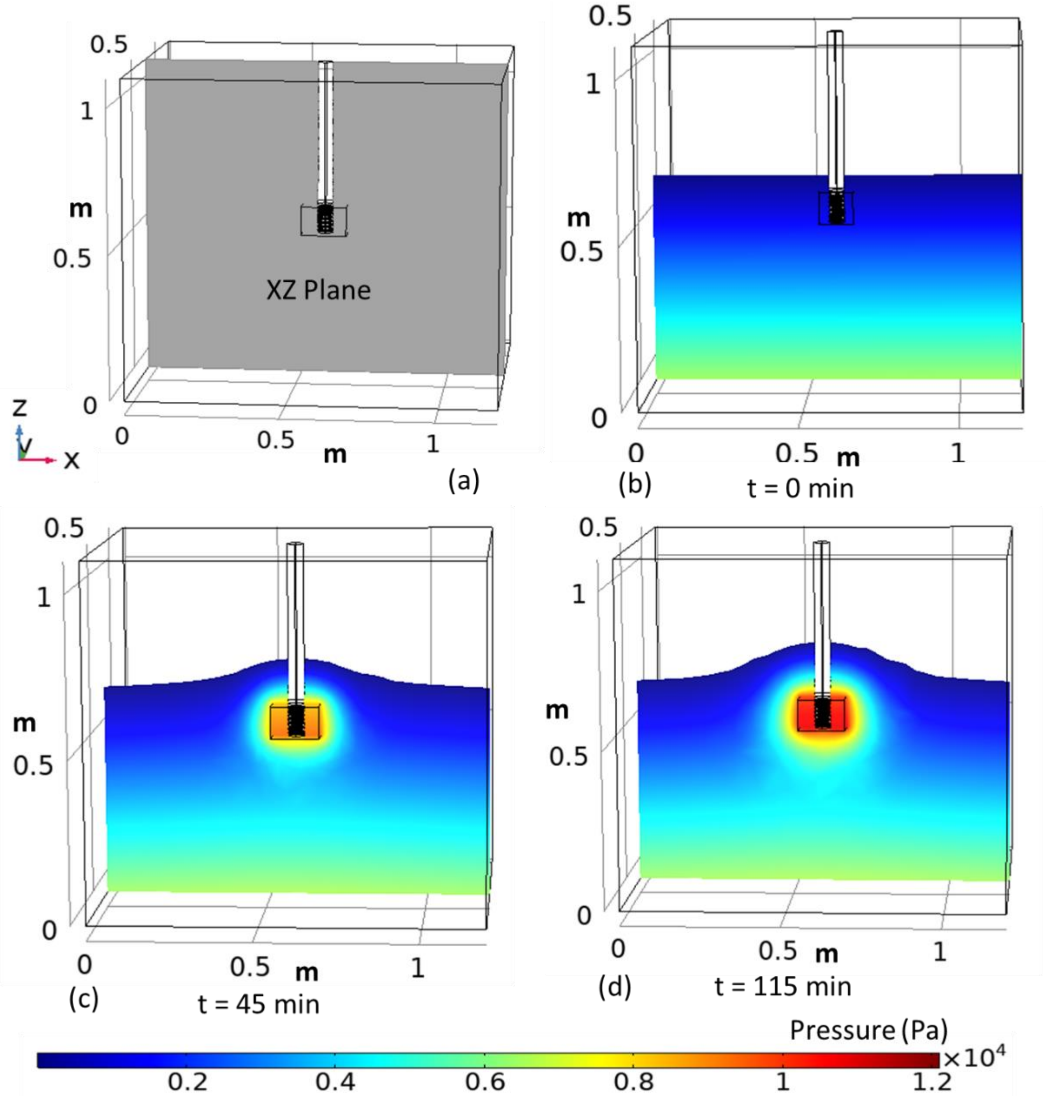

Figure 4-18: (a) XZ plane in the model domain along which the pressure predicted by the model. The model prediction for fluid pressure along the XY plane at time equal to (b) 0 minutes (c) 45 minutes (d) 115 minutes exhibits a continuous increasing pattern as a function of time.

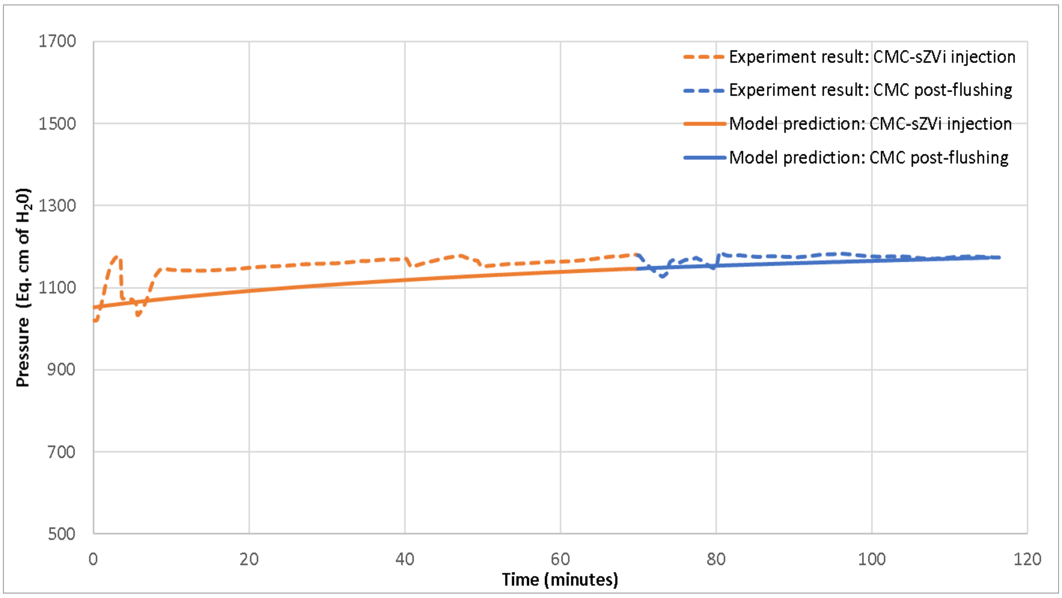

Figure 4-19 Model prediction of the fluid pressure at the well slots during the CMC-sZVi injection (represented by the solid orange curve) and post-flushing with CMC solution (represented by solid blue curve). The model prediction is in close agreement with the fluid pressure measured in the experimental setup (represented by dotted orange curve for CMC-sZVi injection period and dotted blue line for CMC-post-flushing period).

CMC-sZVi injection stage (Stage II): Prediction of ENPs transport in the tank after injection

After 45 minutes of pre-injection with CMC solution, a water solution loaded with ENPs was injected in the sand-filled tank for 70 minutes. The model prediction of the normalized sZVi concentration profile along the streamline for aqueous ENPs at time t =115 minutes (i.e., at the onset of injection) is shown in Figure 4-20a. The model predicts nano-particle transport extending up to 20 cm radially from the well screen, with a maximum concentration of 0.47 $\mathrm{Kg_{particle}{\cdot}m^{-3}{}_{water}}$ just adjacent to the well screen. This result points to a significant mass transfer from mobile nano-particles to settled nano-particles. Such mass transfer is more prominent when sZVi injection is stopped. After 160 minutes, the model prediction shows negligible sZVi concentration remaining in the fluid phase with a maximum value of 0.02 $\mathrm{Kg_{particle}{\cdot}m^{-3}{}_{water}}$ occurring at a radial distance of 8 cm from the well screen (Figure 4-20b). Such low amount can be explained if ripening mechanism of retention is predominant with progress of the injection, resulting in negligible concentration of particle in the aqueous phase at later times.

CMC-sZVi injection stage (stage II): Comparison of model result with experimental data

The model prediction for breakthrough curve and retention profile are compared with that of the provided experimental result to derive relevant insights. Figure 4-21b and Figure 4-21c shows the predicted and experimental breakthrough curves at points P1 and P2 in the tank shown in the Figure 4-21a. The time axis in the breakthrough curve represents 45 minutes of pre-flushing with CMC, 70 minutes of particle injection and 45 minutes of post-flushing, resulting in total time of 160 minutes. The breakthrough curve at P1 (Figure 4-21b) shows that the model predicts the arrival time of effluent sZVi to be 52 minutes, which is 7 minutes after their injection, which is same as measured in the experiment.

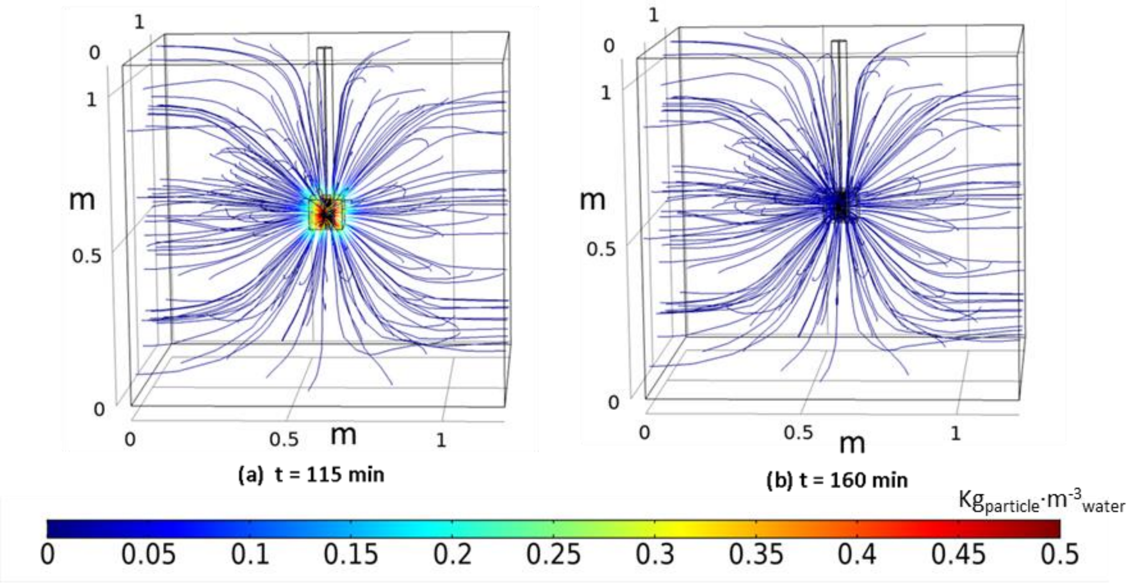

(a) t = 115 min

(b) t = 160 min

Figure 4-20*: Model prediction of the concentration of mobile ENPs on the simulated streamlines of fluid flow for (a) time = 115 min (i.e., end of the nano-particle injection), and (b) time = 160 min (end of the post-flushing with CMC).*

After the arrival time, the model predicts a gradual decrease in the concentration of mobile sZVi, in contrast to the experimental results which show a gradual increase of mobile sZVi after the arrival time. These results mean that the deposition predicted by the model is higher than the experimental result. This is also supported by the model prediction of a negligible effluent concertation at point P2, as compared to a maximum of 0.1 of normalized sZVi concentration observed in the experiment.

The comparison between experimental and modelled mobility of ENPs suggests that a relatively lower attachment coefficient controlling the deposition is observed in the tank experiment. This attachment coefficient is spatially and temporally variable. Also, the net effect of the variable attachment process in the experimental setting is smaller compared to the constant attachment coefficient used for model domain. A complex role of fluid velocity in governing the dynamic attachment and detachment rate is suggested.

CMC-sZVi injection stage (stage II): Prediction of the Radius of Influence (ROI)

The distribution of settled sZVi nano-particles in the model domain after the end of the post-flushing stage (time = 160 minutes) has been analyzed. The model prediction for the different iso-surfaces of settled particles in the tank domain is shown in Figure 4-22. The modelled plume of settled ENPs resembles a nearly spherical geometry extending up to 12 cm in horizontal direction and 9.5 cm in vertical direction for 0.5 $kg_{particle}\cdot m^{-3}$ iso-surface. This result indicates the formation of ENP iso-surfaces not limited only in the radial direction but also in the transverse direction. The model predicts the highest concentration of ENP of 12 $kg_{particle}\cdot m^{-3}$ in the vicinity of the well as shown in the enlarged image (Figure 4-22). Also, the iso-surface of sZVi having value higher than 2 $kg_{particle}\cdot m^{-3}$ is limited to a range of 5 cm from the well. The distribution of the concentration shows a non-linear pattern along the radial length. This is consistent with the formulation used for simulating ripening and straining mechanism.

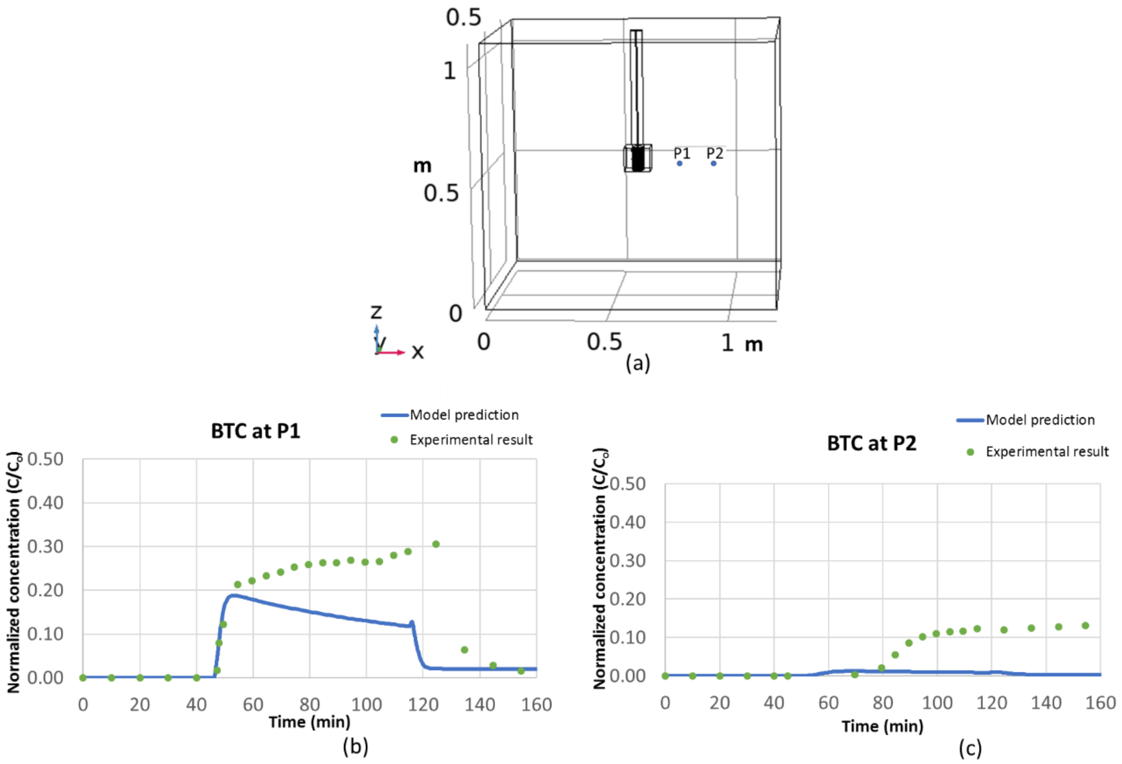

***Figure 4-21**: Comparison between modelled and experimental concentration of mobile ENPs in the tank experiment in two points (Point P1 and P2; location in (a)); (b) point P1 and (c) point P2.*

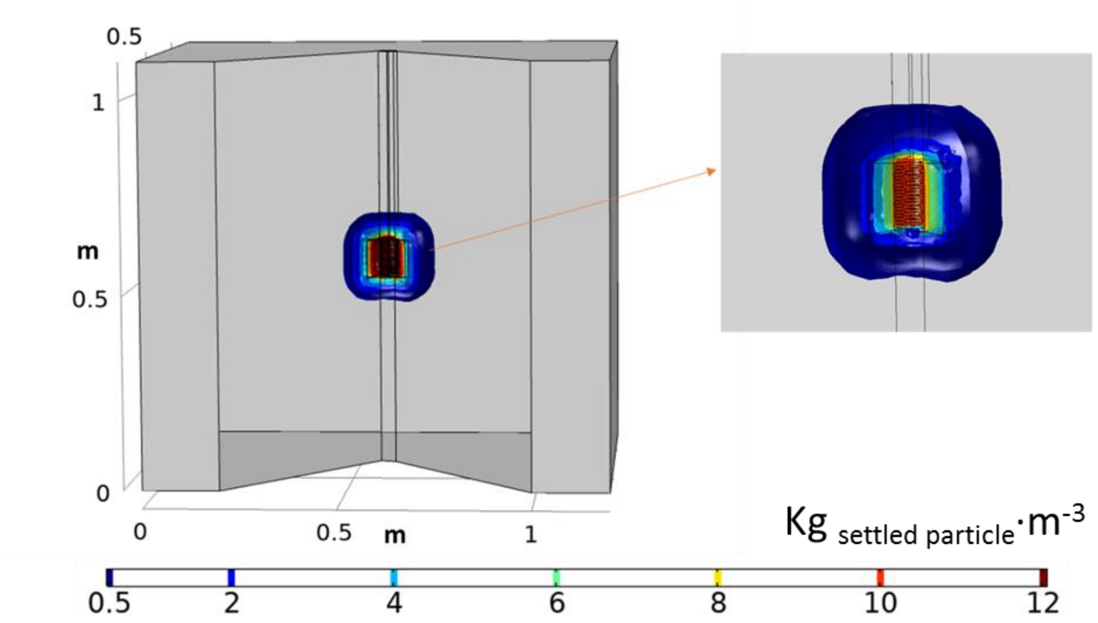

***Figure 4-22**: Model prediction for the iso-surface of the concentration of settled particles in the tank sand (left plot). An enlarged view of the same plot shows a localized deposition of particles in the vicinity of the well screen (right plot).*

For the estimation of the Radius of Influence (ROI), a 1D plot has been built along the red line shown in Figure 4-23a. A complex non-linear retention profile is predicted at different times (Figure 4-23b). This plot also gives a predictive insight for Radius of Influence of ENPs, measured as the distance from the well center to the end of ENPs settlement. In this work, an arbitrary concentration of 0.02 Kg$_{particle}$·m^{-3} has been considered as the limit of ROI. Below this concentration, it is considered that the remediation of sZVi is no longer efficient. In the first 45 minutes of CMC solution injection without nano-particles (Stage I), the model correctly predicts no settlement of ENPs (blue curve in Figure 4-23). After 70 min of fluid injection (with 25 minutes of ENP injection), the predicted ROI is 2 cm from the well screen. After the completion of CMC-sZVi injection (time =115 minutes), the model prediction shows the ROI to extend up to 15 cm. The final retention profile after the post-flushing stage with CMC solution (time = 160 minutes) has been represented by a cyan-colored curve. This cyan curve indicates lower retention compared to the red curve, and this suggests a decreasing retention of the sZVi within the 4-centimeter radius from the well. The decreasing retention of sZVi in post-flushing phase can be attributed to the detachment of the retained particle, since the detachment mechanism results in a reverse mass transfer of ENPs from immobile to mobile state resulting in a lower retained sZVi after the post-flushing with CMC.

The comparison between modelled and measured concentration shows that the model predicts 4 times higher retained sZVi near the well screen compared to the experimental results. This mismatch can be attributed to use of a constant interaction coefficient in the numerical formulation. In reality, the interaction coefficients varies as a function of Darcy velocity of the fluid. As the simplified interaction coefficients have been used in model development, the model overestimates the concentration of retained sZVi.

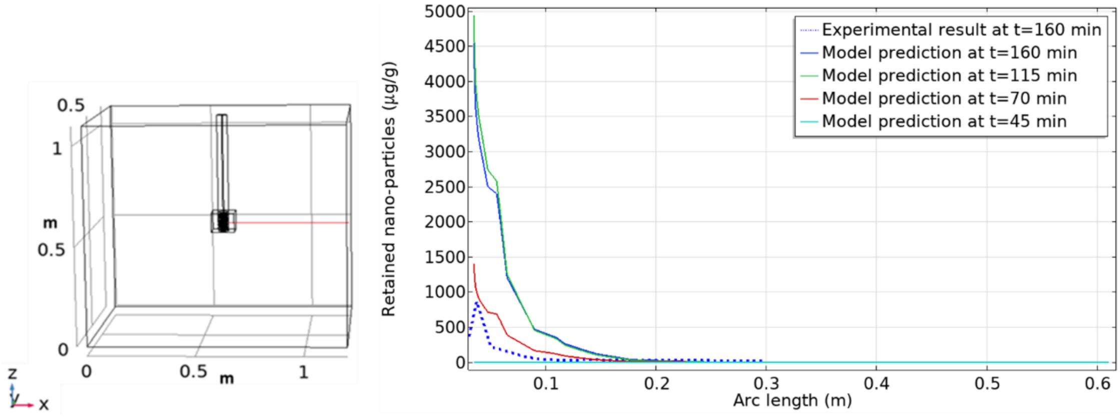

(a) (b)

***Figure 4-23**: Comparison between modelled and measured ENPs retention in the injection experiment in the tank. (a) The red line in the model domain represents the line along which the retained particle is analyzed. (b) Model prediction for concentration of retained particle for times (t) = 45 min, 70 min, 115 min, 160 min, and comparison with retained particles observed after end of the injection (time = 160 minutes).*

CMC-sZVi injection stage (stage II): Transfer of ENPs from mobile to immobile states

The transfer of ENPs between the aqueous phase (mobile) and mineral phase (immobile) has been analyzed. In Figure 4-24, the blue line represents the total injected mass in the tank. A linear increase in the total mass can be explained by a constant flux of sZVi from the well slots of tank. At the end of nano-particle injection after 115 minutes, the model predicts a total of 20.08 grams of ENPs injected in the tank. Out of this 20.08 grams of sZVi, the model predicts 19.9 grams of total retained sZVi remaining at the end of 160 minute (as shown by the green curve), which represents a deposition of 99.1% of the particles after the 45 minutes of post-flushing with CMC. The non-linear shape of the green curve highlights the complex formulation for the deposition of the sZVi implemented in the model. Out of these 19.9 grams, the deposited particle by ripening has been estimated to be 8.4 grams at the end of 115 minutes, as shown by the red curve. In the post-flushing, the model predicts a minor decline in ENPs retained by ripening from 8.4 grams to 7.8 grams.

The cyan curve in Figure 4-24 represents the sZVi deposition by straining, showing a relatively gradual but non-linear increase in the sZVi mass with time. A total of 12.1 grams of sZVi deposited by straining has been predicted by the model. This curve rises rapidly compared to the deposition in ripening mechanism represented by the red curve. Also, it shows an increasing sZVi deposition in the post flushing phase, unlike that for the ripening mechanism, even though the total mass of settled particle remains the same. This suggests that the sZVi released from ripening is later attached to the straining site.

Lastly, the pink curve shows the model prediction for mobile ENPs in the aqueous phase. It shows a maximum of 0.9 grams of mobile nano-particles estimated after 17 minutes of nano-particle injection. This suggests that the transport dominated for the first 17 minutes, and, afterwards, the deposition processes became dominant.

In the post-flushing phase, the model predicts a rapid decline of mobile ENPs down to 0.1 gram. After 20 minutes of post-flushing, the simulated mass of mobile sZVi becomes constant. This constant concentration of mobile sZVi highlights the steady state obtained for the attachment and detachment process in the tank.

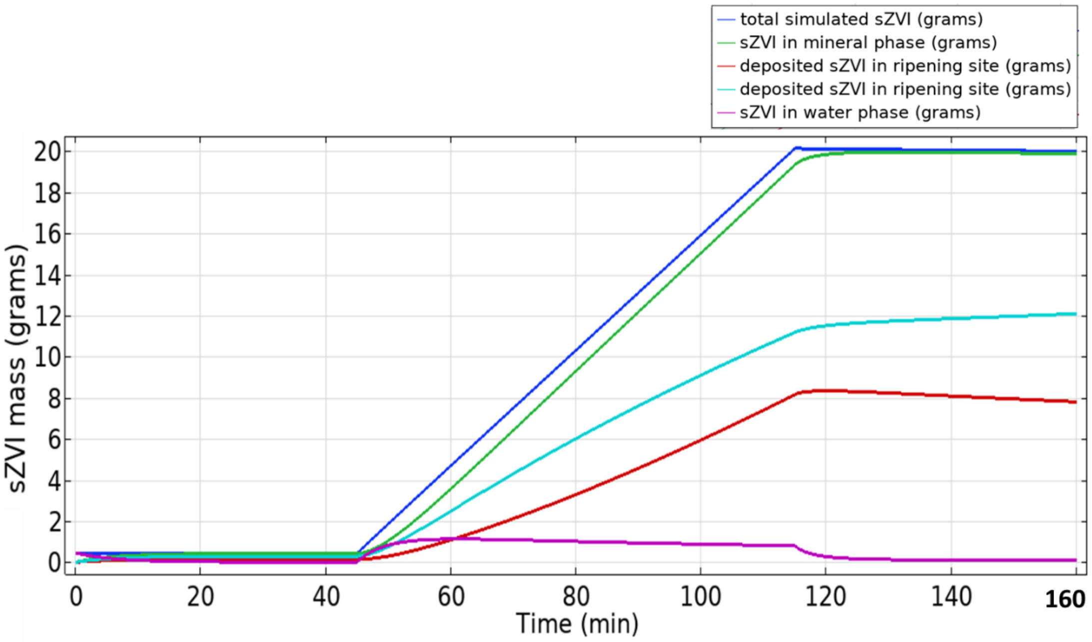

***Figure 4-24**: Model prediction of the mobility of ENPs in the tank sand; total injected mass: blue curve); total deposited mass: green curve); total mass retained by ripening mechanism: red curve; total mass retained by straining mechanism: cyan curve; and total mass in the mobile phase: pink curve.*

CMC-sZVi injection stage (stage II): Porosity reduction

Porosity and permeability change due to nano-particle injection can influence the transport and retention behavior of ENPs. The effect of the porosity and permeability variation on nano-particle mobility have not been implemented in the model for the simplification of the model development. However, the change in porosity during the CMC-sZVi injection has been studied to understand the extent of clogging due to reduction in porosity. The model prediction of the iso-surface of porosity change after 160 minutes of Stage II is plot in Figure 4-25, and shows a negligible reduction in the porosity of the tank. The maximum porosity decrease predicted by model is in the order of 1×10^{-4}, just next to the well screen. Therefore, the model clearly indicates that no significant porosity reduction can be expected in this kind of experiments. This can be attributed to injection of a relativity small quantity of ENPs.

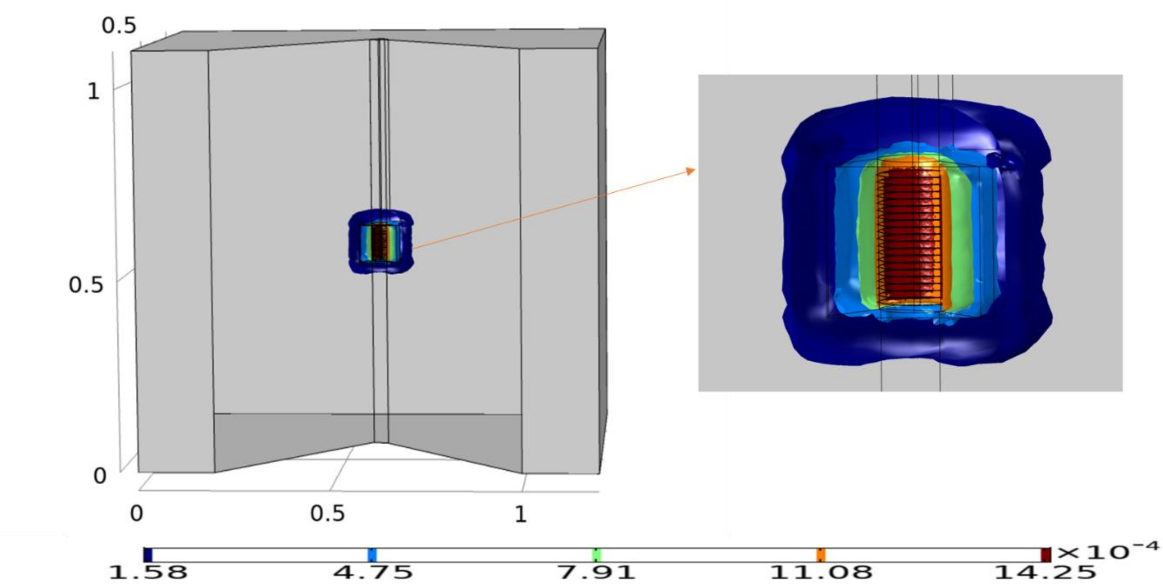

Figure 4-25: *Model prediction for the change in porosity at the end of the Stage II. An enlarged version shows an estimated minimal change in porosity localized in the vicinity of the well screen.*

4.3.8 Discussion

A central aspect of the use of numerical models is the formulation on which the model is based on. With a verified formulation implemented, this model can be used to assess real cases of polluted aquifers. In this work, the numerical formulation has been correctly verified with a benchmark exercise.

Secondly, the model must be fed with hydraulic and ENP mobility parameters from experiments under similar conditions, such as sand-filled columns. The modelling of these experiments suggests that ripening and straining are the two main mechanisms governing the mobility of sZVi in the sand. The existence of these mechanisms can be the consequence of the magnetic nature of the particle that leads to aggregation. The aggregated cluster in the porous medium helps the occurrence of ripening, while the aggregation of mobile particles promotes straining. These mechanisms result in a higher retention, and thus, a limited mobility.

The modelling of sand column experiments also shows that a higher flow rate and lower concentration of injected sZVi promotes a decrease in the attachment whereas the detachment increases. The sensitivity test has been further performed to study the uncertainty derived from the best-fitting curve of the column experiment (Appendix B). The sensitivity analysis shows that the transport and retention characteristics are highly sensitive to the multiplier coefficient and exponential coefficients for both ripening and straining. The transport and retention dynamics of sZVi in the sand are relatively less sensitive to the attachment and detachment rate. Therefore, the result indicates that the uncertainty related to the multiplier and exponential coefficients are relatively lower compared to the attachment and detachment coefficients.

The implementation of the data from column experiments in tank experiments allow a better comprehension of the mobility of the injected ENPs at larger scales. The model calculation of this kind of experiments shows that the pressure in the tank experiment builds up while the velocity is kept at steady state. The increase in pressure can be attributed to both the change in viscosity of the fluid as well as the effect of clogging the periphery of the well screen. The model result incorporates the effect of viscosity, but due to the uncertainty with the data, the clogging model effect is not included. Nevertheless, the fluid pressure predicted by the model resembles the experimental result. The error in the model prediction is only 2% at the beginning of the experiment and the error decreases as the injection experiment proceeds. Therefore, the model result indicates that the effect of clogging is much lower compared to the effect of the viscosity variation of the fluid. This is also supported by the model result indicating negligible decrease in porosity of the sand where sZVi is retained. The pressure buildup at the well screen observed both in the model and experimental setup, ensured a steady state Darcy velocity of the injected fluid. Thus, the model exercise implies that for a higher transport of particle in the field, a constant velocity dependent nano-particle injection could mitigate the effect of viscosity variation on particle transport.

The simulation results for the transport and retention of sand-filled tank does not fully match with the experimental data (Figure 4-21 & Figure 4-23). This mismatch is the consequence of the use of constant coefficients that governs the transport and retention of sZVi in the saturated sand. An important aspect in building field scale model is to determine these particle-mineral interaction parameters as a function of fluid velocity. The previous studies have conducted multiple column experiments to estimate the attachment rate by inverse modeling for each corresponding flow rate (Velimirovic et al., 2020; Bianco et al., 2016). In these studies, the *T & E equation* (Tufenkji and Elimelech, 2004) has been used to determine the value of single-collector efficiency. Once this value is determined, the particle-collector attachment efficiency can be determined using Equation 4.2 (Derived from Equation 2.57).

$$\alpha = \frac{2d_c k_{att}}{(1-\theta)v\eta_o} \qquad \text{(eq. 4.2)}$$

Where d_c is the diameter of a single grain, θ is the effective bed porosity and $\alpha\ and\ \eta_o$ are particle-collector attachment efficiency and single-collector contact efficiency.

As the value of Particle-Collector attachment efficiency is derived, the model can be developed using the attachment rate as a function of flow velocity given by Equation 2.57. Previous studies in the literature (Krol et al., 2013; Tosco et al., 2014) considered a constant Particle-Collector attachment efficiency for the ENP injection. He et al. (2009) reported a varying particle attachment efficiency for CMC-sZVi particles if the flow rate exceeds a certain value. The Particle-Collector attachment efficiency can be determined by plotting k_{att} versus $v\eta_o$.

The velocity dependent attachment rate is less reported in the literature, especially when the mobility of ENPs is governed by ripening and straining mechanisms. This investigation becomes increasingly complicated due to the uncertainty of the multiplier coefficient of ripening and exponential coefficient of both mechanisms. Tosco et al. (2014) conducted several column experiments to determine the attachment coefficient for carbon based ENPs. The deposition mechanism in their study was characterized by blocking process and a multiplier coefficient is considered to be constant for all column injection experiments. However, it is worth examining if such assumption is valid for ripening and straining mechanism of sZVi. The uncertainty especially with the coefficient for ripening gets complicated as the total particle-particle interaction energy changes with time (Raychoudhury, 2011).

For a further research work, a rational approach for determining the nature of these coefficient can be verified by taking a constant initial multiplier and exponential coefficient to derive attachment coefficients from several column experiments. The detachment coefficient as a function of velocity can be similarly derived by using equation 4.3 (Tosco et al., 2014):

$$k_{d_i} = C_i \mu v \qquad \text{(eq. 4.3)}$$

Where k_{d_i} is the detachment rate for each site (ripening and straining), μ is the viscosity of the fluid in porous media, v is the flow rate, and C_i is the empirical constant.

In the following step, the model prediction for nano-particle injection in a tank sand can be better developed. If the model prediction matches with the column result, the hypothesis of constant multiplier and exponential coefficient holds true. Otherwise, the discrepancy in model and experimental result would hint that these rates are not constant temporally or spatially (or both).

4.4 Conclusions

The use of numerical models can be very valuable when planning the remediation of polluted groundwater. With the intention of developing such numerical models, the aim of the modeling exercises in this Chapter 4 has been four-fold: (1) the development of a numerical formulation for transport and retention of ENPs in an aquifer, (2) the use of inverse model to obtain relevant parameters controlling the mobility of ENPs in a column-scale model, (3) the sensitivity analysis for all these relevant parameters, and (4) the development of 3-Dimensional model for injection of ENPs in a real tank experiment, as the latest stage before modelling real cases of aquifer remediation.

All these objectives have been achieved: (1) the numerical formulation has successfully been implemented on Comsol Multiphysics and validated by comparison with the same model run using the MNMs software. (2) Using the experimental data obtained from experiments in the frame of the Metal-Aid project, an inverse model has been developed with the verified numerical formulation to determine the relevant parameters governing the transport of sZVI in the sand-filled columns. (3) A sensitivity analysis for all these relevant parameters demonstrates the extent of uncertainty associated with each parameter estimated from the literature. Finally

(4), a 3-dimensional model has been developed to numerically assess the nano-particle injection in the tank sand. The models results have been satisfactorily compared with the experimental data with the main deviation in transport and retention profile of the sZVi explained by the lack of velocity dependent attachment and detachment coefficient

4.5 References

Becker, M.D., Wang, Y., Paulsen, J.L., Song, Y.-Q., Abriola, L.M., Pennell, K.D., 2015. In situ measurement and simulation of nano-magnetite mobility in porous media subject to transient salinity. Nanoscale 7, 1047–1057.

Berge, N.D., Ramsburg, C.A., 2009. Oil-in-water emulsions for encapsulated delivery of reactive iron particles. Environmental science & technology 43, 5060–5066.

Bianco, C., Tosco, T., Sethi, R., 2016. A 3-dimensional micro-and nanoparticle transport and filtration model (MNM3D) applied to the migration of carbon-based nanomaterials in porous media. Journal of contaminant hydrology 193, 10–20.

Cullen, E., O'Carroll, D.M., Yanful, E.K., Sleep, B., 2010. Simulation of the subsurface mobility of carbon nanoparticles at the field scale. Advances in water resources 33, 361–371.

Danish, M., Gu, X., Lu, S., Naqvi, M., 2016. Degradation of chlorinated organic solvents in aqueous percarbonate system using zeolite supported nano zero valent iron (Z-nZVI) composite. Environmental science and pollution research 23, 13298–13307.

Digiacomo, F., Mangayayam, M.C., Tobler, D.J., Neumann, T., Held, T., 2019. Transport of sulfidized zerovalent iron particles (sZVI) in porous media: need for a particle stabilizer, in: 15th International Conference on Sustainable Use and Management of Soil, Sediment and Water Resources, 20–24 May 2019. Antwerp, p. 91.

Dunphy Guzman, K.A., Finnegan, M.P., Banfield, J.F., 2006. Influence of surface potential on aggregation and transport of titania nanoparticles. Environmental science & technology 40, 7688–7693.

Garcia, A.N., O'Carroll, D.M., Herrera, J., 2019. Field-Scale Implementation of Sulfidated Nano Zerovalent Iron for In-Situ Remediation.

He, F., Gong, L., Fan, D., Tratnyek, P.G., Lowry, G.V., 2020. Quantifying the efficiency and selectivity of organohalide dechlorination by zerovalent iron. Environmental Science: Processes & Impacts 22, 528–542.

He, F., Zhang, M., Qian, T., Zhao, D., 2009. Transport of carboxymethyl cellulose stabilized iron nanoparticles in porous media: Column experiments and modeling. Journal of colloid and interface science 334, 96–102.

Johnson, R.L., Nurmi, J.T., O'Brien Johnson, G.S., Fan, D., O'Brien Johnson, R.L., Shi, Z., Salter-Blanc, A.J., Tratnyek, P.G., Lowry, G.V., 2013. Field-scale transport and transformation of carboxymethylcellulose-stabilized nano zero-valent iron. Environmental science & technology 47, 1573–1580.

Katzourakis, V.E., Chrysikopoulos, C.V., 2014. Mathematical modeling of colloid and virus cotransport in porous media: Application to experimental data. Advances in water resources 68, 62–73.

Kocur, C.M., O'Carroll, D.M., Sleep, B.E., 2013. Impact of nZVI stability on mobility in porous media. Journal of contaminant hydrology 145, 17–25.

Krol, M.M., Oleniuk, A.J., Kocur, C.M., Sleep, B.E., Bennett, P., Xiong, Z., O'Carroll, D.M., 2013. A field-validated model for in situ transport of polymer-stabilized nZVI and implications for subsurface injection. Environmental science & technology 47, 7332–7340.

Lecoanet, H.F., Bottero, J.-Y., Wiesner, M.R., 2004. Laboratory assessment of the mobility of nanomaterials in porous media. Environmental science & technology 38, 5164–5169.

May, R., Li, Y., 2013. The effects of particle size on the deposition of fluorescent nanoparticles in porous media: Direct observation using laser scanning cytometry. Colloids and surfaces A: Physicochemical and engineering aspects 418, 84–91.

Molnar, I.L., Johnson, W.P., Gerhard, J.I., Willson, C.S., O'Carroll, D.M., 2015. Predicting colloid transport through saturated porous media: A critical review. Water Resources Research 51, 6804–6845.

O'Carroll, D., Sleep, B., Krol, M., Boparai, H., Kocur, C., 2013. Nanoscale zero valent iron and bimetallic particles for contaminated site remediation. Advances in Water Resources 51, 104–122.

Phenrat, T., Kim, H.-J., Fagerlund, F., Illangasekare, T., Tilton, R.D., Lowry, G.V., 2009. Particle size distribution, concentration, and magnetic attraction affect transport of polymer-modified Fe0 nanoparticles in sand columns. Environmental science & technology 43, 5079–5085.

Raychoudhury, T., 2011. Transport of surface-modified iron nanoparticles through model subsurface porous media. McGill University (Canada).

Reischer, M., 2020, A novel direct-push probe for studying mobility of tracers and reactive nanoparticles in the subsurface - A contribution to contaminated site characterization, nanoparticle injection and tracing, PhD-thesis, University of Copenhagen, Faculty of Science, p. 336.

Shaikh, W.A., Alam, M.A., Alam, M.O., Chakraborty, S., Owens, G., Bhattacharya, T., Mondal, N.K., 2020. Enhanced aqueous phase arsenic removal by iron nano bio-composite. Environmental Technology & Innovation 100936.

Taghavy, A., Mittelman, A., Wang, Y., Pennell, K.D., Abriola, L.M., 2013. Mathematical modeling of the transport and dissolution of citrate-stabilized silver nanoparticles in porous media. Environmental science & technology 47, 8499–8507.

Torkzaban, S., Kim, Y., Mulvihill, M., Wan, J., Tokunaga, T.K., 2010. Transport and deposition of functionalized CdTe nanoparticles in saturated porous media. Journal of contaminant hydrology 118, 208–217.

Tosco, T., Gastone, F., Sethi, R., 2014. Guar gum solutions for improved delivery of iron particles in porous media (Part 2): Iron transport tests and modeling in radial geometry. Journal of contaminant hydrology 166, 34–51.

Tosco, T., Sethi, R., 2010. Transport of non-Newtonian suspensions of highly concentrated micro-and nanoscale iron particles in porous media: a modeling approach. Environmental science & technology 44, 9062–9068.

Tosco, T., Sethi, R., 2009. MNM1D: a numerical code for colloid transport in porous media: implementation and validation. American journal of environmental sciences 5, 517.

Tratnyek, P.G., Johnson, R.L., 2006. Nanotechnologies for environmental cleanup. Nano today 1, 44–48.

Tufenkji, N., Elimelech, M., 2004. Correlation equation for predicting single-collector efficiency in physicochemical filtration in saturated porous media. Environmental science & technology 38, 529–536.

Uyusur, B., Darnault, C.J., Snee, P.T., Kokën, E., Jacobson, A.R., Wells, R.R., 2010. Coupled effects of solution chemistry and hydrodynamics on the mobility and transport of quantum dot nanomaterials in the vadose zone. Journal of contaminant hydrology 118, 184–198.

Velimirovic, M., Bianco, C., Ferrantello, N., Tosco, T., Casasso, A., Sethi, R., Schmid, D., Wagner, S., Miyajima, K., Klaas, N., 2020. A Large-Scale 3D Study on Transport of Humic Acid-Coated Goethite Nanoparticles for Aquifer Remediation. Water 12, 1207.

Xu, W., Li, Z., Shi, S., Qi, J., Cai, S., Yu, Y., O'Carroll, D.M., He, F., 2020. Carboxymethyl cellulose stabilized and sulfidated nanoscale zero-valent iron: characterization and trichloroethene dechlorination. Applied Catalysis B: Environmental 262, 118303.

5 Predicting the mobility of contaminants and engineered nanoparticles (ENPs) in an aquifer with an Integrated Modeling Approach

5.1 Introduction

Chlorinated solvents such as trichloroethene (TCE) and perchloroethene (PCE) are a class of Dense Non-Aqueous Phase Liquid (DNAPL) widely used in industry since the beginning of 20th century (Lerner et al., 2003). Due to accidental surface release or improper disposal of volatile organic solvents, these chlorinated solvents enter the subsurface (Soga et al., 2004). Owing to their high density, the migration of these chlorinated solvent can be extended to the bottom of the aquifer. This migration can last for few months before the DNAPL phase immobilizes on top of the low permeable clays forming the so-called DNAPL *pool*. Additionally, due to the pore scale instabilities, a residual amount of DNAPL can be immobilized throughout the DNAPL migration pathway as *ganglia*. As DNAPLs are sparingly soluble in water, the pool and ganglia serve as a long-term source of contamination with a wide spatial extent (Pankow and Cherry, 1996). Most of these contaminants are highly toxic and even a trace amount of such contaminant are a risk to human health and the environment (Weis and Susten, 1999).

The contaminant plume evolution in both temporal and spatial scales is controlled by complex non-linear hydrogeological, geo- and biochemical processes (Soga et al., 2004). The success in removing all DNAPL from the aquifer are often hindered by limited knowledge about the extent and dynamics of the contaminant plume. Additionally, owing to the different features of the impacted sites and contamination dynamics, each site requires a customized remediation strategy tailored to the existing hydrogeological and physiochemical conditions and logistics of the remediation methodology. Recently, several remediation operations have used numerical models to better understand the governing processes and predict the optimal conditions for the remediation stage (Oostrom et al., 2004; Clement et al., 2000; Oolman et al., 1995).

In this chapter, numerical modelling has been performed to study the interplay of all the major governing factors controlling the contaminant dynamics and its remediation by using a 2D model. In this case, the modelled domain has been a sandy aquifer with common hydrogeological properties to represent a generic aquifer.

The model has been intended to cover all the major stages encountered when assessing a contaminated site with the objective of planning a remediation operation. These stages have been (

Figure **5-1**):

(1) Stage 1 has dealt with the understanding of the DNAPL infiltration pathway and the formation of secondary sources.
(2) Stage 2 has simulated the dissolution of DNAPL leading to the formation of a contaminant plume in the groundwater.
(3) Stage 3 has been the implementation of the remediation strategy. In this work, stage 3 is represented by the injection of ENPs in the aquifer and its spreading in the subsurface.

The numerical model simulates the transport and deposition process of nano-particles in the sand.

(4) Stage 4 has represented ENPs interaction with contaminant once they have been settled down in the rock pores, leading to contaminant degradation.

The model prediction in the first two stages helps understand the temporal and spatial evolution of contaminant plume and the extent of the remediation application. If the selected option is the injection of ENPs, the model will provide clues on how large and dense must be the ENP barrier to be built underground, i.e., the Radius of Influence (ROI), which is simulated in the Stage 3. Finally, Stage 4 allows to couple the hydrodynamics of the contaminant plume, the rate of contaminant degradation and the rate of ENP consumption.

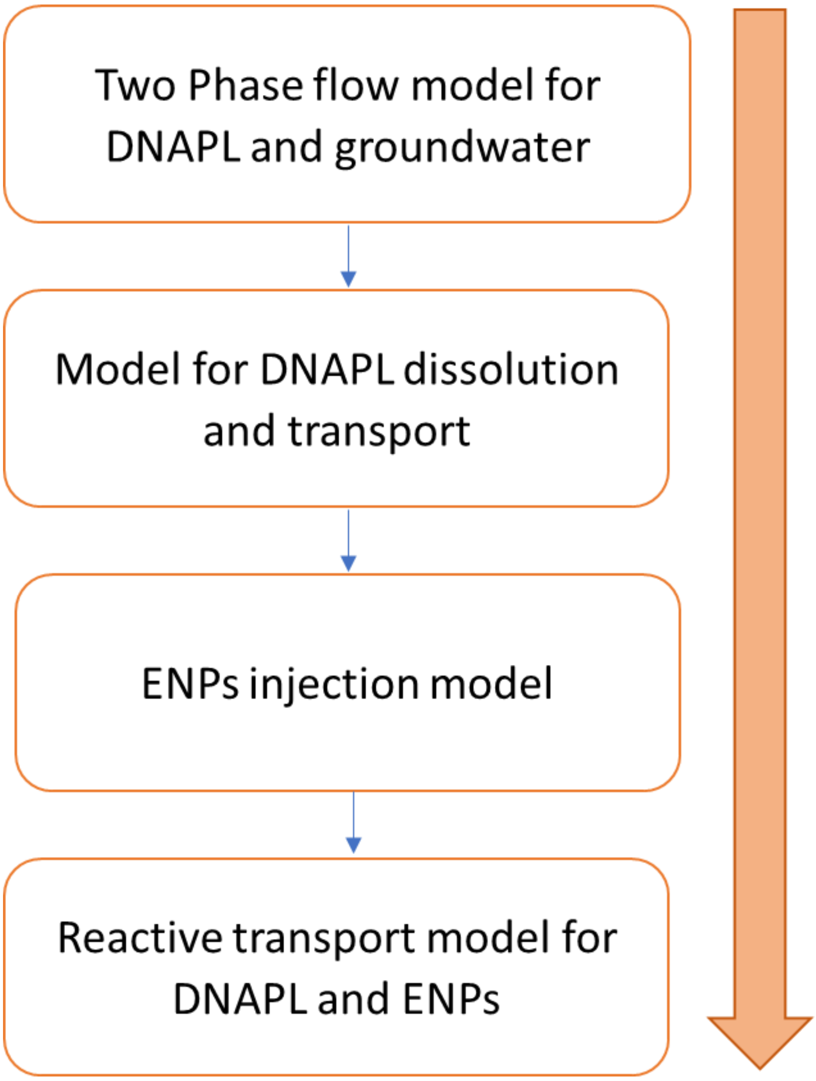

Figure 5-1*: Stages of the integrated modeling approach of DNAPL infiltration in groundwater, contaminant dissolution and transport, ENPs (sZVI) injection, and lastly, the degradation of contamination by the ENPs barrier.*

A large number of numerical models are found in literature simulating individually some of steps mentioned above (Han et al., 2016; Nambi and Powers, 2003; Oostrom et al., 2004; Tosco and

Sethi, 2010). Several attempts have been done to model the consecutive stages of events considering that the outcome of each step depends on the previous one. For example, Kokkinaki (2013) developed an integrated model for the infiltration and dissolution of DNAPL; Fagerlund et al. (2012) performed an integrated model including dissolution and degradation of DNAPL. However, according to the author´s knowledge, there has not been a single model which includes all the major four processes controlling the contaminant and ENPs mobility as well as their mutual reaction.

Such integrated model can help develop a better remediation strategy in the following ways:

1. The integrated model can predict the spatial extent and the degree of contamination and their temporal evolution in the aquifer.
2. The model highlights the governing hydrogeological physical and chemical processes, and their relative contribution to the migration of the contaminant.
4. The model provides insights of the coupled effect of contaminant and the remediation processes in the aquifer. For e.g., the model predicts the disruption in the contaminant plume due to the injection of ENPs.
5. The model provides insights for the design of field and laboratory experiments by predicting the mobility of ENPs in the subsurface. It helps deliver a customized solution for a contaminated site and predict the efficiency of that solution. This includes predicting the time-frame for remediation and the possible reoccurrence of contaminant in the aquifer.
6. The model helps in the optimization of remediation implementation which includes higher removal of contaminant with minimum resources.

5.2 Model implementation

5.2.1 Geometry and sedimentology of the polluted aquifer

The integrated model domain has consisted of a 2D, unconfined aquifer with dimensions of 30 meters width and 12 meters height (Figure 5-2). To model the natural complexity found in a common aquifer, natural heterogeneity has been introduced by two layers of sand with different hydrogeological properties and 6 clay lenses. The sand layers are 6 meters thick. The location and geometry of the clay lenses is random.

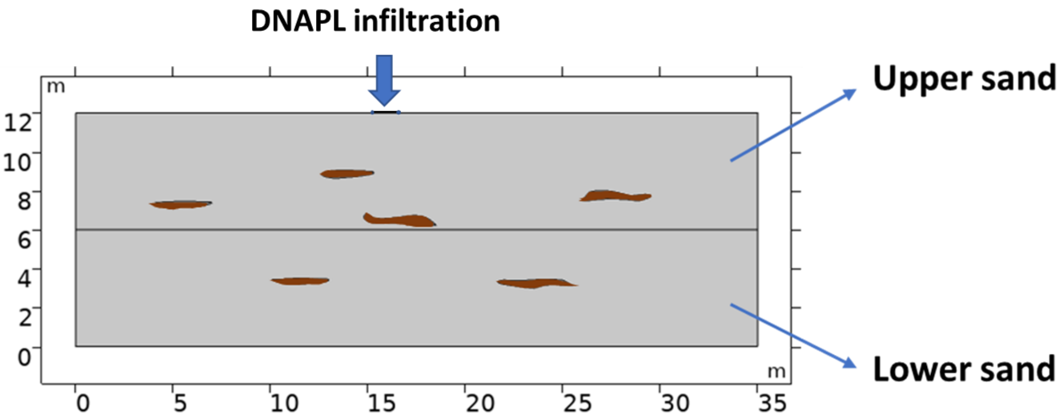

Figure 5-2: Model domain for the simulation of the integrated stages of contamination and remediation. The main components are two sand layers and six clay units (illustrated with brown color) arranged randomly to represent a typical field case.

The hydrogeological properties of aquifer units are generally averaged when implementing them into numerical models, and only the major and distinct layers of sand are considered. However, the reality is that small-scale heterogeneity occur in the subsurface, and it can be important in the simulation of the mobility of both ENPs and contaminants. To incorporate the effect of this small-scale heterogeneity, a logarithmic distribution of permeability and porosity has been implemented (Figure 5-3). The heterogeneity has a normal distribution with a mean value of permeability of 1×10^{-12} m^2 for the upper sand layer and 0.5×10^{-12} m^2 for lower sand layer (Table 5-1). A similar heterogeneity is also estimated for porosity and residual saturation for DNAPL.

Table 5-1: Averaged hydrogeological properties of different geological units (upper sand layer, lower sand layer and clay lenses) in the aquifer used for the integrated modelling.

Property	Upper layer	Lower Layer	Clay lenses
Mean permeability (m^2)	1×10^{-12}	0.5×10^{-12}	1×10^{-13}
Porosity	0.4	0.27	0.25
Mean residual saturation of water	0.08	0.04	0.189
Mean residual saturation of DNAPL	0.08	0.04	0.04
Entry pressure (Pa)	1300	1500	3200

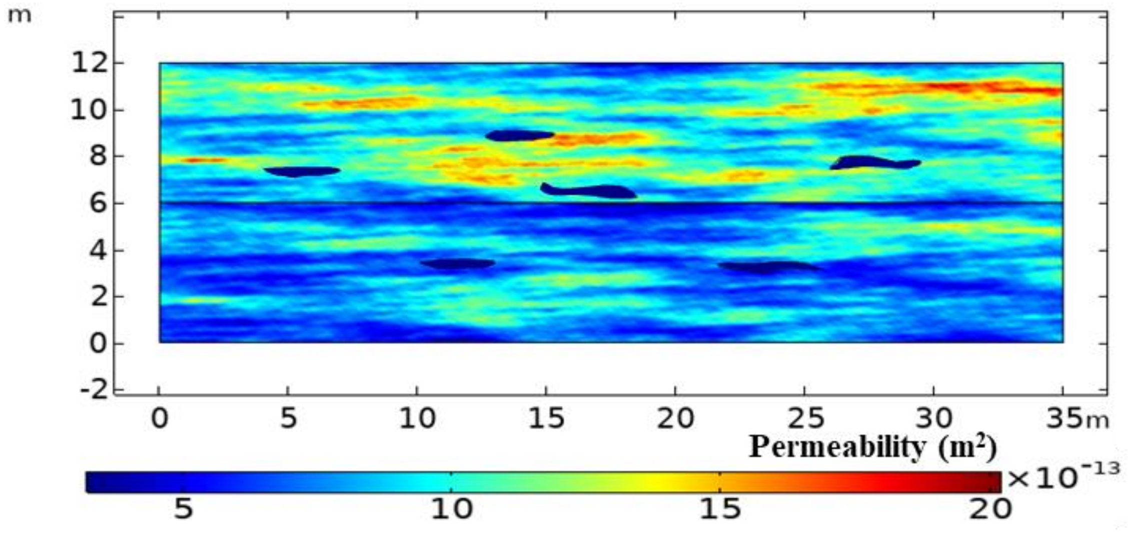

Figure 5-3: Permeability distribution of the porous media in the integrated model, calculated from a logarithmic distribution.

5.2.2 Contaminant properties

In this model exercise, trichloroethylene (TCE) has been selected as DNAPL; TCE is denser than water and less viscous and, thus, it is expected to migrate vertically downward. Both water and TCE have been considered as incompressible, keeping the density constant anytime. TCE solubility in water is 1.27 $kg_{TCE}\cdot m^{-3}{}_{water}$ (Grathwohl, 2012). Due to its sparingly soluble nature, depletion of TCE mass has been found to be much slower than the rate of infiltration in the aquifer. Therefore, TCE dissolution in groundwater during the infiltration of the free phase is considered to be negligible (modelling Stage 1). The chemical and physical properties for both water and TCE are shown in Table 5-2.

***Table 5-2**: Fluid properties used in the simulation of TCE infiltration and dissolution in the groundwater (Grathwohl, 2012).*

Property	Value and units
Water density	1000 $kg\cdot m^{-3}$
DNAPL density	1470 $kg\cdot m^{-3}$
Water viscosity	0.001 Pa·s
TCE viscosity	0.0005 Pa·s
TCE dissolution in water	1.27 $kg\cdot m^{-3}$

5.2.3 Modelling Stage 1: Two-phase flow during contaminant infiltration

The Stage 1 involves simultaneous flow of water and DNAPL underground. The mass conservation equations for both the fluids have been used for the development of the numerical formulation (Equation 2.19, 2.20, 2.21, 2.22). A detailed review of the equations has been done in Chapter 2.

$$\theta \frac{\partial(S_w)}{\partial t} = \nabla.\left(k \frac{k_{rw}}{\mu_w}(\nabla p_w - \rho_w g)\right) + q_w \qquad \text{(eq. 2.19)}$$

$$\theta \frac{\partial(S_n)}{\partial t} = \nabla.\left(k \frac{k_{rn}}{\mu_n}(\nabla p_n - \rho_n g)\right) + q_n \qquad \text{(eq. 2.20)}$$

$$S_n + S_w = 1 \qquad \text{(eq. 2.21)}$$

$$p_c(S_w) = p_d S_e^{\frac{-1}{\lambda}} \qquad \text{(eq. 2.22)}$$

Where S_n and S_w are the saturation of DNAPL and water respectively, p_n and p_w are the pressure of DNAPL and water, θ is porosity, q_w and q_n are the volumetric source term for water and DNAPL respectively, k is the permeability of the sand, p_c is the capillary pressure defined as a function of water saturation.

The Brooks and Corey relationship for the capillary pressure and saturation has been used to close the system of equations. To incorporate the effect of clay lenses in the flow of DNAPL, Phase Pressure Saturation with Interface Condition (PPSIC) has been used as discussed in Chapter 2. The set of equations is solved using an Implicit-Pressure/Explicit-Saturation algorithm.

5.2.3.1 Initial and boundary conditions

The accuracy and convergence of the solution by Finite Element Method depends on the initial and boundary conditions. In this model, a hydrostatic initial condition with water table at the surface (Y=12 m) has been assumed. During the infiltration of TCE, the effect of groundwater flow on TCE migration path is considered to be negligible. The left and right boundaries of the model domain have been considered to be distant enough for the water pressure to be unaffected by the migration of TCE. A Dirichlet boundary condition of 12 meters of hydraulic head is assigned at the left and right boundaries. Also, TCE saturation at these boundaries is considered to be zero. The top and bottom boundaries are assigned with no flow boundary for both water and TCE, except in the area of infiltration.

The model has considered that TCE has infiltrated down during 35 days from the area of infiltration with flow rate of 0.001 kg·m^{-2}s^{-1}. The initial saturation of water has been assigned as one as model domain has been considered to have no DNAPL at time (t)= 0. The left and right boundaries are far away from the TCE migratory path and, thus, the saturation has been expected to remain constant.

After 35 days, the infiltration of TCE is stopped. With 0.001 kg·m^{-2}s^{-1} of infiltration rate, the total amount of TCE which entered the aquifer for 35 days is 166 kg. In the following days, the migration of TCE has been driven by gravity and capillary forces. The model for Stage 1 has been run until the migration of TCE is predicted to stop and the immobilized TCE occurs as residual saturation along the migratory pathways and as a TCE pool at the top of impervious layers.

5.2.3.2 Meshing

The mesh used for simulating the two-phase flow has consisted of a total of 93,100 nodes and 178,911 finite elements (Figure 5-4). The minimum size of the mesh element has been 0.5 mm while the maximum size has been 3m. The different lithological interfaces (sand-sand and sand-clay) as well as the bedrock have been discretized with a relatively finer mesh where a sharp gradient of DNAPL saturation is expected. This sharp gradient of DNAPL saturation forms due to the accumulation of DNAPL at the impermeable layers of the model domain. A much coarser mesh in the range of few meters has been used for the region where DNAPL plume is not expected to infiltrate. Additionally, during the simulation, the formation of sharp gradients of the dependent variables required relatively finer mesh. Therefore, an adaptive meshing algorithm has been used which refines the mesh when the numerical error accumulates due to the occurrence of sharp gradient of the DNAPL saturation.

5.2.4 Modelling Stage 2: TCE dissolution and transport

Once the TCE gets immobilized underground, it is expected to undergo slow depletion due to mass transfer of TCE to the aqueous phase. To study this process, in the Stage 2 the model has simulated the dissolution of TCE in water as well as its transport as dissolved phase in the same model domain as in the Stage. The final condition of the Stage 1 has been taken as a starting point for the Stage 2.

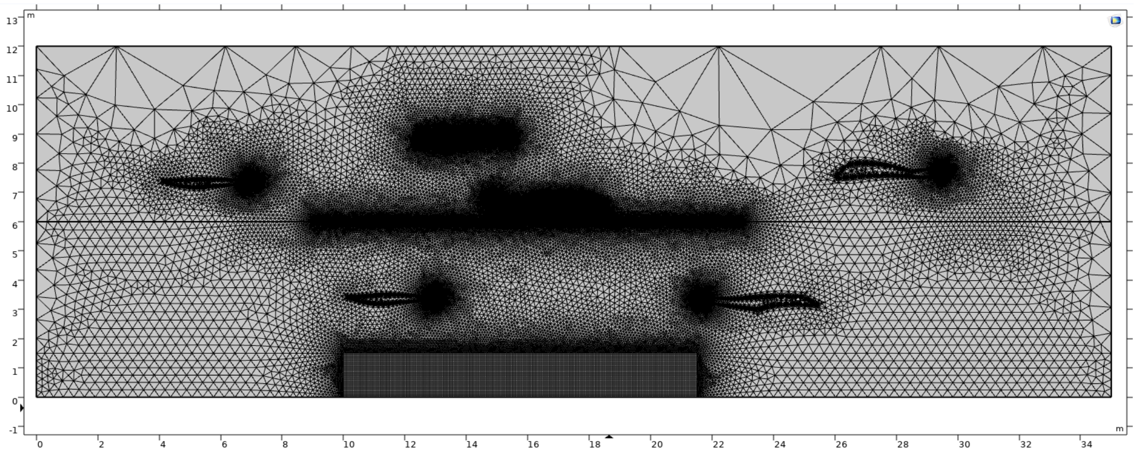

***Figure 5-4**: Mesh with 178,911 finite elements used for spatial discretization of the model domain before implementing the numerical formulation of two-phase flow.*

5.2.4.1 Initial conditions

In the Stage 2, no dissolved TCE in the groundwater is initially considered. Unlike in the Stage 1, the groundwater flow has been considered to transport the TCE. An average groundwater flow rate of 1 cm·day^{-1} and 0.5 cm·day^{-1} have been assigned for upper and lower sand layer, respectively. The heterogeneity in the permeability leads to a heterogenous groundwater flow field as shown by the blue arrows in the model domain (Figure 5-5). The simulated groundwater is diverted when it passes through the clay lens due to their impervious nature. A dispersivity of 2.7 cm has been considered for the contaminant plume.

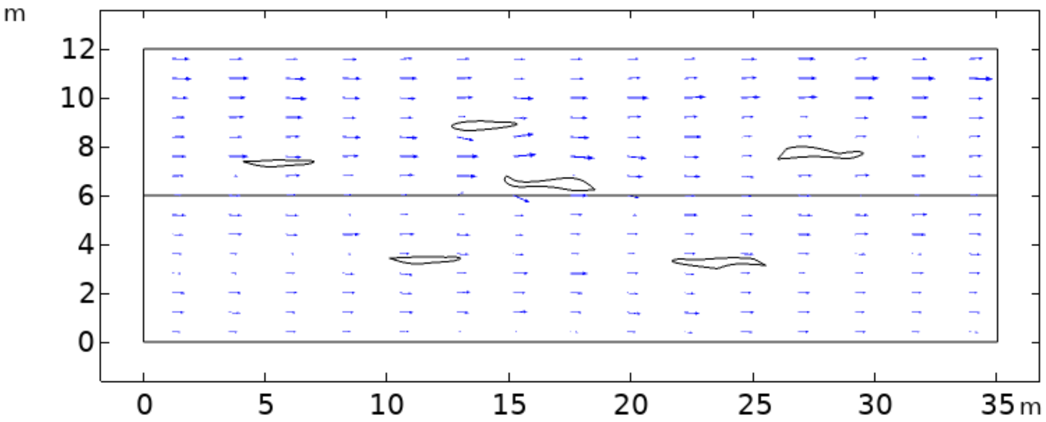

Figure 5-5: Groundwater velocity field for the Stage 2. The average Darcy velocity at the upper sand layer is 1 cm·day^{-1} while the average Darcy velocity in lower sand is 0.5 cm·day^{-1}.

Initially the aquifer is free of dissolved contaminant. The immobilized TCE from Stage 1 has been the source of contamination for the Stage 2. The left and right boundaries of the aquifer have been considered as an open boundary for contaminant flow. The top and bottom boundaries are no flow boundaries. The source for the dissolved contaminants is numerically prescribed by the domain where the model predicts formation of DNAPL pool and ganglia. The dissolution of TCE has been explained in Section 2.2.2.4.

The Stage 2 model is run for 11.5 years after which the majority of DNAPL ganglia gets depleted.

5.2.4.2 Meshing

A total of 223,615 triangular elements was used for spatial discretization of the domain in Stage 2. The mesh uses linear triangular geometry for spatial discretization as shown in Figure 5-6. The meshing of the domain has been done with the objective of optimizing computational time without compromising the accuracy of the solution. The left side of the domain has coarse mesh owing to the unlikelihood of contaminant travelling upstream. In the downstream direction, an extremely fine mesh is used with maximum size of 10 cm for the edge of the triangular elements.

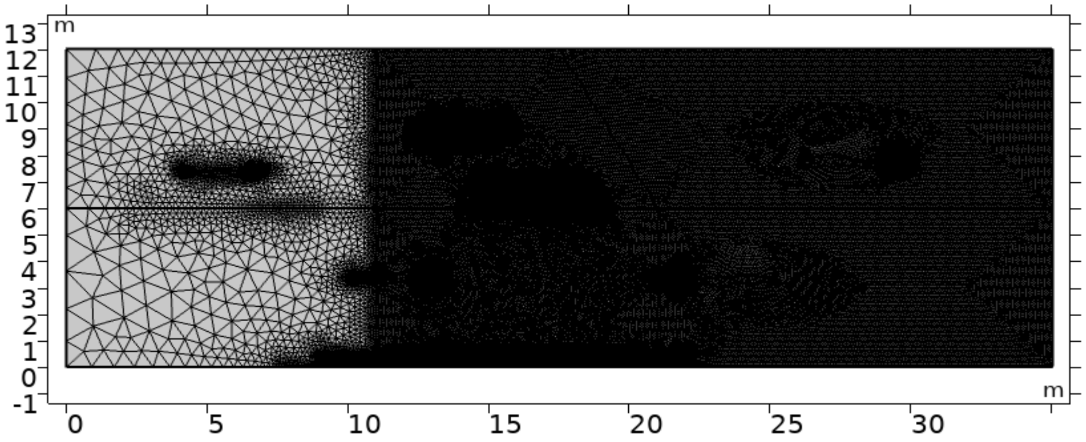

Figure 5-6: Meshing used for simulating the contamination transport in the Stage 2. The very small element size results in a black area in this figure.

5.2.5 Modelling Stage 3: sZVI injection

5.2.5.1 Initial and boundary condition

Stage 3 has been intended to model the injection of ENPs, specifically sZVi, and their interaction with the dissolved TCE. In this Stage, the initial and boundary condition of the ENP injection has been set with the intention of a pilot-scale remediation. The concentration of sZVI in the injection fluid has been taken as 0.5 $kg_{sZVi}\cdot m_{water}^{-3}$ which resembles the configuration for simulation of the tank scale sZVi injection (see Chapter 4).

As already mentioned, the amount of ENPs to be injected in the aquifer depends on the extent and intensity of the pollutant plume, which defines the optimal Radius of Influence (ROI). A ROI smaller than the width of the plume would lead to a bypass from the ENPs barriers. A higher ROI would lead to unreacted ENPs. Therefore, the role of numerical model in Stage 3 is to estimate the ENPs injection concentration and rate to get the optimal ROI.

In the column experiments of injection of sZVi ENPs in sandy soils, a flow rate of 0.1 $mm\cdot s^{-1}$ has been found to allow a significant particle mobility (Chapter 3). In the Stage 3, a similar equivalent averaged flow rate has been implemented (0.3 $mm\cdot s^{-1}$). With this rate, the groundwater velocity profile in the aquifer as a response to the injection can be estimated (Figure 5-7). The ENPs are injected radially since the injection rate is much higher than the groundwater natural velocity, and, therefore, ENPs are predicted to be distributed almost equally in all the directions. An important effect of the injection is that the natural groundwater flow is impacted as well as the plume of contaminants. Due to this, a negligible interaction between the contaminant plume and sZVi is expected during the ENPs injection, and, thus, the reaction during injection phase has not been considered in the Stage 3 model.

A well with two screens of 0.2 m width has been implemented in the domain for the injection of ENPs in the modelled aquifer. With the perspective of a pilot scale injection, the ENPs have been injected for 8 days with a concentration of 0.5 $kg_{sZVi}\cdot m_{water}^{-3}$ and flow rate of 0.3$mm\cdot s^{-1}$. Therefore, the total amount of ENPs injected in the model domain after 8 days is 1.8 kg. After several iterations of simulating sZVi injection, the optimal location of the injection well has been found to be 5 meters downstream from the TCE pool at the upper sand (Figure 5-7).

The model has been developed with the aim to simulate the degradation of the contaminants at the upper sand. As comparatively lesser TCE pool mass exists at the shallower level, the pilot scale injection in the model domain will be more efficient. Additionally, for a shallow level water extraction, the water quality is more vulnerable to the shallower contaminant source. Therefore, the results from the simulation are more applicable for a real field case remediation. After simulating the injection of ENPs injection, the groundwater in the model domain has been set at its natural flow condition.

In addition to the simulation of the sZVi´s mobility, the model simulates the effect of CMC (injected along with sZVi) on the viscosity of the groundwater. The concentration of injected CMC has been set at 5 $kg_{CMC}\cdot m_{water}^{-3}$ to resemble the experimental configuration reported in Chapter 4. The addition of CMC in the injection solution leads to a variable viscosity in the groundwater flow; the evolution of viscosity as a function of CMC concentration has been evaluated by using the Grunberg and Nissan equation (Equation 5.1):

$$ln(\mu_{sol}) = x_{CMC}\, ln(\mu_{CMC}) + x_{water}\, ln(\mu_{water}) \quad \text{(eq. 5.1)}$$

Where μ_{sol} is the viscosity of the aqueous phase carrying CMC, μ_{CMC} is the viscosity of the injected fluid taken to be 6.3×10^5 Pa·s (Krol et al., 2013), x_{CMC} is the mole fraction of CMC, and x_{water} is the mole fraction of water. The viscosity of CMC is different from the one studied in chapter 4, due to the difference in their molecular weight.

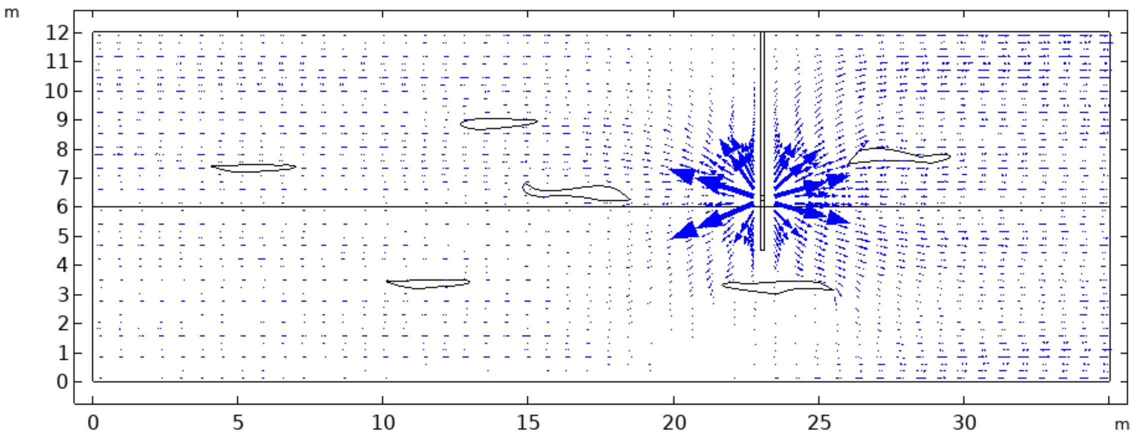

***Figure 5-7**: Flow field during the Stage 3 model case. The plot shows the magnitude of Darcy velocity which is higher only near to the injection well. The blue arrows show the flow direction of the groundwater.*

5.2.5.2 Formulation for ENP transport in Stage 3

The non-linear formulation accounting for transport of ENPs in the groundwater and its deposition within the pore space implemented in the Stage 3 model is based on the equations discussed in Chapter 2 (Equations 2.62, 2.63 and 2.64):

$$\frac{\partial(\theta C)}{\partial t} + \rho_b \frac{\partial(s_1)}{\partial t} + \rho_b \frac{\partial(s_2)}{\partial t} = -\nabla(vc) + \nabla(D_L \frac{dC}{dx} + D_T \frac{dC}{dy} + D_T \frac{dC}{dz}) \quad \text{(eq. 2.62)}$$

$$\rho_b \frac{\partial(s_1)}{\partial t} = \theta k_{a,1}(1 + A s^{\beta_1})c - \rho k_{d,1} s_2 \quad \text{(eq. 2.63)}$$

$$\rho_b \frac{\partial(s_2)}{\partial t} = \theta k_{a,2}\left(1 + \frac{x}{d_{50}}\right)^{\beta_2} c - \rho k_{d,1} s_2 \quad \text{(eq.2.64)}$$

Where k_a is attachment rate [T^{-1}], k_d is detachment rate [T^{-1}], θ is the porosity of sand matrix, C is the aqueous concentration of ENP ($M{\cdot}L^{-3}$), s is the amount of particle deposited relative to the sand mass [-], *A* is multiplier coefficient [-], β is exponential coefficient [-]. The suffix 1 and 2 are the deposition site of ENP on the sand grains.

The governing physiochemical mechanisms for ENPs transport and interaction with mineral grains in the Stage 3 model can be either ripening, straining, blocking or linear. From the column experiments (Chapter 4), both ripening and straining are observed to be dominant, and, thus, these mechanisms are included in the model of the Stage 3. While the attachment and detachment coefficient varies due to the flow rate, the function for those coefficients are not known due to limitation of the data. Therefore, similarly to Chapter 4, the coefficient rate is assumed to remain constant. Table 5-3 shows the values for parameters that have been taken from column scale injection of sZVi in the saturated sand.

***Table 5-3**: Values of governing parameters for the ENP-mineral interaction used for simulation the injection and transport of ENPs in the Stage 3.*

Parameters	Values
Ripening	
Attachment rate (k_a)	0.00918
Detachment coefficient (k_d)	0.00068
Exponential coefficient β	0.702
Multplier coefficient A	1050
Straining	
Attachment rate (k_a)	0.001
Detachment coefficient (k_{dt})	0.000107
Exponential coefficient β	0.23

5.2.5.3 Meshing of domain in the Stage 3

The mesh used for the Stage 3 is similar to the meshing for Stage 2 (Figure 5-8). However, finer triangular elements are used near the well. The total number of triangular elements in the mesh is up to 233,690.

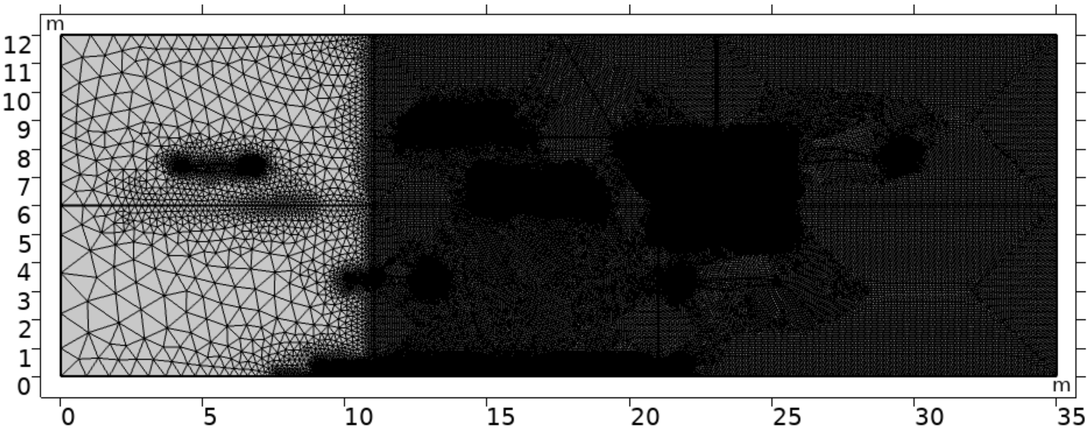

***Figure 5-8**: Meshing used for simulating the contamination transport in the Stage 3.*

5.2.6 Modelling Stage 4: Reactive transport simulations

The purpose of the Stage 4 is to study the interaction between the ENPs and a pollutant plume. Stage 4 starts with the groundwater flow coming back to its natural condition after 8 days of ENP injection (Figure 5-5).

As discussed in Chapter 2, the relevant pathway for TCE reduction with sZVi is beta elimination, although a trace amount of other product is also formed. In the Stage IV model, however, only acetylene formation is considered which enables to express the reaction using first order kinetic law.

The reaction pathways for degradation of TCE to acetylene in presence of sZVI is given by following half reactions:

$\mathrm{FeO} \rightarrow \mathrm{Fe}^{2+} + 2e^-$

$C_2HCl_3 + 8e^- + 5H^+ \rightarrow C_2H_6 + 3Cl^-$

The above half reactions show that for each mole of TCE, 4 moles of Fe(0) are consumed. Given the molar mass of TCE and Fe to be 131.4 g·mol^{-1} and 55.8 g·mol^{-1}, respectively, it can be concluded that 1.7 gram of iron reduces 1 gram of TCE. The reaction between the sZVi and the contaminant has been modeled considering a pseudo-first-order rate kinetics.

The equation for kinetic rate of TCE degradation is represented by equation 2.65 and has been discussed in Chapter 2

$$-\frac{dC}{dx} = K_{TCE}C \tag{eq. 2.65}$$

Where K_{TCE} is the pseudo first order rate constant with dimensions L·T^{-1}, and C is the solute concentration in Kg·m^{-3}.

A surface area normalized rate constant is represented by Equation 2.66:

$$k_{SA} = k_c/(\propto_s \rho_m) \tag{eq. 2.66}$$

Where $\propto_s$ is the surface area m^{2}g^{-1}, and ρ_m is the concentration of the iron distributed in the porous media Kgm^{-3}.

The K$_{sa}$ value depends on the sZVI characterization and for this research work, a value of 0.015 m·s^{-1} is taken from the literature (Xu et al., 2019). A constant value of 25 m^2·g^{-1} is taken for the surface area from the same source in the literature (Xu et al., 2019).

Considering the degradation reaction, the set of governing equations for the mobility of contaminants in the aquifer has been represented by the mass conservation expression (Equation 5.2):

$$\theta\frac{dc}{dt} + v\nabla c - \nabla D(\nabla c) = K_l(C_s - c) - k_{SA} \propto_s \rho_m C \tag{eq.5.2}$$

The depletion of active surface of sZVi due to its reaction with TCE can be calculated by Equation 5.3 after considering the 1.7 grams of iron reducing 1 gram of TCE.

$$\rho_b\theta\frac{ds}{dt} = -1.7k_{SA} \propto_s \rho_m C \tag{eq. 5.3}$$

Where *s* is the concentration of settled ENPs after 8 days.

The model exercise for the Stage 4 uses the same mesh geometry as for Stage 3. The initial condition for Stage 4 has been taken as the final condition of Stage 3.

The TCE phase infiltration (Stage 1) in the model domain has been simulated for 135 days, after which the dissolution and transport of aqueous TCE has been simulated (Stage 2). Beginning from the immobilization of the TCE phase, the simulation of Stage 2 lasts for 11.5 years. In the

Stage 3, the mobility of ENPs in the model domain in simulated considering an injection period of 8 days. In the last stage, the contaminant degradation is simulated for the following 8 years after the injection of ENPs

5.3 Results

5.3.1 Stage 1: Two-phase flow

The outcome of the Stage 1 exercise is to predict (a) the migration pathways of infiltrated TCE, (b) the travel time of TCE before immobilization, and (c) the TCE architecture at the source zone.

After 5 days, 15 days, 25 days and 35 days, the model predicts a TCE entry flux of 0.001 Kg·(m^{-2}·s^{-1}) at the infiltration point (Figure 5-9). The TCE entry saturation has been estimated to be 0.5.

.-

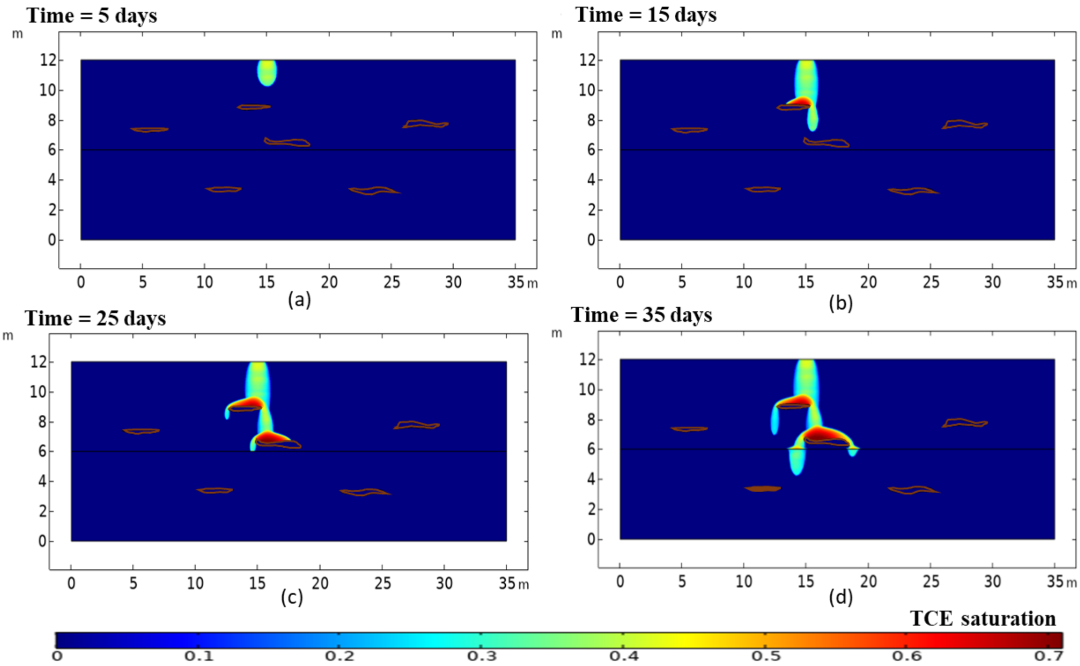

***Figure 5-9**: Model prediction for TCE saturation during the Stage 1. (a) Predicted TCE plume after 5 days of infiltration. (b) after 15 days of infiltration, (c) migration path of controlled by the accumulation of TCE on the clay top after 25 days of infiltration, and (d) prediction of TCE plume geometry after 35 days of infiltration, with lateral and horizontal migration due to clay lens and heterogeneities in sand.*

At (t) = 5 days, the predicted TCE plume moves predominantly in the vertical direction with a negligible lateral movement beyond the extent of the infiltration area (Figure 5-9a). The result shows the dominance of gravitational forces over the capillary and viscous forces. When the TCE plume encounters the upper clay unit, the model predicts the accumulation of TCE at the top of the clay lens (Figure 5-9b). This result illustrates that the entry pressure of upper clay is higher than the capillary pressure at the overlying sand. This model prediction shows the successful implementation of numerical formulation for PPSIC theory, which governs the infiltration from higher permeable sand to lower permeable sand.

After 25 days, the model predicts the TCE vertical motion as the two branches of TCE plume are formed at the two edges of the upper clay lens (Figure 5-9c). The vertical migration of both branches of TCE is predicted to continue before the lower clay lens is encountered. The model estimates a maximum saturation of 0.7 at the top of both the clays due to accumulation. Eventually, after time (t) = 35 days, the model prediction shows the vertical downward motion of the TCE plume from the four branches each formed at the edges of clay lenses (Figure 5-9d). As no additional TCE infiltrates from the top of model domain after 35 days, the TCE plume is extended 7.8 meters to the bottom of the aquifer (Figure 5-9d).

The model estimates a different TCE migration behavior at the underlying, lower permeable sand, compared to that of clay. The accumulation of TCE at the top of the interface can be attributed to the higher entry pressure of the lower sand compared to the upper sand. The threshold saturation for the lower sand unit is 0.3, only 0.05 higher than the plume front. Therefore, the model estimates that the accumulation of TCE at the sand interface occurs until the saturation reaches the threshold value, following which the simulated plume infiltrates the lower sand.

The model assumes that after 35 days, the 166 kg of TCE have been already infiltrated down. During this period, the model predicts the effect gravity and capillary forces in the aquifer. The model predicts a gradual decrease in the TCE saturation (Figure 5-10). Three TCE plumes, PF1, PF2 and PF3 are developed, with lengths of 5.6 meters, 8.7 meters, and 7.2 meters, respectively (measured from the water table) after 40 days. After 60 days, these plumes have already entered the lower sand (Figure 5-10b), and PF1, touches down the bedrock of the aquifer domain. After 85 days, the model estimates the formation of a TCE pool at the bedrock by PF2 front (Figure 5-10c). Finally, after 135 days, the model predicts an integration of TCE pool formed by both PF2 and PF3 plume resulting in 13 m horizontal extent of TCE at the bedrock (Figure 5-10d).

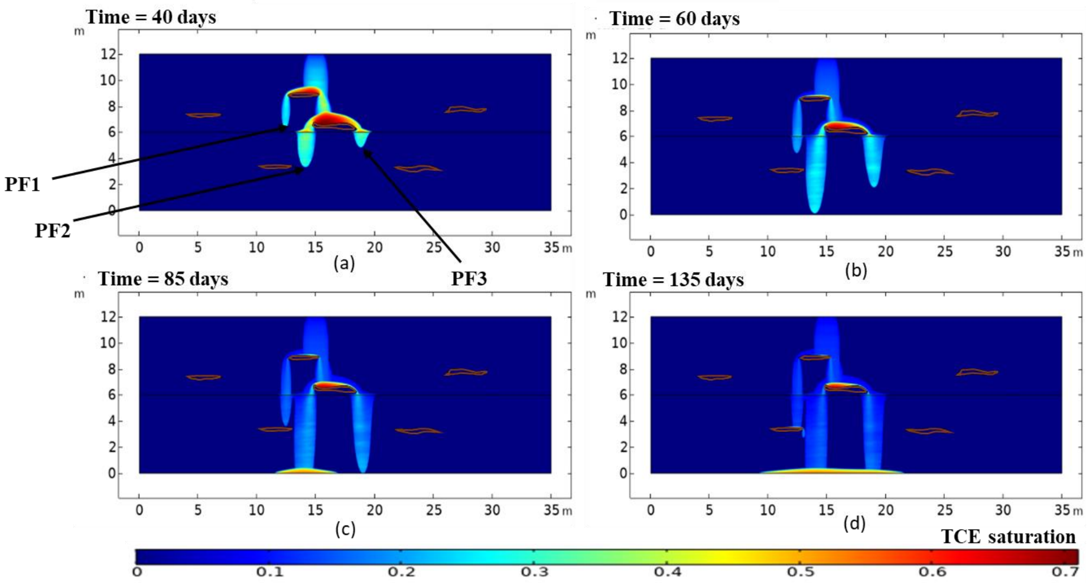

Figure 5-10: Model prediction for TCE migration after the halt in the infiltration from the ground. (a) TCE plume after 40 days; (b) Prediction of the arrival of TCE plume (PF2) at the bedrock after 60 days of infiltration; (c) TCE saturation profile along the migration path and accumulation at the impervious layer after 85 days.

The TCE plume saturation along its migration path is predicted to be slightly higher than the residual saturation of TCE. This indicates that an extremely slow motion of TCE before the saturation becomes as residual saturation. After 135 days, a static TCE plume with a horizontal extent of 13 meters and vertically extending throughout the aquifer is predicted. The factor governing this architecture are the sand hydraulic properties, clay geometry and location, and TCE source location. Therefore, the results of the Stage 1 show that the contaminant architecture will be unique for each case.

Out of 166 Kg of TCE entered in the aquifer, 65% is predicted to reach at the bedrock forming a pool. The TCE at this pool and on top of the clay lens amounts to 118 kg, while the remaining 58 kg forms ganglia. The saturation of TCE pool is 0.4 for both the clays and the bedrock while the ganglia saturation is in the range of 0.01-0.2.

The TCE saturation distribution at time (t) = 135 days (Figure 5-10d) is considered to be the initial TCE architecture for dissolved contamination in Stage 2.

5.3.2 Stage 2: Dissolution and transport of TCE

The model prediction for contaminant transport shows that within 1 month, the TCE aqueous concentration reached the solubility limit of 1.27 $kg_{TCE}{\cdot}m^{-3}{}_{water}$ (Figure 5-11a). The attainment of equilibrium concentration of aqueous TCE despite of kinetic mass transfer formulation indicates that the mass transport flux due to groundwater flow is much slower than the kinetic mass transfer flux at the TCE-water interface. This results in the control of groundwater flow over the contaminant dissolution, which is in agreement with the previous studies that reported equilibrium aqueous concentration of contaminant for slow groundwater flow systems (Pankow and Cherry, 1996).

The predicted maximum horizontal movement of dissolved TCE from the source is 2.1 meters (Figure 5-11b), which is a consequence of the slow groundwater flow. However, the dissolved TCE is present at all vertical height of the domain. The geometry of the contaminant plume front is determined by the hydraulic properties and TCE source zone architecture, and the dissolved TCE plume has a greater horizontal extent in the lower sand compared to the upper sand (Figure 5-11a and b).

After 0.7 months, the dissolved TCE plume is predicted to reach the boundaries of the domain. A finger-shaped plume front is drawn by the model, which is the consequence of the heterogeneity in the hydraulic properties. The plume front has same horizontal extent in both upper and lower sand layers. Upstream, the prediction of the geometry of the contaminant plume does not show a significant change through time (Figure 5-11c & d). In general, the results for Stage 2 indicate relatively small changes in TCE saturation through time compared with the evolution of dissolved TCE plume.

Between 1 and 2 years, the plume of dissolved TCE and TCE saturation shows the same shape within the model domain, reaching a steady state (Figure 5-12). A depletion of TCE ganglia in the upstream region is predicted while in the downstream region remains intact. This can be explained by the kinetic mass transfer formulation for TCE dissolution which becomes zero for the regions in the model domain where the TCE concentration is at equilibrium concentration. Therefore, for these regions, the model predicts no depletion in TCE saturation (Figure 5-12b).

The beginning of discontinuity in the vertical profile of TCE plume from the top of the aquifer domain after 2 years is shown in Figure 5-12d. This result is the consequence of TCE ganglia depletion from the top (Figure 5-12c). This event is considered as the onset of Stage 2 of contaminant transport.

The model prediction of the TCE transport at longer times (t) = 3 years, (t) = 6 years and (t) = 11 years shows depletion of TCE ganglia mainly from the upper sand (Figure 5-13), with a relatively smaller ganglia depletion in the lower sand. After 6 years, the dissolved TCE plume originates mainly from the TCE pool in the clay units of upper sand layer (Figure 5-13d).

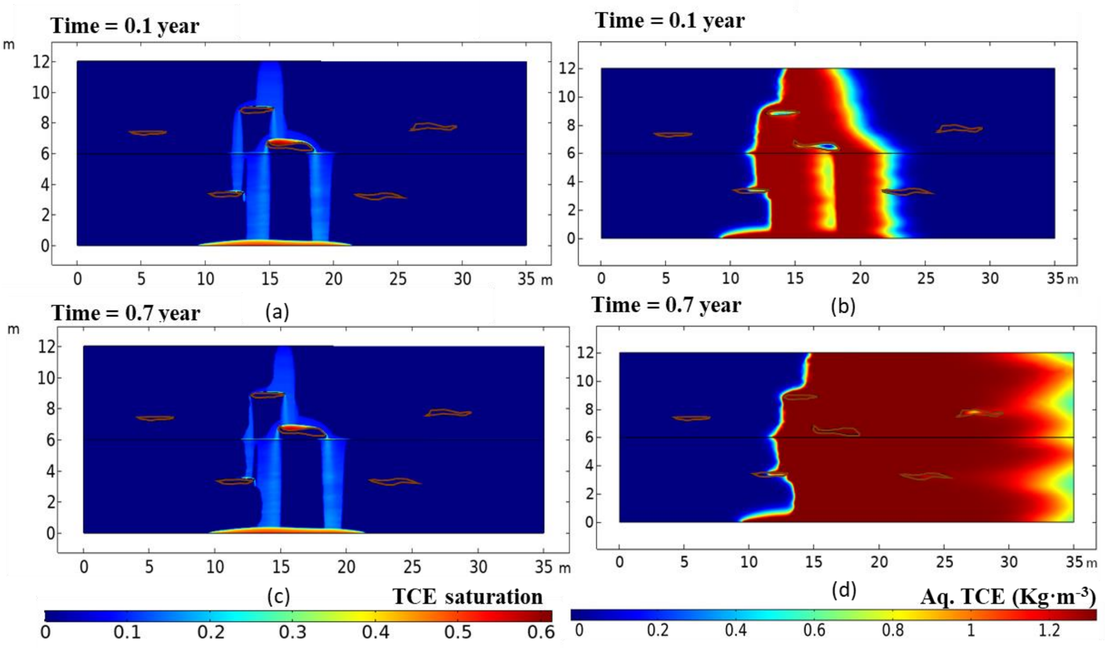

Figure 5-11*: Model prediction of the evolution of TCE saturation (a and c) and dissolved TCE in water (b and d) in the modelled domain in Stage 2 after 0.1 and 0.7 years from the end of Stage 1.*

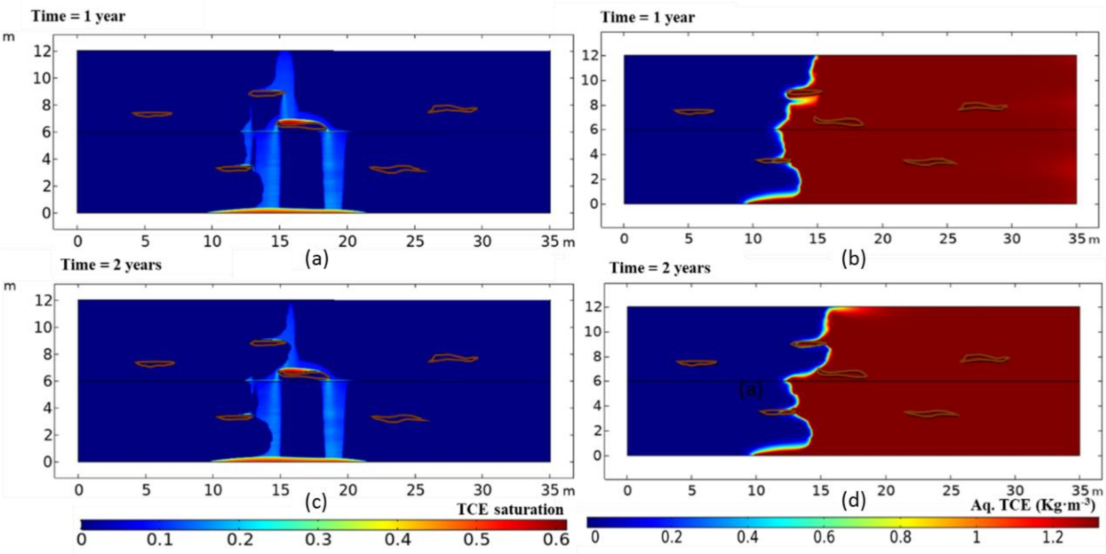

Figure 5-12*: Model prediction of the evolution of TCE saturation and dissolved TCE after 1 and 2 years after the beginning of Stage 2.*

The plume geometry is controlled by the evolving TCE source zone in the model domain, which shows TCE ganglia remaining mainly in the lower sand (Figure 5-13c). As the lower sand has higher TCE immobilized form at time (t) = 0 (Figure 5-10d), the longevity of the aqueous TCE is higher compared to that in overlying sand. After a period of 11 years of TCE dissolution, the model predicts two localized TCE plume in the aquifer domain, each having its origination point as TCE ganglia at the upper clay bedrock (Figure 5-13f). The plume geometry is governed by the remaining TCE source in the aquifer domain (Figure 5-13e). The model also shows that only a TCE pool at upper clay and bedrock remains at time (t) = 11 years, while the TCE ganglia is exhausted. A small remnant of TCE is present at the sand interface, resulting in a minor source of aqueous TCE from the interface (Figure 5-13e). Due to the vertical dispersion of aqueous TCE, the model predicts the concentration of TCE reaching at the aquifer wall is 0.5, i.e, half of the concentration compared to the equilibrium concentration of TCE.

As a general outcome, the results indicate that the modeling can predict the occurrence of TCE source zone, even after decades after TCE spillage in the aquifer.

5.3.2.1 Transport of TCE within clay lens

The sparse clay lens occurring the sandy rock are expected to play a significant role in the spatial and temporal evolution of the contaminant plume. The model of the Stage 2 predicts a bypass of the contaminant plume when it encountered the clay lens after 0.4 years (indicated by brown arrow, Figure 5-14). This can be explained by considering the role of advection and diffusion in the contaminant transport. As the advection in the clay lens is negligible due to its impervious nature, the transport occurs only through diffusion. Since diffusion is slower compared to advection, the plume evolution is hindered. A larger spatial extent of plume in the surrounding sand than the clay lens is predicted. However, as shown previously in Figure 5-14, after 0.7 years of TCE dissolution, the transport of TCE in clay attains steady state due to hydrodynamic dispersion.

At longer times, the back-diffusion of TCE in the clay lens becomes significant. The model prediction shows a higher persistence of aqueous TCE in the clay media compared to the surrounding sand after 3.6 years of TCE dissolution (Figure 5-14b). This promotes later mass transfer of aqueous TCE from clay to sand as a back-diffusion process. The diffusion of contaminant from clay to sand results in higher longevity of contaminant originating from sand as shown in the Figure 5-14b. The model predicts that the back-diffusion process from the clay (indicated by brown arrow) continues for nearly 2 years, after which the TCE concentration drops to 500 times compared to the equilibrium concentration. Therefore, the longevity of contaminant due to back-diffusion is lower compared to the contaminant due to TCE source zone. This has implication for field characterization and monitoring tasks since the contaminant origin cannot only be attributed to the TCE source zone but can also be the result of back-diffusion from clay sands. However, the model predictions show that unlike the TCE source, the contaminant originating from clay lens has a lower concentration than the solubility limit and it further declines with time. The lower longevity of contaminant back-diffusion enables the pump-and-treat method to be an option as a remediation technique.

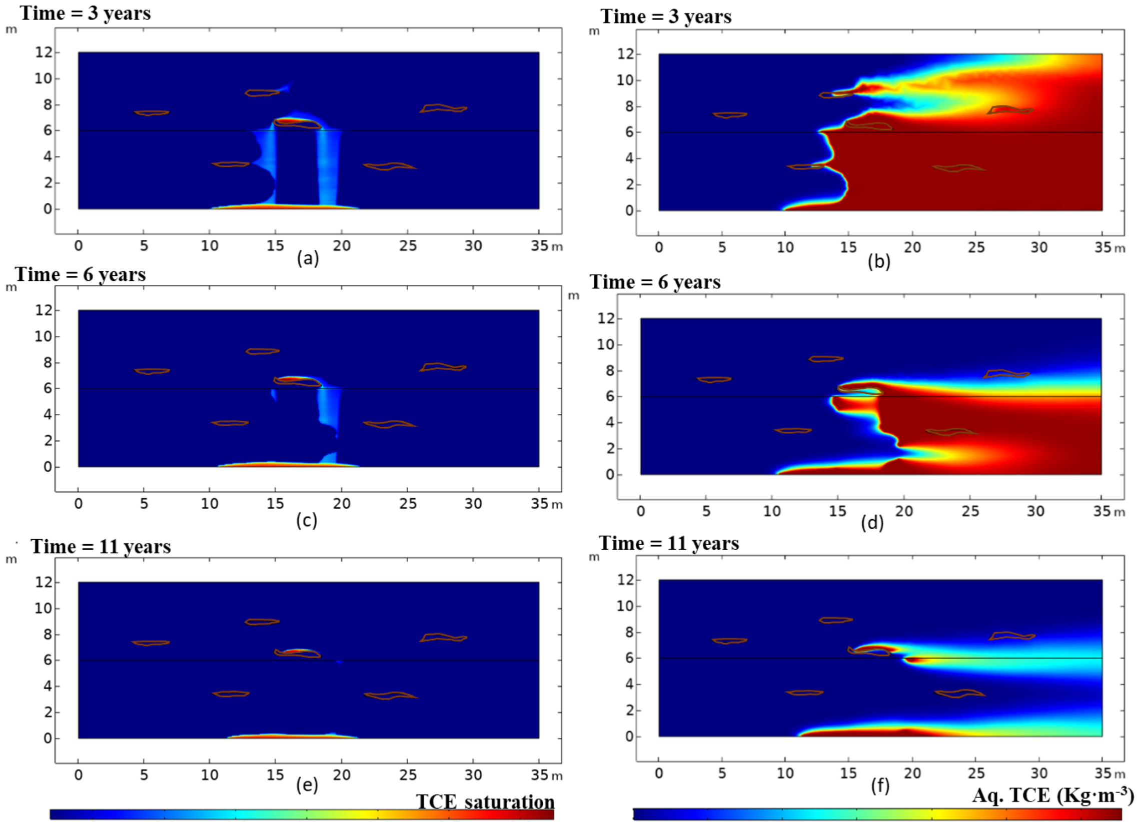

Figure 5-13: *Model prediction of the evolution of TCE saturation (a, c, e) and dissolution (b, d, f) in the Stage 2, after (a) 3 years, (c) 6 years, and (e) 11 years, respectively.*

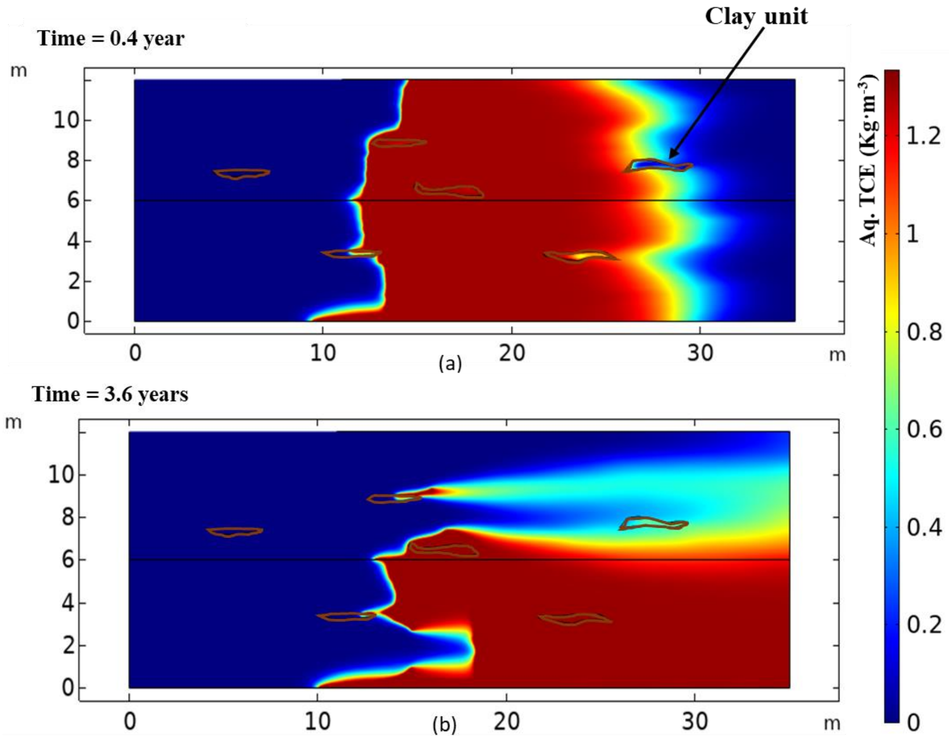

Figure 5-14: *Model prediction of aqueous TCE concentration in the Stage 2, and the impact of heterogeneity in the porous media. The transport in the clay lenses (indicated by brown arrow) (a) after 0.4 year is governed predominantly by diffusion process, and (b) after 3.6 years is governed by back-diffusion process. The time t =0 is the onset of the TCE dissolution in the aquifer.*

5.3.3 Stage 3: Injection of ENPs

Before the implementation of a remediation strategy of any contaminated aquifer, it is indispensable to perform robust calculations to determine the key parameters. In the case of the use of ENPs, parameters like length of the injection, concentration of ENPs, viscosity change due to CMC and groundwater flow field variation are needed to be estimated in advance, and this is the focus of the Stage 3 modeling. The starting point for the Stage 3 is the outcome of Stage 2 model at 11.5 years (Figure 5-15). The figure 5.15a show the remaining TCE mass represented by its saturation profile in the model domain. The enlarged image of the clay lens in the upper sand shows the saturation of remaining TCE pool on the top of the clay lens. Additionally, the model predicts a tiny mass of TCE ganglia formed at the sand interface (encircled by white dashes in Figure 5-15b) remains undepleted. These two sources along with a relatively large DNAPL pool leads to the continuous dissolution and transport of aqueous TCE in the model domain.

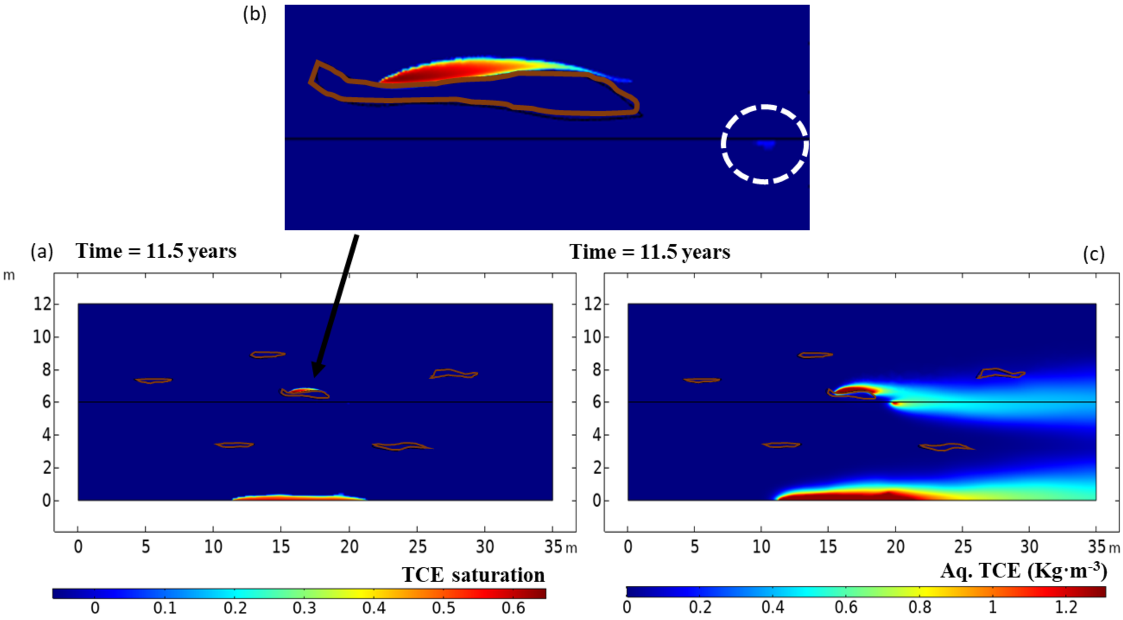

***Figure 5-15**: Initial condition for the modelling of the Stage 3, which corresponds to 11.5 years since the onset of dissolution of TCE. (a) TCE saturation distribution. (b) enlarged image for the DNAPL pool and the ganglia at the upper sand (c) Simulated TCE plume originating from the TCE pool and the small residual of ganglia.*

5.3.3.1 Impact of the injection fluid on the contaminant plume flow and the effect of viscosity

The injection of ENPs is expected to impact the natural groundwater flow. Figure 5-16 shows the model prediction for this impact if the injection fluid would be pure water; this results in the formation of a pollutant-free area within a radius of 0.6 m from the well after 1 hour of the injection (Figure 5-16a), reaching 3.4 meters after 1 day (Figure 5-16b). After 4 days of injection, the model predicts that the injection prevents downstream movement of the TCE plume (in 2 dimensions) (Figure 5-16c). Interestingly, the transport of contaminant is predicted to occur in the opposite direction due to the reversal of simulated groundwater flow near the well. After 8 days of injection, the model predicts a maximum horizontal transport of 2.5 meters opposite to the groundwater direction (Figure 5-16d). The simulation also estimates that the change in groundwater flow field due to ENP injection results in the change in the dissolved TCE originating from bedrock. The shape of the contaminant plume is primarily governed by new flow field, which depend on clay lens geometry and heterogeneity.

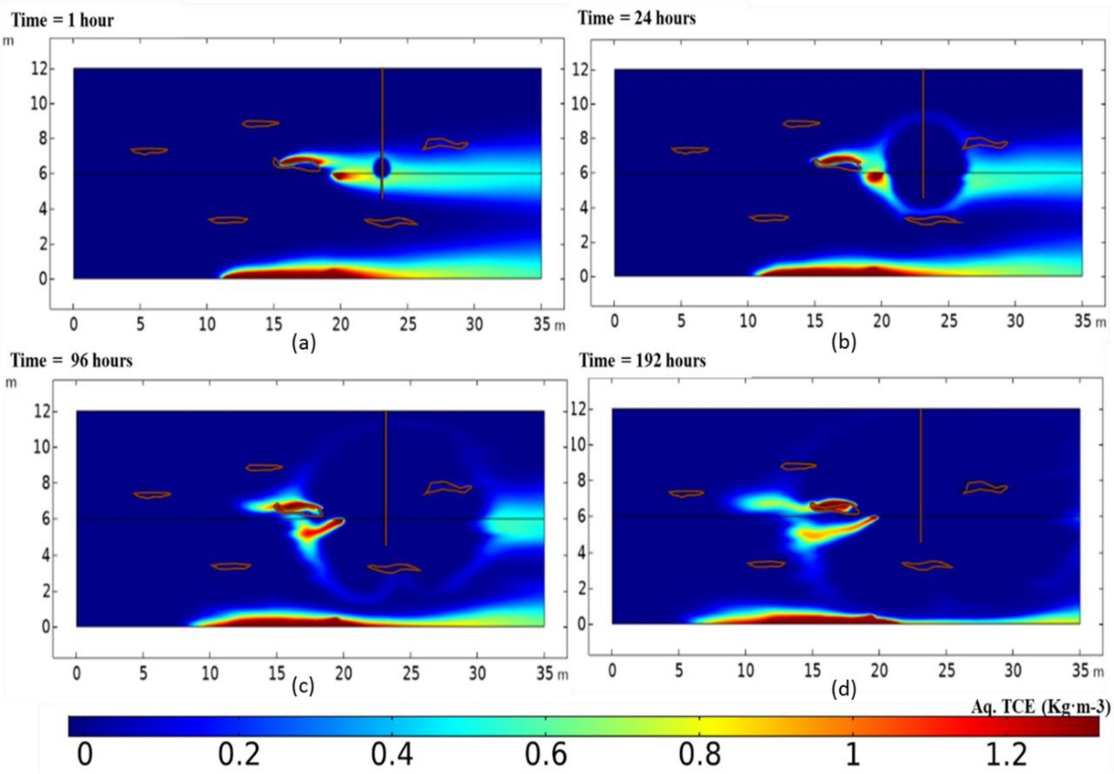

Figure 5-16: Model prediction of the impact of the injection of water on the TCE plume (Stage 3), (a) after 1 hour, (b) after 24 hours (c) after 96 hours, and (d) after 192 hours.

The ENP considered in this model exercise is the CMC-sZVI. Once suspended in the carrier fluid, this solution has a viscosity higher than water, and this is going to have an influence on the flow and transport mechanism in the simulated aquifer. With higher viscosity of CMC-ZVI injection, the impact on the natural fluid flow is expected to be less important compared to the injection with pure water (Figure 5-17). The model prediction of viscosity for a CMC-bearing injection after 2 hour of injection shows a nearly ellipsoid shaped plume centered with maximum radius of 0.9 meters measured from the well screen. For the CMC plume with the concentration of 5 kg·m^{-3}, the model predicts a corresponding viscosity of 0.002 Pa·s. The plume geometry of CMC and the viscosity distribution is the same due to their log-linear correlation given by equation 4.1. After 96 hours, the extent of CMC and viscosity change reaches up to 7.3 meters from the well (Figure 5-17c). This result indicates that the clay lens and heterogeneity give rise to a unique geometry of CMC plume. While the CMC and viscosity change evolution is predicted to occur in all directions, the groundwater flow leads to an asymmetrical plume geometry trending towards downgradient direction.

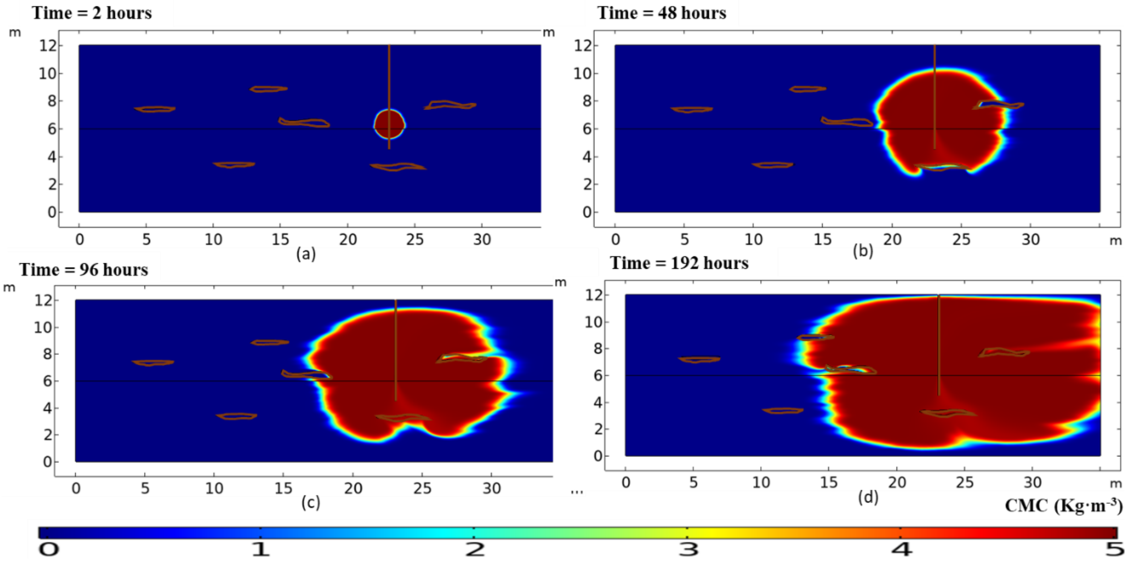

Figure 5-17: Model prediction for the CMC concentration after injection of CMC-sZVI solution after (a) 2 hours, (b) 48 hours, (c) 96 hours, and (d) 192 hours. The profile of viscosity in the simulated aquifer is same as the CMC concentration profile, due to the log-linear relationship between viscosity and CMC concentration.

5.3.3.2 Injection of ENPs

The injection and transport of ENPs is the key aspect in the Stage 3. The model predicts deposition of ENPs forming an underground barrier over the period of 192 hours (Figure 5-18). A symmetrical deposition around the well screen is predicted after 24 hours of injection. After 48 hours, the simulation estimates a Radius of influence (ROI), i.e., the maximum extent of the deposited ENPs measured radially from the well, of 0.4 meter (Figure 5-18b). The relatively larger deposition in the upper sand illustrates the role of hydrogeological properties in the mobility of the ENPs. As expected, a higher porosity and permeability lead to a higher spatial extent of ENP deposition. In the modelled case in this work, the deposition of sZVi occurs in both vertical directions forming an ellipsoidal-like geometry. The spread of sZVi in the lower sand layer is limited due to smaller permeability. The predicted barrier of deposited ENPs keeps growing as injection proceeds: ROI= 1.1 meters after 4 days, 1.5 meters after 8 days. The higher vertical spatial extent of ENPs in the upper sand layer is favorable to counter the contaminant from the relatively large TCE source. Similarly, the smaller spatial extent of deposited particle in the lower sand layer of the model domain is optimized for smaller TCE ganglia. The distance between the predicted TCE source and the estimated rim of the sZVI barrier is 3.2 meters. The amount of ENPs settled in the sand is calculated to be 1.8 Kg.

5.3.4 Stage 4: Contaminant degradation through interaction with ENPs

The reaction between TCE and sZVI is simulated to see (1) the time frame for aquifer remediation, (2) if the injection design is optimized, and (3) the occurrence of contaminant and quantify the amount of contaminant still left in the aquifer.

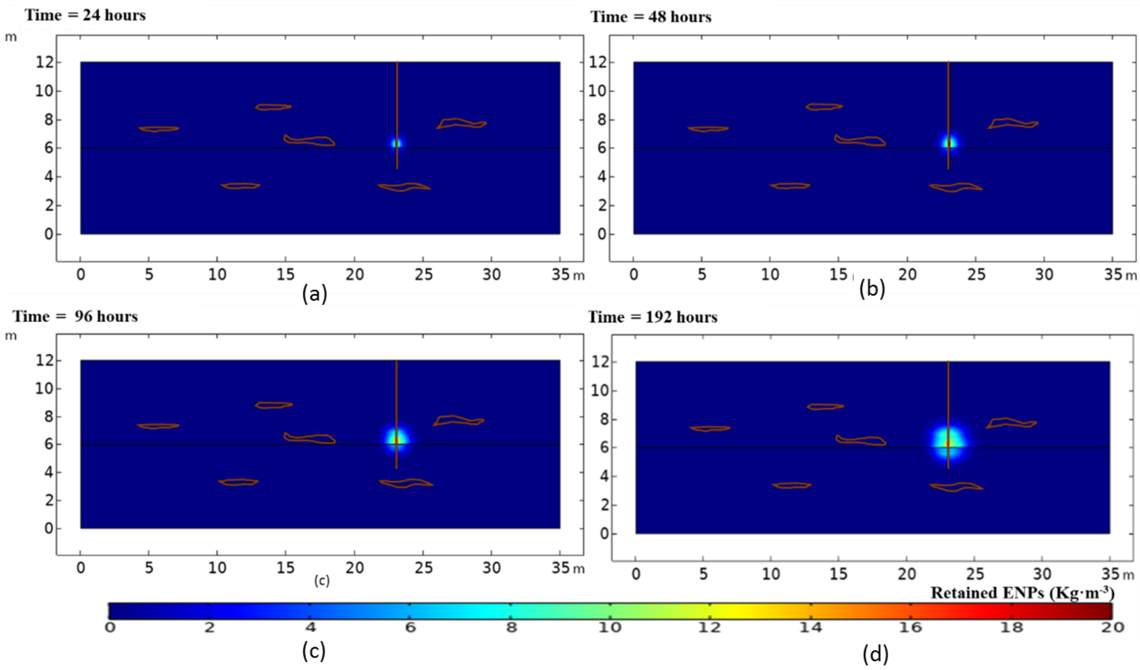

Figure 5-18: *Model prediction of the deposited ENPs (Radius of influence, ROI) after injection in kg·m^{-3} (Stage 4). (a) after 24 hours of injection (b) after 48 hours of injection (c) after 96 hour of injection (d) ROI of ENPs is 1.5 meters after 192 hours of injection.*

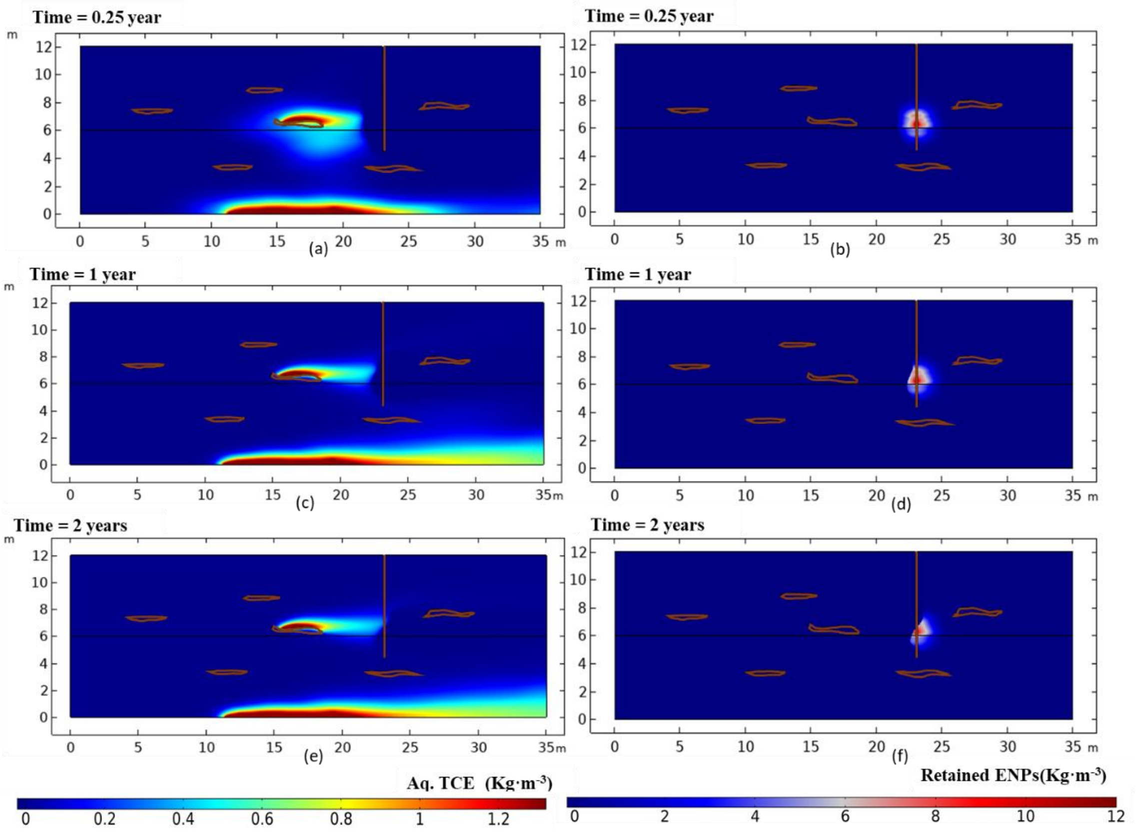

Figure 5-19: *Modelled distribution of dissolved TCE in kg$_{TCE}$·m$^{-3}_{water}$ and unreacted ENPs in Kg$_{sZVI}$·m^{-3} (a, b) 0.25 years, 1 year (c, d), 2 years (e, f) after the injection of ENPs in the aquifer (Stage 4).*

90 days after the injection of the sZVi, the model predicts a sharp termination of the TCE plume at the rim of the unreacted ENPs in the sand (Figure 5-19a). This result indicates that the ENPs successfully stops the progress of dissolved TCE plume in the downgradient direction, resulting in clean groundwater. Importantly, the model considers the reacted ENPs with dissolved TCE to be no longer active for further degradation, so the barrier is progressively exhausted (Figure 5-19b). After 1 year, the model predicts a minor progress of TCE plume in the downstream and depletion of unreacted ENPs, respectively (Figure 5-19, c and d). This implies that the slow groundwater flow controls the transport and amount of TCE degradation in the aquifer. This is also observed 2 years after the injection, when the model predicts 79% of unreacted ENPs still available for TCE degradation (Figure 5-19f).

The predicted mobility of sZVi and the contaminant plume in the following years is shown in Figure 5-20. After 3 years, the model estimates that the deposited sZVi is still sufficient to degrade the majority of TCE plume (Figure 5-20a). But after 5 years, the reduction in the ROI leads to the resumption of TCE plume, channelized around the ROI (Figure 5-20b), especially in the upper sand. After 8 years, the model predicts the 97% depletion of unreacted ENPs (Figure 5-20f) leading to full recovery of TCE plume geometry (Figure 5-20e). The prediction for plume geometry of TCE is same as the plume geometry before injection of the ENPs. However, the concentration of simulated aqueous TCE reaching at the aquifer boundary is different in both the cases (point p1 in Figure 5-20e). The predicted concentration after 8 years or remediation at point P1 is 0.18, 2.6 times lower than the concentration before remediation.

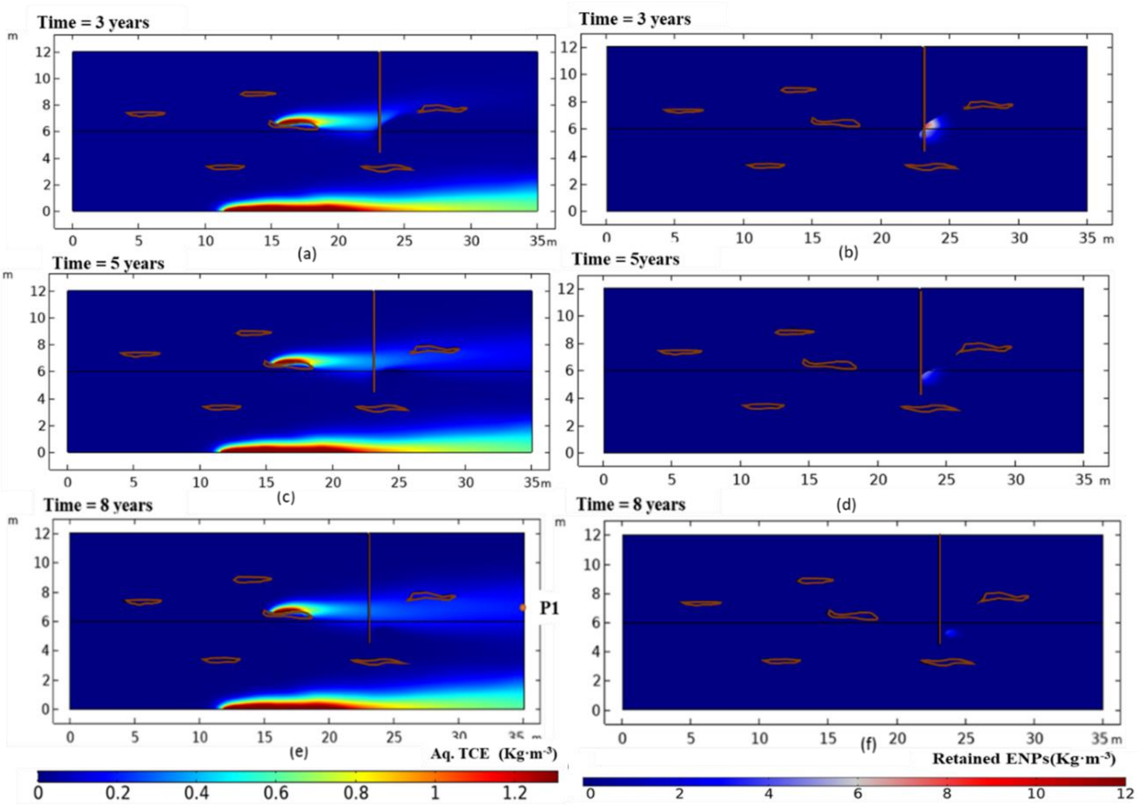

***Figure 5-20**: Modelled distribution of dissolved TCE in $kg_{TCE}{\cdot}m^{-3}{}_{water}$ and unreacted ENPs in $kg_{sZVi}{\cdot}m^{-3}$(a, b) 3 years, 5 years (c, d), 8 years (e, f) after the injection of ENPs in the aquifer (Stage 4).*

The general result of the Stage shows that while the limited amount of ENPs is not likely to remediate the groundwater completely, it is expected to clean the impacted groundwater for the time period for which is active for TCE degradation. The contaminant plume reactivates after the depletion of active ENPs but the reactivated plume would have lower concentration of pollutant as compared to before the reaction.

5.4 Conclusions

In this Chapter 5, an integrated numerical framework providing end-to-end modeling solution has been proposed and tested. Such numerical framework is useful as it bridges the gap of information between each key aspects of a remediation strategy and evaluates the interplay of each governing mechanisms related to contamination-remediation dynamics in the groundwater. The modeling exercise demonstrates the relevant predictive insights that can be used for characterizing the field and predicting the performance of remediation tasks. For this purpose, the model uses a hypothetical aquifer, with realistic hydrogeological properties including a natural groundwater flow. The event of contaminant and subsequent planning of remediation have been divided into four stages. The model successfully simulates the primary stage of TCE phase infiltration in the 2-dimensional aquifer domain. The result shows the predicted DNAPL source zone architecture which otherwise is challenging to be obtained from field. Using the result of first stage as the starting point, the model further simulates the dissolution of TCE and transport of aqueous contaminant aquifer over the decade (Stage 2). Thus, the result shows the simulation can successfully help in the reconstruction of past contamination event in a real aquifer. For the degradation of contaminant, a predictive analysis is required to study the efficiency of remediation process and optimization of its implementation. Therefore, in the Stage 3, the transport and retention of sZVi in the model domain has been simulated. The results demonstrate that the predictive insight of sZVi behavior can be used for designing the optimized deployment of sZVi in the contaminant site. In the last step, a reactive transport modeling of aqueous TCE degradation due to sZVi has been developed. The result from this step determines the time frame, amount of TCE degradation and possibility of reoccurrence of contaminant in the simulated aquifer. The uniqueness of this modeling exercise lies in its integrated approach for studying contamination and remediation process. With multi-stage modeling, the numerical tool offers an end-to-end modeling solution for developing remediation strategy. Additionally, the model can be upscaled to 3D field scale domain incorporating complex geometry and interaction of groundwater, contaminant, and ENPs. Thus, this research study opens a new numerical approach for the assessment of field site and development of remediation strategies. Further studies are required to use real field data and calibration for the industrial scale use of the model.

5.5 References

Clement, T.P., Johnson, C.D., Sun, Y., Klecka, G.M., Bartlett, C., 2000. Natural attenuation of chlorinated ethene compounds: model development and field-scale application at the Dover site. J. Contam. Hydrol. 42, 113–140.

Fagerlund, F., Illangasekare, T.H., Phenrat, T., Kim, H.-J., Lowry, G.V., 2012. PCE dissolution and simultaneous dechlorination by nanoscale zero-valent iron particles in a DNAPL source zone. J. Contam. Hydrol. 131, 9–28.

Grathwohl, P., 2012. Diffusion in natural porous media: contaminant transport, sorption/desorption and dissolution kinetics. Springer Science & Business Media.

Han, Y., Yan, W., 2016. Reductive dechlorination of trichloroethene by zero-valent iron nanoparticles: reactivity enhancement through sulfidation treatment. Environ. Sci. Technol. 50, 12992–13001.

Kokkinaki, A., 2013. Modelling of dissolution and bioremediation of chlorinated ethene DNAPL source zones (PhD Thesis).

Krol, M.M., Oleniuk, A.J., Kocur, C.M., Sleep, B.E., Bennett, P., Xiong, Z., O'Carroll, D.M., 2013. A field-validated model for in situ transport of polymer-stabilized nZVI and implications for subsurface injection. Environ. Sci. Technol. 47, 7332–7340.

Lerner, D.N., Kueper, B.H., Wealthall, G.P., Smith, J.W.N., Leharne, S.A., 2003. An illustrated handbook of DNAPL transport and fate in the subsurface.

Li, J., Bhattacharjee, S., Ghoshal, S., 2015. The effects of viscosity of carboxymethyl cellulose on aggregation and transport of nanoscale zerovalent iron. Colloids Surf. Physicochem. Eng. Asp. 481, 451–459.

Nambi, I.M., Powers, S.E., 2003. Mass transfer correlations for nonaqueous phase liquid dissolution from regions with high initial saturations. Water Resour. Res. 39.

Oolman, T., Godard, S.T., Pope, G.A., Jin, M., Kirchner, K., 1995. DNAPL flow behavior in a contaminated aquifer: Evaluation of field data. Groundw. Monit. Remediat. 15, 125–137.

Oostrom, M., Rockhold, M.L., Thorne, P.D., Last, G.V., Truex, M.J., 2004. Three-Dimensional Modeling of DNAPL in the Subsurface of the 216-Z-9 Trench at the Hanford Site. Pacific Northwest National Lab. (PNNL), Richland, WA (United States).

Pankow, J.F., Cherry, J.A., 1996. Dense chlorinated solvents and other DNAPLs in groundwater: History, behavior, and remediation.

Soga, K., Page, J.W.E., Illangasekare, T.H., 2004. A review of NAPL source zone remediation efficiency and the mass flux approach. J. Hazard. Mater. 110, 13–27.

Tosco, T., Sethi, R., 2010. Transport of non-Newtonian suspensions of highly concentrated micro-and nanoscale iron particles in porous media: a modeling approach. Environ. Sci. Technol. 44, 9062–9068.

Weis, B.K., Susten, A.S., 1999. Groundwater contamination by PCE and TCE: ATSDR's approach to evaluating public health hazard. Agency for Toxic Substances and Disease Registry, Atlanta, GA (US).

Xu, J., Wang, Y., Weng, C., Bai, W., Jiao, Y., Kaegi, R., Lowry, G.V., 2019. Reactivity, Selectivity, and Long-term Performance of Sulfidized Nanoscale Zerovalent Iron with Different Properties. Environ. Sci. Technol.

6 Final summary and future perspectives

The field scale remediation of groundwater requires a lot of scientific investigation and technical resources, owing to complexity and the limited accessibility of the contamination-groundwater system. Therefore, it is necessary to develop a robust remediation strategy which includes laboratory scale and field scale studies as well as application of numerical tool. The success in the remediation effort is often limited by lack of detailed understanding of the contaminant and hydrogeological properties of the aquifer. While, the information of contamination-aquifer dynamics can be studied at field, knowledge on the continuous and consistent contamination behavior on both temporal and spatial scale is often missing. The integrated numerical model can be used for bridging the gap between the field studies and the relevant insights required for groundwater remediation.

In this study, the infiltration of DNAPL in aquifer and the dependence of the DNAPL migration pathway on clay lenses have been studied in a two-phase flow model in Chapter 3. For the first research work in this doctoral study (RW1; Chapter 1), the objective has been the development a numerical formulation for two-phase flow in a porous media using Comsol software and verify it with benchmark models. The numerical formulation has been developed and a two-step verification approach has been conceptualized in Chapter 3. In the first step, the DNAPL infiltration in a 1 -dimensional small-scale homogeneous sand has been developed and matched with the benchmark model. In the second stage, a 2-dimensional model has been built with the aquifer domain consisting of several sand layers. The result shows that the numerical formulation is in good agreement with the results from benchmark model. With this verified numerical formulation, the upscaled 3D model is developed with a general groundwater system scenario. The objective for this exercise includes a comprehensive study of migration of DNAPL in the real field scenario (RW 2). As only with the field characterization, the understanding of the DNAPL flow behavior remains incomplete, the developed model demonstrates its potential in understanding the migration pathways and timeline. Overall, the result shows the model potential for serving as an excellent numerical tool in developing and facilitating the remediation of groundwater contaminants.

For an efficient remediation, an optimized implementation of nano-particle injection in the aquifer is indispensable. While the performance of the remediating particles is not well known before the injection, the numerical tools can help predict the fate of ENPs in the aquifer. With the aim of developing a numerical tool to facilitate such studies, several models were developed in both column scale and tank scale sand. A profound literature survey for the mechanism and equation governing the ENP´s fate has been presented in Chapter 2. With these equations a numerical formulation has been developed on Comsol software (Chapter 4) and verified using the benchmark models published in literature, which was also one of the main objectives (RW 3) of this thesis. On this verified formulation, the inverse model has been built to determine the parameter values driving the ENPs mobility in sand-filled columns. The sensitivity analysis has been also performed to demonstrate the extent of the uncertainty associated with each estimated parameter. Finally, the parameter obtained has been used to simulate the ENPs injection in a sand-filled tank. The model, however, uses a simplistic velocity independent parameter for simulation in absence of necessary data, and, thus, the predictive results have been different from the results observed in laboratory. Nevertheless, the modeling exercise shows the potential of the numerical approach to simulate nano-particle injection in the aquifer which was one of the main objectives of the thesis (RW 4).

Once individual numerical models are designed and applied for the study of both contaminant and remediation aspects, an integrated numerical framework has been built (RW 5). Such numerical approach can serve as a robust tool for facilitating the study involved in each stage of groundwater remediation strategy. Therefore, in Chapter 5, the capability of models from previous chapters are extended to cover the entire numerical assessment of remediation schemes. For this, the contamination infiltration in a 2-dimensional domain is simulated using the same two-phase formulation as in Chapter 3. The DNAPL source zone architecture predicted by the model has been used for modeling the dissolution and transport of aqueous contaminant in the following stage. The model results from this stage predicts the spatial and temporal distribution of contaminant which is important for nano-particle remediation process. Considering these results as the extent of contamination in the aquifer domain, in the subsequent stage, a model has been developed to simulate the injection of ENPs in the aquifer. The result from this modeling exercise predicts the transport and retention of ENPs in the model domain. In the final stage, with the aim of studying the contaminant degradation, a reactive transport model has been developed which simulates the transport of aqueous contaminant as well as their degradation due to presence of ENPs. The study demonstrates the development of a robust numerical approach that can provide an end-to-end modeling solution for a general remediation strategy using ENPs injection in a contaminated aquifer.

The modeling is a representation of the reality and most of the time is simplified to focus on the main aspects of interest. In this work as well, several assumptions have been made for the simplification. The model in the Chapter 3 assumes the DNAPL to be immiscible with water and consider the porosity to be inelastic. The model also considers that there is no mass loss of DNAPL by chemical degradation or mineral surface adsorption. The effect of groundwater flow rate or recharge has not been considered on DNAPL flow rate. In Chapter 4, the tank scale model has been developed considering the constant interaction coefficients which is simplification of the general case. The effect of clogging on the ENPs transport and retention in the sand-filled tank has been considered to be negligible. Similarly, in Chapter 5, the model considers no natural chemical degradation of TCE, and the clogging due to ENPs has not again considered for the simplification of the model development.

This doctoral work opens the scope of incorporating this numerical approach in different aspects of groundwater remediation. This work could further be strengthened by validating it with the data from field scale studies. Such a study would improve the simulation capabilities of the integrated framework correct functioning on a field scale. From the numerical side as well, the work opens the scope of developing a coupled multiphase multicomponent reactive transport model that also includes the ENPs injection. This will be particularly helpful for an active DNAPL site which has undergone a recent event of contaminant spillage.

Furthermore, the vadose zone plays an important role in governing the contaminant in the aquifer. Therefore, numerical studies of contaminant in unsaturated zone and their influence in the underlying aquifer becomes important. Additionally, the real case aquifer can have high macro and micro scale heterogeneities and have fluctuating groundwater dynamics. Incorporating of these complex dynamics in the numerical model can further strengthen its capability. This research work overall serves as a good reference point for a profound integration of numerical model and field as well as studies for groundwater remediation.

7 Resumen final y perspectivas de futuro

La remediación de aguas subterráneas a escala de campo requiere mucha investigación científica y recursos técnicos, debido a la complejidad y la accesibilidad limitada del sistema de contaminación-aguas subterráneas. Por lo tanto, es necesario desarrollar una estrategia de remediación sólida que incluya estudios a escala de laboratorio y de campo, así como la aplicación de herramientas numéricas. El éxito en el esfuerzo de remediación a menudo se ve limitado por la falta de un conocimiento detallado de las propiedades hidrogeológicas y de contaminantes del acuífero. Si bien la información sobre la dinámica de la contaminación y el acuífero se puede estudiar en el campo, a menudo se carece de conocimiento sobre el comportamiento continuo y constante de la contaminación, tanto a escala temporal como espacial. El modelo numérico integrado se puede utilizar para cerrar la brecha entre los estudios de campo y los conocimientos relevantes necesarios para la remediación de aguas subterráneas.

En este estudio, la infiltración de DNAPL en el acuífero y la dependencia de la migración de DNAPL en capas de arcilla se han estudiado en un modelo de flujo de dos fases en el Capítulo 3. Para el primer trabajo de investigación en este estudio de doctorado (RW1; Capítulo 1), el objetivo ha sido el desarrollo de una formulación numérica para flujo bifásico en un medio poroso utilizando el software Comsol y verificarlo con modelos de referencia. Se ha desarrollado la formulación numérica y se ha conceptualizado un enfoque de verificación de dos pasos en el Capítulo 3. En el primer paso, la infiltración de DNAPL en una arena homogénea de pequeña escala unidimensional se ha desarrollado y acoplado con el modelo de referencia. En la segunda etapa, se ha construido un modelo bidimensional con el dominio del acuífero formado por varias capas de arena. El resultado muestra que la formulación numérica está de acuerdo con los resultados del modelo de referencia. Con esta formulación numérica verificada, el modelo 3D mejorado se ha desarrollado con un escenario general del sistema de agua subterránea. El objetivo de este ejercicio ha incluido un estudio integral de la migración de DNAPL en el escenario de campo real (RW 2). Con sólo la caracterización de campo, la comprensión del comportamiento del flujo de DNAPL sigue siendo incompleta, y por tanto, el modelo desarrollado demuestra su potencial para comprender las vías de migración y la línea de tiempo. En general, el resultado muestra el potencial del modelo como una excelente herramienta numérica para desarrollar y facilitar la remediación de contaminantes del agua subterránea.

Para una remediación eficiente, es indispensable una implementación optimizada de la inyección de nanopartículas en el acuífero. Si bien el rendimiento de las partículas de remediación no se conoce bien antes de la inyección, las herramientas numéricas pueden ayudar a predecir el destino de los ENP en el acuífero. Con el objetivo de desarrollar una herramienta numérica que facilite dichos estudios, se desarrollaron varios modelos tanto en arena a escala de columna como a escala de tanque. En el Capítulo 2 se ha presentado un estudio detallado de la literatura sobre el mecanismo y la ecuación que rigen el destino de la ENP. Con estas ecuaciones se ha desarrollado una formulación numérica en el software Comsol (Capítulo 4) y se ha verificado utilizando los modelos de referencia publicados en la literatura, que fue también uno de los principales objetivos (RW 3) de esta tesis. Sobre esta formulación verificada, se ha construido el modelo inverso para determinar los valores de los parámetros que impulsan la movilidad de los ENP en columnas rellenas de arena. El análisis de sensibilidad también se ha realizado para demostrar el alcance de la incertidumbre asociada con cada parámetro estimado.

Finalmente, el parámetro obtenido se ha utilizado para simular la inyección de ENPs en un tanque lleno de arena. Sin embargo, el modelo utiliza un parámetro simplista independiente de la velocidad del flujo para la simulación ya que no existen de los datos experimentales necesarios y, por lo tanto, los resultados predictivos han sido ligeramente diferentes de los resultados observados en el laboratorio. Sin embargo, el ejercicio de modelado muestra el potencial del enfoque numérico para simular la inyección de nanopartículas en el acuífero, que fue uno de los principales objetivos de la tesis (RW 4).

Una vez que se han diseñado y aplicado los modelos numéricos individuales para el estudio de los aspectos tanto de los contaminantes como de la remediación, se ha construido un marco numérico integrado (RW 5). Este enfoque numérico puede servir como una herramienta sólida para facilitar el estudio involucrado en cada etapa de la estrategia de remediación de aguas subterráneas. Por lo tanto, en el Capítulo 5, la capacidad de los modelos de los capítulos anteriores se ha ampliado para cubrir la evaluación numérica completa de los esquemas de remediación. Para ello, se simula la infiltración de contaminación en un dominio bidimensional utilizando la misma formulación de dos fases que en el Capítulo 3. La arquitectura de la zona de origen de DNAPL predicha por el modelo se ha utilizado para modelar la disolución y el transporte de contaminantes acuosos en lo siguiente etapa. Los resultados del modelo de esta etapa predicen la distribución espacial y temporal de contaminantes que es importante para el proceso de remediación de nanopartículas. Considerando estos resultados como la extensión de la contaminación en el dominio del acuífero, en la etapa posterior se ha desarrollado un modelo para simular la inyección de ENPs en el acuífero. El resultado de este ejercicio de modelado predice el transporte y la retención de ENP en el dominio del modelo. En la etapa final, con el objetivo de estudiar la degradación de contaminantes, se ha desarrollado un modelo de transporte reactivo que simula el transporte de contaminantes en disolución, así como su degradación por presencia de ENPs. El estudio demuestra el desarrollo de un enfoque numérico robusto que puede proporcionar una solución de modelado de extremo a extremo para una estrategia de remediación general utilizando la inyección de ENP en un acuífero contaminado.

El modelado es una representación de la realidad y la mayoría de las veces se simplifica para centrarse en los principales aspectos de interés. También en este trabajo, se han hecho varias asunciones para la simplificación. El modelo del Capítulo 3 asume que el DNAPL es inmiscible con agua y considera que la porosidad es inelástica. El modelo también considera que no hay pérdida de masa de DNAPL por degradación química o adsorción de superficie mineral. El efecto del flujo de agua subterránea o la recarga no se ha considerado en el flujo de DNAPL. En el Capítulo 4, el modelo a escala del tanque se ha desarrollado considerando los coeficientes de interacción constantes, lo cual es una simplificación del caso general. El efecto de la obstrucción en el transporte y retención de los ENP en el tanque lleno de arena se ha considerado insignificante. De manera similar, en el Capítulo 5, el modelo no considera la degradación química natural del TCE y la obstrucción debida a los ENP no se ha considerado nuevamente para la simplificación del desarrollo del modelo.

Este trabajo de doctorado abre la perspectiva de incorporar este enfoque numérico en diferentes aspectos de la remediación de aguas subterráneas. Este trabajo podría fortalecerse aún más al validarlo con los datos de estudios a escala de campo. Un estudio de este tipo mejoraría las capacidades de simulación del funcionamiento correcto del marco integrado a escala de campo. También desde el punto de vista numérico, el trabajo abre el campo de desarrollo de un modelo de transporte reactivo multicomponente multifásico acoplado que también incluye la inyección de ENP. Esto será particularmente útil para un sitio DNAPL activo que ha sufrido un evento reciente de derrame de contaminantes.

Además, la zona vadosa juega un papel importante en el control del contaminante en el acuífero. Por lo tanto, los estudios numéricos de contaminantes en zonas no saturadas y su influencia en el acuífero subyacente se vuelven importantes. Además, el acuífero del caso real puede tener importantes heterogeneidades a macro y microescala y tener una dinámica de agua subterránea fluctuante. La incorporación de estas dinámicas complejas en el modelo numérico puede fortalecer aún más su capacidad. Este trabajo de investigación en general sirve como un buen punto de referencia para una profunda integración del modelo numérico y de campo, así como los estudios para la remediación de aguas subterráneas.

Appendix A: Review of Formulation for two phase flow.

A.1 Variables for mathematical formulation of two-phase flow in porous media

The DNAPL infiltration in an aquifer requires solving two phase flow equation in porous media. These equations represent the interdependence of DNAPL and groundwater flow on a macroscopic scale. For two-phase flow involving water and DNAPL, the governing equations are equations A.1, A.2, A.3 and A.4. Please refer to chapter 2 for a detailed review.

$$\theta \frac{\partial(S_w)}{\partial t} = \nabla.\left(k \frac{k_{rw}}{\mu_w}(\nabla p_w - \rho_w g)\right) + q_w \qquad \text{(eq. A.1)}$$

$$\theta \frac{\partial(S_n)}{\partial t} = \nabla.\left(k \frac{k_{rn}}{\mu_n}(\nabla p_n - \rho_n g)\right) + q_n \qquad \text{(eq. A.2)}$$

Where S_n and S_w are the saturation of DNAPL and water, respectively, p_n and p_w are the pressure of DNAPL and water, θ is porosity, and k is permeability of the sand. q_w and q_n are the volumetric source term for water and DNAPL respectively.

$$S_n + S_w = 1 \qquad \text{(eq. A.3)}$$

$$p_n - p_w = p_c(Sw) \qquad \text{(eq. A.4)}$$

Where p_c is the capillary pressure defined as a function of water saturation.

With four variables and four equations, the system of equations can be approximated using the Finite Element Method (FEM). However, the four primary variables for solving the set of equations results in higher degrees of freedom (DOFs) for the model. Solving the model with relatively higher DOFs requires big computational resources and time. To reduce the DOFs, several studies have used algebraic modifications to represent the mass conservation equations with reduced degrees of freedom (Chen et al., 2006; Wu and Forsyth, 2001). Using the linear combination of constitutive relationships, the system of equations can be reduced to two equations, with two primary variables. Several studies in literature have used different pairs of primary variables for developing numerical formulation of two-phase flow equations (Kolditz et al., 2012; Wu and Forsyth, 2001; Helmig, 1997). Each of such pairs of primary variables has its own advantages and disadvantages in terms of numerical solution. A brief review for each relevant pair has been done in the next section.

A.1.1 Pressure-Pressure formulation

In this formulation, the pressure of each phase is taken as primary variables for solving set of PDEs equation. This is implemented by defining a pressure derivative with respect to saturation which allows skipping the saturation term in the Equations A.5, A.6 and A.7.

$$\theta c \frac{\partial(P_w)}{\partial t} = \nabla.\left(k \frac{k_{rw}}{\mu_w}(\nabla p_w - \rho_w g)\right) + q_w + \theta c \frac{\partial(P_n)}{\partial t} \qquad \text{(eq. A.5)}$$

$$\theta c \frac{\partial(P_n)}{\partial t} = \nabla.\left(k\frac{k_{rn}}{\mu_n}(\nabla p_n - \rho_n g)\right) + q_n + \theta c \frac{\partial(P_w)}{\partial t} \quad \text{(eq. A.6)}$$

$$c = -\frac{\partial(S_w)}{\partial P_c} \quad \text{(eq. A.7)}$$

The above system equation is highly nonlinear and coupled. However, this formulation has limited utility due to its poor prediction capability for smaller capillary gradients, as well as in dry conditions (Wu and Forsyth, 2001; Helmig, 1997).

A.1.2 Capillary Pressure - Phase Pressure formulation

This Capillary Pressure - Phase Pressure formulation uses the capillary pressure and a fluid pressure as primary variables (Kolditz et al., 2012). The set of equations is built by defining pressure derivative with respect to saturation and, thus, eliminating the temporal saturation gradient term (eq. A.8 and eq. A.9).

$$-\theta c \frac{\partial(P_c)}{\partial t} = \nabla.\left(k\frac{k_{rw}}{\mu_w}(\nabla p_w - \rho_w g)\right) + q_w \quad \text{(eq. A.8)}$$

$$\theta c \frac{\partial(P_c)}{\partial t} = \nabla.\left(k\frac{k_{rn}}{\mu_n}(\nabla p_w + \nabla P_c - \rho_n g)\right) + q_n \quad \text{(eq. A.9)}$$

Having capillary pressure as a primary variable is advantageous as the continuity in capillary pressure becomes useful in conditions like heterogeneous porous media (Park et al., 2011). However, it may be difficult to assign meaningful initial and boundary conditions for field case scenarios.

A.1.3 Coupled Phase Pressure-Phase Saturation Formulation

In the Coupled Phase Pressure-Phase Saturation formulation mass conservation equations are represented by pressure of one of the phases while saturation is used to represent the other phase (eq. A.10 and eq. A.11).

$$\theta \frac{\partial(S_w)}{\partial t} = \nabla.\left(k\frac{k_{rw}}{\mu_w}(\nabla p_w - \rho_w g)\right) + q_w \quad \text{(eq. A.10)}$$

$$-\theta \frac{\partial(S_w)}{\partial t} = \nabla.\left(k\frac{k_{rn}}{\mu_n}\left(\nabla p_w + \frac{\partial(p_c)}{\partial(S_w)}\nabla S_w - \rho_n g\right)\right) + q_n \quad \text{(eq. A.11)}$$

As the pressure and saturation are continuous throughout the underground system, the convergence criteria of the model are easily achieved. Unlike the pressure-pressure formulation, the advantage of the coupled phase pressure-phase saturation is that it works well in the region where capillary gradient is low and, therefore, it is an ideal formulation for heterogeneous media. Its easy implementation has made it a preferred method in the past (Thorenz, 2001; Kueper and Frind, 1991). However, due to the absence of the explicit capillary pressure term in the expression, it does not work well in the heterogeneous media with different entry pressure unless additional conditional equations are applied.

A.1.4 Decoupled Phase Pressure-Phase Saturation Formulation

Combining equations 2.21 and 2.22 can allow skipping the temporal derivative of saturation term from each equation. This leads to the system of equations as follows (eq. A.12 and eq. A.13):

$$\nabla.\left(k\frac{k_{rw}}{\mu_w}(\nabla p_w - \rho_w g)\right) + \nabla.\left(k\frac{k_{rn}}{\mu_n}\left(\nabla p_w + \frac{\partial(p_c)}{\partial(S_w)}\nabla S_w - \rho_n g\right)\right) = q_w + q_n \qquad \text{(eq. A.12)}$$

$$\theta\frac{\partial(S_w)}{\partial t} = \nabla.\left(k\frac{k_{rw}}{\mu_w}(\nabla p_w - \rho_w g)\right) + q_w \qquad \text{(eq. A.13)}$$

This equation system can be solved using pressure of water as the primary variable for the first equation and the saturation of DNAPL for the second equation. This formulation has been widely used in a numerical scheme known as Implicit Pressure, Explicit Saturation (IMPES) (Kolditz *et al.*, 2012; Hoteit and Firoozabadi, 2008; Chen et al., 2006). Here, the pressure is estimated firstly with an implicit numerical scheme that is independent of saturation. Once the pressure for that time step is known, Equation 2.33 is used to calculate the saturation of the phase. In this thesis, the IMPES formulation has been used to simulate DNAPL infiltration in the aquifer system. This selection has been made because the IMPES numerical scheme will be convenient in terms of computational time and numerical accuracy since the study cases are related to a field scale heterogeneous porous media with significant capillary forces.

A.1.5 Global Pressure – Phase Saturation Formulation

The concept of global pressure was first introduced by Antontsev (1972) and Chavent and Jaffré (1986) and has been used widely in the literature to solve two-phase flow problems. This method first defines a fractional flow function (eq. A.14 and A.15).

$$f_o = \frac{\lambda_n}{\lambda_n + \lambda_w} \qquad \text{(eq. A.14)}$$

$$f_w = \frac{\lambda_w}{\lambda_n + \lambda_w} \qquad \text{(eq. A.15)}$$

Where f_w and f_n is defined as the fractional flow of water and DNAPL phase,

λ_w and λ_n are defined as the mobility of water and DNAPL phase which are given by Equations A.16 and A.17:

$$\lambda_w = \frac{k_{rw}}{\mu_w} \qquad \text{(eq. A.16)}$$

$$\lambda_n = \frac{k_{rn}}{\mu_n} \qquad \text{(eq. A.17)}$$

Then, the global pressure*(p)* and total velocity*(u)* is defined as Equations A.18 and A.19:

$$\nabla.p = f_w\nabla.p_w + f_o\nabla.p_n \qquad \text{(eq. A.18)}$$

$$u = u_w + u_n = -k\,(\lambda_w + \lambda_n)(\nabla p - (\rho_w f_w + \rho_n f_n)g\nabla z) \qquad \text{(eq. A.19)}$$

An algebraic modification of the mass conservation equation for an individual phase in Equations A.18 and A.19 leads to Equations A.20 and A.21 (Chen et al., 2006).

$$\nabla.u = \frac{q_w}{\rho_w} + \frac{q_n}{\rho_n} \qquad \text{(eq. A.20)}$$

$$-\nabla.(k\,\lambda(\nabla p-\ (\rho_w f_w+\ \rho_n f_n)g\nabla z)=\frac{q_w}{\rho_w}+\frac{q_n}{\rho_n} \tag{eq. A.21}$$

Where *u* can be given by equation A.19 using the following Equation A.22 and A.23

$$u_w=\ f_w u+k\lambda_n f_w\nabla p_c+k\lambda_n f_w(\rho_w-\rho_n)g\nabla z \tag{eq. A.22}$$

$$u_n=\ f_n u+k\lambda_w f_n\nabla p_c+k\lambda_w f_n(\rho_w-\rho_n)g\nabla z$$
(eq. A.23)

Once the total velocity is calculated from Equation A.22, the saturation of water can be obtained from Equation A.24:

$$\theta\frac{\partial(S_w)}{\partial t}=-\nabla.\left(f_w u+k\lambda_n f_w\left(\frac{\partial p_c}{\partial S_w}\nabla S_w+(\rho_w-\rho_n)g\nabla z\right)\right)+\ \frac{q_w}{\rho_w} \tag{eq. A.24}$$

The use of this equation has the advantage that by introducing the global pressure, the equation becomes analogous to a single fluid flow system which reduces the coupling between equations (Chen et al., 2006). The mobility and pressure of the global fluid system are always continuous spatially and temporally, thus facilitating the achievement of the numerical convergence of the equation system solution. However, the global pressure variable is not an actual physical property of the system, and, therefore, it may become difficult to define both initial and boundary conditions of this variable.

A.2 References

Antontsev, S.N., 1972. On the solvability of boundary value problems for degenerate two-phase porous flow equations. Dinamika Splosnoi Sredy Vyp 10, 28–53.

Chavent, G., Jaffré, J., 1986. Mathematical models and finite elements for reservoir simulation: single phase, multiphase and multicomponent flows through porous media. Elsevier.

Chen, Z., Huan, G., Ma, Y., 2006. Computational methods for multiphase flows in porous media. SIAM.

Forsyth, P.A., Wu, Y.S., Pruess, K., 1995. Robust numerical methods for saturated-unsaturated flow with dry initial conditions in heterogeneous media. Advances in Water Resources 18, 25–38.

Helmig, R., 1997. Multiphase flow and transport processes in the subsurface: a contribution to the modeling of hydrosystems. Springer-Verlag.

Hoteit, H., Firoozabadi, A., 2008. An efficient numerical model for incompressible two-phase flow in fractured media. Advances in Water Resources 31, 891–905.

Kolditz, O., Görke, U.-J., Shao, H., Wang, W., 2012. Thermo-hydro-mechanical-chemical processes in porous media: benchmarks and examples. Springer Science & Business Media.

Kueper, B.H., Frind, E.O., 1991. Two-phase flow in heterogeneous porous media: 1. Model development. Water Resources Research 27, 1049–1057.

Sainz-Garcia, A., 2017. Dynamics of underground gas storage. Insights from numerical models for carbon dioxide and hydrogen. (PhD Thesis). Université Toulouse 3 Paul Sabatier (UT3 Paul Sabatier).

Thorenz, C., 2001. Model adaptive simulation of multiphase and density driven flow in fractured and porous media.

Wu, Y.-S., Forsyth, P.A., 2001. On the selection of primary variables in numerical formulation for modeling multiphase flow in porous media. Journal of contaminant hydrology 48, 277–304.

Appendix B: Sensitivity analysis for ENPs transport and retention in saturated sand

Sensitivity analysis has been performed to study the effect of uncertainty in the relevant parameters governing the transport and retention of ENPs in a sand-filled column. The advantage of such sensitivity analysis are manifolds. It indicates the interplay of different parameters influencing the transport and retention behavior of the particle. The complexity of inverse model is largely determined by number of unknown parameters and their non-linear co-dependence. The parameters estimated from the inverse modeling have different degree of uncertainty. With the sensitivity analysis, the degree of uncertainty can be speculated. If the transport and retention characteristic of ENPs is highly sensitive to a parameter, then the degree of uncertainty for that parameter is relatively less. In contrast, a higher degree of uncertainty is possible for the parameter for which the ENP´s mobility has a relatively lower sensitivity. From the numerical approach point of view, the robustness of the calculation depends on the model performance compared to experimental result. With the sensitivity analysis, the inaccuracy of the inverse modeling result can be diagnosed by determining the parameters which has high degree of uncertainty.

The model developed for sZVi injection in sand filled column (section 4.2.2; setup 1) has been considered as the reference model. The model considers that the retention of sZVi in the sand-filled column is governed by ripening and straining mechanisms. Five different parameters governing the ENPs behavior, namely, column length, attachment rate, detachment coefficient, multiplier coefficient and exponential coefficient, are studied. Each parameter is varied within a relevant range while keeping other parameters constant. The base values for each parameter are taken from the value obtained estimated through the reference model. Thus, the result of the sensitivity analysis will certainly be applicable for the model set up used in Chapter 4 but may not be generalized for other cases.

B.1. Sensitivity analysis for column length

The sensitivity analysis has been performed to understand the effect of sand column length on nano-particle transport and retention. The Figure B-1 shows the sensitivity of nano-particle transport with respect to column length of 6.25 cm, 12.5 cm and 25 cm, respectively. The model predicts relatively higher arrival time for the column with higher column length. However, the predicted breakthrough concentration is distinctly different for each column length. The model predicts that the peak of effluent concentration decreases with increase in column length. Thus, the result indicate as the porous medium becomes larger, a larger fraction of mass would settle in the column. This characteristic is the consequence of higher deposition sites available due to larger length as evident in the retention profile in the Figure B-1. This figure shows that while the nature of retention remains independent of column length, and the retention increases only due to increase in deposition sites. The result means that the upscaling of model, i.e., field-scale injection, requires an injection strategy for higher mobility of the ENPs.

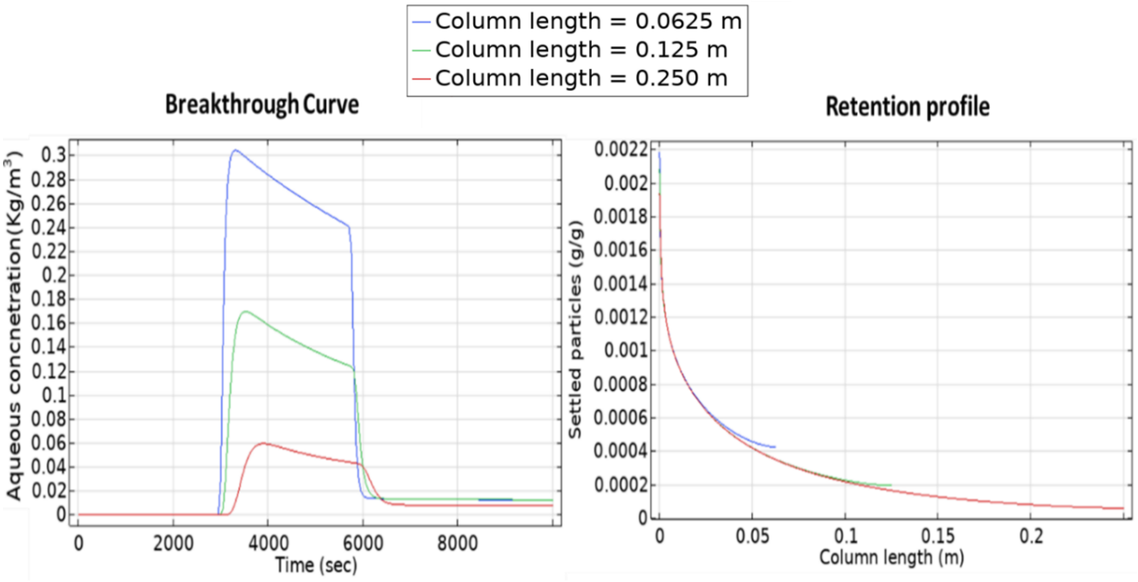

Figure B-1*: Model prediction of breakthrough curve (left plot) and retention profile (right plot) for three different values for the length of the column sand through which the nano-particle transport is simulated.*

B.2. Sensitivity analysis of Attachment rate (for ripening)

The model for sensitivity analysis of three different attachment rates, i.e., 0.00005 s^{-1}, 0.001 s^{-1} and 0.002 s^{-1}, has been run. Figure B-2 shows the predicted breakthrough curve illustrating a non-linear decrease in effluent concentration with respect to increase in attachment rate. For the attachment rate 0.00005 s^{-1}, 0.001 $s^{-1}$and 0.002 s^{-1}, the predicted mass coming out of the system is 40%, 30% and 14%, respectively. The breakthrough curve shows that the once the peak is obtained, the simulated nano-particle concentration decreases due to ripening. However, the non-linear decrease in effluent concentration with higher attachment rate shows the complex effect of ripening mechanism on particle mobility. The impact of ripening also reflects in retention profile which shows the settled particle significantly higher for higher attachment rate.

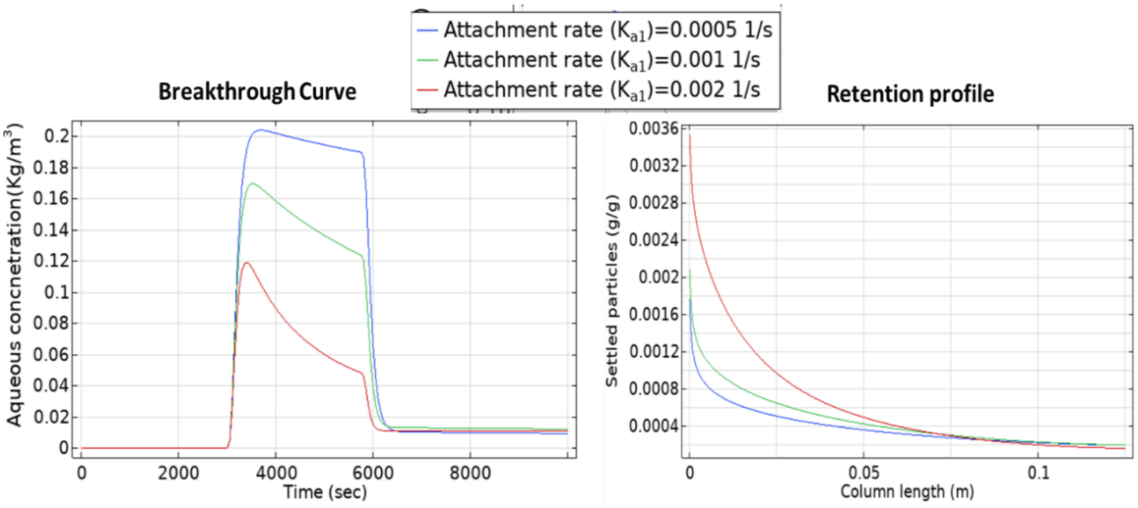

Figure B-2*: Model prediction of breakthrough curve (left plot) and retention profile (right plot) for three different values of attachment rate for the ripening mechanism.*

B.3 Sensitivity analysis of Detachment coefficient

Figure B-3 shows the model prediction for breakthrough curve and retention profile for different detachment coefficients. The breakthrough curve shows that the transport behavior of particle is relatively less sensitive to the change in detachment rate. Figure B-3 shows the effect of higher detachment rate reflecting as tailing effect in breakthrough curve. The retention profile also has a relatively less sensitive to detachment rate with lower settled particle concentration. The lower sensitivity of curves with the detachment coefficient can be attributed to lower base value of 6.810^{-5} s^{-1}.

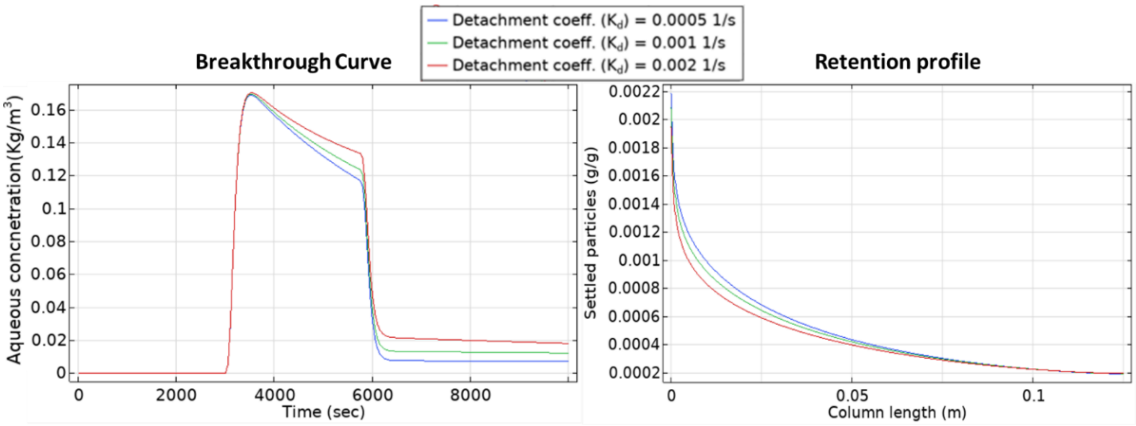

Figure B-3*: Model prediction of breakthrough curves (left plot) and retention profiles (right plot) for three different values of detachment coefficient for the ripening mechanism.*

B.4. Sensitivity analysis of multiplier coefficient

The multiplier coefficient has implications on the extent of ripening and blocking mechanism governing the retention of ENPs in the host rock. The positive value of multiplier coefficient indicates ripening behavior while negative value of multiplier coefficient represents blocking mechanism. The inverse model predicted the ripening behavior to be dominant, and the multiplier coefficient of 1050. A sensitivity analysis has been performed to see the change in characteristic for multiplier coefficient of 840, 1050 and 1250, respectively (Figure B-4). The breakthrough curve shows that the effluent concentration is moderately sensitive to the multiplier coefficient value. The model predicts a higher retention for higher multiplier coefficient as shown in the retention profile. For the multiplier coefficient value of 840, 1050 and 1260, the fraction of the effluent mass is 28%, 30% and 32%, respectively. The same figure shows a similar moderately sensitive retention profile with respect to multiplier coefficient is predicted by model.

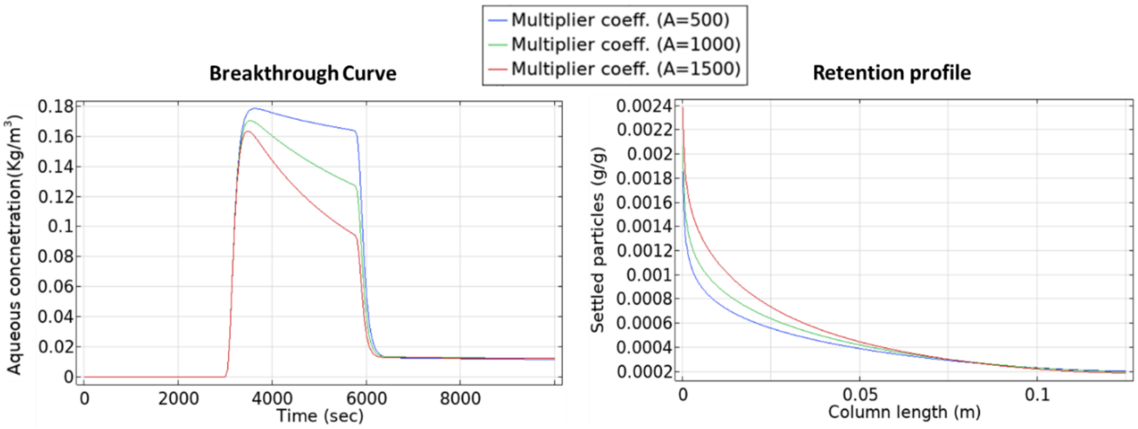

***Figure B-4**: Model prediction of breakthrough curves (left plot) and retention profiles (right plot) for three different values of multiplier for the ripening mechanism.*

B.5 Sensitivity analysis of attachment rate (for straining)

Figure B-5 shows a relatively high sensitivity of ENPs mobility on the attachment rate for straining as predicted by model. For the increasingly higher attachment rate, 0.0055 s^{-1}, 0.011 s^{-1}, and 0.022 s^{-1}, the estimated mass recovery is 36%, 29% and 9%, respectively. The plot shows that the retention profile exhibits an increase in the retention, with an increase in attachment rate, like that of ripening attachment rate. However, with the increase in the attachment rate, the simulated effluent concentration after the first arrival has a more gentle declining slope. The result thus indicates that with increase in attachment rate, the effect of straining mechanism on ENPs transport compared to ripening mechanism is higher. However, the ripening is overall dominant even for the highest attachment rate of straining, represented by red line. Therefore, the result implies that the transport dynamics in more sensitive to ripening mechanism compared to the straining mechanism.

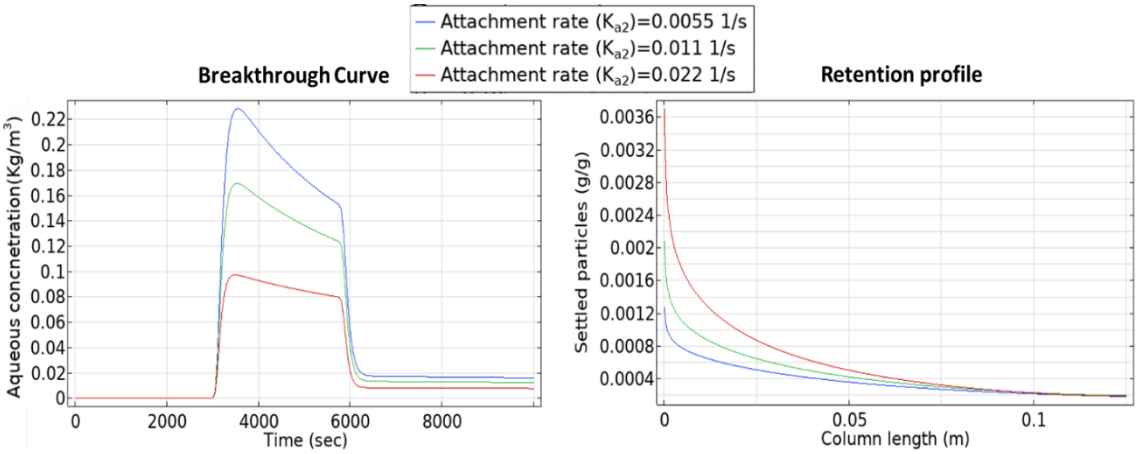

***Figure B-5**: Model prediction of breakthrough curves (left plot) and retention profiles (right plot) for three different values of multiplier coefficient for the straining mechanism*

B.6. Sensitivity analysis of exponential coefficient

The transport dynamics of ENPs is expected to be very sensitive to the exponential coefficient of both ripening and straining mechanism. Thus, the exponential coefficients are varied only withing the range of 20% from the base value. Figure B-6 shows the sensitivity of transport characteristics with respect to exponential coefficient of both the mechanisms. The effluent concentration appears to be highly sensitive to the exponential coefficients, with a non-linear inverse relationship, i.e., with the decrease in exponential coefficient, effluent concentration decreases. The model predicts the breakthrough curve and retention profile to be relatively higher sensitive to the exponential coefficient of the ripening (Figure B-6, a&b). The lower value of exponential coefficient shows a steeper slope of the breakthrough curve after attaining peak. Thus, the result predicts a higher intensity of ripening with decrease in exponential coefficient. For the exponential coefficient of straining, the transport dynamics is relatively less sensitive as shown in Figure B-6 (c&d). While the maximum deposition of ENPs is predicted for the exponential coefficient of b_2=0.0184, the breakthrough curve trend still indicates predominance of ripening mechanism. Thus, a comparative analysis of the transport and retention profile illustrates that the ripening process remain dominant irrespective of the values for exponential coefficient of straining.

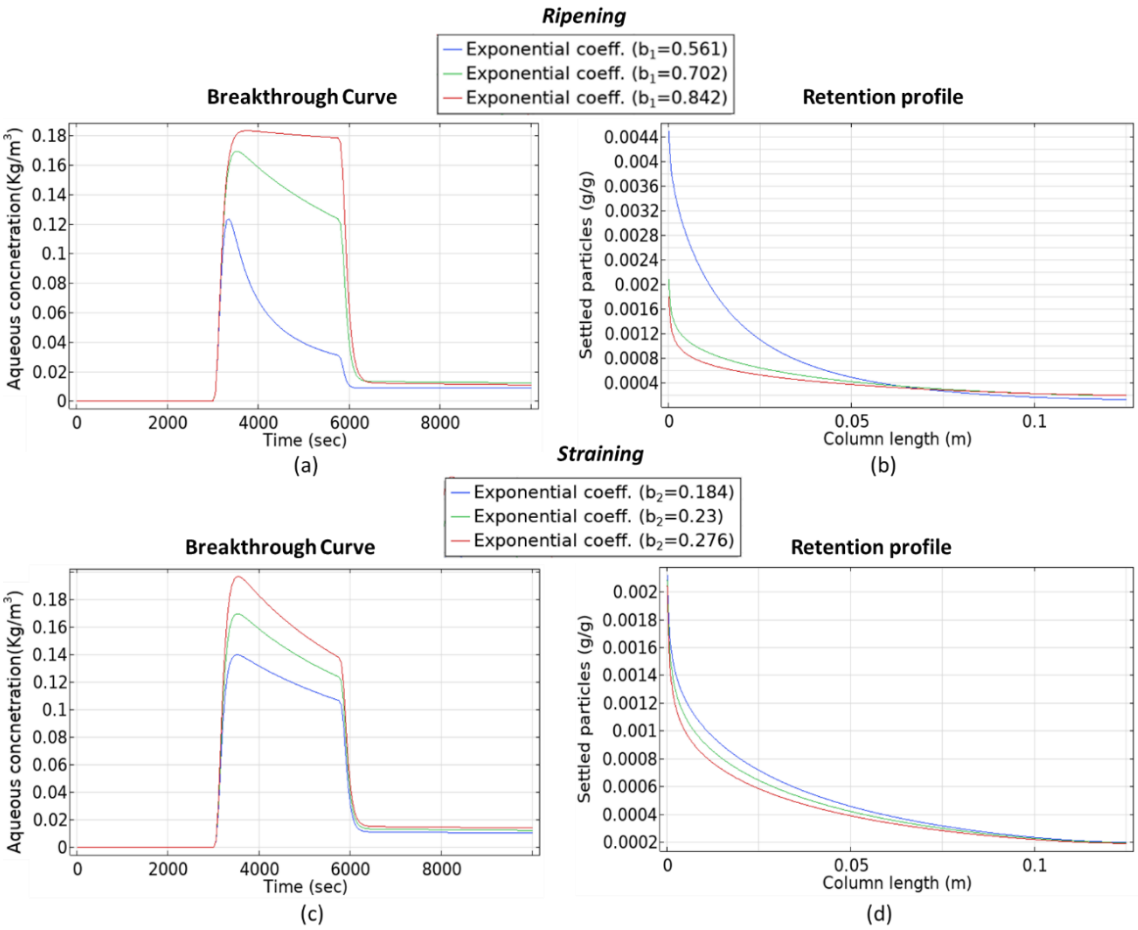

(a) (b) (c) (d)

Figure B-6: Model prediction of breakthrough curves and retention profiles for three different values of exponential coefficient for ripening mechanism (a & b), and straining mechanism (c & d)